Development of platino-iridium/ruthenium telluride nanoalloy electrode systems for possible application in ammonia fuel cell

RESPICE PROSPICE

UNIVERSITY of the
WESTERN CAPE

By

Noluthando Mayedwa

A thesis submitted in fulfilment of the requirements for the degree of Philosophiae Doctor in the Department of Chemistry, University of the Western Cape

Supervisor: Prof. Emmanuel I. Iwuoha

November 2015

Keywords

Alloys

Electrochemical characterization

Fuel cell materials

Nanomaterial

Electrocatalysis

Ammonia oxidation

Current density

Charge transfer resistance

Hydrogen

Overpotential

Development of platino-iridium/ruthenium telluride nanoalloy electrode systems for possible application in ammonia fuel cell

N. Mayedwa

PhD Thesis, Department of Chemistry, University of the Western Cape, November 2015.

Abstract

South Africa is undergoing a serious consideration of hydrogen economy in an effort to develop safe clean and reliable alternative energy sources for fossil fuels. Ammonia is one of the promising candidates due to its low production cost, ease in liquefaction at ambient temperatures, and high energy density as compared to methanol. Ammonia has a high content of hydrogen atoms per unit volume and can easily be cracked down into hydrogen and nitrogen. In the last four years carbon intensive coal dependent South Africa has become one of the leading global destinations for renewable energy investment. Another driving force behind the technology is the prevalence of platinum reserves found in South Africa. Platinum group metals are the key catalytic materials used in most fuel cells, and with more than 75 % of the world's known platinum reserves found within South Africa. In this thesis, I have developed novel electrocatalysts that are highly specific and selective for production of hydrogen using ammonia as a fuel source. The electro-oxidation of ammonia on platinum electrode drop coated platinum nanoparticles (PtNP), platinum iridium nanoparticles (PtIrNP), platinum ruthenium nanoparticles (PtRuNP), platinum telluride nanoparticles (PtTeNP) and ternary nanoparticles (PtIrTeNP) finally (PtRuTeNP) was systematically studied in alkaline solution of potassium hydroxide (KOH) by cyclic voltammetry (CV) and electrochemical impedance spectroscopy (EIS). The electrocatalysts were synthesised using sodium borohydride as a reducing agent and polyvinylpyrrolidone (PVP) as a stabilising agent from aqueous solutions of H_2PtCl_6/$IrCl_3$/$RuCl_3$/NaHTe mixtures. XRD confirmed that the binary and ternary electro-catalyst displayed characteristic patterns which indicated that all catalysts have shown the Pt face-centred-cubic (fcc) crystal structure and that the nanoparticles were poly-orientated. The structural characterization was further confirmed with FTIR and UV-vis, FTIR showed the most striking evidence that the PVP stabilized Pt presented a broad peak between 1288 cm^{-1} and 1638 cm^{-1} which corresponded to C-N stretching motion and C=O stretching motion of monomer for PVP, respectively. The narrow absorption peak centered at 1420 cm^{-1} and 2880 cm^{-1} occurred in which was ascribed to the C–H bonding due to the presence of PVP. This was due to the formation of coordinate bond between the nitrogen atom of the PVP and the Pt^{2+}, Ir^{3+}, Ru^{3+} and Te^{2+} ions. UV-vis was able to show the oxidation state of the nanoparticles and obtained an exponential graph shape which indicated complete reduction because there was no peak observed. Morphological characterization in the form of high resolution scanning electron microscope (HRSEM) revealed the formation of poly-orientated nanoparticles with average particle size of 23- 46 nm with slightly aggregated crystalline materials. The elemental composition of the alloy nanoparticles measured using energy dispersive spectroscopy (EDS) showed the presence of the four elements; Pt, Ir, Ru and Te. High resolution transmission electron microscopy (HRTEM) revealed the formation of crystalline non-aggregated 0.6-5 nm sized nanoparticles. The elemental composition of the alloy nanoparticles measured using energy dispersive X-ray (EDX) showed the presence of the four elements; Pt, Ir, Ru and Te. Selected area electron diffraction pattern (SAED) nanoparticles showed characteristic electron diffraction rings of Pt, PtIr, PtRu, PtTe, PtIrTe and PtRuTe, confirmed the phase and crystallinity of the materials. The electrocatalytic behaviour of the PtIrTe and PtRuTe nanoparticles for ammonia oxidation in KOH solution showed reduced overpotential properties and an increased current density compared to the bare Pt nanoparticles electrode thus providing a promising alternative for development of low-cost and high-performance electrocatalyst for electro-oxidation of ammonia. In terms of minimising the ammonia oxidation overpotential, catalyst selection were ranked as follows PtTe > PtRuTe > PtIr > PtRu > PtIrTe > Pt, with regards to maximising the exchange current density, the ranking was PtTe > PtIrTe > Pt > PtRu > PtIr > PtRuTe. The results were further interrogated with EIS which revealed in terms of minimising charge transfer resistance (R_{ct}) the nano catalysts selection were ranked as follows PtRuTe > PtIrTe > PtRu > PtIr > Pt > Bare Pt electrode > PtTe. That meant that the conductivity of the catalysts facilitated the flow of charge through the nanoalloys onto the surface of the electrode. The difference in charge transfer resistance revealed that PtRuTe and PtIrTe nanoalloys had an obvious advantage in reaction activity. The application of ternary metal nanoparticles had significantly enhanced the catalytic activity toward ammonia oxidation. The role of the third component (Te) had improved the catalysts in reducing N_{ads} adsorption on Pt. The enhanced catalytic activity has been attributed by a number of factors including the change in Pt–Pt inter atomic distance, number of Pt nearest neighbours, Pt 5d band vacancy, and Pt metal content on particle surface.

Dedication

I dedicate this thesis to

My late mother

Mrs. Thembeka Julia Myedi, my loving husband Mr. Mziwoxolo Mayedwa

&

My children Buhle Mayedwa (daughter) and Zwelande Tambo Mayedwa (son)

Declaration

I declare that *Development of platino-iridium/ruthenium telluride nanoalloy electrode systems for possible application in ammonia fuel cell* is my own work, that it has not been submitted for any degree or examination in any other university, and that all sources I have used or quoted have been indicated and acknowledged by complete references.

Noluthando Mayedwa **November 2015**

Signed...

Acknowledgements

I would like to thank the Creator of life and my ancestors (those who have been here on this earth before my existence by creating excellent choices to prepare the world to reserve me) for watching over me and giving me the strength throughout my studies and everything I do. Giving me an opportunity to use my life as an expression of gratitude towards the creator by doing meaningful things in this life, very grateful for the gift.

I wish to express my earnest appreciation to my supervisor Professor Emmanuel I Iwuoha for his guidance and encouraging words, for believing in me while I was an undergraduate student and recognising that I posses a potential to go as far as PhD. This project would not have been possible without the constant support from my supervisor always building my confidence to become the best I can be in academic world. Dr Tesfaye Waryo with whom I have worked very closely during my Msc who had helped me to develop further my expertise in electrochemistry in particular and scientific thinking in general. Dr Fanelwa Ajayi who is a very good friend of mine, we have a friendship that is very rare to find in this world. Always have words that are encouraging and always chooses to see the beautiful things in me and people in general, she has a very gently way of highlighting things I need to improve on. She is always willing to discuss my academic work anytime of the day accompanied with a sense of humour. I would like to thank Dr Brett Kuyper for taking his time to read and edit my grammar; I appreciate the time and effort.

I would like to appreciate members of sensor lab research group for their valuable input and suggestion throughout my research. My friends who have shown interest in my studies and engaged me with useful conversations that add valuable input to my research are in no particular order Dr. Nolubabalo Matinise, Dr. Masikini Milua, Dr. Oluwakemi Tovide, Dr.

Abebaw Tsegaye, Dr. Bilibana Mawethu, Dr. Hlamulo Makelani, Dr. Godfrey Fuku, Dr. Njagi Njomo, Dr. Chinwe Ikpo, Dr. Abdul A. Baleg, Abogile Jijana, Lindsay Wilson, Candice Rassie, Suru Vivian John, Xolani Ngema, Wonderboy Hlongwa, Sinazo Qakala, Francis N Muya and Lisebo Maruza Phelane

My two little sisters Zinziswa and Nomthandazo Myedi for constantly showing me the love and patiently behind me in every step that I take, they are my greatest supporters always praying and cheering for me. My older brothers Mxolisi and the late Lwandile Myedi for always telling me how I remind them of my late mother because I posses patience and always working hard. I am very resolute and I have a clear idea of what I want, there is no limit to reach my dreams while alive only death is the limit. They always told me they know I am special and I will do great things in this world, those words have contributed a lot in my life and have kept me centred.

Most of all I would like to acknowledge my late mother Thembeka Myedi who passed on 2006 before I could even obtain my bsc. She was a strong believer of education and knew that one day I will be educated. I want to thank her for her teachings and giving me necessary tools for survival in life. To also thank my late sister Nomaledi Myedi who passed away 2006 for showing me what is the meaning of education and opening doors for me to come to university, I will be forever grateful. I have lost so much in this world at the same time I have gained much more because of the teachings of all my late loved ones, I thank God every day for have giving me the chance to be part of their life no matter how short or long what counts I was there.

I wish to thank my loving husband Mziwoxolo Mayedwa for his support in my academics and life in general, this was all possible because of him. Always putting himself behind and pushing me forward, he is a true reflection of a strong man. Always taking care of our children in all possible ways you can imagine to give me a chance to do my academic work and make all my dreams come through. He believes so much in me even if I don't believe; he has been a positive role model in my life. He is a very hard working individual who never complains or feel discouraged, he knows why he is on this earth and what he is set out to do. I love you so much baby for being a breath of fresh air. Last but not least my beautiful children Buhle Mayedwa (daughter) and Zwelande Tambo Mayedwa (son) they are my everything. I thank God everyday for choosing me to be their mother, it is a great honour. It is prove from him that he has not given up on human kind by giving me a blessing of children. They are the reason I wake up each and every moment. They inspire me to be more than what I am and to also be a better mother on a daily basis.

To the South African Nuclear Human Assert Research Program (SANHARP) and Department of Science and Technology (DST), your financial assistance towards this research is hereby acknowledged.

Table of contents

List of Figures

List of tables

List of schemes

List of publications

Paper	**Status**
Hlamulo R. Makelane, Suru V. John, Tesfaye T. Waryo, Abd Baleg, **Noluthando Mayedwa**, Candice Rassie, Lindsay Wilson, Priscilla Baker, Emmanuel I. Iwuoha. AC-voltammetric Transductions and Sensor Application of a Novel Dendriticpoly(propylene thiophenoimine)-co-poly(3-hexylthiophene) Star Co-polymer. Sensors & Actuators: B. Chemical, 227 (2016) 320-327.	Published
Natasha Ross, Emmanuel I. Iwuoha, Chinwe O. Ikpo, Priscilla Baker, Njagi Njomo, Stephen N. Mailu, Milua Masikini, Nolubabalo Matinise, Abebaw Tsegaye, **Noluthando Mayedwa**, Tesfaye Waryo, Kenneth I. Ozoemena, Avril Williams. Amplification of the Discharge Current Density of Lithium-ion Batteries with Spinel Phase Li(PtAu)0.02 Mn1.98O4 Nano-materials. Electrochimica Acta, 128 (2014) 178-183.	Published
Njagi Njomo, Tesfaye Waryo, Milua Masikini, Chinwe O. Ikpo, Stephen Mailu, Oluwakemi Tovide, Natasha Ross, Avril Williams, Nolubabalo Matinise, Christopher E. Sunday, **Noluthando Mayedwa**, Priscilla G.L. Baker, Kenneth I. Ozoemena, Emmanuel I. Iwuoha. Graphenated Tantalum(IV) Oxide and Poly(4-styrene sulphonic acid)-doped Polyaniline Nanocomposite as Cathode Material in an Electrochemical Capacitor. Electrochimica Acta, 128 (2014) 226-237.	Published

Noluthando Mayedwa, Nolubabalo Matinise, Suru. V John, Emmanuel. I Iwuoha. Development of PtMeTe (Me= Ir, Ru) nanoalloy electrode system for electrocatalytic oxidation of ammonia in alkaline solution. Acta Materialia, (2015).	Submitted
Noluthando Mayedwa, Natasha West, Njangi Njomo, Hlamulo R. Makelane, Emmanuel I. Iwuoha. Structural and electrochemical studies of platinum based binary nanoalloys (PtIr, PtRu and PtTe) for electrocatalysis of ammonia in potassium hydroxide for hydrogen production. Electrochimica Acta, (2015)	Submitted
Noluthando Mayedwa, Emmanuel. I Iwuoha. Electrocatalytic effect of PVP capped Pt nanoalloys electrodeposited on Pt electrode for ammonia oxidation. Diamond & Related Materials, (2015)	Submitted
Noluthando Mayedwa, Tesfaye T. Waryo*, Emmanuel I. Iwuoha Electrochemical studies of conjugated dienes [1.3-Cyclohexadiene (CHD), 1.3-Cyclooctadiene (COD), 2-Methyl-1.3-Butadiene (MBD) and trans-1.3-Pentadiene (PD)] in acetonitrile. Chemical Engineering, (2016).	In preparation to Submit

List of conferences and workshops attended

- Material, Analytical and Physical Electrochemistry Today *Conference* (University of the Western Cape , 2015)
- Central Analytical Facilities, W*orkshop* on ICP-MS solutions. (Stellenbosch University, 2013)
- Energy Post Graduate *Conference* (EPC) (Ithemba Lab Cape Town, 2013)
- Woman in Nuclear South Africa (WINSA) *Conference* (NECSA Phelindaba, 2013)
- International Society of Electrochemistry (ISE) *Conference* (CSIR Pretoria, 2013)
- 2nd International *Symposium* on Electrochemistry: Electrochemistry for Energy. (University Of The WesternCape, 2012)
- Joined institute for nuclear research (JINR) international intergovernmental scientific research organization involving experimental studies in elementary particle physics, nuclear physics, and condensed matter physics. *Summer school* (Dubna University, Russia, 2012)
- South African Nuclear Human Asset and Research Programme (SANHARP Life skills *Workshop* (Pretoria 2012)
- SANHARP postgraduate *Conference* (Ithemba Lab, 2011)
- Department of Science and Technology Intern *Conference* (University of Pretoria, 2011)
- Electrochemical SA *workshop* (Nelson Mandela Metropolitan University, 2010)
- Annual Research Open Day For Post Graduate Students (University Of The WesternCape, 2010)

List of abbreviations

AFC	Alkaline Fuel Cell
CV	Cyclic Voltammetry
XRD	X-ray diffraction
R_{ct}	Charge transfer resistance
Ep,a	Peak anodic potential
Ep,c	Peak cathodic potential
Ip,a	Peak anodic current
Ip,c	Peak cathodic current
CPE	Constant phase element
PtIrTeNP	Platinum-iridium-telluride nanoparticles
I_o	Exchange current
˚C	Degree Celsius
EIS	Electrochemical impedance spectroscopy

CHAPTER 1

Summary

This chapter introduces the research topic of the thesis by highlighting the area where it was derived by specifying the main perspective. By giving a detailed background study of platinum group metals for the electrocatalysis of ammonia for fuel cell application, by reviewing current research, relevant history and previous research done on this issue to effectively show the relevance of the study. The research problem is given to give a concise description of issues that need to be addressed. The general and specific objectives of the research are set out and the hypothesis of the study highlighting the research approach, design and methodology. The thesis research outline and layout is given in this chapter with an overview of the structure of the thesis this will describe how the thesis will unfold and the main topic of each chapter of the thesis.

1.1 Background

In modern society there is an enormous demand for energy. There are several studies around the world that indicate that the crude oil and natural gas production rate in the planet will peak in the coming years. The reserves of the most abundant fossil fuel, coal are also limited. It is widely accepted that the use of fossil fuel causes an increase in CO_2 concentration in the atmosphere which will have dramatic consequences around the globe [14, 129, 167]. An unavoidable consequence of fossil fuels is the extensive/excessive use of fossil fuel in the transportation sector which have resulted in harmful effects on human health and welfare as well as the environment. Therefore, there is a strong need to come up with environmentally friendly and sustainable alternatives. Significant studies propose to convert the fossil fuels and renewable energy sources to hydrogen as an ideal synthetic fuel [86].

Fuel cells are emerging devices for electricity generation in a new economic era where energy is increasingly obtained from renewable sources. They have been reported to operate with higher efficiencies as compared to internal combustion engines. This is due to the direct conversion of chemical energy to electrical energy by electrochemical reaction [29] . Fuel cells are electrochemical energy conversion devices in which the fuel (e.g. hydrogen, methanol, ammonia etc) is supplied continuously to the anode where it is oxidised to release electrons, which are transferred to the cathode side through an external circuit, reducing the oxidant species usually oxygen. The efficiency of energy conversion in fuel cells is dependent on the catalytic activities of the catalyst material used at the electrode [9, 159]. Hydrogen is the main fuel source for power generation in fuel cells; however its low volumetric energy density is the main obstacle to its application in transportable devices and automobiles. To overcome this problem, hydrogen carriers such as methanol and sodium borohydride ($NaBH_4$) have been proposed as alternative fuels for fuel cell systems application. The growth of legislation promoting a hydrogen economy has made its production a very important aspect in the global scientific community.

Ammonia is one of the promising candidates due to its low production cost, ease in liquefaction at ambient temperatures, and high energy density [189]. Ammonia has a high content of hydrogen atoms per unit volume. It has also been used occasionally in the past as a fuel for internal combustion engines and fuel cells [160]. One mole of ammonia contains 1.5 mol of hydrogen which is 17.8 % by weight or 108 kg H_2. m^{-3} embedded in liquid ammonia at 20℃ and 8.6 bars. Note that this density is 4 times higher than that of the most advanced storage methods in metal hydrides which reach about 25 kg H_2. m^3 [149]. Most of the literature is devoted to the thermal decomposition or the catalytic cracking of ammonia into nitrogen and hydrogen, with fewer articles addressing electrolysis or electro-oxidation [34, 174]. Liu et al [105] proposed technology for the electrolysis of ammonia, which showed promising results for the production of high-purity hydrogen at much cheaper price. This process also had a much lower energy consumption when compared with water electrolysis [105]. The hydrogen evolution reaction for the production of high-purity hydrogen in an alkaline electrolytic cell is as follows [56, 174]:

$$2NH_3(aq) + 6OH \rightarrow N_2(g) + 6H_2O + 6e^- \ldots (1)$$

$$6H_2O + 6e^- \rightarrow 3H_2(g) + 6OH \ldots\ldots\ldots\ldots\ldots\ldots. (2)$$

$$2NH_3(aq) \rightarrow N_2(g) + 3H_2(g) \ldots\ldots\ldots\ldots\ldots\ldots.\quad (3)$$

In addition, the decomposition of ammonia by electro-oxidation provides a significant advantage in clean energy supply. [190]

The properties of Pt nanoparticles have been the subject of numerous studies in electrochemistry and catalysis not only because of the importance in the design of practical gas diffusion electrodes and catalyst but also for understanding of some interesting properties such as the influence of the size and surface structure of the nanoparticles on its electrocatalytic and catalytic properties [109]. Several studies have been devoted to the development of efficient electrocatalysts for ammonia oxidation in alkaline and neutral solutions. Platinum was regarded as the most active catalyst for this process; however it is expensive and becomes deactivated easily. Various bi and multi metallic catalysts was investigated e.g. Pt-Ir, Pt-Ir-Rh, Pt-Ru and Pt-Ni [62]. Ammonia electro-oxidation was studied using metal oxide electrodes, e.g. IrO_2 in alkaline and neutral solution, as well as PtO_x, IrO_x and Ni/NiO_x electrodes [61, 70, 132]. On metal oxides, besides N_2, the oxygenated nitrogen species (NO and N_2O) are formed. All above mentioned works were done using bulk metal or metal oxide electrodes with high precious metal loading. Whereas in order to develop efficient and economically viable electrodes, the amount of precious metals used need to be reduced. This can be achieved by using electrocatalysis in the form of nanoparticles dispersed on conductive supports [46].

The noble transition metals (Pt, Pd, Rh and Ir) are found to be the most active catalysts. However the coinage metals (Cu, Ag and Au) were found to be less active than the other transition metals and the metal oxides. Similarly to the oxidation in water, the most active catalyst for the selective oxidation to dinitrogen is iridium. The electrocatalytic activity for the ammonia oxidation varied in the order of Ru < Rh < Pd < Ir < Pt. This order in catalytic activity reflected the difference in the affinity of N_{ad} for the metal surface. The activity enhancement of Pt-based catalysts was achieved by using the Pt-M binary alloys (M = Ir, Ru) [54, 62, 77]. As described above, the ammonia oxidation in an alkaline aqueous solution was significantly affected by the formation of N_{ad} and the electrode materials. For direct ammonia fuel cells, however, the influence of these factors on the performance has not yet discussed in detail.

Tellurium adopts a polymeric structure consisting of a zig zag chains of Te atoms, the grey material resists oxidation by air and non volatile. It is primarily used in alloys to improve machinability, application in solar panels and as a semiconductor material also consume a considerable fraction of tellurium production. Tellurium as a semiconductor that shows a greater electrical conductivity in certain directions which depends on atomic alignment, the conductivity increases slightly when exposed to light (Photoconductivity) [25, 43]. Some significant features of platinum group metal compounds with tellurium primarily focusing on binary compounds. Their structural patterns are rationalised in terms of common structural systems. Some application of these compounds in catalysis and material science are described, and emerging trends in designing molecular precursors for the syntheses of these materials are highlighted [83].

The structural diversity and catalytic application of platinum group metals offer new avenues for research. Clear trends seem to be emerging in molecular precursor chemistry for the preparation of binary metal alloys. It is believed that such trends would provide opportunities to isolate not only known stable or metastable phases at low temperature but also as yet unknown stoichiometries [113]. Furthermore, tellurium is one of the metalloids and has particular interesting electronic properties, nanostructured metalloids/ semiconducting films with one or more critical dimension in the nanometer range can be expected to possess unusual electronic and optical properties. These may be of relevance to understanding the fundamental physics of low dimensionality structures and potentially to applications in sensors, optical devices and solar cells [124, 157, 164]. South Africa holds about 88 % of the total known platinum reserves, the future economic growth is tied of South Africa to a transition towards innovation, beneficiation and high technology development rather than simply just speeding up the extraction of non-renewable resources [49, 140]. This is the only way of building an effective and sustainable basis for South Africa over the long-term.

1.2 Problem Statement

Direct oxidation of ammonia is a lethargic reaction on noble metals and new electrocatalysts should be found to improve the behaviour of direct ammonia fuel cell. In spite of the fact that this reaction has been scrutinized for through many years, very few papers have been focused on the search of new electrocatalysts [135, 153]. Vidal-Iglesias et al [172] have shown that ammonia oxidation on platinum is an extremely surface sensitive reaction which takes place almost completely on surface sites with (100) symmetry [172]. Rosca et al [145] also studied the electrocatalytic oxidation of ammonia on Pt (111) and Pt (100) using various techniques to interrogate the behaviour of electrocatalyst [145].

Gerischer et al [72] proposed a widely accepted mechanism for ammonia oxidation that after the ammonia molecules being adsorbed is dehydrogenated to different adsorbed intermediate species. N_{ad} formed by further dehydrogenation remains strongly adsorbed on the surface acting as a poison [72].It is difficult to catalytically produce hydrogen from ammonia at low temperatures, in other words, it is hard to break the N-H bond in NH_3 at low temperature. For the anode reaction to happen in the ammonia fuel cell it is essential that the N-H bonds in NH_3 have to split to react with OH ions with aid of a good catalyst [54, 72]. New catalysts must be developed for this application because the available commercial catalysts do not meet the stringent limitations imposed by the current generation fuel cells and their operating conditions [148, 154].

1.3 Objectives of the research work

1.3.1 General objectives

The aim of this research is to develop novel electrocatalysts that are highly specific and selective for production of hydrogen using ammonia as a fuel source. The electrocatalysts will be prepared by synthesis of binary and ternary alloys from platinum group metals and telluride for ultra sensitivity for high performance fuel cell.

1.3.2 Specific Objectives

- Chemically synthesis of water soluble Te and characterized with ultraviolet visible (UV-vis) spectrometry.
- Chemically synthesis of binary nanoparticles Pt-Ir, Pt-Ru and Pt-Te and characterize with UV-vis, high resolution transmission electron microscope (HRTEM), x-ray diffraction (XRD) and high resolution scanning electron microscope (HRSEM).
- Immobilized by drop coating the binary nanoalloys on Pt working electrode for electrocatalysis of ammonia by voltammetry and impedance.
- Chemically synthesis of ternary nanoparticles Pt-Ir-Te and Pt-Ru-Te and characterize by microscopic (HRTEM, HRSEM), X-ray diffraction and spectroscopic (UV-vis) techniques.
- Applied ternary nanoalloys for electrocatalysis of ammonia by drop coating on Pt working electrode and used voltammetry and impedance for hydrogen production.

- Impedimetric studies included Nyquist modelling of cell responses in the presence and absence of ammonia, to suitable equivalent circle; and also the determination of the Bode electronic profile and frequency modulation of the reactivities of the electrode systems.

1.4 Hypothesis of the study

Ammonia is an important basic chemical and is produced at a scale of 150 million tons per year. Half of hydrogen produced in chemical industry is used for ammonia production. Ammonia contains 17.5 wt % hydrogen is an ideal carbon free fuel for fuel cells. Compared to hydrogen, ammonia has many advantages being the suitability of ammonia as a fuel for fuel cells, the development of different types of fuel cells using ammonia as the fuel and the potential applications of ammonia fuel cells [98]. Ammonia is a good energy vector for on board hydrogen storage [74]. However, safety is regarded as the major drawback of using ammonia as the fuel. Ammonia is toxic but it is detectable by humans in concentrations of just 1 ppm .anhydrous ammonia is lighter than air then tends to disperse in the atmosphere. Ammonia would be as safe as the use of gasoline as a transportation fuel [103, 178, 196]. The ammonia released from an ammonia tank during a car accident may cause potential safety problems but this can be solved through the application of metal amines with low ammonia partial pressure [152, 181]. Compared to hydrogen, ammonia is easier to be transported. It is much more energy efficient and much lower cost to produce, store and deliver hydrogen as ammonia than as compressed [51].

Many studies on the electrochemical ammonia oxidation over Pt electrode drop coated with platinum group metal nanoparticles in an alkaline aqueous electrolyte have been reported [6, 26, 45, 62, 77, 81]. As South Africa is the one of the world’s leading producer and exporters of platinum group metals, the beneficiation of platinum group metals (PGM) hold great promise. Thus a fundamental research investigation of nanostructured PGM catalyst there is vital. Noble metal nanoparticles with narrow size distribution are valuable technological importance because of the unique physiochemical properties and application in the field of catalysis [93, 125].

Narrow size distribution with a range of 1-100 nanometres (nm) is more effective than conventional catalysts because they yield a tremendous surface area to volume ratio. Secondly, when materials are fabricated at a nanoscale, they achieve properties not found within macroscopic counterparts accounting for versatility and effectiveness of nano-catalysts [100]. This research involves the synthesis of novel nano materials using platinum group metals and transitional metal to form binary and ternary nanoparticles for the catalysis of ammonia for application in high performance fuel cells. This is one of important developments that hold a great promise for South Africa in terms of beneficiation and application of PGM to be realised.

1.5 Research Framework

The framework is in accord with the general objectives of the research work.

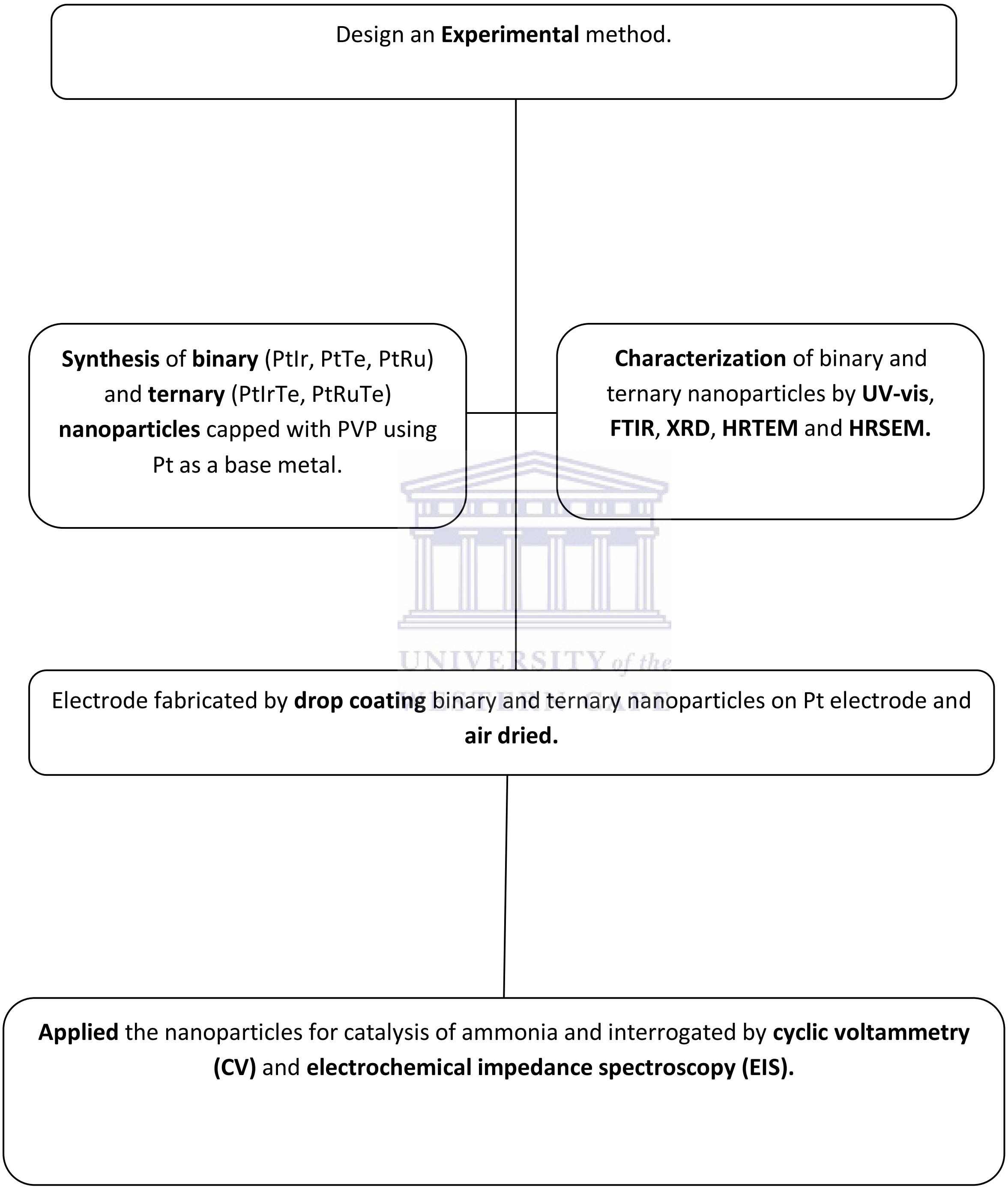

Design an **Experimental** method.

Synthesis of **binary** (PtIr, PtTe, PtRu) and **ternary** (PtIrTe, PtRuTe) **nanoparticles** capped with PVP using Pt as a base metal.

Characterization of binary and ternary nanoparticles by **UV-vis**, **FTIR**, **XRD**, **HRTEM** and **HRSEM.**

Electrode fabricated by **drop coating** binary and ternary nanoparticles on Pt electrode and **air dried.**

Applied the nanoparticles for catalysis of ammonia and interrogated by **cyclic voltammetry (CV)** and **electrochemical impedance spectroscopy (EIS).**

Scheme 1. 1: Research framework.

1.6 Thesis layout

- **Chapter 2:** Introduction to fuel cells and literature review. Presents a theoretical background of the research. Highlights different types of fuel cells classification which determines the kind of electro-chemical reactions that take place in the cell, the kind of catalysts required, and the temperature range in which the cell operates and fuel required. The electrocatalysis and structural effects have been highlighted; taking into account platinum based binary and ternary nano catalysts for ammonia oxidation. Non platinum based catalysts have been discussed more especially telluride and its properties and how can it enhance catalytic ability. Finally a detailed method of preparation of platinum based electrocatalysts have been explained and concluding the chapter gives an overview of the study in order to have a detailed understanding of the aims and objectives of the study by laying out a solid and relevant literature foundation.
- **Chapter 3:** Experimental. Procedure outlining the methods employed when producing Pt based nanoparticles, and the principles supporting the characterization techniques when testing the catalysts for oxidation of ammonia for the production of hydrogen.
- **Chapter 4:** Results and discussion of mono-metallic platinum-based nanoparticles catalysts outlining and discussing the results obtained from this study dealing specifically with the characterisation of monometallic Pt nanoparticles and its subsequent application in the oxidation of ammonia. Structural characterization was done with XRD and spectroscopic methods such as FTIR and UV-vis. Morphological characterization was carried out by HRTEM and HRSEM and the electrochemical properties of these nanoparticles were interrogated using techniques such as CV,

SWV and EIS. The potential application of the nanoparticles as electrocatalysts for ammonia electro-oxidation was further investigated.

- **Chapter 5:** Results and discussion of binary platinum-based nanoparticles catalysts, this is the second part of three chapters outlining and discussing the results obtained from this study. This chapter deals specifically with the characterisation of binary nanoparticles such as PtIr, PtRu and PtTe for its subsequent applications in the oxidation of ammonia. Characterized by spectroscopic methods such as FTIR, UV-vis, HRTEM, and HRSEM for morphological analysis and XRD for structural analysis. The electrochemical properties of these nanoparticles were interrogated using techniques such as CV, SWV and EIS. The potential application of the nanoparticles as electrocatalysts for ammonia electro-oxidation for fuel cell application was further investigated.
- **Chapter 6:** Results and discussion of ternary platinum-based nanoparticles catalysts, this is the third and final part of three chapters outlining and discussing the results obtained from this study. This chapter deals specifically with the characterisation of ternary nanoparticles such as PtIrTe and PtRuTe for its subsequent applications in the oxidation of ammonia. The chapter clearly illustrates how the nanoparticles were successfully characterized by spectroscopic methods such as FTIR, UV-vis, HRTEM, and HRSEM for morphological analysis and XRD for structural analysis. The electrochemical properties of these nanoparticles were interrogated using techniques such as CV, SWV and EIS. The potential application of the nanoparticles as electrocatalysts for ammonia electro-oxidation for fuel cell application was further investigated and concluded.
- **Chapter 7:** Outlines general conclusion of research work
- **Chapter 8:** References

CHAPTER 2

Summary

The literature review presented in this chapter covers an introduction to fuel cells, detailing South Africa as one of the leading global destinations for renewable energy investment. This is due to a serious consideration of hydrogen economy in an effort to develop safe clean and reliable alternative energy sources to fossil fuels. The chapter highlights different types of fuel cells classification which determines the kind of electro-chemical reactions that take place in the cell, the kind of catalysts required, and the temperature range in which the cell operates and fuel required. It will further discuss ammonia as an alternative fuel source as well as the problems and solutions associated with ammonia, taking in consideration of reaction mechanism of ammonia. The electrocatalysis and structural effects have been highlighted; taking into account platinum based binary and ternary nano catalysts for ammonia oxidation. Non platinum based catalysts have been discussed more especially telluride and its properties and how can it enhance catalytic ability. Finally a detailed method of preparation of platinum based electrocatalysts have been explained and concluding the chapter to give an overview of the study in order to have a detailed understanding of the aims and objectives of the study by laying out a solid and relevant literature foundation.

2.0 Literature review

2.1 Introduction of fuel cells

In the last four years carbon intensive coal dependent South Africa has become one of the leading global destinations for renewable energy investment. This investment can be attributed to the unprecedented take off of the country Renewable Energy Independent Power Producers Programme (RE IPPP). This organisation asserts that energy must be studied within the broader economic, political and social forces in which it is embedded [16]. South Africa is undergoing a serious consideration of hydrogen economy in an effort to develop safe clean and reliable alternative energy sources to fossil fuels [140].

Hydrogen is an energy carrier and is used to store and distribute energy and can be combined with the use of fuel cell technology to produce electricity. Another driving behind the technology is the prevalence of platinum reserves found in South Africa. Platinum group metals are the key catalytic materials used in most fuel cells, and with more than 75 % of the world's known platinum reserves found within South Africa [16, 140, 173]. There is a great potential for socio-economic benefits to be obtained from these natural resources.

Fuel cells are an electrochemical device that continuously converts the chemical energy in a fuel into electricity and heat. The basic component of a fuel cell consists of an electrolyte layer in contact with porous anode and cathode on either side [94]. Fuel cells are different from batteries in that they require a continuous source of fuel and oxygen or air to sustain the chemical reaction, whereas in a battery the chemicals present in the battery react with each other to generate an electromotive force. Fuel cells can produce electricity continuously for as long as these inputs are supplied [24, 118].

2.1.1 Types of fuel cells

Fuel cells are classified primarily by the kind of electrolyte they employ. This classification determines the kind of electro-chemical reactions that take place in the cell, the kind of catalysts required, the temperature range in which the cell operates, the fuel required, and other factors. These characteristics, in turn, affect the applications for which these cells are most suitable. There are several types of fuel cells currently under development, each with its own advantages, limitations, and potential applications [123]. A schematic representation of a typical proton exchange membrane fuel cell (PEMFC) with the reactant/product gases and the ion conduction flow directions through the cell is in (**Figure 2.1**) below [29].

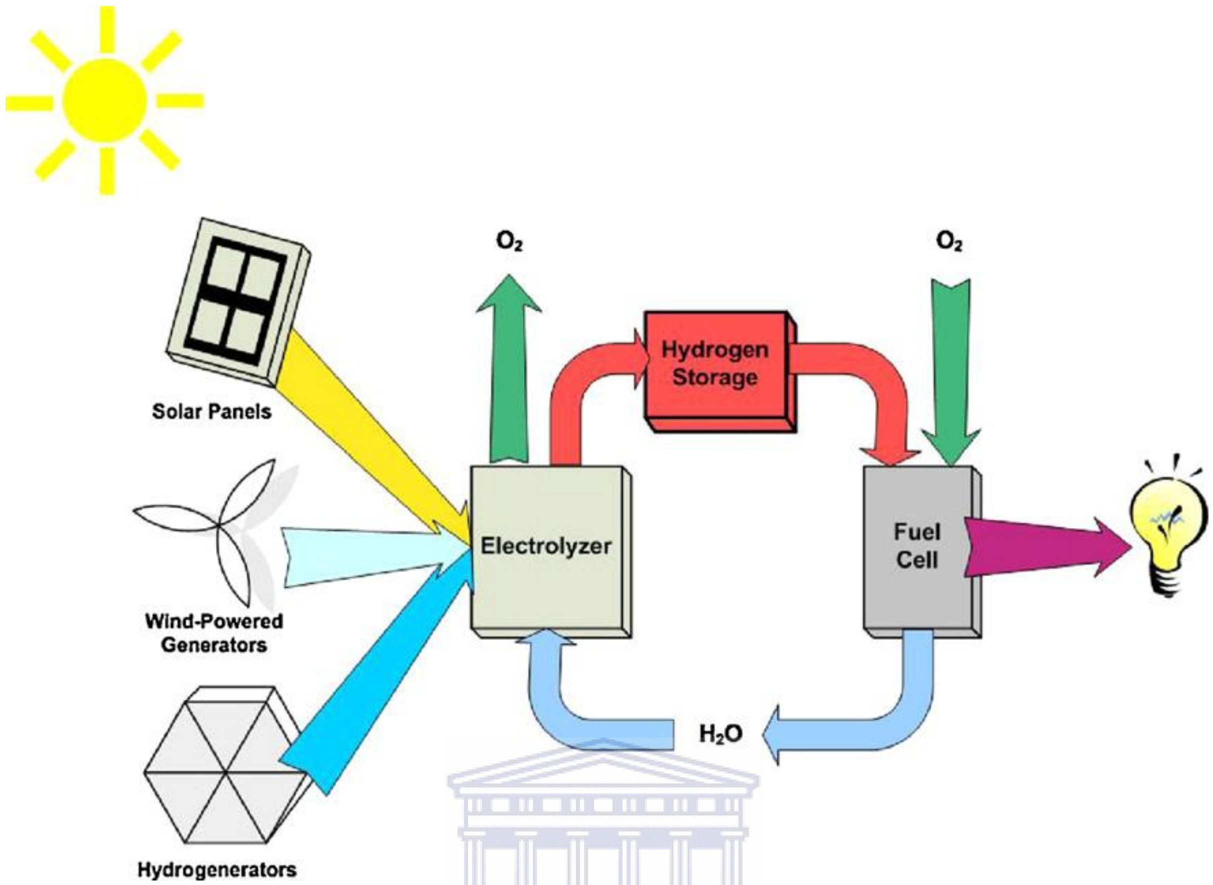

Figure 2. 1: Electricity production from renewable sources using hydrogen [29].

The fuel is fed continuously to the anode (negative electrode) compartment and an oxidant being the oxygen from air is fed continuously to the cathode (positive electrode) compartment, which is a typical process that takes place in a fuel cell (**Figure 2.1**) [168]. The electrochemical oxidation of the fuel at the anode generates electrons, which flow through an external load to the cathode. The electrons cause the electrochemical reduction of the oxidant at the cathode. The ions that are generated can be either positive or negative, meaning that an ion carries either a positive or negative charge (excess or shortage of electrons). In theory, any fluid can be used as a fuel source and can be subjected to oxidation at the anode. This hold true so long as the fluid is supplied continuously and its chemical oxidation is possible. Similarly, the oxidant can be any fluid that can be reduced at a sufficient rate, fuel can be pure hydrogen (H_2) and also any hydrocarbon such as natural gas, methanol, gasoline or even biomass if the fuel cell system is coupled with a fuel processor [37].

There are many types of fuel cell and they are as follows;

- Alkaline fuel cell (AFC),
- Proton exchange membrane fuel cell (PEMFC),
- Direct methanol fuel cell (DMFC),
- Molten carbonate fuel cell (MCFC),
- Phosphoric acid fuel cell (PAFC),
- Solid oxide fuel cell (SOFC).

Each fuel cell type has its own unique chemistry, such as different operating temperatures, catalysts, and electrolytes. A fuel cell operating characteristics help define its application – for example, lower temperature PEM and DMFC fuel cells are used to power passenger vehicles and forklifts, while larger, higher temperature MCFC and PAFC fuel cells are used for stationary power generation. Researchers continue to improve fuel cell technologies, examining different catalysts and electrolytes in order to improve performance and reduce costs. New fuel cell technologies, such as microbial fuel cells, are also being examined in the laboratory [37, 155] .

It is estimated that globally there are about 20 types of fuel cell technology being pursued: all are at various stages of development, with some already commercialised. The more established in the (**Table 2.1**) below [155].

Types	**Electrolyte**	**Fuel**	**Operating temperature (degree Celsius, ℃)**	**Power level, kW**	**Typical applications**
Alkaline fuel cell (AFC)	Potassium hydroxide	hydrogen	50-200	10-100	Space, power generation
Proton exchange membrane fuel cell (PEMFC)	Sulphonic acid incorporated into a solid membrane	hydrogen	50-90	0.01-1000	Transport, power supplies, CHP, distributed power
Direct methanol fuel cell (DMFC)	Sulphonic acid incorporated into a solid membrane or sulphuric acid solution	methanol	50-110	0.001-100	Portable electronic systems, mobile consumer electronics
Molten carbonate fuel cell (MCFC)	Molten lithium carbonate	hydrogen	630-650	1000-100 000	Large stationary power
Phosphoric acid fuel cell (PAFC)	Phosphoric acid	hydrogen	190-210	100-5000	CHP, power generation
Solid oxide fuel cell (SOFC)	Ceramic, solid oxide, zirconia	hydrogen or methane	700-1000	100-100 000	CHP, power generation, transport
Intermediate temperature SOFC(IT-SOFC)	Ceramic, solid oxide cera-gadolinia	hydrogen	500-650	100-100 000	CHP, power generation, transport

Table 2. 1: The main types of fuel cell technology.

2.1.2 Alkaline fuel cell (AFC)

While alkaline fuel cells typically use potassium hydroxide as the electrolyte others us an alkaline aqueous solution. These fuel cells usually operate at temperatures below 100 ℃. Depending on the application the electrolyte concentration, operating temperature and pressure of AFCs all vary. The fuel cell produces power through a redox reaction between hydrogen and oxygen. At the anode, hydrogen is oxidized according to the reaction:

$$2\mathrm{H_2} + \ 4\mathrm{OH^-} \ \rightarrow 4\mathrm{H_2} + \ 4\mathrm{e^-} \ \ldots\ldots\ldots.(\text{anode reaction})$$

Producing water and releasing two electrons. The electrons flow through an external circuit and return to the cathode, reducing oxygen in the reaction:

$$\mathrm{O_2} + \ 2\mathrm{H_2O} + 4\mathrm{e^-} \ \rightarrow 4\mathrm{OH^-} \ldots\ldots\ldots..(\text{cathode reaction})$$

$$2\mathrm{H_2} + \ \mathrm{O_2} \ \rightarrow 2\mathrm{H_2O} \ldots\ldots\ldots\ldots\ldots\ldots\ldots..(\text{overall reaction})$$

The net reaction consumes one oxygen molecule and two hydrogen molecules in the production of two water molecules. Electricity and heat are formed as by-products of this reaction [119].

This fuel cell was the first generation system that was used by NASA in the 1960s for space missions. It was employed as a power source in form of electrical energy for space vehicles and water on-board spacecraft. However because the presence of carbon dioxide degraded the cell performance, the stationary application that used hydrocarbon fuels was limited Since alkaline fuel cells are poisoned easily by small quantities of CO_2 and are thus deployed primarily in controlled aerospace and underwater environments.

Cost was less of a factor for remote locations, such as in space or under the sea. However, to compete effectively in most mainstream commercial markets, these fuel cells had to become more cost-effective. To be economically viable in large-scale utility applications, AFCs needed to reach operating times exceeding 40,000 hours, something that has not yet been achieved due to material durability issues. This obstacle is possibly the most significant in commercializing this fuel cell technology [13, 19, 95].

2.1.3 Proton exchange membrane fuel cell (PEMFC)

Proton exchange membrane fuel cell (PEMFC) are straight forward, the chemical energy present in a fuel usually hydrogen and an oxidant, oxygen is cleanly, silently and efficiently converted directly into electrical energy. The hydrogen was oxidised at the anode and the oxygen reduced at the cathode of a single cell. The power required in fuel cell technology was achieved by combining a number of single cells in series to produce a fuel cell stack, and a number of stack modules are then combined in series to produce the power plant. Hydrogen was delivered to the anode side of the membrane electrode assembly (MEA) and at the anode side it was catalytically split into protons and electrons. The hydrogen oxidation reaction is represented as;

$$\mathrm{H_2} \rightarrow 2\mathrm{H^+} + 2\mathrm{e^-} \dots\dots\dots \text{(anode reaction)}$$

The protons permeate through the polymer electrolyte membrane to the cathode side. Once there the oxygen molecules react with the protons permeating through the polymer electrolyte membrane. The electrons arriving through the external circuit to form water molecules. The oxygen reduction reaction is represented as;

$$\frac{1}{2}O_2 + 2H^+ + 2e^- \rightarrow H_2O \ldots\ldots\ldots \text{(cathode reaction)}$$

$$H_2 + \frac{1}{2}O_2 \rightarrow H_2O \ldots\ldots\ldots\ldots\ldots\ldots... \text{(overall reaction)}$$

PEMFCs operate at relatively low temperatures with a high power density and the output can be varied quickly to meet shifts in power demand. PEMFCs are well-matched to power applications where a quick start-up is required such as automobiles or forklifts [194-195].

The membrane electrode assembly (MEA) is at the heart of the single cell, it is the critical component of the PEMFC, since it is the site of the fuel cell reactions. The MEA is less than a millimetre thick and consists of a solid polymer, proton conducting membrane electrolyte, with a layer of platinum-based catalyst. A gas-porous electrode support material on both sides of it, forming the anode and cathode of the cell. The membrane electrolyte is typically bonded to the electrodes by hot pressing at a temperature above the glass transition temperature of the membrane [102, 106]. High-temperature PEM fuel cells are similar to PEM fuel cells, but operate at higher temperatures, between 121.1 ℃ and 198.9 ˚C. High temperature PEMs are often integrated with fuel reformers, permitting operation using wider variety of input fuels. High temperature PEMs can be used to power vehicles as range extenders for batteries, and small scale commercial buildings and homes [35, 111].

2.1.4 Direct methanol fuel cell (DMFC)

Most fuel cells are powered by hydrogen, which can be fed to the fuel cell system directly or can be generated within the fuel cell system by reforming hydrogen-rich fuels such as methanol, ethanol, and hydrocarbon fuels. Direct methanol fuel cells (DMFCs), however, are powered by pure methanol, which is usually mixed with water and fed directly to the fuel cell anode. DMFCs are similar to PEM fuel cells in that they both use a polymer membrane as the electrolyte. However, in DMFC systems the anode catalyst itself draws the hydrogen from liquid methanol, thus eliminating the need for a fuel reformer. The low operating temperature DMFCs makes them attractive for small applications such as cell phones, laptops and battery chargers for consumer electronics, to mid-size applications powering electronics on RVs, boats, or camping cabins [116]. The equations that driving these cells are as follows;

$$\mathrm{CH_3OH} + \mathrm{H_2O} \rightarrow 6\mathrm{H^+} + 6\mathrm{e^-} + \mathrm{CO_2} \ldots\ldots\ldots \text{(anode reaction)}$$

$$\frac{3}{2}\mathrm{O_2} + 6\mathrm{H^+} + 6\mathrm{e^-} \rightarrow 3\mathrm{H_2O} \ldots\ldots\ldots\ldots\ldots\ldots. \text{(cathode reaction)}$$

$$\mathrm{CH_3OH} + \frac{3}{2}\mathrm{O_2} \rightarrow 2\mathrm{H_2O} + \mathrm{CO_2} \ldots\ldots\ldots\ldots\ldots. \text{(overall reaction)}$$

In order to improve the performance of the DMFC it is necessary to eliminate or reduce the loss of fuel across the cell which is usually termed methanol crossover. Membrane technology is one of the alternatives used to try and solve this problem. Direct methanol fuel cells do not have many of the fuel storage problems typical of other fuel cell systems. This is because methanol has a higher energy density than hydrogen even though it is less than gasoline or diesel fuel. Methanol is also easier to transport and supply to the public using current infrastructure-because it is a liquid, like gasoline. DMFCs are often used to provide power for portable fuel cell applications such as cell phones or laptop computers [64, 85, 120, 128].

2.1.5 Molten carbonate fuel cell (MCFC)

Molten carbonate fuel cells use carbonate salts of alkali metals as the electrolyte. Due to the highly corrosive nature of the electrolyte, various counter measures have been developed.

MCFCs are expected for high-efficiency power generation systems using hydrocarbon fuels, such as natural gas and coal gas. Since MCFC operate at extremely high temperatures of 650℃ and above, non precious metals can be used as catalysts at the anode and cathode which reduces costs drastically. The high operating temperatures of MCFCs means that hydrocarbon fuels can be converted to hydrogen within the fuel cell itself meaning it is internally reforming. MCFCs are not prone to CO or CO_2 poisoning because they can even use carbon oxides as fuel making them more attractive for fuelling with gases made from coal [11, 38, 115]. The electrochemistry occurring in the cell is as follows;

$$2H_2 + 2CO_3^{2-} \rightarrow 2H_2O + 2CO_2 + 4e^- \ldots\ldots\ldots.. \text{(anode reaction)}$$

$$2CO_2 + O_2 + 4e^- \rightarrow 2CO_3^{2-} \ldots\ldots\ldots\ldots\ldots\ldots\ldots. \text{(cathode reaction)}$$

$$2H_2 + O_2 \rightarrow 2H_2O \ldots\ldots\ldots\ldots\ldots\ldots\ldots\ldots\ldots\ldots\ldots\ldots \text{(overall reaction)}$$

MCFCs are ideal for large stationary power and are available as commercial products, with dozens of power plants deployed at food and beverage processing facilities, manufacturing plants, hospitals, prisons, hotels, colleges and universities, utilities, and wastewater treatment plants worldwide. One of the big advantages is that MCFCs are more resistant to impurities than any other fuel cell. However, the main disadvantage of MCFCs is their durability. The extremely high temperature at which these cells operate and the corrosive electrolyte used accelerates breakdown and corrosion thereby decreasing the cell life [33, 57, 65, 170].

2.1.6 Phosphoric acid fuel cell (PAFC)

Phosphoric acid fuel cell (PAFC) is a type of fuel cell that uses liquid phosphoric acid as an electrolyte. They were the first fuels to be commercialized, developed in the mid 1960s and field tested since the 1970s. Since then they have improved significantly in stability, performance and cost. A substantial number of natural gas fuelled 200 kW PAFC systems are already in operation. Also, numerous examples of plant experience are available. Although PAFCs have evolved to where the performance reliability and other engineering parameters required of practical power plants are to a considerable degree satisfactory, further refinement is required for economic market penetration. PAFCs can operate using reformed hydrocarbon fuels or biogas. Anode and cathode reactions are similar to PEMs, but since operating temperatures are higher, PAFCs are more tolerant of fuel impurities. PAFCs are frequently used in a cogeneration mode, in which by-product heat is captured for onsite heating, cooling, and hot water also called combined heat and power. PAFCs are commercially available today with systems operating around the world at high-energy demand sites such as hospitals, schools, office buildings, grocery stores, manufacturing or processing centres, and wastewater treatment plants [44].

PAFCs require Pt catalyst and the fact that it requires an expensive platinum catalyst raises the cost of the fuel cell. Another problem associated with PAFC is electrode flooding and drying and this has been recognized as the major cause of the declining cell performance. Migration of H_3PO_4 between the matrix and the electrodes during cell load cycling is a further contributing factor responsible for these problems. Recent studies have shown that by introducing H_3PO_4 into polymer bearing functional groups like alcohols, amides, imines or ethers the cell performance can be improved [117, 161].

2.1.7 Solid oxide fuel cell (SOFC)

Solid oxide fuel cells operate in a temperature region between 650 °C and 1000 °C by using an oxygen ion conductor as the electrolyte. The ionic transported species are oxygen ions that allow the use of hydrogen and carbon monoxide as well as directly applied methane as fuels while the oxidant is oxygen provided by air. The state-of-the art SOFC consists of an yttria-stabilized zirconia (YSZ) electrolyte, a ceramic metallic composite, a Ni-YSZ cermets as the fuel electrode and a ceramic composite of strontium doped lanthanum manganite and YSZ as the air electrode. The SOFC is, therefore, an all-solid state system for which different designs may apply. High-temperature SOFCs are capable of internal reforming of light hydrocarbons such as natural gas, but heavier hydrocarbons (gasoline, jet fuel) can be used, though they require an external reformer [151].

There are two configurations of SOFC fuel cell systems: one type uses an array of meter-long tubes, and another uses compressed discs. Tubular SOFC designs are closer to commercialization and are being produced by companies around the world. SOFCs are suitable for large stationary applications, and are being deployed across the country at data centres, office buildings and retail stores. SOFCs are also being demonstrated for use as vehicle auxiliary power units and tested for small stationary applications. Scientists are currently exploring the potential for developing lower-temperature SOFCs operating at or below 700 °C that have fewer durability problems and cost less. Lower-temperature SOFCs have not yet matched the performance of the higher temperature systems, however, and stack materials that will function in this lower temperature range are still under development [151].

2.2 Ammonia as an alternative fuel source

Ammonia provides high hydrogen storage densities as a liquid with mild pressurization and cryogenic constraints: It can also be stored as a liquid at room temperature and pressure when mixed with water. Ammonia is the second most commonly produced chemical in the world and a large infrastructure for making, transporting, and distributing ammonia already exists. Ammonia can be reformed to produce hydrogen with no harmful waste, or can be mixed with existing fuels and under the right conditions burn efficiently [51-52]. Ammonia decomposition to produce hydrogen can be represented by the following equation [41].

$$\mathrm{NH_3} \rightarrow 1.5\mathrm{H_2} + 0.5\mathrm{N_2}$$

This reaction is carried out in a temperature range of 793–853 K and a pressure range of 1–2 bar using a Ni-Pt catalyst. This reaction is endothermic with a heat of reaction of 46 kJ .mol^{-1} of ammonia. In the temperature range stated above, the reaction is irreversible and the reaction rate is represented [41].

Alagharu et al [1] discussed the reaction engineering principles utilized to analyze process conditions for producing sufficient hydrogen in an ammonia decomposition reactor for generating net power of 100 W in a fuel cell. It was shown that operating the reactor adiabatically results in a sharp decrease in temperature due to the endothermic reaction, which resulted in low conversion of ammonia. For that reason, the reactor was heated electrically to provide heat for the endothermic reactions. It was observed that when the reactor was operated in non-adiabatically, it was possible to get over 99.5 % conversion of ammonia. The weight of absorbent to reduce ammonia to ppb levels was calculated. An energy balance on the reactor exit gas indicates that there was sufficient heat available to vaporize enough water to achieve 100 % relative humidity in the fuel cell. A suitable fuel cell stack was designed and it was shown that this stack is able to provide the necessary power to electrically heat the reactor and produced net power of 100 W [1].

2.2.1 Problems and solutions associated with ammonia as an energy source

There are problems related to hydrogen as a fuel source which are difficult to overcome which relates to the fact that hydrogen provides extremely low quantities of energy per unit of volume as compared to the conventional fuels used in transportation vehicles. Another problem is that development of the hydrogen distribution infrastructure includes complicated safety issues because hydrogen is volatile and has wide flammability limits, presenting high explosion danger and its flame is invisible [97].

To overcome these problems the hydrogen has been stored and transported via other chemical compounds such as alcohols, hydrocarbons, ammonia etc. In many ways ammonia is an excellent hydrogen carrier [97, 138];

- Liquid ammonia represents a convenient way of storing supplies of hydrogen, boasting specific energy density (kW .h1^{-1}) 50 % higher than liquefied hydrogen.
- Ammonia is also easily condensed at ambient temperature (under 8 bars of pressure), which makes it a good choice for transportation and storage.
- Even though ammonia is flammable with in defined limits 16-25 % by volume in the air and toxic above 25 ppm, its presence can be detected by its characteristic odour above 5 ppm.

- Ammonia is produced worldwide in large quantities more than 100 million ton .year^{-1}, which allows the effect of economy of scale on the cost of production.
- The decomposition of ammonia by electrooxidation in alkaline media at low overpotential is NO_x and CO_x free with nitrogen and water as products of reaction.

The feasibility of ammonia as a fuel source depends on two factors:

1) Development of green and efficient methods of synthesizing ammonia.

2) Development of technologies to burn it in power generation plants [187].

The fact that ammonia is already a widely produced and used commodity with well established distribution and handling procedures would allow for its smooth transition as an alternative fuel (**Table 2.2**) below.

Fuel	**Density, kg.L^{-1}**	**LHV MJ.kg^{-1}**	**LHV MJ. L^{-1}**	**H_2 Density kgH_2. m^{-3}**	**% H_2 Energy**
Ammonia	0.76	18.6	14.1	136	100
Diesel	0.84	42.8	35.8	126	42
Methane	0.47	50.1	23.3	116	58
Gasoline	0.70	42.5	29.8	110	44
Propane	0.51	45.8	23.2	106	48
Ethanol	0.78	27.0	21.1	102	59
Methanol	0.79	20.1	15.9	98	75
Hydrogen	0.07	120.1	8.4	70	100

Table 2. 2: Comparison of energy efficiency of ammonia and other alternative fuel sources with other different properties.

2.2.2 Reaction mechanism of ammonia decomposition

Electrolysis or electro-oxidation is another method of extracting hydrogen from ammonia. It has the advantage of scalability and versatility to interface with renewable energy sources including those whose electricity production varies with time [32, 160]. Hydrogen can also be produced at moderate temperatures. It was first discussed by Vistse et al [174] proposed the coupling of ammonia oxidation in an alkaline medium at the anode with the reduction of water at the cathode [174]. Various studies have investigated the reaction mechanism of ammonia decomposition; the original idea presented here consists of the coupling of the ammonia electro-oxidation reaction with the hydrogen evolution reaction for the production of high-purity hydrogen in an alkaline electrolytic cell [66, 172, 174]:

$2NH_3\,(aq) + 6OH^- \rightarrow N_2(g) + 6H_2O + 6e^-$ (1)

$6H_2O + 6e^- \rightarrow 3H_2\,(g) + 6OH^-$ (2)

$2NH_3\,(aq) \rightarrow N_2\,(g) + 3H_2\,(g)$ (3)

At 25 ^{o}C the ammonia oxidation potential is −0.77 V versus the standard hydrogen electrode (SHE), only 0.06 V less negative than the value of −0.83 V versus SHE for hydrogen evolution in alkaline solution. Therefore, thermodynamic values are in favour of the production of hydrogen coupled to the oxidation of ammonia compared to hydrogen production by electrolysis of water, for which the theoretical cell voltage is 1.223 V. The advantage of this process is its ease of integration with renewable energy sources. Because the energy consumption is low, the cell could operate with renewable energy (or by stealing part of the energy of a PEM hydrogen fuel cell if the ammonia electrolytic cell operates close to the theoretical potential) [32, 172, 189].

2.2.3 Ammonia as an enabler for stranded renewable energy sources

Most of the renewable energy sources such a solar or wind has very low capacity factors (10-30 %). This requires a backup power system instead of connecting to the grid (utilities companies would charge for this), by the use of excess power to make ammonia which can be stored and burned in a micro turbine to generate electricity and heat when needed. This required the development of an efficient synthesis technology for ammonia (from water and air).Since ammonia is a widely used fertilizer, it is used in electricity generation in rural/agricultural areas makes perfect economical sense [29]. This is an established distribution and handling measures that would permit for smooth transition of ammonia as an alternative fuel source is (**Figure 2.2**) below.

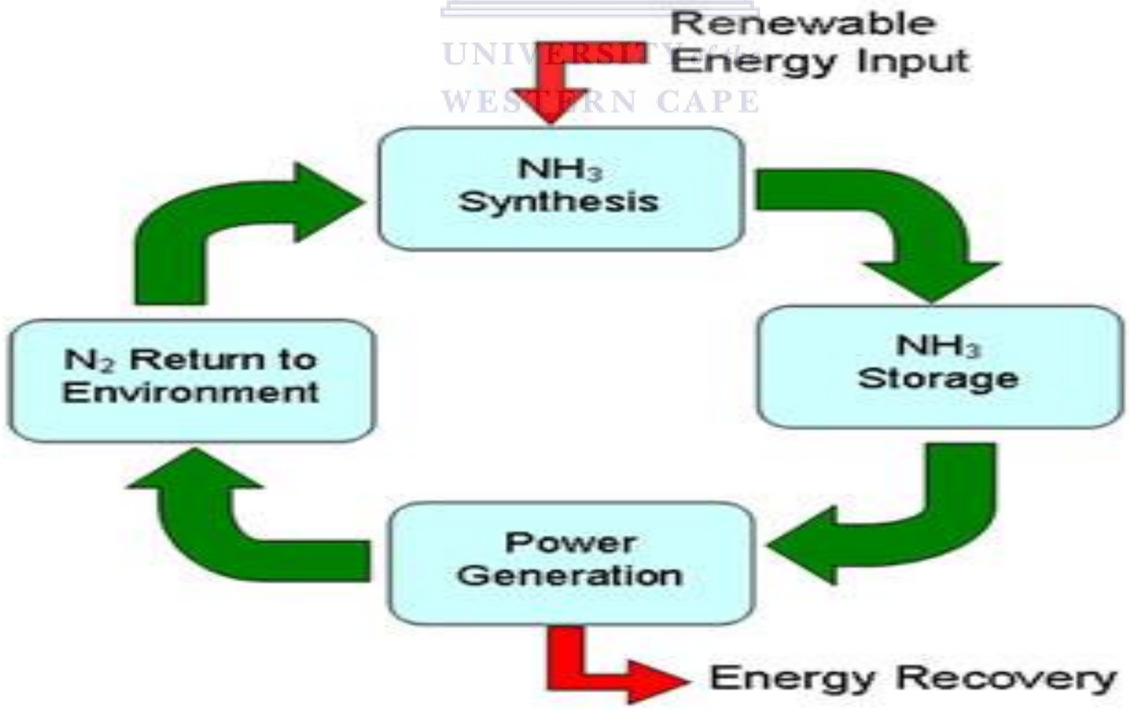

Figure 2. 2: Established distribution and handling procedures allowing a smooth transition of ammonia as an alternative fuel.

Stranded renewable energy sources are most of the renewable energy sources such as solar, geothermal or winds are not accessible by the existing electric grid system. Extending the grid to remote areas is not economical. In most cases the extension of the grid system is politically difficult (if not impossible). Ammonia as an energy carrier has the potential to solve the stranded renewable energy problem. Using a synthesis method such as solid state ammonia synthesis (SSAS) ammonia can be produced at the stranded site from water and air. The produced ammonia can be shipped via trucks, railroad or pipelines to the power generation plants to generate electricity [29].

2.3 Electrocatalysis

2.3.1 Introduction of electrocatalyst

Electrocatalysis is a special field in Electrochemistry that has gained a special growth after the late eighties. This is due to the application of new hybrid techniques with in this discipline. However, most of the applications have been run for academic purposes and not for technical uses in the industry. Nowadays the application of new concepts of electrocatalysis for industrial electrochemical processes has appeared as a necessity field. This has began attracting attention of not only chemists but also engineers [176].

An electrocatalyst is a catalyst that involves the use of some electrical current as well. So they are materials in which an electrochemical reaction involved. An electrochemical reaction is where there is a chemical reaction taking place, but its either putting out some electrical power or it requires some electrical power to run it. Electrocatalysts are a precise form of catalysts that function at the electrode surfaces or maybe the electrode surfaces itself. The electrocatalyst assists in transferring electrons between the electrode and reactants, and facilitates an intermediate chemical transformation described by an overall half-reaction. An electrocatalyst can be heterogeneous such as a platinum surface or nanoparticles or homogeneous like a coordination complex or enzyme [55, 169].

The industrial electrocatalytic processes have only been presented in the literature from the chemical engineering point of view with few further electrochemical explanations and mainly during the late seventies. The design and preparation of an electrocatalyst (electrodes for technological uses) are based on new concepts such as a controlled surface roughness, atomic topographic profiles, defined catalytic centre sites, atomic rearrangements, and phase transitions in the course of the electrochemical reactions [55, 169].

2.3.2 The effect of electrocatalysts on reaction rate

Chemical reactions require a specific amount of energy to facilitate them to proceed to completion at a reasonable rate. This energy barrier is described as the activation energy and can cause potential problems for some reactions if it is too high. Electrocatalysts are substances that lower this activation energy, thus causing an increase in the rate at which the reaction occurs Collisions only result in a reaction if the particles collide with a certain minimum energy called activation energy for the reaction. To increase the rate of a reaction you need to increase the number of successful collisions. One possible way of doing this is to provide an alternative way for the reaction to happen which has a lower activation energy. Adding a catalyst has exactly this effect on activation energy [55]. A catalyst provides an alternative route for the reaction. That alternative route has lower activation energy. Showing this on an energy profile in (**Figure 2.3**) below.

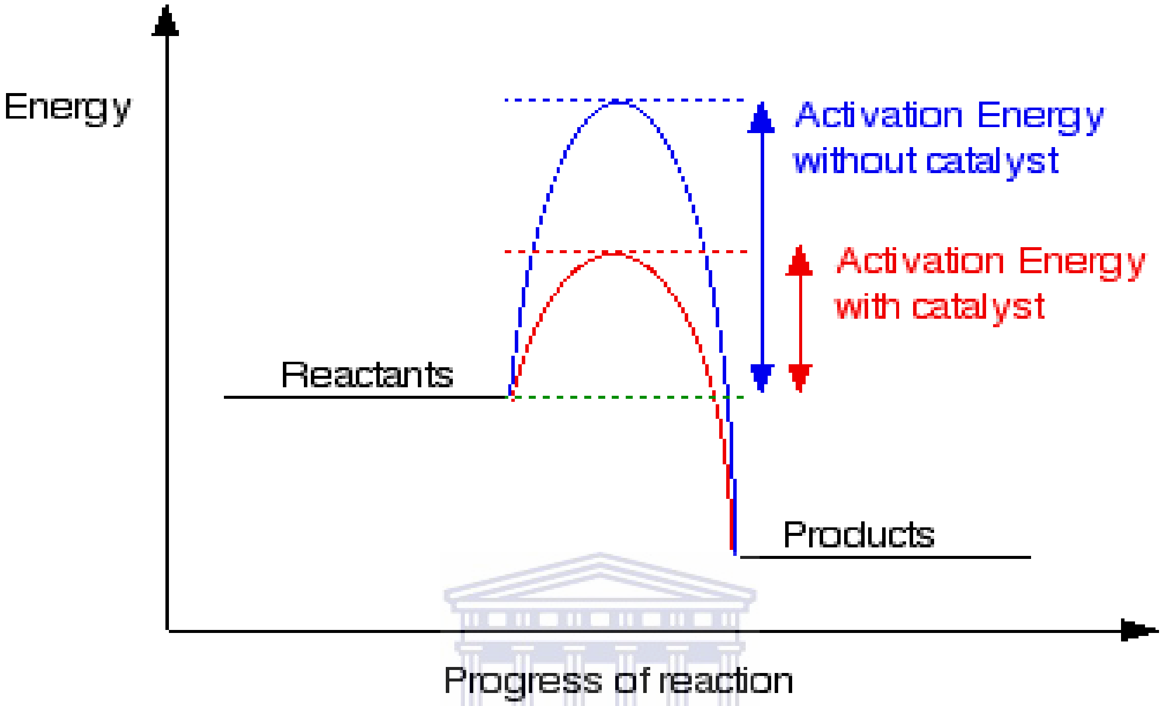

Figure 2. 3: Energy diagram showing the effect of a catalyst in a reaction.

The rate of a reaction depends on the temperature at which it is run. As the temperature increases, the molecules move faster and therefore collide more frequently. The molecules also carry more kinetic energy. Thus, the proportion of collisions that can overcome the activation energy for the reaction increases with temperature [55].

2.3.3 Heterogeneous structure of the electrocatalysts

A heterogeneous catalyst functions in a different phase to that of the reactant. The most common heterogeneous catalyst occurs as a solid catalyst and liquid reactants. Heterogeneous catalysts are normally supported which means the catalyst is dispersed on a secondary material to increase its surface area of contact that enhances the effect. Electrocatalysis is not limited to heterogeneous catalysts: molecular catalysts, either in solution or immobilized on a conductive but otherwise inert support, may also catalyze redox reactions. Redox proteins are nature’s electrocatalysts and essentially function as galvanic cells, very much like in a discharging battery. Therefore, the field of electrocatalysis bridges many areas of catalysis. Industrial electrocatalysts are typically produced either as nanoparticles or (porous) extended layers to increase the overall useful surface. If a nanoparticulate material is used, the nanoparticles are immobilized on a conducting support developed to work under conditions of catalyzed electrochemical reactions [8, 17].

It should be well-known that ready to use electrocatalytic materials are complex systems where the resultant performance, i.e., activity, selectivity and stability, depends on many factors. Even a single- supported nanoparticles in contact with an electrolyte represents a multiparametric system different facets, surface defects, interactions with the support material, surface and bulk composition, size effects, specific properties of the electrochemical interface, electrolyte composition, and other parameters control its catalytic properties [8, 69], in (**Figure 2.4)** below.

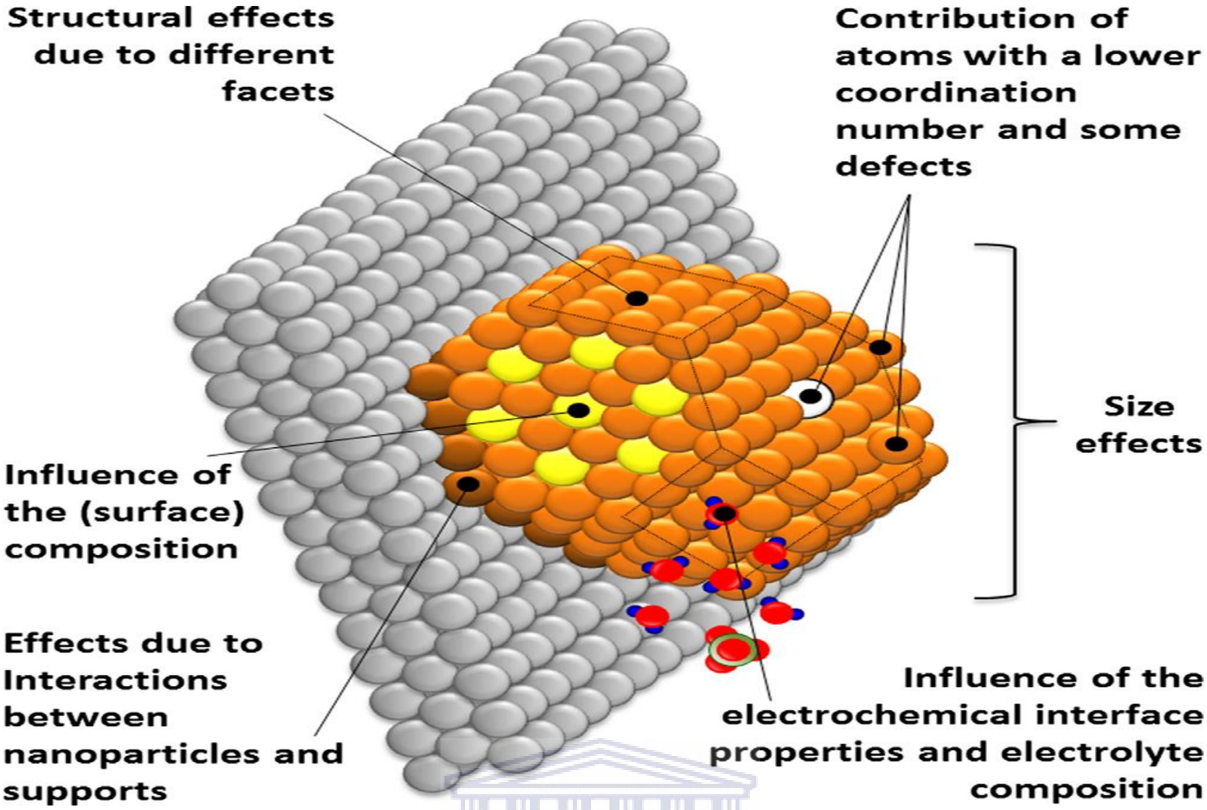

Figure 2. 4: Real-world high surface-area nanoparticulate electrocatalysts are complex systems where the resultant electrocatalytic activity depends on many parameters.

2.3.4 Homogeneous structure of the electrocatalysts

Homogeneous catalysts function in the same phase as the reactant. These types of catalyst are typically dissolved in a solvent and added to the substrate which is also in liquid form. Although the average composition (based on bulk composition) is generally used to correlate with the catalytic behaviour of an alloy catalyst, the distribution of elements within the nanoparticles is found to have remarkable effects on the local electronic structures and catalytic behaviour of the material [156]. Moreover, catalyst durability is highly dependent on the elemental homogeneity of an alloy catalyst. For example, one element may be more volatile than the other components in an alloy catalyst under specific reaction conditions, and a catalyst with an inhomogeneous distribution of the alloying components is thus less stable because of dissolution of the volatile element from the near-surface region. The homogeneity of alloys and their compositional profiles have been successfully addressed on extended surfaces however; such insight to corresponding nanoscale alloy materials is still lacking [107, 177, 183]. The treatments that are established to induce the proper elemental distribution on extended surfaces may not be always applicable to nanocatalysts for a number of reasons, such as particle sintering and the change of particle size. These compromise the assessment of catalytic performance. Catalysis and polymer functionalization using the tools and precepts of synthetic organic chemistry to prepare functional polymers that in turn are used to either effect catalysis in a greener, more environmentally caring way or to more efficiently functionalize polymers in (**Figure 2.5**) below [22, 104].

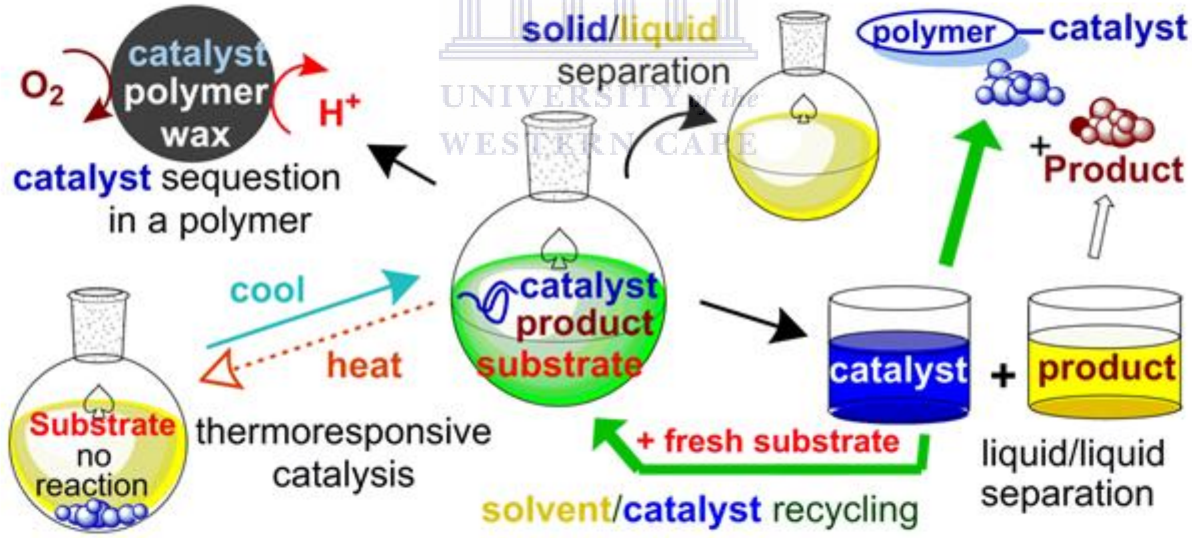

Figure 2. 5: Strategies of using soluble polymers to facilitate homogeneous catalysis [104].

2.3.5Platinum group metals for electrocatalysis

Platinum group metals (PGMs) are known to be good catalysts for various chemical and electrochemical reactions. The production of such catalytic surfaces with a range of particle sizes and surface are of prime importance. Catalysts of platinum group metals (PGM: Pt, Pd, Rh, Ir, Ru, and Os) are of technological importance. Here they are used indispensably in modern chemical industry, petrochemical industry, automobile exhaust purification, and fuel cells, owing to their excellent activity and stability. The reduction of precious metal salts to the metallic state has become a focus in material science dealing with nanoparticles [23]. The deposition of precious metals either chemically or electrochemically plays an important role in the development of technologies where these metals are used. This is particularly true in the area of electrodeposition as each method with different operating parameters such as temperature, pH and current density is likely to produce different kinds of deposit structures [12].

Platinum group metals, namely, Ru, Rh, Pd, Os, Ir and Pt are noble in their character and placed at the bottom of the electromotive force (emf) series. The emf values show that it is extremely easy to reduce their ions and as a consequence, they try to remain in the metallic state. Hence these elements are often found in the earth's crust as metals or alloys such as osmoiridium, siserskite [121]. However, the price of PGM is extremely high due to the low abundance on the earth. The performances of existing PGM catalysts are always behind the expectation of fast development of relevant industries. For example, the failure of large-scale commercialization of low-temperature fuel cells is due to unacceptably high cost mainly caused by high loading of Pt catalysts. The key issue in the development of this field is to find and design new types of PGM catalysts with enhanced activity and stability [53, 126].

2.3.6 Structural effects in electrocatalysis

The suggestion that the activity of a heterogeneous catalyst depends on the structure of its surface was originally proposed by Taylor in 1925 [71]. At that time he proposed the concept of the active site. During the past decades, surface scientists have systematically studied the surface structure-catalytic functionality by using metal single-crystal planes as model catalysts. It has been discovered that surfaces with open structure usually exhibit much enhanced activity and stability [27, 71]. The surface-science approach to identifying the active site on a surface is to study the reaction under consideration on a number of single-crystal surfaces. Such studies should give insight into which arrangement of surface atoms leads to the highest activity and should thereby identify the active site(s) for a reaction. Many relevant electrocatalytic reactions have been studied using this surface science approach, having generated a wealth of information of the activity of a large variety of electrocatalytic reactions on single-crystal surfaces of different metals [17, 91, 163]. Ideally, these surfaces sample a relevant part of the stereographic triangle, as illustrated for face centered cubic (fcc) metals in (**Figure 2.6**) below;

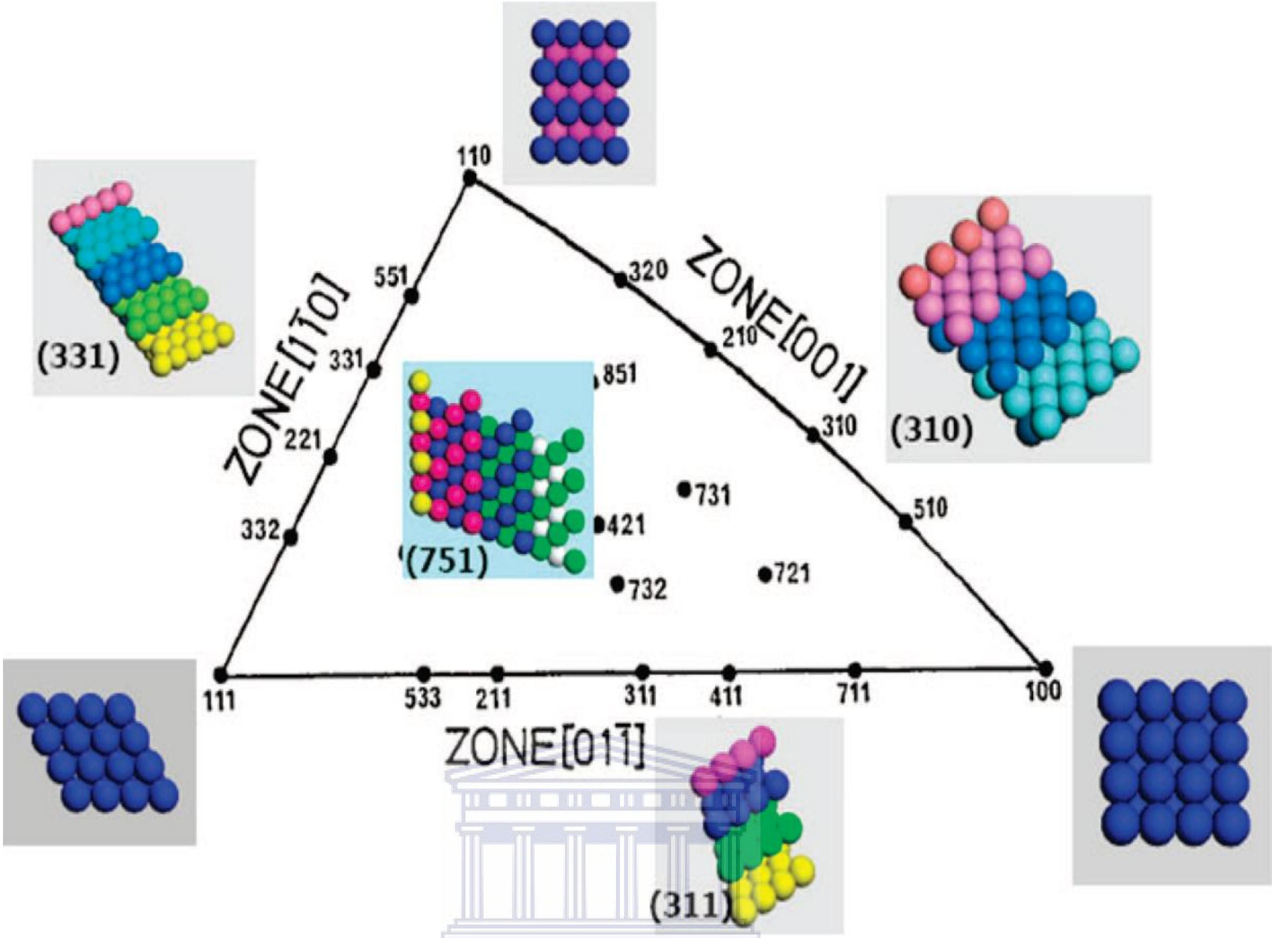

Figure 2. 6: Unit stereographic triangle of face centered cubic fcc single-crystal surfaces and their corresponding surface atomic arrangements [91, 163] and [17].

Three vertexes of the triangle represent the three low-index planes or basal planes that is (111), (100), and (110). Among them, the (111) and (100) planes are atomic-scale flat with closely packed surface atoms, whereas the (110) plane is rough with step atoms. The coordination numbers of to player atoms on (111), (100), and (110) are 9, 8, and 7, respectively. Other planes lying in the sidelines and locating inside the triangle are high-index planes. The three sidelines of the triangle represent [011], [110], and [001] crystallographic zones, in which the planes exhibit terrace-step structure and are thus also called stepped surfaces [91]. Numerous studies have been made in the past decades to study the intrinsic relationship between surface structure and electrocatalytic properties by using metal single crystal electrodes with well defined surface structures. Taking ammonia synthesis as an example, it is an extremely high structure sensitive reaction since it involves the dissociation of a very strong N≡N bond. Ru is of hexagonal closest packing (hcp) lattice and Ru (0001) is the closest packed surface while Fe is body centered cubic (bcc) lattice and Fe (110) is the closest packed surface. The catalytic activity of Fe (111) and Fe (211) is a few orders of magnitude higher than that of the other surfaces, which may be attributed to the facile adsorption of N_2 on the top-layer atoms with coordination number 4 and the second- and third-layer atoms coordination number 7 in sequence to weaken the N≡N bond gradually on such open surfaces by density functional theory calculations [17, 91].

Recent comparison of single crystal studies suggested that many electrocatalytic reactions fall within one of three categories of structure sensitivity;

- Electrocatalytic reactions that take place preferentially on step and defect sites within (111) terraces. Typically, the key step in these reactions involves the breaking or making of an O–H or C–H bond, such as the oxidation of methanol or the oxidation of carbon monoxide (which depends on the activation of water).
- Electrocatalytic reactions that take place preferentially on (100) terrace sites. For these reactions, steps and defects in the (100) terraces lead to a decrease in catalytic activity. These reactions invariably involve the breaking or making of a C–O, C–C, N–O, N–N, or O–O bond.
- Electrocatalytic reactions that do not appear to have a clear preference for a particular site or crystal surface. Typically, these reaction exhibit high structural sensitivity to the presence of other ingredients in the electrochemical interface, such as anions. This is especially the case if the specific adsorption of these anions is structurally

sensitive. These reactions often involve intermediates that are only relatively weakly adsorbed on metal surfaces.

2.4 Binary and ternary Pt based electrocatalysts for ammonia oxidation reaction

2.4.1Pt based binary catalyst

Pt-based bimetallic materials PtMe (Me = Ir, Ru, Ni, Pd, Rh, Cu, Ag and Au) are the most commonly used catalysts in ammonia oxidation reaction [62]. The increased activity over these multicomponent catalysts compared to their monometallic Pt counterpart has predominantly been attributed to bifunctional effect and ligand or electronic effect [46, 193]. The oxidation of ammonia on a platinum catalyst in water can take place either electrochemically or using oxygen as an oxidizing agent. In both scenarios the presence of oxides at the surface determines the selectivity of the reaction. if no surface oxides are present N_2 is formed whereas oxygen containing products like N_2O and N_2O^- are formed in the presence of surface oxides [30]. In the bifunctional effect, the transition metal (Ir, Ru) has a strong interaction with water to form an oxygenated species (e.g. OH_{ads}). In the mean time Pt actively adsorbs dissociates the ammonia in the electronic effect. The electronic back-donation from the transition metal changes the d band structure of Pt. This therefore weakens the bond strength between the adsorbents and Pt [54, 77, 163].

At the electrochemical interface no surface oxides are formed at potentials lower than 0.8 V (vs RHE). In the case of oxidation with oxygen no oxides are formed when the supply of O_2 is diffusion limited. This suggests that the mechanism of ammonia oxidation in both cases should be similar, and that electrochemical methods can be used to obtain mechanistic information that is also relevant to the liquid-phase oxidation using oxygen, which would be the preferred method in a catalytic reactor [165]. The noble transition metals (Pt, Pd, Rh, Ru and Ir) are found to be the most active catalysts. The coinage metals (Cu, Ag, Ni and Au) were found to be less active than the noble transition metals, but more active than the other transition metals and the metal oxides. Similarly to the oxidation in water, the most active catalyst for the selective oxidation to dinitrogen is iridium [54, 75, 77, 110].

Endo et al [62] reported that saturated j60 at a high oxidation potential was higher on $Pt_{1-x}Ir_x$ ($x \leq 0.8$) or $Pt_{1-x}Ru_x$ ($x \leq 0.4$) than on Pt, which suggested a positive cooperation of Ir and Ru with Pt in the electrocatalysis. On the other hand, Ni added as a solute to Pt contributed to lower j60 with x in $Pt_{1-x}Ni_x$ ($0 \leq x \leq 0.7$) and did not lower the starting potential of ammonia oxidation at all. The reason why Ir and Ru enhance the activity might be explained by their activity at the dehydrogenisation steps of NH_3 at a lower potential, at which ammonia oxidation can never start on the surface of pure Pt [62]. These studies are all supportive of a mechanism for the dinitrogen formation originally suggested by Gerischer and Mauerer (1970) [72]:

$\mathrm{NH_3\ (aq)} \rightarrow \mathrm{NH_{3,ads}}$ ………………………………….. (1)

$\mathrm{NH_{3,ads}} \leftrightarrow \mathrm{NH_{2,ads}} + \mathrm{H^+} + \mathrm{e^-}$ ……………………….. (2)

$\mathrm{NH_{2,ads}} \rightarrow \mathrm{NH_{ads}} + \mathrm{H^+} + \mathrm{e^-}\ \mathrm{(rds)}$ ……………… (3)

$\mathrm{NH_{x,ads}} + \mathrm{NH_{y,ads}} \rightarrow (\mathrm{x}+\mathrm{y})\,\mathrm{H^+} + (\mathrm{x}+\mathrm{y})\,\mathrm{e^-}$ …. (4)

$\mathrm{NH_{ads}} \rightarrow \mathrm{N_{ads}} + \mathrm{H^+} + \mathrm{e^-}$ ……………………………… (5)

With x, y = 1 or 2. From the observed Tafel slope of 39 mV dec^{-1} in the potential range of 0.45–0.6 V, Oswin et al [136] concluded that the third step in this scheme is the rate-determining reaction [136]. At potentials higher than 0.6 V Gerischer et al [72] observed that the platinum electrode deactivates. From an ex situ analysis of a deactivated electrode using temperature programmed desorption, only N_2 was detected and no H_2. Hence these authors concluded that the deactivation of the electrode was related to the formation of N_{ads}. This inactivity of N_{ads} towards N_2 formation is in sharp contrast to the gas-phase ammonia oxidation. Gerischer and Mauerer (1970) also observed that between 0.45 and 0.6 V the kinetic order in the concentration of NH3 is zero [72].

de Vooys et al [54] disturbed that the potential at which NH_{ads} or N_{ads} was formed is metal dependent. The observed trend in the strength of adsorption of N_{ads} was Ru > Rh > Pd > Ir > Pt >> Au, Ag, Cu. This trend corresponded well with the trend observed in the calculated heat of adsorption of atomic nitrogen, with iridium being an exception. Platinum was the best catalyst for this reaction because N_{ads} was formed at high potential, compared to rhodium and palladium, but seemed to stabilize NH_{ads} rather well. Gold, silver and copper did not form NH_{ads} or N_{ads}, and showed only an activity when the surface became oxidized. The metal electrodissolution was enhanced by ammonia under those conditions. Most metals produced oxygen that contained products, like NO and N_2O, at potentials where the surface became oxidized [54].

Vitse et al [174] showed that the efficiency of the electrolytic cell was improved by using bimetallic electrodeposited catalysts at both electrodes containing Pt and a low concentration of secondary metals (Ru, Ir). Pt–Ir deposits showed the highest activity toward ammonia oxidation. An experimental procedure was shown which minimized the reversible deactivation of the electrode. Significant current densities were obtained (above 100 mA cm^{-2}) during electrolysis testing at relatively low metal loading, low cell voltages, and high cell efficiencies. These results pointed to ammonia electrolysis as a promising candidate for an alternative process for low-cost, low-temperature, high-purity hydrogen production [174].

Lomocso et al [109] showed that ammonia electro-oxidation was studied in alkaline solution on carbon-supported Pt and bimetallic Pt_yM_{1-y} (M = Pd, Ir, SnOx and y = 70, 50 at %) nanoparticles. XRD revealed the structure of all bi-metallic particles to be face-centered cubic and confirmed alloy formation for Pt_yPd_{1-y} (y = 70, 50 at %) and Pt_7Ir_3 nanoparticles, as well as partial alloying between Pt and SnOx. Electrochemical behaviour of ammonia on Pt and PtM nanoparticles was comparable to that expected for bulk Pt and PtM alloys. Addition of Pd to Pt at the nanoscale decreased the onset potential of ammonia oxidation if compared to pure platinum nanoparticles; however stability of the catalyst was poor. For Pt_7 $(SnOx)_3$, current densities were similar to Pt, whereas catalyst stability against deactivation was improved. It is found that carbon supported Pt_7Ir_3 nanoparticles combine good catalytic activity with enhanced stability for ammonia electro-oxidation. Electronic effect generated between two metals in the bimetallic nanoparticles might be responsible for increase in the catalytic activity of Pd and Ir containing catalysts, caused weakening of the adsorption strength of poisonous N_{ads} intermediate [109].

2.4.2 Pt based ternary catalyst

Many studies have been conducted an investigation have been made to improve the performance of the Pt–Ru binary catalysts with the incorporation of a third metal, such as W, Mo Sn, Os, etc. The application of ternary metal nanoparticles can significantly enhance the catalytic activity toward ammonia oxidation. The role of the third component is to help in reduce NH adsorption on Pt [10]. The enhanced catalytic activity has been attributed by a number of factors including the change in Pt–Pt inter atomic distance, number of Pt nearest neighbours, Pt 5d band vacancy, and Pt metal content on particle surface. To further improve the catalytic activity for oxygen reduction of platinum, ternary catalysts formed by various transition metals are currently investigated [9].

The key parameters in the preparation of Pt–M1–M2 ternary catalysts are:

(1) The actual Pt: M1: M2 atomic ratio, which can be other than the nominal one.

(2) The amount ofM1 andM2 alloyed with Pt and the amount of metal oxides present in the catalysts.

(3) The metal particle size, as the electrocatalytic activity depends on the metal surface area.

Antolini et al [9-10] showed that Pt-based ternary catalysts have been proposed as electrode materials for low temperature fuel cells. Pt–Ru-based ternary catalysts were tested as anode materials with improved CO tolerance or enhanced activity for methanol or ethanol oxidation. Ternary catalysts based on platinum alloyed with first row transition metals were tested as cathode materials with improved activity for the oxygen reduction. The paper presents an overview of the preparation methods and structural characteristics of these ternary catalysts [9-10]. The literature findings regarding some Pt–Ru based ternary catalysts can be summarized as follows, Pt–Ru–Mo and Pt–Ru–W. Generally, Mo and W are present in the catalyst in an oxide form and do not form ternary alloy Pt–Ru–Ni. On the basis of the value of the lattice parameters, all the work dealing on the synthesis of ternary Pt–Ru–Ni catalysts indicated the formation of a ternary Pt–Ru–Ni alloy Pt–Ru–Os, Pt–Ru–Ir, Pt–Ru–Pd and Pt–Ru–Rh. The few works carried out on these catalysts seems to indicate that they form ternary alloys [15, 81-82].

Stability tests were done and it indicated that Pt electrodes was found to perform poorly, this electrode was the most stable for methanol oxidation. The order of stability was: Pt > Pt–Ru–

W, Pt–Ru–Pd > Pt–Ru. Steady-state performances were found to be in the order: Pt–Ru–W, Pt–Ru–Pd > Pt–Ru > Pt [114, 191]. Herbani et al [78] showed that Gold–platinum–silver (Au–Pt–Ag) ion mixtures produced nanoparticles alloys with an average particle size of 5 nm after co-reduction of metal ions by femtosecond laser irradiation of aqueous solutions in the presence of ammonia and polyvinylpyrrolidone, which was used as a stabilizer. The nanoparticles had elemental composition ratios close to the molar ratios of ions in the mixed solutions, implying a high reduction yield. HRTEM images of nanoparticles revealed that the particles were crystalline and were not phase segregated. Binary nanoparticles from Au–Pt and Ag–Pt immiscible systems were also synthesized to confirm the applicability of this method to ternary systems [78].

Hung et al [81-82] preliminary results illustrated the surface peak current density and potential electrochemical characterizations of PtPdRh electrocatalytic materials led to a significant enhancement in catalytic performance, which was measured using a cyclic voltammetry for electrochemical oxidation of ammonia reaction. Overall, the PtPdRh alloy catalyst was found to play a profound role in the NH_3 electrocatalytic process. Moreover, according to a fluorescent spectrometry evaluation, PtPdRh alloy catalyst yielded fluorescent peaks at 300/400 nm at room temperature. An electrochemical characterization was performed revealed that the oxidation ability may explain the significant activity of the catalysts based on the CV over a wide potential range reveal. In electrochemical oxidation of NH_3, the electrocatalytic material could be a candidate for electrode materials in H_2 production, as it is an attractive alternative renewable biofuel generated from NH_3 decomposition and is applicable in fuel cell [81-82].

2.5 Non-Pt based alternative electrocatalysts for ammonia oxidation reaction

The development of Pt-free electrocatalysts is another approach for the significant cost reduction of the electrocatalysts, thus contributing to its application on a technological scale. These non-Pt electrocatalysts mainly include metal oxides (e.g Ni/Ni(OH)2, IrO2 andRuO2) and boron-doped diamond (BDD).In contrast to the level of detail available on Pt and its alloys, little is known about the mechanism of ammonia electro-oxidation on these materials. Systematic studies of the intermediate species formed during the oxidation and the current efficiency as a function of the potential, as well as the deactivation mechanism, have been very limited. In particular, there is no direct information yet available concerning whether the ammonia oxidation process is governed by the active NH_x intermediates on non-Pt anodes like Pt [184-185].

Compared to ammonia electro-oxidation on Pt based electrocatalysts, ammonia electro-oxidation on metal oxides and BDD generally occur at a high overpotential, leading to a low current efficiency. In addition, ammonia on Pt-based electrocatalysts can be selectively oxidized to N_2 in the potential region where Pt is devoid of adsorbed oxygen, whereas oxygenated nitrogen species (e.g., NO, N_2O, nitrite and nitrate) besides N_2 have also been found during ammonia oxidation on most metal oxides and BDD electrodes. However, it should be noted that in many applications, such as ammonia-based fuel cells, and the remediation of ammonia-contaminated wastewaters, the desired oxidation product of ammonia is elemental nitrogen [184-185].

2.5.1 Telluride nanoparticles

The telluride ion is the anion Te^{2-} is formed from the reduction of the tellurium metal. The redox potential of pure Te metal is fairly negative, -1.14 V. The acid hydride of tellurium, hydrogen telluride, H_2Te, is unstable compound that decomposes to tellurium metal. It is strongly acidic, dissociating into hydrogen telluride ion (HTe^-) in aqueous solutions. The Te^{2-} anion only exists in aqueous solutions in basic conditions [83]. Transition-metal telluride represents a class of compounds which is widely attracted for using in optoelectric and thermoelectric applications due to their high thermoelectric power values. In addition, the ability to dope as n- or p-type materials provides a wide range of physical and chemical properties [80]. Su et al [157] showed a variety of strategies have been attempted to improve the performance of thermoelectric materials. The primary approach was to employ low-dimensional materials to reduce the lattice thermal conductivity as described by the Wiedemann–Franz law which was to decrease the thermal conductivity, rattling structures, point defects, vacancies and nanocomposites have been used to efficiently scatter phonons within or between the unit cell crystals. Complex crystalline structures have been used to decouple the electrical conductivity and thermal conductivity to achieve this goal. Based on such considerations, TiO_2 nanotubes were prepared from titanium foils. These nanotubes are low-dimensional, thus, preferable to achieve low lattice thermal conductivity to generate favourable thermoelectric properties. Moreover, scattered Te–Bi–Pb nanoparticles have been deposited on the surface of the TiO_2 nanotubes via electrochemical method. The purpose of the nanoparticles was to further enhance the performance of the thermoelectricity [157].

Mtungwana et al [124] reported a simple route to HDA capped ZnTe nanoparticles using NaHTe and $ZnCl_2$ as the tellurium and zinc sources respectively. The solution based high temperature route employed the use of readily available starting reagents. The particles synthesized at reaction temperatures of 230 °C and 270 °C were spherical in shape. The blue shift in the absorption spectra confirmed that the particles undergo quantum confinement. The photoluminescence studies showed that the particles emit at a wavelengths close to their band edge [124].

Huang et al [80] showed that soluble poly (ethylene glycol) (PEG)-supported telluride 2 was designed and synthesized for catalytic Wittig-type reactions. It was found that the catalytic loading could be reduced from 20 to 2 mol % by the introduction of PEG (even to 0.5 mol % when some telluride salts were used as the catalyst). Under the catalytic reaction conditions, a wide variety of aldehydes with different structures could react with bromoacetate to afford â-substitutited or R,â- isubstituted unsaturated esters in high yields with excellent E-stereoselectivity. The modified process, by using sodium bisulfite instead of triphenyl phosphite, represented a very simple product isolation procedure. The roles of PEG for promoting the ylide formation and stabilizing the catalytic species were disclosed. The mechanism was also studied [80].

Tubtimtae et al [164] studied $Cu_{2-x}Te$ quantum dots on ZnO nanoparticles were synthesized and were solely orthorhombic $Cu_{1.44}Te$ phase. The growth mechanism was supposed that it based on ions deposition. The energy gap of as-synthesized $Cu_{2-x}Te$ QDs was determined to be 1.1 eV and the smallest energy gap of 0.76 eV was obtained, equal to that of bulk material. These characteristics suggest a promising implication for a potential broadband sensitizer of quantum dot solar cells (QDSCs) [164]. Lowndes et al [113] studied the size distributions of Si and ZnTe nanoparticles produced by low energy density ArF (193 nm). ZnTe nanoparticles formed by ablation into nitrogen at E_d= 0.74 J.cm^{-2} consisted of a crystalline

ZnTe core surrounded by an amorphous ZnO shell. Growth defects and surface steps were clearly visible in the ZnTe crystalline core. The dependencies of the mean diameter of ZnTe nanocrystals on nitrogen pressure and D_{ts} were qualitatively similar to those found for Si in He [113].

Chen et al [43] reported successful synthesis of Ag_2Te nanosheets for the first time. In facile one-pot synthesis method, TOP was used as both solvent and stabilizer, and the produced Ag_2Te nanosheets had either roundish or hexagonal disk shapes the diameter and side length of which were~32 and 20–40 nm, respectively. Through systematic studies identified reaction temperature, molar ratio of $AgNO_3$ to tellurium powder, precursor-solution concentration, and reaction time as critical influential factors for Ag_2Te-nanosheet synthesis, and, moreover, discussed a plausible mechanism for Ag_2Te-nanoplate formation. The good electrical conductivity of 102.1 $S.cm^{-1}$ estimated from the room-temperature I–V curve, together with a large surface-to-volume ratio due to anisotropic shape, indicated a great potential of Ag_2Te nanosheets as a building block for nanodevices [43].

2.6 Methods for Preparation of Pt-based Electrocatalyst

Methods for catalyst preparation were very diverse and each catalyst was produced via different routes. Preparation usually involved several successive steps. Many supported metal and oxide catalysts were prepared by the succession of impregnation, drying, calcinations, and activation [47].

Three fundamental stages of catalyst preparation may be distinguished:

1. Preparation of primary solid associated with all the useful components;

2. Processing of that primary solid for obtained catalyst precursor;

3. Activation of the precursor to give the active catalyst: reduction to metal, formation of sulphides, deammoniation. Activation may take place spontaneously at the beginning of the catalytic reaction.

In recent years, methodological development for Pt-based catalyst preparation has been one of the major topics catalyst explorations. Four main routes exist for preparing the primary solid: deposition, precipitation and co-precipitation, gel formation and selective removal [192].

2.6.1 Wet-Chemical Synthesis Methods

The preparation or synthesis of an electrocatalyst was a very important step when it comes to the development of electrocatalysts, as the catalyst preparation method had a great influence on catalytic activity. If a catalyst was prepared for a particular reaction, its activity will be directly proportional to the surface area exposed to the reacting species. Moreover, size and shape of the particles in a bulk catalyst affect the activity of a catalyst [84, 144]. The principle of the catalyst preparation technique involved two stages, the first rendering a metal-salt component in a fine form onto a support and secondly, conversion of the supported metal salt to a metallic or oxide state. The first stage is known as dispersion and is achieved by impregnation, adsorption from the solution, co-precipitation, or deposition, while the second is the thermal treatment in either an inert atmosphere or an active atmosphere of either oxygen or hydrogen [76, 134, 142].

When the active atmosphere is hydrogen the process is known as reduction although reduction can cause major problems in catalyst preparation on the large scale, it is a generalization to say that once the metal species has been bound to the support surface its degree of dispersion and location will be retained during subsequent treatment. The catalytic surface area of a supported catalyst (its dispersion) depends significantly on the preparation procedure. Parameters that influence catalyst dispersion include the nature and concentration of the precursor and support, the duration, temperature and atmosphere (in contact with the catalyst surface) of the preparation steps [101].

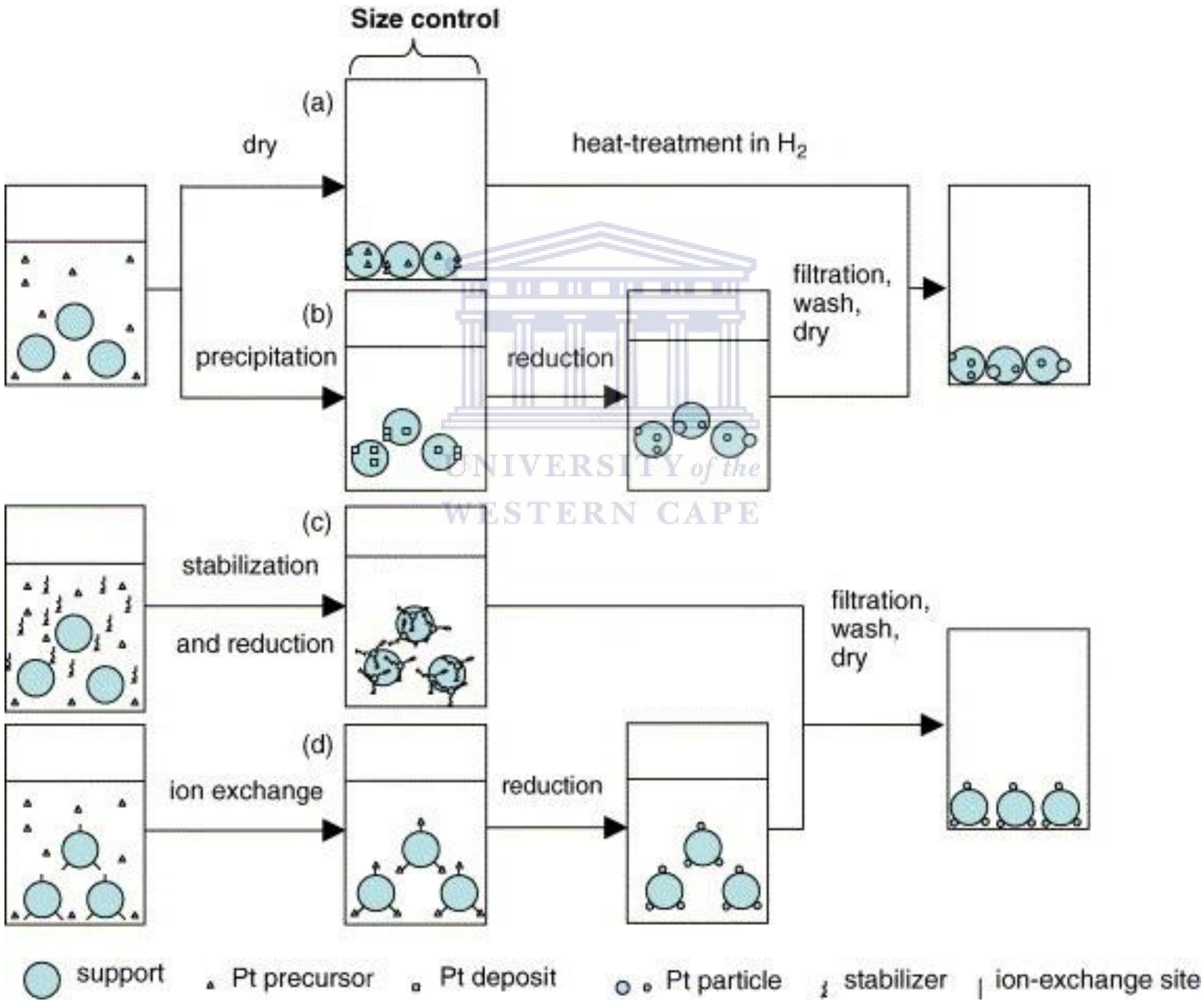

Figure 2. 7: Schematic depiction of various methods for producing supported metal catalysts (a) Impregnation (b) Precipitation (c) Colloidal (d) Ion-Exchange Methods [101].

If the discussion is restricted to the preparation of Pt-based fuel cell catalysts, five general methods have been employed [101]:

- Impregnation, as a means of preparing a supported catalyst, is achieved by filling the pores of a support with solution of the metal salt from which the solvent is subsequently evaporated (**Figure 2.7 (a)**).
- The preparation of supported catalysts by the co-precipitation of metal ions with support ions usually produces an intimate mixing of catalyst and support (**Figure 2.7 (b)**).
- Adsorption is the selective removal of metal salts or metal ions form their solution by a process of either physisorption or chemical bonding with active sites on the support.
- Deposition, as used in preparing supported catalysts, is the laying down or placing of the active components on the exterior surface of a support (**Figure 2.7 (c)**).
- Electrochemical deposition is a versatile technique by which a thin desired metallic coating can be obtained on to the surface of another metal by simple electrolysis of an aqueous solution containing the desired metal ion or its complex (**Figure 2.7 (d)**).

2.6.2 Chemical Vapour Deposition Method

Chemical Vapour Deposition (CVD) is an advanced manufacturing technology for surface coating currently enjoying intense development. It is a chemical process used to produce high-purity, high-performance solid materials. In a typical CVD process, the wafer (substrate) is exposed to one or more volatile precursors, which react and/or decompose on the substrate surface to produce the desired deposit. Frequently, volatile by-products are also produced, which are removed by gas flow through the reaction chamber [20, 92, 130]. The advantages of this method are:

- The produced materials are mainly on the external surface of the support.
- It has little effect on the porous structure of the support due to the use of gases as precursors.
- Many of the traditional steps in catalyst preparation, such as saturation, drying, and reduction, can be eliminated
- The properties of the deposited material are easily controlled [20, 92, 130].

The CVD method has been believed that it allows the production of deposits in a controlled manner and on a large scale; it could be applied to the preparation of supported catalysts.

CHAPTER 3

Summary

This chapter presents the details of experimental outline and methods employed when producing catalysts. Giving a detailed theoretical background of instruments used, procedures for chemical synthesis of Pt, PtRu, PtIr, PtTe, PtRuTe and PtIrTe nanoparticles are observed using different analytical techniques. The microscopic, spectroscopic and electrochemical characterization of nanoparticles is outlined; the experimental parameters used in the investigation are also described. Also described in this chapter are procedures for the fabrication of the nanoparticles towards the oxidation of ammonia for production of hydrogen is outlined.

3.0 Experimental methods and background theory

3.1 Reagents and materials

Chloroplatinic acid hexahydrate (H_2PtCl_6. $6H_2O$), iridium (III) chloride hydrate ($IrCl_3$. xH_2O), ruthenium (III) chloride hydrate ($RuCl_3$. xH_2O), Tellurium (Te), ammonium hydroxide (NH_4OH), sulphuric acid (H_2SO4, 98 %), sodium borohydride ($NaBH_4$), polyvinylpyrrolidone (PVP, MW = 55000), potassium hydroxide (KOH), were all purchased from Sigma-Aldrich (Cape Town, South Africa). All chemicals were of analytical reagent grade and were used without further purification. Deionised water (18.2 MΩ cm) purified by a Milli-QTM system (Millipore) was used as reagent water for aqueous solution preparations. Analytical grade argon gas was purchased from Afrox Company, South Africa. Alumina polishing pads and powder (0.05, 0.3 and 1.0 µm) were obtained from Buehler, Illinois, USA and were used for polishing the Pt electrodes.

3.2. Measurements and instrumentations

The synthesised nanoalloys were characterised using electrochemical, microscopic and spectroscopic techniques. The electrochemical techniques used for characterisation of the nanoalloys were mainly cyclic voltammetry (CV), square wave voltammetry (SWV) and electrochemical impedance spectroscopy (EIS). The voltammetric measurements were performed on a BAS 100W electrochemical workstation from BioAnalytical Systems Incorporation (Lafayette, USA) using a three-electrode cell system consisting of nanoalloy modified Pt electrode (1.6 mm 87 diameter, 0.0201 cm^2), Ag/AgCl (saturated NaCl) and platinum wire as working, reference and counter electrodes, respectively. The platinum auxiliary electrode was cleaned by burning in a flame for several minutes and the Ag/AgCl electrode was cleaned by rinsing with copious amounts of distilled water. All experimental solutions were purged with high purity argon gas and blanketed with the same during measurements. The experiments were carried out at controlled room temperature (25 ºC). The electrochemical impedance spectroscopy (EIS) measurements were done on a Voltalab PGZ 402 from Radiometer Analytical (Lyon, France) using a three electrode configuration set up described above. The microscopic and spectroscopic techniques used were high resolution transmission electron microscopy (HRTEM), high resolution scanning electron microscopy (HRSEM), and spectroscopic techniques used were Infrared spectroscopy and Ultra-violet visible spectroscopy (UV-vis).

3.3 Theoretical background of instrumentations used

3.3.1 Electrochemical characterisation

3.3.1.1 Cyclic Voltammetry (CV)

Cyclic voltammetry is one of the most widely applied techniques in modern electrochemistry due to its ability to allow probing of the mechanics of redox and transport properties of a system in solution. Cyclic voltammetry is usually performed using a three electrode configuration whereby the potential relative to some reference electrode is scanned at a working electrode while the resulting current flowing through a counter (or auxiliary) electrode is monitored in a quiescent solution. In the cyclic voltammetry experiment, an applied potential (E) is swept from an initial value (E_i) to a more oxidizing or reducing value (E_f) and then back to the initial value [48, 171]. The potential at any time (t) and voltage scan rate (ν) on the forward and reverse sweep can be calculated using the equation 3.1 and 3.2 below

$$E_{Foward} = E_i + \upsilon t \ldots\ldots\ldots\ldots.(3.1)$$

And

$$E_{reverse} = 2E_f + E_i - \upsilon t \ldots\ldots\ldots\ldots.(3.2)$$

If the potential at the working electrode is more positive than that of an electroactive species in the solution, electrons move from the solution to the electrode and the electroactive species is oxidized. In the process, an anodic current is produced. In the International Union of Pure and Applied Chemistry (IUPAC) convention, the anodic current is positive while in polarographic convention, it is negative. Similarly, on the return scan, as the working electrode potential becomes more negative than the reduction potential of a redox couple, reduction (i.e. electrons flowing away from the electrode) may occur to cause a cathodic current, which is negative in IUPAC convention and positive in polarographic convention.

The magnitude of the observed faradaic current can provide information on the overall rate of the many processes occurring at the working electrode surface. As is the case for any multi–step process, the overall rate is determined by the slowest step. For an oxidation-reduction process induced at a working electrode, the rate determining step may be any one of the following individual step depending on the system: rate of mass transport of the electro-active species, rate of adsorption or desorption at the electrode surface, rate of the electron transfer between the electro-active species and the electrode, or rates of the individual chemical reactions which are part of the overall reaction scheme.

For an oxidation reaction of the form

$$M_{Reduced} \leftrightarrow M_{Oxidized} + n\bar{e} \ldots\ldots\ldots.(3.3)$$

Where $M_{reduced}$ is the reduced species, $M_{oxidized}$ is the oxidized species and n is the number of electrons; the relationship between the potential and the concentrations of the reduced and oxidized species at equilibrium is described by the Nernst equation below;

$$E = E^0 + \frac{0.059}{n}\log\frac{[M_{Oxidized}]}{[M_{Reduced}]} \ldots\ldots\ldots(3.4)$$

Where E is the applied potential and E^0 the formal potential; $[M_{oxidized}]$ and $[M_{reduced}]$ represent surface concentrations at the electrode/solution interface, but not bulk solution concentrations. It is important to note that the Nernst equation may or may not be obeyed depending on the system or on the experimental conditions [48, 146, 171].

A typical cyclic voltammogram highlighting the key anodic and cathodic parameters is shown in (**Figure 3.1**) below. It shows a case where the scan starts at a slightly negative potential (A, where E_i = -400 mV) up to some positive switching value (B, where E_f = 700 mV) at which the scan is reversed back to the starting potential. The current is first observed to peak at $E_{p,a}$ (with value $I_{p,a}$) indicating that an oxidation is taking place and then drops due to depletion of the reducing species from the diffusion layer. During the return scan the processes are reversed (reduction is now occurring) and a peak current is observed at $E_{p,c}$ (corresponding value, $I_{p,c}$).

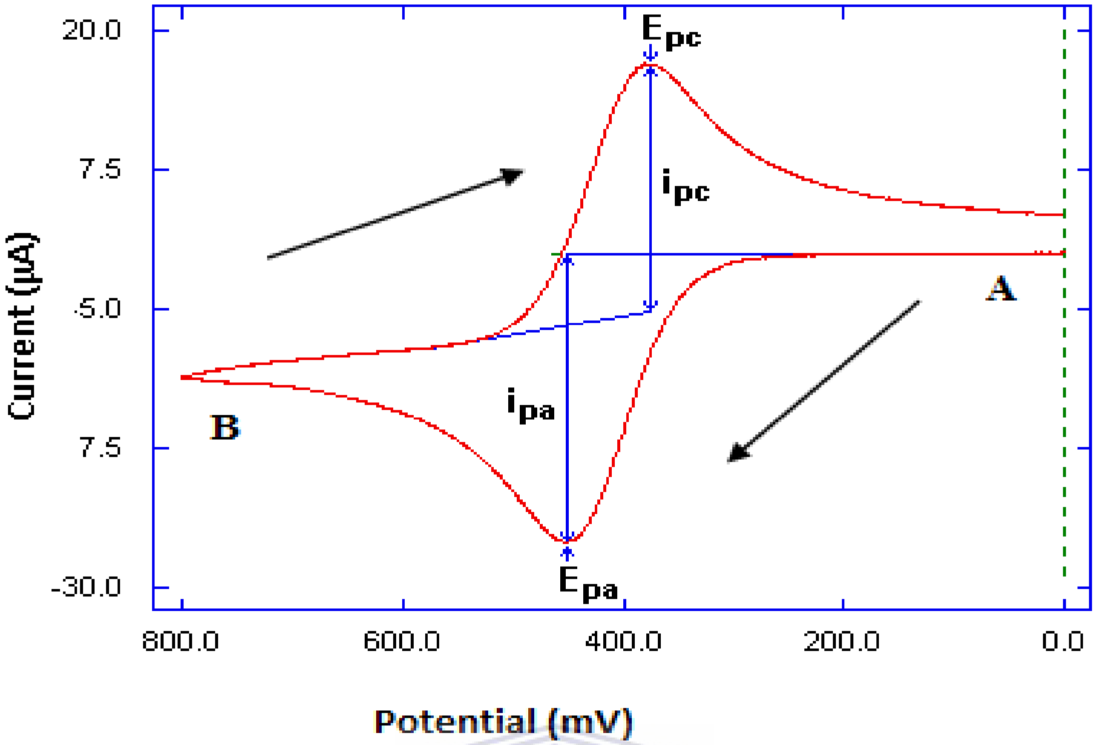

Figure 3. 1: Typical cyclic voltammogram indicating some important anodic and cathodic peak parameters.

In cyclic voltammetry, the position of both the cathodic and anodic peaks gives us thermodynamic information of the redox couple used. The anodic and cathodic peak potentials also enable the calculation of the formal electrode potential, $E^{o\prime}$, as follows:

$$E^0 = \frac{E_{pa} + E_{pc}}{2} \dots \dots \dots . (3.5)$$

The formal electrode potential (normally called the formal potential or the formal redox potential) is in concept similar to the standard electrode potential, E^0.

The power of cyclic voltammetry results from its ability to rapidly provide considerable information on the thermodynamics of redox processes, on the kinetics of heterogeneous electron-transfer reactions, and on coupled chemical reactions or adsorption processes. It is often the first experiment performed in an electroanalytical study. In particular, it offers a rapid location of redox potentials of the electroactive species, and convenient evaluation of the effect of media upon the redox processes [48, 146, 171]. Some important information about the sample under investigation can be obtained from the peak parameters. This includes whether the electrochemical process displayed by the sample is reversible, irreversible or quasi-reversible. It also gives insight into how fast the electron transfer process is, relative to other processes such as diffusion.

3.3.1.1.1 Reversible systems

The peak current for a reversible couple is given by Randles-Sevčik equation; Randles-Sevčik equation the magnitude of the peak current of a reversible couple, I_p, in a cyclic voltammogram is a function of the temperature (T), bulk concentration (C_0), electrode area (A), the number of electrons transferred (n), the diffusion coefficient (D), and the speed at which the potential is scanned (ʋ), according to Randles-Sevčik equation as follows [131];

$$I_p = 0.4463 nFA \left(\frac{nF}{RT}\right)^{1/2} D^{1/2} \upsilon^{1/2} C_0 \ldots\ldots\ldots (3.6)$$

At 25 °C the above equation reduces to

$$I_p = 2.686 \times 10^5 n^{3/2} A D^{1/2} \upsilon^{1/2} C_0 \ldots\ldots\ldots (3.7)$$

Where A is the electrode area (cm^2) and F, R, and T are as explained in equation 3.6. Accordingly, the current is directly proportional to the concentration and increases with the square root of the scan rate. The Randles-Sevčik equation is obeyed if a plot of peak current (I_p) against analyte concentration (C_0) yields a straight line. It also means that if the electrolyte composition is constant in terms of temperature, solvent, swamping electrolyte, then the Randles-Sevčik equation can be used to determine the concentration of analyte by the construction of a suitable calibration curve. When the peak current is plotted against the square root of the scan rate, with I_p as the y-axis and $v^{½}$ as the x-axis, often called a Randles-Sevčik plot, a straight line is obtained that passes through the origin and the slope of the linear plot can be used to determine the concentration of the analyte (C_0) if the diffusion coefficient D is known precisely (**Figure 3.2**). In addition, a Randles-Sevčik plot is also the best way to determine an experimental value of the diffusion coefficient, D, if it is not available in literature, in the case of a reversible reaction [90].

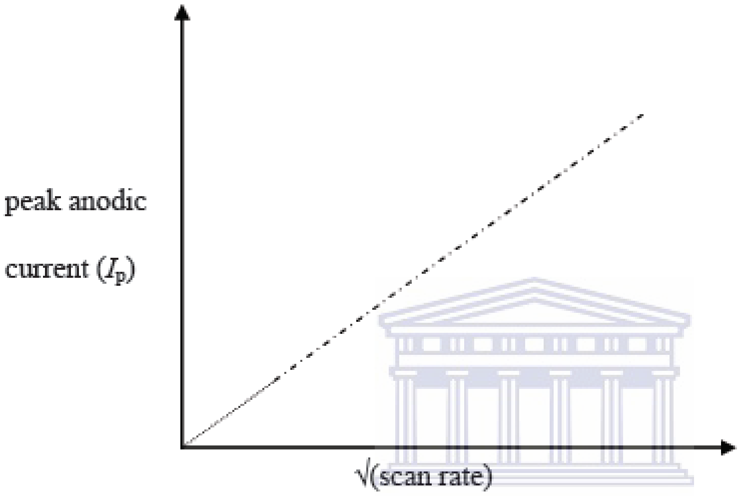

Figure 3. 2: A Randles-Sevčik plot of I_p against $\upsilon^{½}$.

From the Randles-Sevčik equation, it is also possible to calculate the other variables listed in equations 3.5 and 3.6. That is, if the peak current (I_p) at a certain scan rate (v) is measured, and the area of the electrode (A), the diffusion coefficient (D) and the concentration (C_0) of the species under study are known, one is able to calculate the number of electrons (n) involved in the redox change. Similarly, if the number of electrons (n) is known, one can calculate the diffusion coefficient (D) of the species, and any of the other variables [131].

3.3.1.1.2 Diagnostic criteria to identify a reversible process

To prove reversibility of the system when cyclic voltammetry is performed, the following Conditions should hold:

- the ratio of the currents passed at reduction (I_{pc}) and oxidation (I_{pa}) is near unity ($I_{pa} = I_{pc}$ or $I_{pa} / I_{pc} = 1$)
- the peak potentials (E_{pa} and E_{pc}) are independent of the scan rate, *v*
- the formal potential (E^0) is positioned midway between E_{pa} and E_{pc}, so that $E^0 = (E_{pa}+E_{pc}) / 2$
- the peak current (I_p) is proportional to $v^{½}$
- the separation between the peak potentials E_{pa} and E_{pc} is 59 mV/n for an n-electron couple at 25 ºC or; $|E_{pa}-E_{pc}|$ would be 59 mV for a 1 electron process and 30 mV for a 2 electron process. Thus, the separation can be used to determine the number of electrons transferred and as a criterion for Nernstian behaviour.

Moreover, if the electron transfer is fast relative to the diffusion of electroactive species from the bulk solution to the surface of the electrode, the reaction is said to be electrochemically reversible and the peak separation (ΔE_p) is given by equation 8 below.

$$\Delta E_p = \left|E_{pa} - E_{pc}\right| = 2.30\frac{RT}{nF} \ldots\ldots\ldots(3.8)$$

Where ΔE_p is the peak separation (V), E_{pa} is the anodic peak potential (V), E_{pc} is the cathodic peak potential (V), n is the number of electrons transferred, F is the Faraday constant (96,485 C .mol^{-1}), R is the gas constant (8.314 J .mol^{-1} .K^{-1}) and T is the absolute temperature (K). According to equation 8, for reversible one-electron processes, the peak-to-peak separation assumes different values as a function of the temperature. When the value of ΔE_p is measured, a departure of 10 – 20 mV from the theoretical value, especially at high scan rates, does not compromise the criterion for reversibility. This is due to the fact that the eventual presence of solution resistance, if not adequately compensated by the electrochemical instrumentation, tends to shift the forward/reverse peaks system, thereby increasing the relative value of ΔE_p [48, 90, 131, 146, 171].

3.3.1.1.3 Irreversible systems

The most important characteristic of a cyclic voltammogram of a totally irreversible system is the total absence of a reverse peak. For totally irreversible systems, the peak potential shifts with the scan rate. In addition, the individual peaks are reduced in size and widely separated as shown in (**Figure 3.3**) (Curve A).

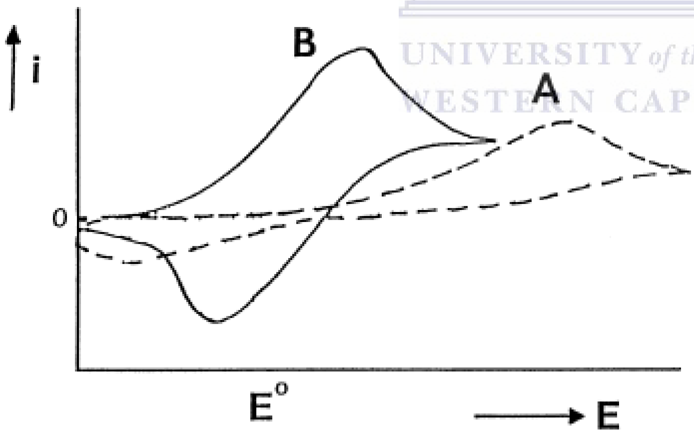

Figure 3. 3: A typical cyclic voltammograms for an irreversible electrochemistry process.

3.3.1.1.4 Diagnostic criteria to identify an irreversible process

The following conditions are required to identify whether an electrochemical process is irreversible:

- there is no reverse peak
- the I_{pa} or I_{pc} is proportional to $v^{1/2}$
- the value of E_p shifts –30/α.n for each decade increase in *v*
- $\left|E_p - E_{p/2}\right| = \frac{48}{\alpha n}$ mV

Totally irreversible systems are characterized by a shift of the peak potential with the scan rate:

$$E_p = E^0 - \frac{RT}{\alpha n_\alpha F}\left[0.78 - \ln\left(\frac{K^0}{D^{1/2}}\right) + \ln\left(\frac{\alpha n_\alpha F\upsilon}{RT}\right)^{1/2}\right] \dots\dots\dots(3.9)$$

Where K^0 is heterogeneous rate constant and α is the transfer coefficient and n_a is the number of electrons involved in the charge-transfer step. Thus, E_p occurs at higher potentials than $E^{0'}$, with the over-potential related to K^0 and α. In a case where E_p is independent of K^0, the shift of the peak potential could be compensated by an appropriate change of the scan rate. The peak potential and the half-peak potential (at 25 °C) will differ by 48/ αn mV. Therefore, when αn decreases, the voltammogram could become more drawn out. Equation 3.9 also allows for the calculation of the heterogeneous rate constant, K^0, if the values of E^0 and D are known.

The peak current for an irreversible process is given by:

$$I_p = (2.99 \times 10^5)n(\alpha n_\alpha)^{1/2}AC_0D^{1/2}\upsilon^{1/2} \dots\dots\dots(3.10)$$

For the irreversible process, the peak current (I_p) is proportional to the bulk concentration (C_0) but can be lower in value depending on the value of the transfer coefficient (α). Assuming that $\alpha = 0.5$, the ratio of reversible-to-irreversible peak current will be 1.27 (i.e. the peak currents for the irreversible process is about 80 % of the peak for the reversible one). The chemical meaning of an irreversible electrochemical process implies that a large activation barrier to the electron transfer takes place causing breakage of the original molecular frame with the formation of new species [48, 90, 131, 146, 171].

3.3.1.1.5 Quasi-reversible systems

A quasi-reversible process refers to one occurring in the transition zone between reversible and irreversible behaviour. A typical cyclic voltammogram for a quasi-reversible process is shown in (**Figure 3.3**) (Curve B). A quasi-reversible process is characterised by determining either the thermodynamic parameter E^0 (formal potential) or the kinetic parameters, α (transfer coefficient) and K^0 (rate constant) [131].

3.3.1.1.6 Diagnostic criteria to identify a quasi-reversible system

For a quasi-reversible system, the following conditions should hold:

- $|I_p|$ increases with $v^{1/2}$ but is not proportional to it
- $I_{pa} = I_{pc}$ or $I_{pa} / I_{pc} = 1$ provided $\alpha_c = \alpha_a = 0.5$
- ΔE_p is greater than 59/n mV and increases with increasing v
- E_{pc} shifts negatively with increasing v.

The current for quasi-reversible process (with $10^{-1} > K^0 > 10^{-5}$ cm.s^{-1}) is controlled by both charge transfer and mass transport. In such a case, the shape of the CV is a function of $\frac{K^0}{\sqrt{\pi a D}}$ (Where; $a = \frac{nF\upsilon}{RT}$). When the values of $\frac{K^0}{\sqrt{\pi a D}}$ increase, the quasi-reversible process approaches the reversible system and when its values decrease (i.e., at very fast scan rate) an irreversible process behaviour is observed. Compared to reversible system, cyclic voltammograms of a quasi-reversible system are more drawn-out and have a larger peak potential separation [48, 90, 131, 146, 171].

3.3.1.1.7 Study of adsorption processes

Cyclic voltammetry can also be used for evaluating the interfacial behaviour of electroactive compounds. Both the reactant and the product can be involved in an adsorption –desorption process. Such interfacial behaviour can occur in studies of numerous organic compounds, as well as of metal complexes (if the ligand is specifically adsorbed) [60]. In some cases, the sample to be characterized may be immobilised onto the surface of a working electrode (chemically modified electrodes). In such a case, the surface concentration (Γ) of the absorbed species could be estimated from a plot of current (I_p) versus scan rate (ν) in accordance with the Brown Anson model using the equation [31].

$$I_p = \frac{n^2F^2\Gamma A\upsilon}{4RT} \ldots\ldots\ldots (3.11)$$

where Γ is the surface concentration (mol/ cm^2).

During the reduction or adsorption of the adsorbed layer, the quantity of the charge (Q) consumed can also be used to calculate the surface coverage or surface concentration (Γ).

$$Q = nFA\Gamma \ldots\ldots\ldots (3.12)$$

Where Q is the charge in Coulomb (C) and Γ is a surface coverage in mol/ cm^2

Cyclic voltammetry is a good technique for studying the electrochemistry of nanomaterials [31, 60].

3.3.1.2 Square Wave Voltammetry (SWV)

Square wave voltammetry (SWV) has proved to be a suitable method to investigate redox reactions with overlapping waves. The excitation signal in SWV consists of a symmetrical square wave pulse of amplitude superimposed on a staircase wave form of step height ΔE. The forward pulse coincides with the staircase step. The net current (I_{net}) is obtained by taking the difference between the forward and the reverse currents (I_{fwd}- I_{rev}) and is centred on the redox potential. In SWV, the peak height is directly proportional to the concentration of the electroactive species and direct detection limit as low as 10^{-8} M is possible. SWV is associated with some advantages over cyclic voltammetry. These advantages include excellent sensitivity and rejection of back ground currents. The scanning speed in SWV is also high. This high speed coupled with computer control and signal averaging allows for experiments to be performed repetitively and this increases the signal to noise ratio. SWV is also applied in study of electrode kinetics with regard to preceding, following or catalytic homogeneous chemical reactions and determination of some species at trace levels [112].

3.3.1.3 Electrochemical Impedance Spectroscopy (EIS)

Electrochemical Impedance spectroscopy (EIS) is a non-destructive and effective method for probing the features of surface-modified electrodes. It offers a label free detection and allows for analysis of both resistance and capacitance properties of materials. The measurement of EIS involves application of a sinusoidal voltage to an electrochemical cell, and measuring the current response. A frequency response analyzer generates time-invariant amplitude (A), phase (θ) and angular frequency (ω) voltage-current waves. The ratio of voltage (E) to current (I) gives the impedance and has the units of resistance (ohms), in accordance with the Ohm's law; Voltage (E) = Current (I) x Resistance (R). Impedance is run over a wide range of frequencies, giving rise to several electrochemical reactions at the electrode-electrolyte interface [4, 21]. The total impedance is therefore a function of frequency and is expressed in a complex form, with real and imaginary components as follows

$$Z(j\omega) = \frac{E\,(j\omega)}{I(j\omega)} = Z'(\omega) + jZ''(\omega) \ldots\ldots\ldots.(3.13)$$

Where $Z'(\omega)$ and $jZ''(\omega)$ are the real and imaginary terms respectively, $j = \sqrt{-1}$ and is an imaginary number while ω is the radial frequency (rad.s^{-1}) and equals $2\pi f$, f being the exciting frequency (Hz). Impedimetric data is graphically represented in various forms. The most common is the Nyquist plot whereby the imaginary part of the impedance (Z_i) is plotted against the real part (Z_r). The real part of the impedance represents the resistive component of the system while the imaginary part is due to insulating layers such as the double layer capacitance or any additional layers in the system [28, 39]. In the Nyquist plot, the low frequency data is represented on the right side while the high frequency data is represented on the left side of the diagram. The figure below shows a typical shape of a Faradaic impedance spectrum (typical Nyquist diagram) and the corresponding Randle's circuit. It includes a semicircle region lying on the axis followed by a straight line. The semicircle portion, observed at higher frequencies, corresponds to the electron transfer-limited process, whereas the linear part is characteristic of the lower frequencies range and represents the diffusion-limited electrochemical process. In the case of very fast electron transfer processes, the impedance spectrum could include only the linear part whereas a very slow electron-transfer step results in a large semicircle region that is not accompanied by a straight line. The electron transfer kinetics and diffusion characteristics can be extracted from the spectra [73]. The semicircle diameter equals to the electron transfer resistance Rct.

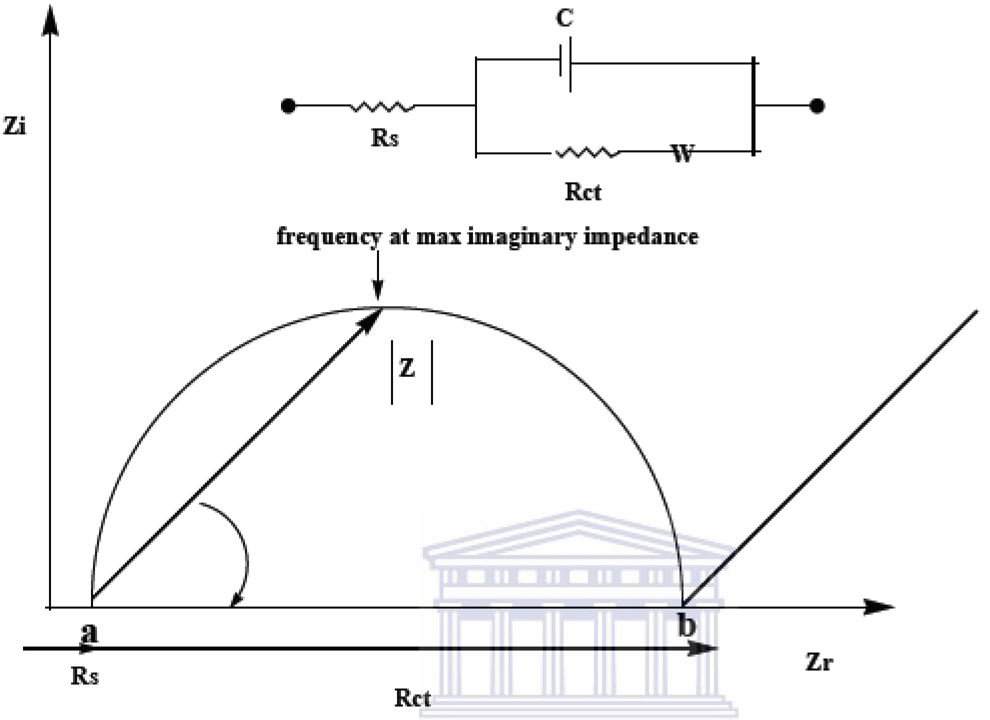

Figure 3. 4: Nyquist plot and the corresponding Randles circuit.

At high frequencies ω→∞, the real Z axis intercepts the semicircle and the intercept equals solution resistance (R_s) while at lower frequencies, the intercept between the real Z and the semicircle yields a value corresponding to $R_s + R_{ct}$. The frequency at maximum imaginary impedance (ωmax) of the semicircle in the Nyquist plot corresponds to $Z_{im} = 0.5\ R_{ct}$ and relates to the Rct and Cdl according to the following equation

$$\varpi_{\max} = \frac{1}{R_{ct} \times C_{dl}} \ldots\ldots\ldots.(3.14)$$

It is also related to the reciprocal of the time constant (τ) according to equation 3.15

$$\tau = R_{ct} \times C_{dl} \ldots\ldots\ldots.(3.15)$$

Exchange current, (Calculated using equation 3.16) and heterogeneous rate constant *k* (calculated using equation 3.17)

$$I_0 = \frac{RT}{nFR_{ct}} \ldots\ldots\ldots.(3.16)$$

$$k = \frac{I_0}{nFAC_0} \ldots\ldots\ldots.(3.17)$$

The advantage of Nyquist plot is that it shows unique impedance arcs, characterized by activation –controlled processes with distinct time constants. Since the total electrode impedance consists of the contributions of the electrolyte, the electrode solution interface and electrochemical reactions taking place on the electrode, the shape of the impedance curves provides meaningful information regarding the different electrochemical transformations at the electrode-electrolyte interface. The total impedance is determined by several parameters:

(1) Electrolyte solution resistance (R_s)

(2) Double layer capacitance (C_{dl}),

(3) Electron or charge transfer resistance (R_{ct})

(4) Warburg impedance (w).

These parameters can be modelled by extracting components of the electronic equivalent circuits that correspond to the experimental impedance spectra. The Randles electronic equivalent circuit is commonly used to model interfacial phenomena and provides an effective simulation of the impedance characteristics of a fast charge transfer reaction at a planar electrode. All electronic characteristics of the equivalent circuit and the corresponding physical parameters of the real electrochemical system can be extracted from such analysis. Since the variable parameters of the system represent the functions of the modifying layer and its composition, they can be used to quantitatively characterize the layer. Analysis of the

Z_{re} (ω) and Z_{im} (ω) values observed at different frequencies allows the calculation of the important parameters.

A representative plot of frequency as x-axis versus logarithm of real impedance as y^1-axis, and phase angle as y^2-axis called Bode plot is presented in (**Figure 3.5** and **3.6)**. Bode plot is a plot of log magnitude of impedance and phase angle versus log of frequency [73, 89, 153].

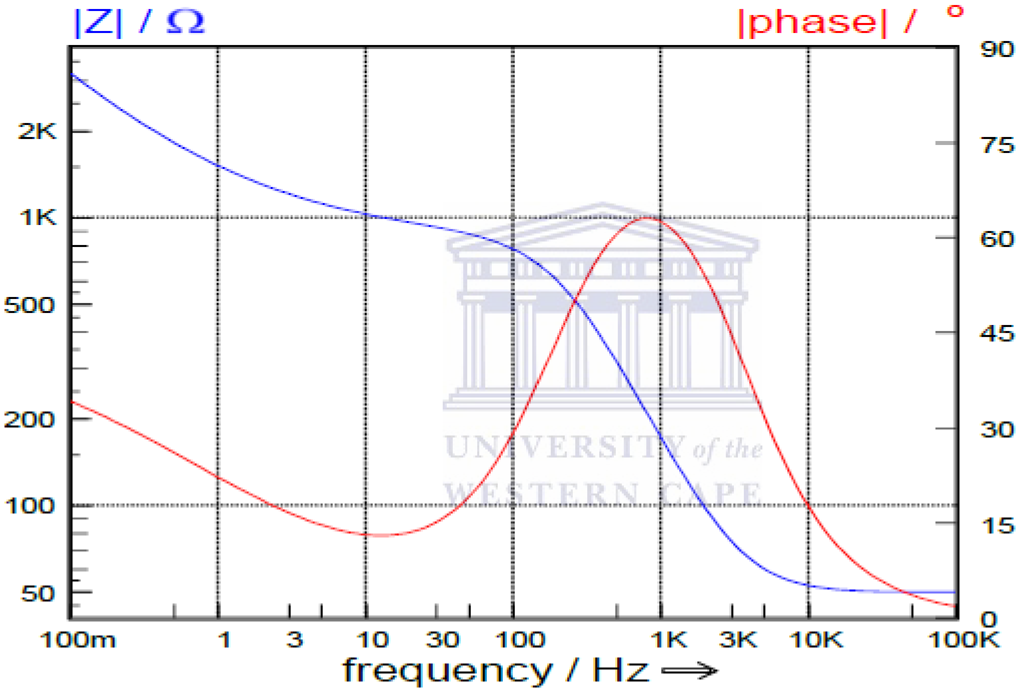

Figure 3. 5: A typical Bode plot showing variation of impedance and phase angle with changes in frequency.

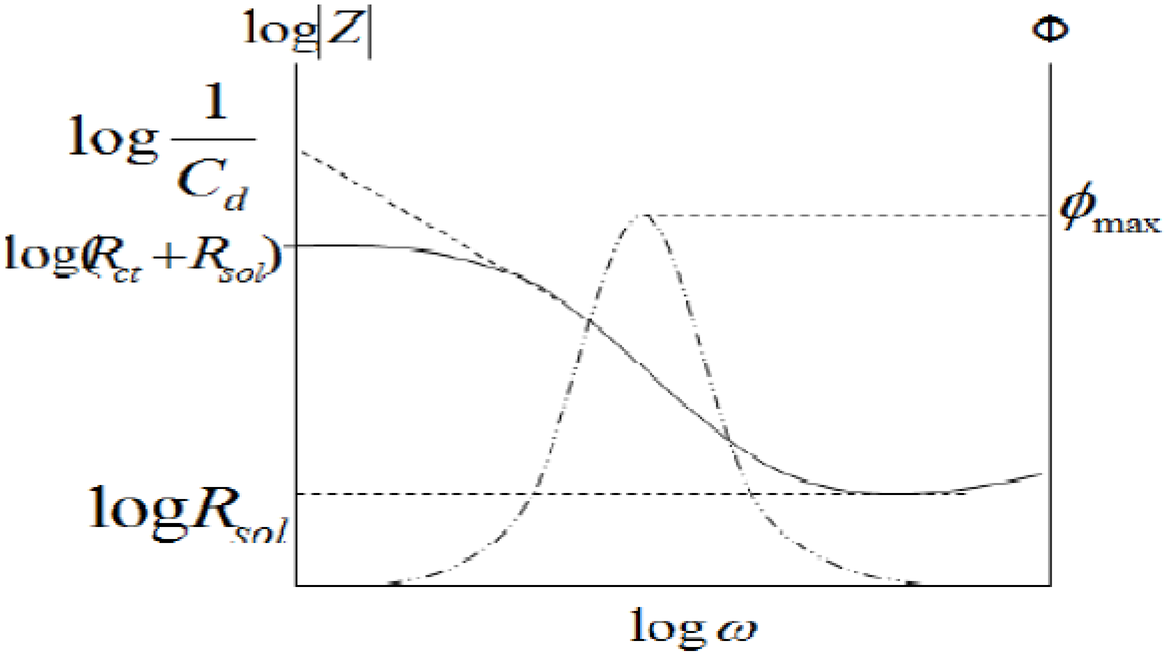

Figure 3. 6: A Bode plot showing some kinetic parameters.

The Bode plot gives direct information on the frequency and phase angle. The frequency at maximum phase is a useful parameter in determining the double layer capacitance using equation 18:

$$\omega_{\emptyset max} = \frac{(1 + \frac{R_{ct}}{R_{sol}})}{R_{ct}C_{dl}} \ldots \ldots \ldots . (3.18)$$

In most applications however, analysis of both Bode and Nyquist plots is highly advised in order to conclusively study electrochemical processes at interfaces. The technique is rapidly developing for interrogating interfacial electrical properties, mechanisms of electrochemical reactions, transport properties of materials as well as exploration of the properties of porous electrodes [88-89, 133, 141, 143, 158, 186, 188].

3.3.2 X-Ray Diffraction (XRD)

X-ray diffraction (XRD) is a powerful non-destructive technique for characterizing crystalline material. It provides information on structures, phases, preferred crystal orientation, and other structural parameters such as, crystalline or grain size, crystallinity, and crystal defects. It is therefore, an indispensable tool for material characterization and thus, forms an integral part in a comprehensive characterization study of nanophase electrocatalyst. XRD in this study was utilized for the direct examination of crystalline structure, phase identification, particle size, and lattice parameter [147]. XRD parameters for Bruker AXS D8 Advance from Ithemba labs (Cape Town)

X-ray Diffractometer: Bruker AXS D8 Advance from Ithemba labs	
Tube	Copper
Detector	Sodium Iodide
Monochromator	Graphite
Electron Intensity	40 kV
X-ray Source	CuKα ($\lambda = 1.5418$ Å)
Current	40 mA
Scan Range	$10^{o} < 2\theta < 100$

Table 3. 1: Experimental parameters for XRD analysis.

In a typical XRD analysis, X-rays are generated in a cathode ray tube by heating the filament to produce electrons. The produced electrons are then accelerated toward the target material by applying voltage and bombarding the target material with electrons. When the electrons have enough energy to dislodge the inner shell electrons of the target material, characteristic X-ray spectra are produced. Copper is generally the most used target material for single-crystal diffraction, with a CuKα radiation of 1.5418 Å. These X-rays are collimated and directed onto the sample. As the sample and detector are rotated, the intensity of the reflected X-rays is recorded. The interaction of the incident rays with the sample produces constructive interference and a peak in intensity occurs when the conditions satisfies Bragg's law equation 3.19. A detector records and processes this X-ray signal and converts the signal to a count rate which is then output to a device such as computer or printer.

$$n\lambda = d \sin\theta \ldots\ldots\ldots.(3.19)$$

By varying the angle θ, the Bragg's law conditions are satisfied by different d-spacing in polycrystalline materials. Plotting the angular positions and intensities of the resultant diffracted peaks of radiation produces a pattern, which is a representative of the sample where a mixture of different phases is present. The addition of an individual pattern then brings about a diffractogram. Now based on the principle of X-ray diffraction, a wealth of structural, physical and chemical information about the material being investigated can therefore be acquired [147].

XRD can be used quantitatively for the determination of average particle size as mentioned above, using the Scherrer equation given below as:

$$D = \frac{0.9\,\lambda}{\beta \cos\theta} \ldots\ldots\ldots.(3.20)$$

Where D is the particle size, 0.9 the shape factor, λ the wavelength of the X-ray, β is the peak width at half peak height (radians), and θ being the angle of reflection. The lattice parameter (a_o) could also be calculated using the following equation:

$$d_{hkl} = \frac{a_0}{\sqrt{h^2 + k^2 + l^2}} \ldots\ldots\ldots.(3.21)$$

$$a_0 = \frac{d_{hkl}}{(h^2 + k^2 + l^2)^{1/2}} \dots\dots\dots. (3.22)$$

Where h, k, and l constitute the Miller indices of a crystal facet, and d is the interplanar spacing determined using Bragg's equation. Crystalline size determination is performed by measuring the broadening of a particular peak in a diffraction pattern associated with a particular planar reflection from within the crystal unit cell. Particle size is inversely related to the half-width at half maximum of an individual peak. Typically the narrower and more intense the peak, the more crystalline the sample is. A broad peak is usually associated with small particle size and an amorphous material [147].

3.3.3 Morphological characterisation (Microscopic techniques)

3.3.3.1 High resolution transmission electron microscopy (HRTEM)

High resolution transmission electron microscopy (HRTEM) is almost exclusively used in the investigation of average particle size, particle shape and particle size distribution of electrocatalysts. In this study, HRTEM was used to determine the morphology, particle size and the particle size distribution of the catalysts [87, 175, 180]. All prepared samples were viewed and photographed using a Tecnai G2 electron microscope at the University of the Western Cape. The experimental parameters are given in (**Table 3.2**)

Parameter Setting	
Accelerating voltage (kV)	200
Current (µA)	20
Condenser aperture	1
Objective aperture	3
Exposure time	3

Table 3. 2: Tecnai G2 transmission electron microscope operational parameters.

3.3.3.2 Atomic force microscopy (AFM)

Atomic force microscopy has become a standard technique for high-resolution imaging of the topography. It enables one to see nanoscopic surface features. This powerful probe microscopy operates by measuring the force between the probe and the sample. This force is attributed to repulsion generated by the overlap of the electron cloud at the probe tip with the electrode cloud at surface atoms. It depends in part on the nature of the electrode, the distance between the electrode and the tip, any surface contamination and the tip geometry. The interaction of the force fields is sensed by a cantilever beam, to which the tip is attached. An image (revealing individual atoms) is created as the probe is rastered across the surface. Such images can be formed by constant–force or constant-height mode (with known or measured deflections of the cantilever, respectively). Since AFM doesn’t involve passage of current between the tip and the surface, it is useful for exploring both insulating and conducting regions [122]. A fine tip is brought into close (but not touching) contact with the sample and senses the small repulsive force between the probe tip and the surface. The tip is rastered over the sample to measure the surface topography. AFM provides a number of advantages over conventional microscopy techniques. It probes the sample and make measurements in three dimensions; x, y, and z (normal to the sample surface), thus enabling the presentation of three-dimensional images of a sample surface. This provides a great advantage over any microscope available previously [122]. With good samples (clean, with no excessively large surface features), resolution in the x-y plane ranges from 0.1 to 1.0 nm and in the z direction in 0.01 nm (atomic resolution) is possible. AFM requires neither a vacuum environment nor any special sample preparation, and they can be used in either. Atomic force spectroscopy (AFM) using a Veeco NanoMan V model (Cambridge, USA) at Ithemba lab, the parameters used are as follows in (**Table 3.3**) below.

Parameter Setting	
Resonance frequency (kHz)	60-100
Spring Constant (N.m^{-1})	1-5
Tip	Silicon tip
Substrate	Glass
Drying sample	Room temperature

Table 3. 3: Atomic force spectroscopy (AFM) using a Veeco NanoMan V model (Cambridge, USA) Parameters.

3.3.3.3 High resolution scanning electron microscopy (HRSEM)

High resolution scanning electron microscopy (HRSEM) is a versatile imaging technique capable of producing three-dimensional profiles of material surface. HRSEM was used in this study to extract quantitative and qualitative information pertaining to particle morphology, surface appearance of supported nanophase electrocatalysts, and elemental analysis using the energy dispersive spectroscopy (EDS) detector [3, 5, 63, 175]. Specimens had to be coated with carbon in order to be used in an HRSEM. Hitachi X-650 SEM operational parameters are as follows in (**Table 3.4**) at University Of The Western Cape (Physics Department).

Parameter setting	
Accelerating voltage (keV)	25
Tilt Angle (^{o}C)	0
Aperture (mm)	0.4
Resolution (nm)	3
Working distance (mm)	10
Magnification (k)	50

Table 3. 4: Hitachi X-650 SEM operational parameters.

3.3.3.4 Energy dispersion spectroscopic analysis (EDS)

Energy dispersive spectroscopy (EDS) detector which is connected to the HRTEM and HRSEM was used in this study to investigate the elemental composition of the electrocatalyst synthesized. After taking HRTEM and HRSEM images, the samples would then be scanned on six different areas to obtain the average wt. % of the metals [96, 179].

3.3.4 Spectroscopic techniques

3.3.4.1 Infrared spectroscopy (IR spectroscopy)

IR (including Fourier transform IR (FT-IR)) spectroscopy is widely used to study the vibrational spectra of small molecules adsorbed on metallic clusters and nanoalloys. For example, by making comparisons with pure metal clusters or surfaces, IR spectroscopy of small molecules (e.g., CO) adsorbed on bimetallic nanoparticles can be used as a probe for the surface composition and structure of the sample [36].

3.3.4.2 UV-visible spectroscopy

It is a spectroscopic technique that involves the spectroscopy of photons in the UV-visible region. It uses light in the visible and adjacent (ultraviolet (UV) and near infrared (NIR) ranges). In UV-visible spectroscopy, one can monitor the colour of a material and current at the same time. The colour monitored is the wavelength at which the maximum of the absorption band(s) occurs, $\lambda_{max,}$ together with the absorbance at each of these wavelengths. The optical absorbance, *Abs*, is defined according to the equation [67, 166]:

$$\text{Abs} = \log_{10}\left(\frac{\text{T with no sample}}{\text{T with sample}}\right) \ldots\ldots\ldots(3.23)$$

Where T is the transmittance of light following its passage through the cell. Any changes in the absorbance relates to the amount of electroactive material as converted by the flow of current. The absorption spectrum tells us the nature of the material generated. It is a major technique that is used in the quantitative determination of solutions of transition metal ions and highly conjugated compounds. For example, if a material absorbs UV-visible light, then we can monitor its concentration using Beer-Lambert relationship;

$$\text{Abs} = \varepsilon \text{C}_0 \text{l} \ldots\ldots\ldots(3.24)$$

Where the absorbance is determined at fixed wavelength λ, ε is the extinction coefficient (cited at the same value of λ), and l is the optical pathlength. If the magnitude of the extinction coefficient at λ is known, then the amount of analyte (C_0) can be quantified simply by determining the optical absorbance and inserting the values into equation (24). Most of the analytical techniques are not particularly useful for telling us what ‘something’ is, but are excellent at telling us how much of that ‘something’ is present, or has been formed or has been changed. However, UV-visible spectroscopy is one of the best ways of identifying an analyte. This is because each specific analyte absorbs energy in the form of photons at different wavelengths.

Furthermore, with the goal of revealing the formation processes of bimetallic ternary and quaternary nanoparticles, that is, the reduction of metal ions and the aggregation process, the observation of UV-vis spectral changes during reduction can provide quite important information [67, 166].

3.3.5 Solid state nuclear magnetic resonance (Solid-state NMR)

NMR spectroscopy probes the local magnetic environment of a nucleus with non-zero magnetic moment in terms of its chemical shift (which depends on the amount of diamagnetic and paramagnetic shielding or deshielding) and line splitting due to magnetic coupling to the nuclear spins of neighbouring atoms. In the case of quadrupolar nuclei, the line shape and number of peaks can also give information on the symmetry of the atomic environment. Regarding mono- and bimetallic nanoparticles, NMR spectroscopy has been performed on metallic nuclei (e.g., 63Cu, 103Rh, 195Pt, and 197Au), where the chemical shift is dominated by the knight shift, arising from the conduction electrons, thereby giving a measure of the metallic nature of the particles. Nanoparticles paramagnetism and ferromagnetism can also be probed by NMR. It has also been used to investigate the structures of adsorbed organic molecules (including passivating molecules and polymers), for which the most useful nuclei are ^{1}H, ^{13}C and ^{31}P [79].

Electrochemical NMR spectroscopy (EC-NMR) was introduced in the late 1980s for the study of electrochemical surfaces, providing an electronic level description of electrochemical interfaces based on the local density of states at the Fermi level. 13C and 195Pt are particularly useful nuclei for investigating electrochemical interfaces and probing nanoparticles and nanoalloys [79].

3.4 Catalyst synthesis

3.4.1. Synthesis NaHTe

Te powder and $NaBH_4$ was combined in a dry test tube. The tellurium was the limiting factor, so the Te and $NaBH_4$ were combined in the ratio Te: $NaBH_4$ 1: 4. The test tube was shaken and tapped to mix the powder before addition of water. 3 mL of distilled water was then be added to the test tube to give the powder the medium in which to react. The test tube is shaken to mix the powder in to the water. Generally a black layer of powder was formed at the top of the water and there was some powder at the bottom with bits floating in the liquid. At this point bubbles were observed within the test tube which translated in the formation of hydrogen gas; this following reaction will be taking place;

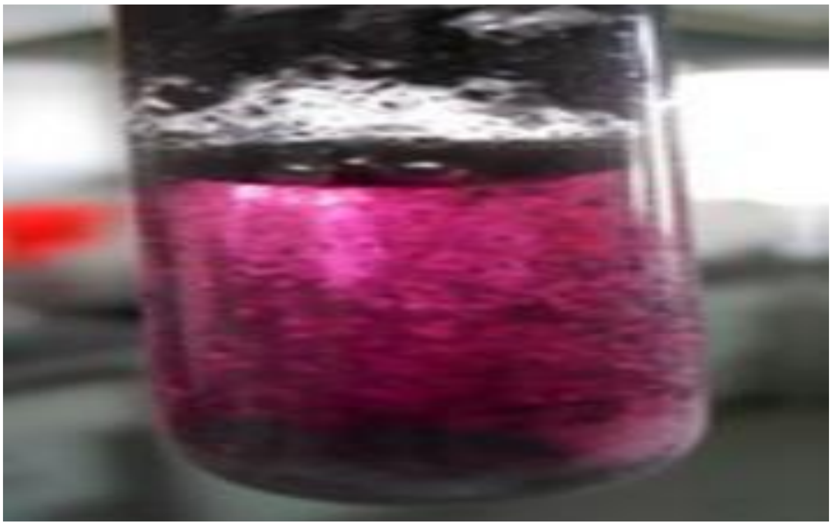

Scheme 3. 1: Synthesized NaHTe and sediments.

$$\mathrm{NaBH_4 + \ Te + dH_2O \ \rightarrow NaHTe + \ H_2 + \ Sediments}$$

The test tube was sealed with plastic wrap and a hole was made with a micropipette on the plastic wrap so that hydrogen gas can escape. The test tube was place in ice for 24 hours, $NaBH_4$ and Te was allowed to react fully as possible to form NaHTe as shown in scheme 3.1.

3.4.2. Synthesis of Pt, PtRu, PtIr and PtTe nanoparticles

Solution A: Pt nanoparticles

All solutions were prepared in ultra pure water.

Pt nanoparticles were synthesised by adding drop wise 10 mL of 0.00168 M $NaBH_4$ solution aged for 3 h to 20 mL of a 0.00018 M H_2PtCl_6 solution with vigorous stirring into a round bottom flask at a temperature of 90 °C. Followed by the addition of a surfactant PVP and the reaction were left for 16 hours to reach completion. After complete reduction of the Pt nanoparticles were centrifuged and then washed 3–4 times with ultra-pure water.

Solution B: PtRu, PtIr and PtTe nanoparticles

PtRu, PtIr and PtTe nanoparticles were synthesised by adding drop wise 10 mL of 1.68 mM $NaBH_4$ solution aged for 3 h to aqueous solution

- 20 mL of fixed 0.00018 M H_2PtCl_6, was varied 0 to 0.00018 M $RuCl_{3,}$
- 20 mL of 0.00018 M $H_2PtCl_{6,}$ was varied 0 to 0.00018 M $IrCl_3$ and
- 20 mL of H_2PtCl_6 and NaHTe

Was added into three different round bottom flask was stirred vigorously at 90 ^{o}C followed by the addition of surfactant PVP. The reaction was left over night for the reaction to be complete. The binary nanoparticles were centrifuged and washed 3-4 times with ultrapure water.

3.4.3 Synthesis of Pt based ternary nanoparticles PtRuTe and PtIrTe.

In a typical synthesis of PtRuTe and PtIrTe ternary nanoalloy, 0.00018 M aqueous solution of H_2PtCl_6/ $RuCl_3$ or $IrCl_3$/ NaHTe mixtures was added to a 40 mL of highly purified water. To the solution, 10 mL of 0.00168 M $NaBH_4$ (reducing agent) was added. After 15 s, an aqueous solution of PVP (5 mg/mL, 1.5 mL) was added (as a capping agent) drop wise with vigorous stirring and the solution was stirred under reflux at 90 ^{o}C for 12 hours. The resulted ternary nanoparticles were centrifuged and washed with ultra pure water to remove excess PVP. The synthesis of nanoparticles is represented by scheme 3.2 below:

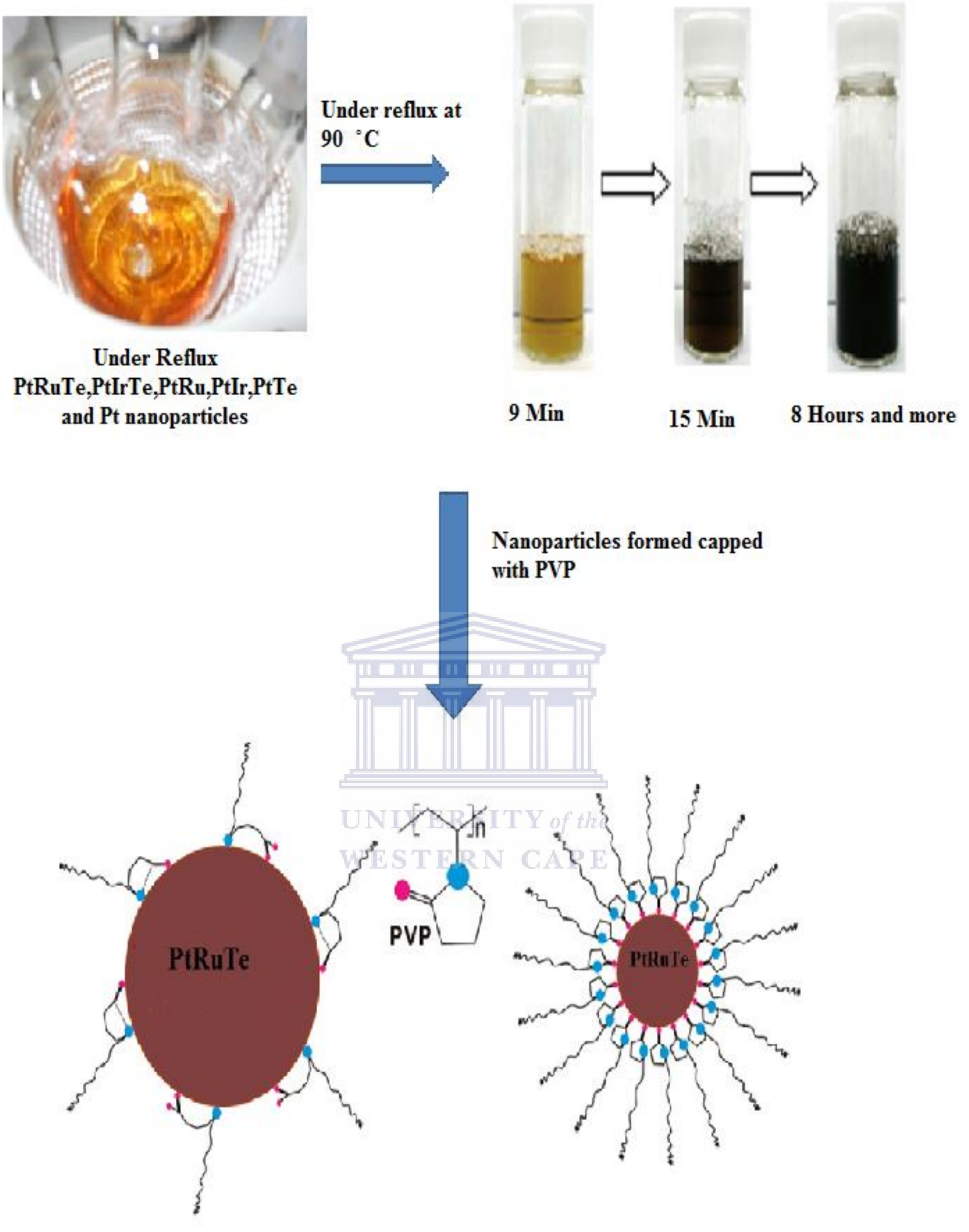

Scheme 3. 2: Methodology of synthesis of Pt based nanoparticles being binary and ternary are represented.

3.5 Fabrication of Pt electrode with nanoparticles

Prior to modification, the bare Pt electrode was polished to a mirror finish with 1.0, 0.3, and 0.05 µm alumina slurries, respectively, and rinsed thoroughly with distilled water in between polishing with different sized alumina slurries followed by sonication in ethanol and water in the end. 6 µL solutions of already synthesised nanoalloys were drop-coated onto the Pt electrode and allowed to air dry at room temperature. The modified electrodes were taken out and rinsed with water and were ready for electrochemical characterisation and application.

3.6 Characterisation of the nanoalloys

3.6.1 Electrochemical characterisation

3.6.1.1 Cyclic Voltammetry (CV) and Square Wave Voltammetry (SWV)

To study the electrochemistry of the nanoparticles, the nanoalloy modified Pt electrodes (as described in section 3.5 above) were gently rinsed with de-ionized water to remove any excess or weakly adsorbed nanoalloys and were further used for electrochemical characterisation. The voltammograms (CV and SWV) were recorded under argon atmosphere. Electrochemical measurements were performed in 10 mL of 0.5 M H_2SO_4 and 1 M KOH solutions over a potential range of -400 mV to +1500 mV and -1000 mV to 400 mV respectively at different scan rates. 0.5 M H_2SO_4 solution was used as the test solution for the polyoriented nanoalloys. Fresh electrolyte solutions were prepared every time an experiment was carried out.

To study the electrooxidation of the Pt-based nanoparticles on ammonia, 10 mL of the freshly prepared 1 M KOH solution was used as an electrolyte and purged with argon gas for 10 min.

electrochemical measurements were performed over a potential range of -1000 mV to 400 mV.

3.6.1.2 Electrochemical impedance spectroscopy (EIS)

Electrochemical impedance spectroscopy (EIS) of the nanoalloy modified electrodes were measured using Voltalab PGL 402 from Radiometer Analytical (Lyon, France) in 1 M KOH solution and plotted in the form of complex plane diagrams (Nyquist and bode plots) at a perturbation amplitude of 10 mV within a frequency range of 100 kHz to 100 mHz

3.6.2 X-Ray Diffraction (XRD)

In the XRD analysis Pt based nanoparticles solid catalytic samples were mounted upon in plastic sample holders and the surface was flattened to allow maximum X-ray exposure. Experimental parameters for XRD analysis are given as above 3.3.2, the measurements were done in X-ray Diffractometer: Bruker AXS D8 Advance.

3.6.3 Morphological characterisation (Microscopic techniques)

3.6.3.1 High resolution transmission electron microscopy (HRTEM)

The HRTEM samples were prepared by suspending the supported catalyst powder in ultra pure water solution and depositing a drop of the suspension on a standard copper grid and nickel grid. Samples were mounted in a sample holder, which was introduced directly into the shaft of the microscope. Measurements were done using Tecnai G2 transmission electron microscope instrument.

3.6.3.2 Atomic force microscopy (AFM)

Surface morphology of the nanoparticles was studied by atomic force spectroscopy (AFM) using a Veeco NanoMan V model (Cambridge, USA). The preparation of samples for AFM analysis was as follows: 10 μL of liquid nanoparticles sample was dropped on a glass substrate and left to dry at room temperature. The samples were scanned with a silicon tip at a spring constant of 1-5 N/m and resonance frequency of 60-100 kHz.

3.6.3.3 High resolution scanning electron microscopy (HRSEM)

HRSEM samples were prepared by placing double-sided conductive carbon tape on an aluminium specimen stub. A very small amount of the sample was deposited on the specimen stub and flattened with a spatula, then gently tapped to remove the excess and loose sample.

Nanoparticles catalysts did not require any coating, as they were conductive enough to be imaged without charging. The samples were then introduced into the vacuum chamber of the microscope for analysis.

3.6.4 Spectroscopic techniques

3.6.4.1 Infrared spectroscopy (IR spectroscopy)

Analysis was performed using a Perkin Elmer Paragon 1000 FTIR Spectrophotometer. The analysis of all Pt-based nanoparticles samples used was the dried and prepared pellets using a presser which were place in the instrument for analysis.

3.6.4.2 UV-visible spectroscopy

Freshly prepared samples were used for UV-vis analysis. UV–visible absorption measurements of samples were obtained in quartz cuvettes using a Nicolet Evolution 100 UV–visible spectrometer (Thermo Electron Corporation, UK) at a wavelength of 200 nm to 800 nm.

CHAPTER 4

Summary

This is the first of three chapters outlining and discussing the results obtained from this study. This chapter deals specifically with the characterisation of monometallic Pt nanoparticles and its subsequent application in the oxidation of ammonia. The chapter clearly illustrates how the nanoparticles were successfully synthesised by a simple chemical reduction method using sodium borohydride as a reducing agent under reflux capped with polyvinylpyrrolidone (PVP). Structural characterization was done with XRD and spectroscopic methods such as FTIR and UV-vis. Morphological characterization was carried out by HRTEM and HRSEM and the electrochemical properties of these nanoparticles were interrogated using techniques such as CV, SWV and EIS. The potential application of the nanoparticles as electrocatalysts for ammonia electro-oxidation was further investigated.

4.0 Results and Discussion (Part 1)

4.1 Mono-Metallic Catalyst

The noble transition metals (Pt, Pd, Rh and Ir) are found to be the most active catalysts. The coinage metals (Cu, Ag, and Au) were found to be less active than the noble transition metals, but more active than the other transition metals and the metal oxides. Similarly to the oxidation in water, the most active catalyst for the selective oxidation to dinitrogen was iridium [137]. Many studies on the electrochemical ammonia oxidation over Pt electrode in an alkaline aqueous electrolyte have been reported. Gerischer et al [72] proposed the ammonia oxidation mechanism including the production of poisoning species [72]. de Vooys et al [54] studied the ammonia oxidation over the platinum group metals (Pt, Ru, Pd, Rh, and Ir), and found that N_{ad} served as a poisoning species on those metals. The electrocatalytic activity for the ammonia oxidation varied in the order of Ru < Rh < Pd < Ir < Pt. This order in catalytic activity reflected the difference in the affinity of N_{ad} for the metal surface. The activity enhancement of Pt-based catalysts was achieved by using the Pt–M binary alloys (M = Ir, Ru) which is discussed more in detail in (chapter 5) [54].

4.1.2 Structural Characterization by XRD, IR spectroscopy and UV-vis.

4.1.2.1 X-ray diffraction structural characterization of PtNP

The powder X-ray diffraction of the synthesized Pt nanoparticles electro-catalysts recorded at 2θ range of 20^o to 100^o are presented in (**Figure 4.1**) below. As well as the crystalline nature of the Pt nanoparticles was confirmed by recording the X-ray power diffraction (XRD) spectrum (**Figure 4.1**) of PtNP chemical synthesis under reflux. The peak at 2θ 39.7˚, 46.2˚, 67.4˚, 81.2˚ and 85.7˚ can be assigned to the (111), (200), (220),(311) and (222) crystalline planes of face centred cubic (fcc) Pt, respectively, which indicated that the Pt nanoparticles are composed of pure crystalline Pt. The XRD was commonly employed to calculate the mean particle size of the electrocatalyst nanoparticles material using Scherrer's equation explained in detail in chapter 3, and used the platinum diffraction peak (111). The strongest and sharpest diffraction peak for the samples at around $2\theta = 39.7^{\circ}$ is indexed as (111)

$$D = \frac{0.9\,\lambda}{\beta \cos\theta} \qquad (4.1)$$

The catalyst showed relatively small particle size which is known to enhance the electrochemical surface area of the catalyst. Lattice parameter was calculated using the following equation [127, 147]:

$$a_{fcc} = \frac{\sqrt{2}\lambda}{\sin\theta} \qquad (4.2)$$

The calculated values of the average particle size and lattice parameter are presented in (**Table 4.1**) below.

Catalyst	**Particle size (nm)**	**Lattice parameter (a_{fcc}) (nm)**
PtNP	0.018	2.085

Table 4. 1: Summary of average particle size and lattice parameter of PtNP electrocatalyst obtained from XRD measurements.

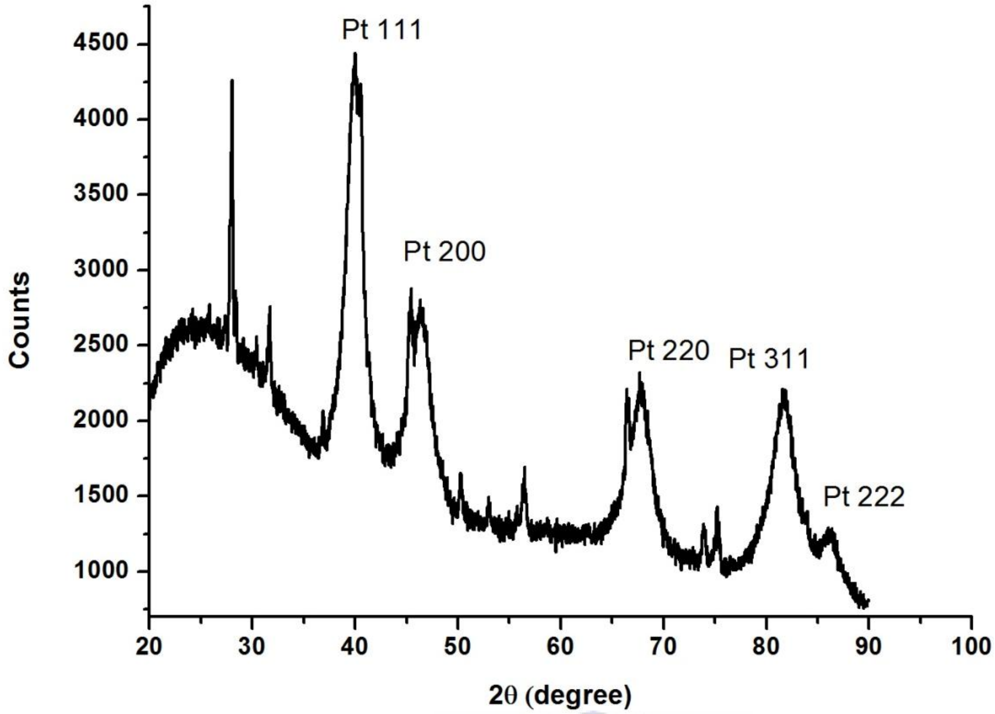

Figure 4. 1: XRD pattern of Pt nanoparticles.

4.1.2.2 Fourier transformer infra-red spectroscopy structural characterization of PtNP

FTIR spectrum in (**Figure 4.2**) shows the IR spectra in the 400–4500 cm^{-1} range of PVP capped Pt nanoparticles; the broad absorption band centered at 3420 cm^{-1} is attributed to O-H stretching mode of H_2O absorbed on the surface of the product. The most striking evidence from FTIR spectrum of the PVP stabilized Pt is the broad peak between 1182 and 1645 cm^{-1} which corresponds to C-N stretching motion and C=O stretching motion of monomer for PVP, respectively [36, 67]. Alvarez et al [2] found similar findings that the narrow absorption peak centered at 1428 cm^{-1} and 2876 cm^{-1} occurred in (**Figure 4.2**) is ascribed to the C–H bonding due to the presence of PVP. This may be due to the formation of coordinate bond between the nitrogen atom of the PVP and the Pt^{2+} [2].

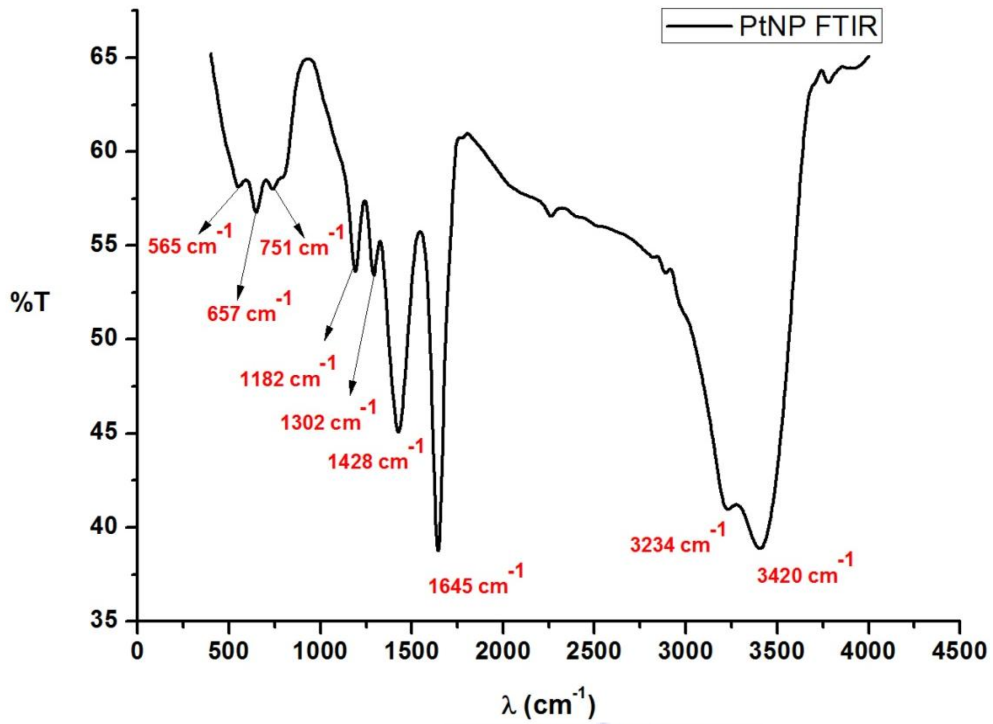

Figure 4. 2: FTIR spectrum of PVP capped Pt nanoparticles.

4.1.2.3 Ultra violet visible spectroscopy structural characterization of PtNP

The formation of the nanoparticles by reduction of $PtCl_6^{2-}$ ions was confirmed by the use of UV-visible spectroscopy. (**Figure 4.3**) shows the UV-visible spectra of the starting materials $H_2PtCl_6.H_2O$ salts and shows the UV-visible spectra of Pt nanoparticles. The absorption peaks observed at 264 nm for Pt^{4+} ions disappeared after 8 h of reduction indicating that the metal ions were completely reduced this findings are also supported by literature [42, 68, 99]. The synthesised platinum nanoparticles showed no absorption peaks, it showed an exponentially shaped graph indicating a complete reduction of the metal salts. The colour of the solution turned from pale yellow to dark brown then finally to black.

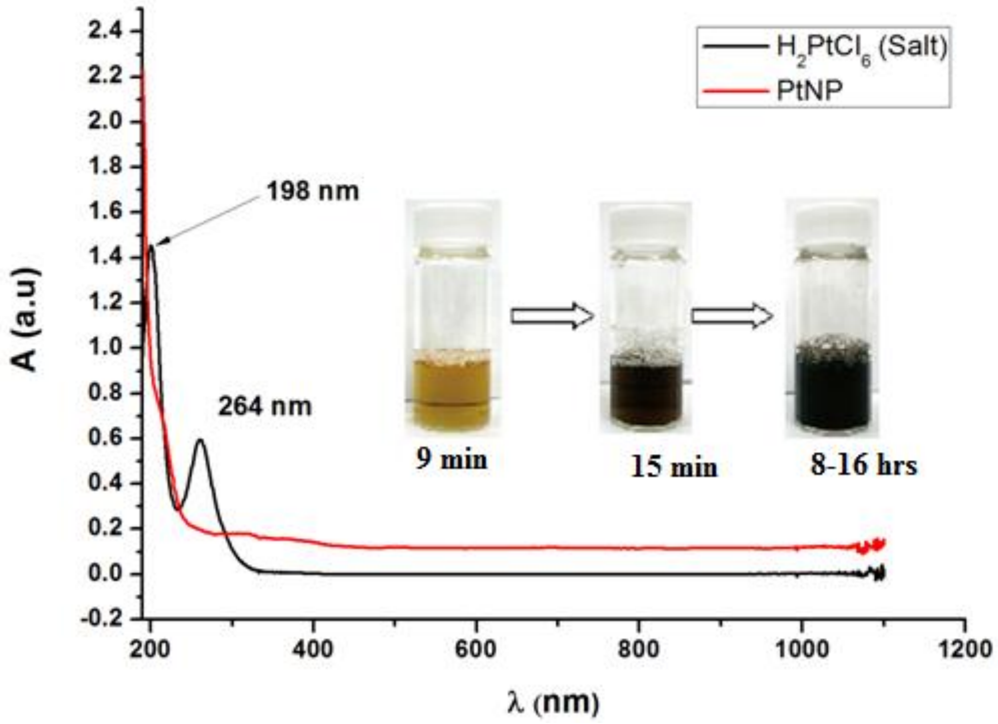

Figure 4. 3: UV-visible spectra of H_2PtCl_6 salt and Pt nanoparticles.

4.1.3 Morphological Characterization by HRTEM and HRSEM

4.1.3.1 HRTEM and EDX for morphological characterization of PtNP

Since the particle size and particle morphology greatly influences the electro-chemical activity of the catalyst owing to the relationship between catalytic activity and surface structure, HRTEM analysis of Pt nanoparticles electro-catalyst was therefore carried out before the comparison of its catalytic activity. [**Figure 4.4 (a) and (b)**] shows typical HRTEM images of the prepared Pt nanoparticles. The nanoparticles produced were found to be well dispersed, with an average diameter of 5-20 nm. HRTEM image of a single particle (not shown) revealed atomic lattice fringes demonstrating the crystalline nature of the nanoparticles. It was observed that the spherical metal nanoparticles are uniformly dispersed on the Cu grid with few agglomerates on some parts of the sample. The uniformity of the catalyst particle distribution is known to be important factor for electro-catalytic activity. It can clearly be revealed at

(**Figure 4.4 (b)**) at 5 nm resolution that nanoparticles are poly-orientated which is in agreement with the results obtained in the XRD that Pt nanoparticles exhibited different diffraction patterns. Selected area electron diffraction pattern (SAED shown in [**Figure 4.4 (c)**] shows characteristic electron diffraction rings of Pt, further indicating that the catalyst structure is made of nanoparticles. The crystallite size L_v was determined using the simple Scherrer equation:

$$L_v = \varphi \frac{\lambda}{\text{FWHM} \ \cos \varnothing} \qquad (4.3)$$

Where L_v is the Scherrer length, φ is the shape factor (0.89 for spherical crystallite), λ the radiation wavelength (1.5406 Å), FWHM the full width at half-maximum, and θ the angle at the maximum intensity. Apparently Lv is extracted from the diffraction peak located close to $2\theta = 40°$, which corresponds to the (111) crystallographic plane of platinum. The average particle size for Pt nanoparticles is 2.1 nm – 5 nm show that the platinum nanoparticles clusters agglomerate to some extent [87, 175, 179-180].

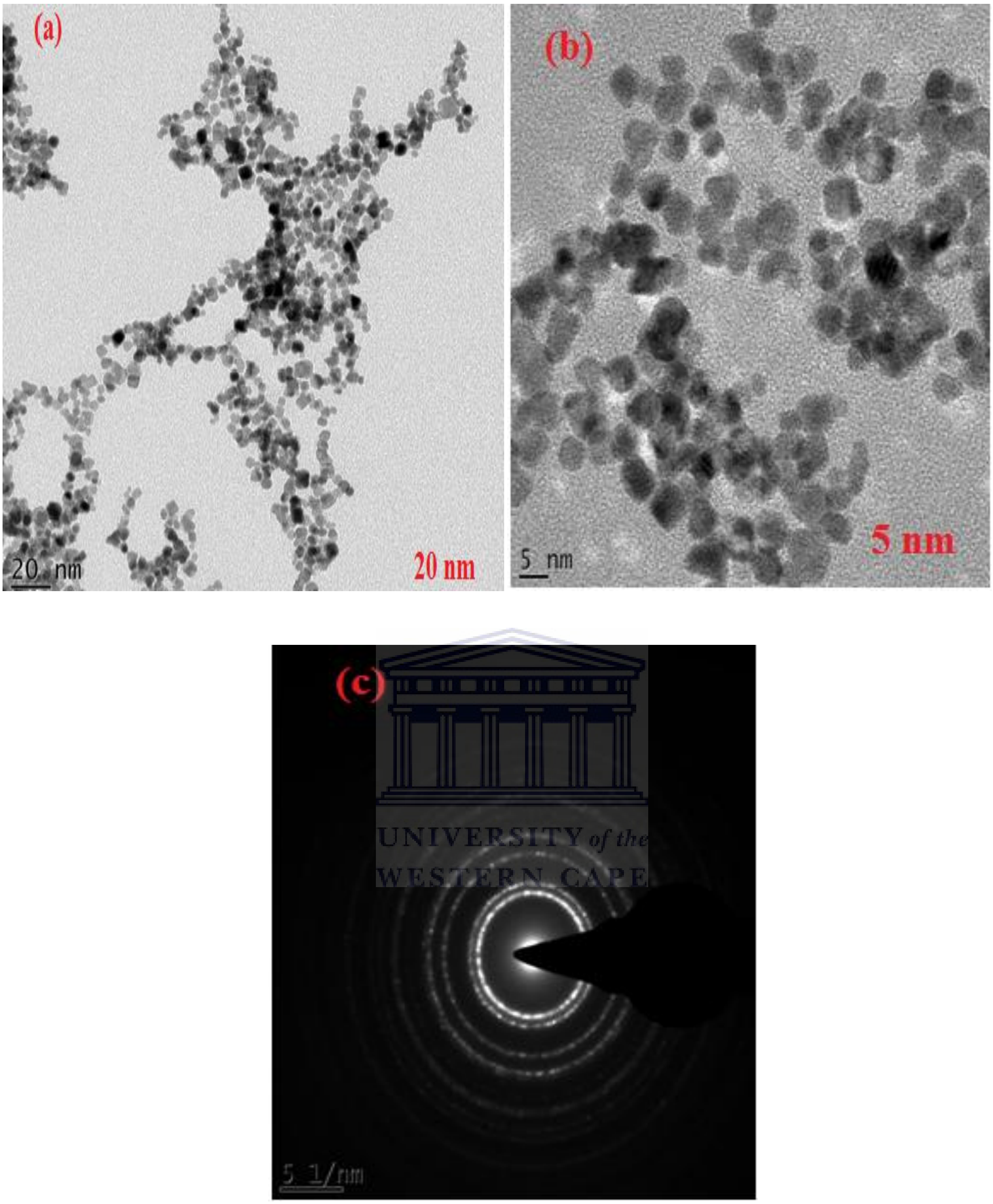

Figure 4. 4: HRTEM images of Pt nanoparticles (a) and (b) on Cu grid and selected area electron diffraction pattern (SAED) at (c).

To investigate the elemental composition of the prepared nanoparticles, the Pt nanoparticles were characterised using EDX. The EDX analysis **Figure 4.5** of the synthesised Pt nanoparticles revealed the elemental composition of the nanoparticles and showed that Pt element were present in the nanoparticles nanoclusters system. However, other elemental signals were also recorded namely; carbon, oxygen and copper. The presence of carbon may have originated from contamination during sample preparation, the oxygen was due to the presence of PVP in the nanoparticles while copper is as a result of the copper grid onto which the nanoparticles were drop coated for the HRTEM analysis.

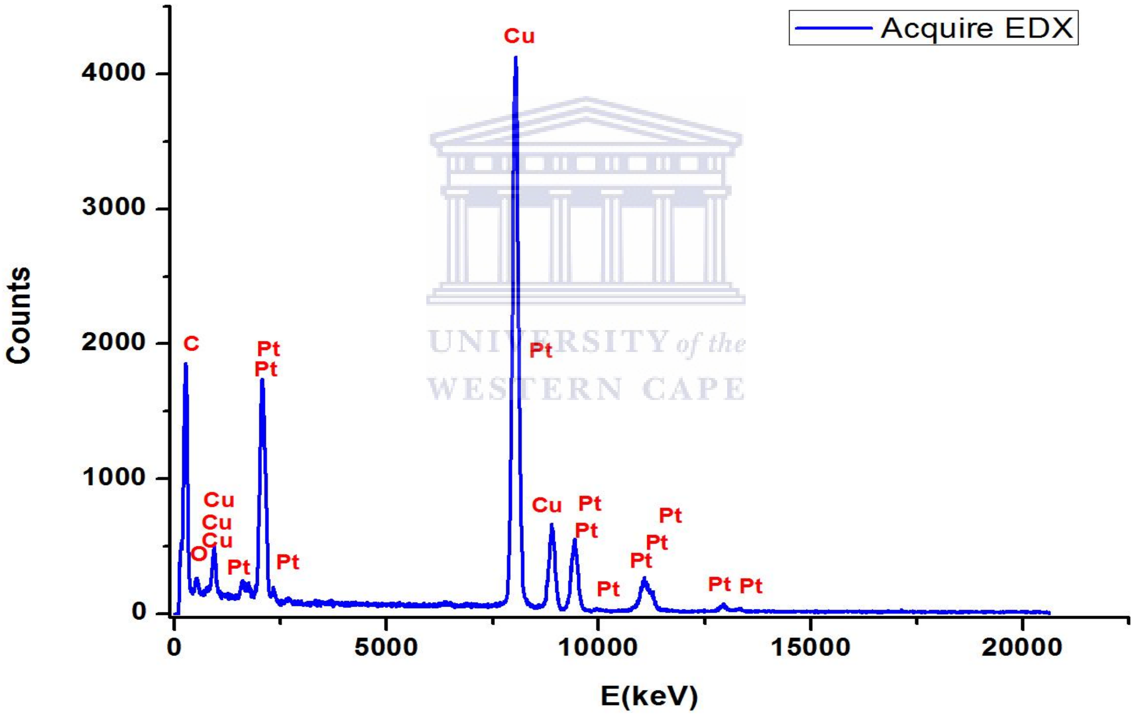

Figure 4. 5: Energy dispersive X-ray (EDX) spectrum of Pt nanoparticles.

4.1.3.2 HRSEM and EDS for morphological characterization of PtNP

In order to verify the particle size of the deposited platinum, HRSEM analyses was carried out for all the Pt nanoparticles, which were prepared by platinum nanoparticles deposited on to carbon supports, as shown in [**Figure 4.6 (a) and (b)**]. In general, the particles exhibit uniform size and cubic, spherical shape in general poly-orientated as observed using XRD and HRTEM. They appear to be homogeneously distributed over the entire support surface. In the case shown the particles are approximately 36 nm in diameter for all different types of carbon electrode. The platinum particle size, as seen in HRSEM images, is rather bigger than that which was calculated via XRD and HRTEM. This may be due to either the impossibility of observing small particles by HRSEM or because the observed particles are, in fact, aggregations of smaller particles. In order to overcome these problems, HRTEM observations were made with the Pt nanoparticles on Cu grid as a means of characterisation. In an fcc unit cell the atoms touch along the face diagonals and the lattice parameter may be calculated from the following equation;

$$4\mathrm{r} = \mathrm{a}(2)^{1/2} \qquad (4.4)$$

Where r is the radius of Pt = 0.177 nm

For the hcp close packing arrangement, the lattice parameters a (=b) and c may be calculated from the radius as follows using equations 4.5 and 4.6:

$$\mathrm{a} = 2\mathrm{r} \qquad (4.5)$$

And

$$2a = \left[\left({}^{a}/_{\sqrt{3}}\right)^{2} + \left({}^{c}/_{2}\right)^{2}\right]^{1/2} \qquad (4.6)$$

The lattice parameter a = 5 x 10^{-10} nm for platinum nanoparticles with small particle size and irregular shape and size distribution[139].

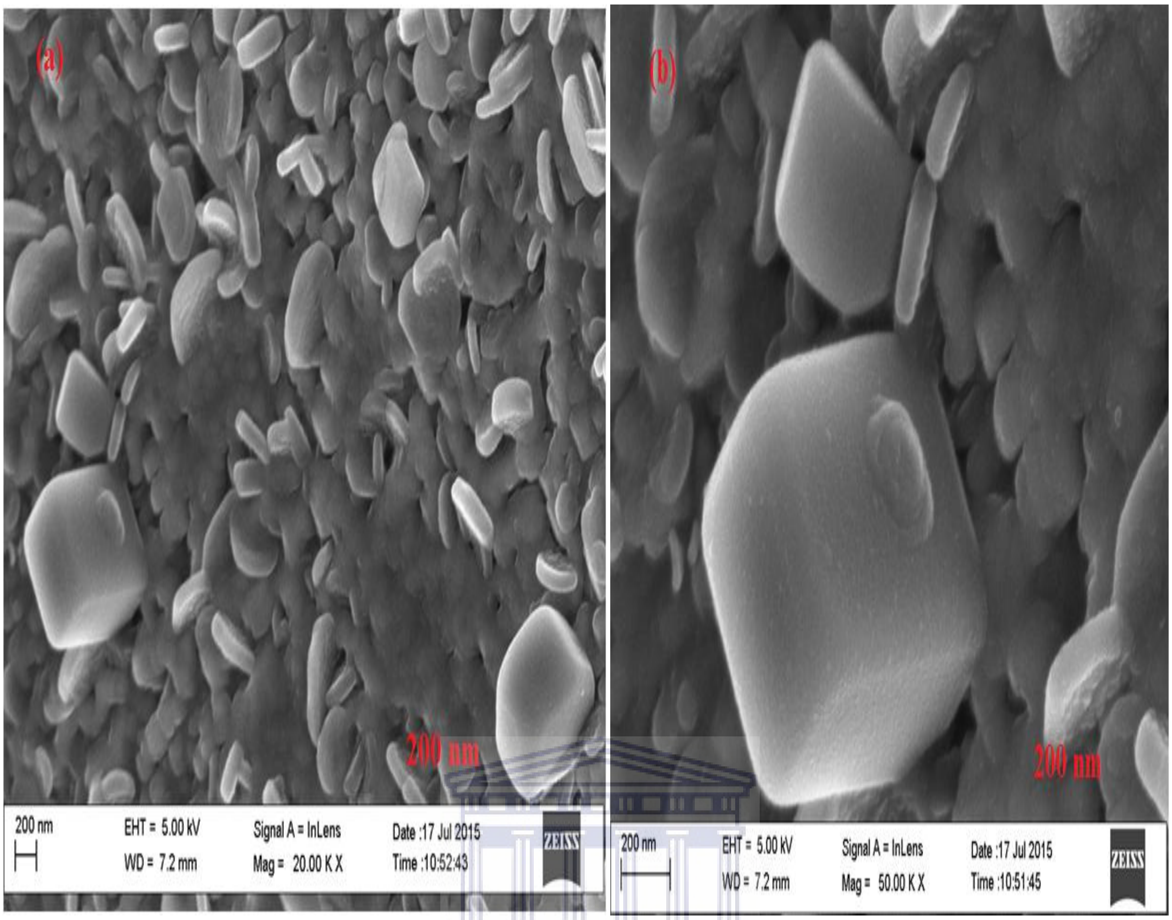

Figure 4. 6: HRSEM image of Pt nanoparticles.

Energy dispersive spectroscopy (EDS) detector which is connected to the HRSEM was used in this study to investigate the elemental composition of the electrocatalyst synthesized shown in (**Figure 4.7**) below. It can be observed there is sodium, chloride which could be contaminates obtained during sample preparation and carbon is from the carbon paste used to prepare the sample. After taking HRSEM images, the samples was then scanned on six different areas to obtain the average wt. % of the metals which can be observed in (**Table 4.2**) giving the elemental analysis of Pt nanoparticles.

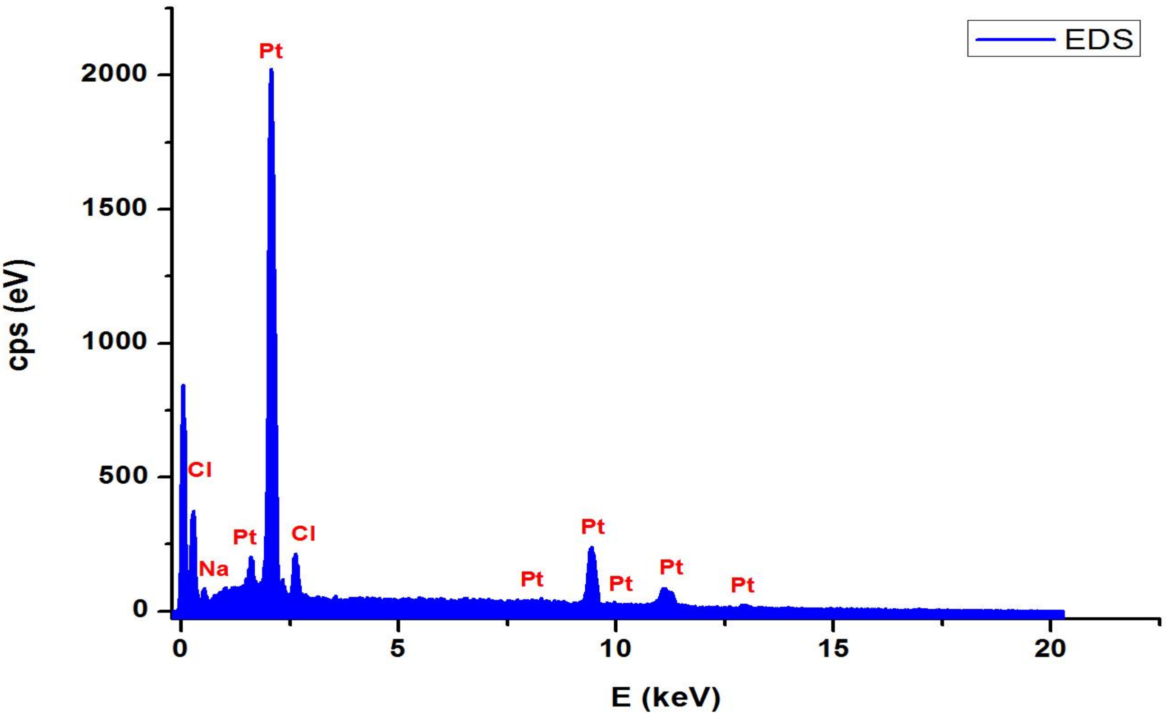

Figure 4. 7: Energy dispersive spectroscopy (EDS) analysis of Pt nanoparticles electro catalyst.

Element	**Atomic %**
C	66.64
Pt	23.69
Cl	2.33
Na	6.88
Total:	100

Table 4. 2: Energy dispersive spectroscopy (EDS) elemental analysis results for PtNP.

4.1.4 Electrochemical characterization of Pt nanoparticles by CV, SWV and EIS

4.1.4.1 Electrochemical characterization of PtNP in 0.5 M H_2SO_4

(**Figure 4.8**) shows the base voltammograms corresponding to the pure metal nanoparticles employed in this study in 0.5 M H_2SO_4. The voltammogram shows voltammetric profiles very similar to those obtained for the corresponding metals in bulk state. No evidence was found in relation to the presence of preferential surface orientation and therefore, the surface of the nanoparticles can be considered as polyoriented or polycrystalline. This relates very clearly with the information obtained in XRD, HRTEM and HRSEM. Although HRTEM and HRSEM techniques are able to show the size and ex situ shape of nanoparticles, the analysis of a statistically significant number of nanoparticles seems unrealistic and only partial information can be obtained for a given sample of nanoparticles and the real global distribution of surface sites in the nanoparticles cannot coincide with the partial distribution found using HRTEM and HRSEM. In order to characterise in situ the structure of the Pt nanoparticles and nanoalloys, a surface sensitive technique or process has to be used. Electrochemistry provides some surface sensitive reactions that can be used as a tool to characterise the surface structure. In addition, these voltammogram clearly shows evidence of cleanliness of the surface of the nanoparticles: in the case of Pt nanoparticles the sharpness and the symmetry of the peaks (I) and (I') at -124 mV which involve fast adsorption desorption processes (H and anion) prove this statement at first sight. The potential window was -200 to 1500 mV and prominent reduction peak can be observed at (II') at 350 mV and there is also oxidation peak at 905 mV but it’s not as prominent which is characteristics of Pt nanoparticles on Pt electrode which can be attributed to reduction of Pt oxide formed during the anodic scanning.

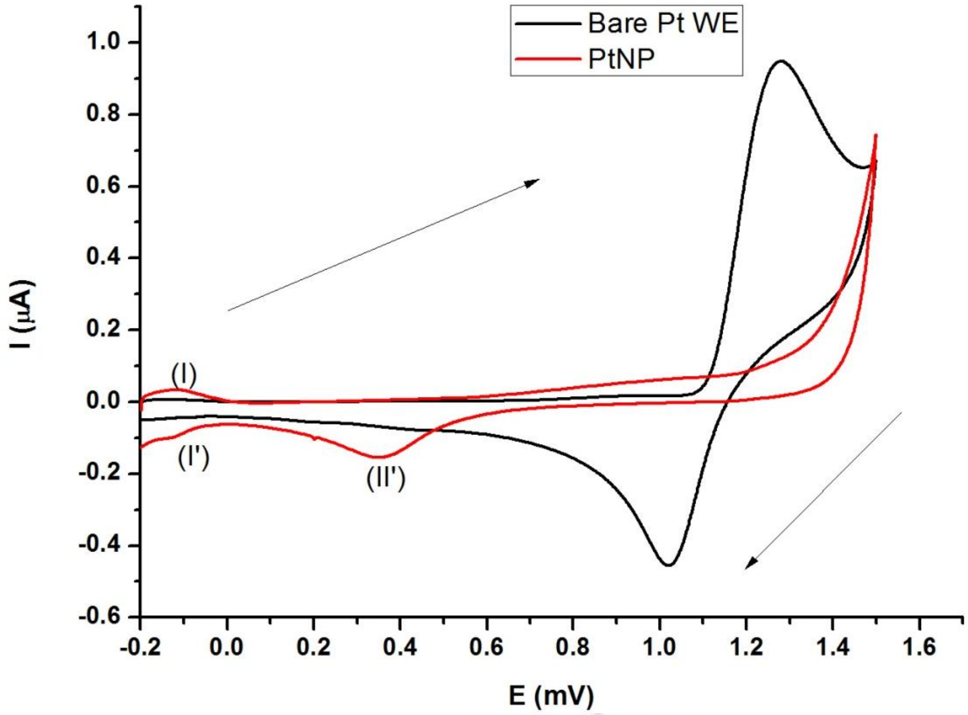

Figure 4. 8: Cyclic voltammograms of Pt nanoparticles modified Pt electrode;. Test solution, 0.5 M H_2SO_4: Scan rate, 50 mV.s^{-1}.

The results of cyclic voltammetry of Pt nanoparticles on Pt electrode in the potential window -1500 mV to +200 mV at different scan rates in test solution 0.5 M H_2SO_4 are shown in (**Figure 4.9**). The cathodic peak current (I_{pc}) of Pt nanoparticles electrode is linearly dependent on the scan rate (υ) gave a regression equation $I_{pc\,(II')} = 0.27071\ x + 2.55155$ ($R^2 = 0.996$). This revealed that the electrode contained a thin electroactive surface bound catalyst film; the kinetic process that controls the peak is diffusion controlled reaction. This was confirmed by plotting log of cathodic current against the log of scan rate which gave a slope of 0.4865. Based on plotting peak potential against log scan rate the reduction of Pt nanoparticles behaved in an irreversible manner ($I_{pa}/I_{pc} \neq 1$ and $\Delta E_p > 59$ mV). The number of electrons transferred was estimated by integrating CV of the reduction peak to obtain the amount of charge (c) involved in the reaction and substituting appropriately in the Laviron's equation [48, 60, 146]. It showed that the nanoparticles electrochemistry is a one- electron process, this findings can be related to de Vooys et al [54].

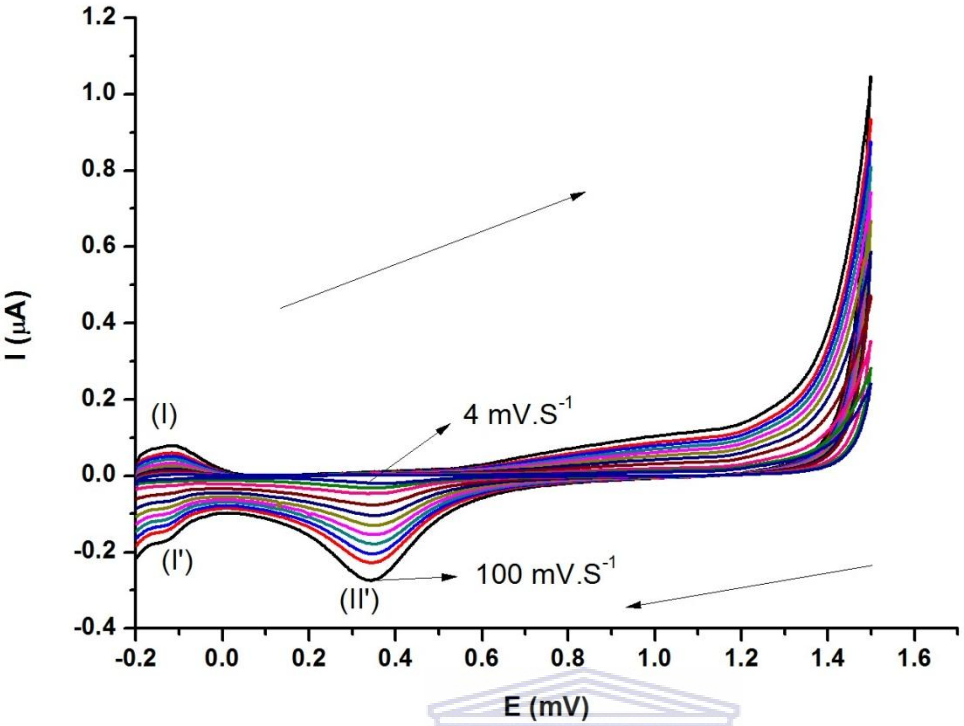

Figure 4. 9: Cyclic voltammogram in test solution 0.5 M H_2SO_4 of Pt nanoparticles modified on Pt electrode at different scan rates; 4, 6, 10, 20, 30, 40, 50, 60, 70, 80, and 100 mV.s^{-1} respectively.

Randles-Sevčik equation was used to study the kinetics of the electrode, in (**Figure 4.10**) indicated that the electrochemical reaction rate is fast and the reduction of PtO on Pt electrode is a typical diffusion-controlled process. A linear relationship between $E_{p,\ c}$ and log *v* was obtained, indicated the reduction of PtO was an irreversible electrode process.

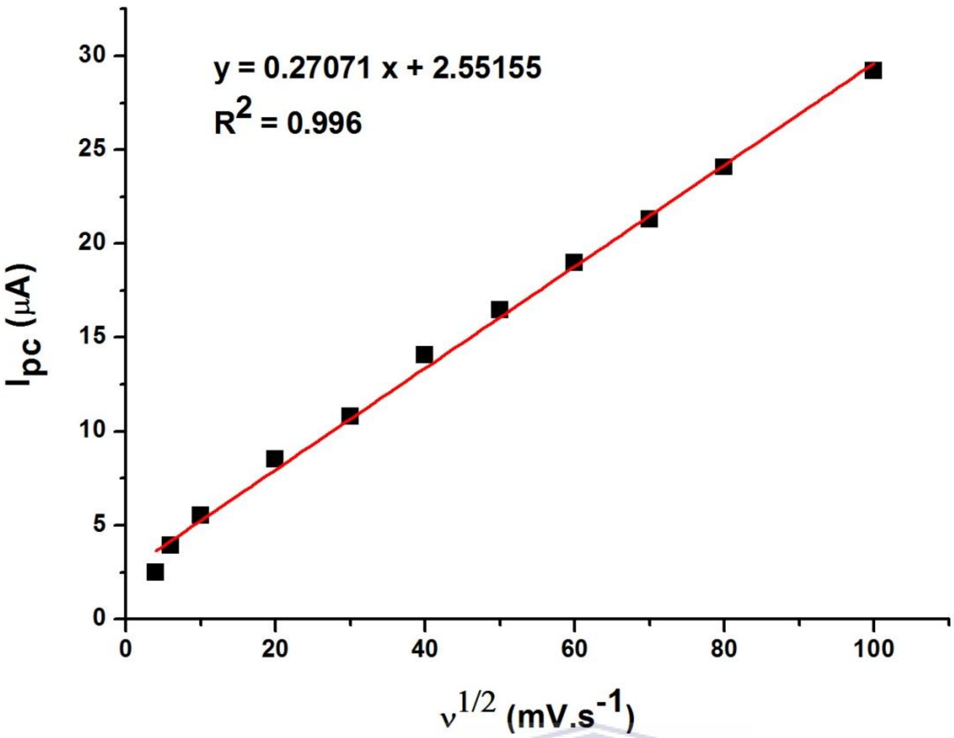

Figure 4. 10: Randles-Sevčik plot of PtNP/Pt. Conditions are as in Figure 4.9.

4.1.4.2 Electrochemistry of the Pt nanoparticles for oxidation of ammonia in 1 M KOH

Ammonia oxidation takes place effectively in alkaline medium. It is thus of interest to interrogate the behaviour of the nanoparticles in alkaline medium. The CV was recorded over a potential range of -1000 mV and +400 mV at a scan rate of 50 mV.s^{-1}. Three oxidation peaks were observed; peak (I), E_{pa} = -839 mV followed at more positive potentials by peaks (II), E_{pa} = -769 mV and (III), E_{pa} = -431 mV. On the cathodic scan, Three reduction peaks were also observed (III'), E_{pc} = -656 mV, followed by (II') E_{pc} = -801 mV and (I'), E_{pc} = -899 mV (**Figure 4.11**). The CV measurements using Pt drop coated Pt nanoparticles clearly show that various platinum redox processes can occur. These observed peaks are related to platinum oxidation states such as Pt (0) that undergoes several redox reactions such as Pt (0) nanoparticles deposit or Pt (0) oxidation to Pt (II) and Pt (IV) and platinum oxidation. The shape of the peaks (I)/ (I') and (II)/ (II') in the voltammograms are explained taking into consideration one of the most important properties of Pt which is the ability to adsorb, on its surface, and absorb, within its lattice, hydrogen. Peaks (II') and (I') are due to the reduction of hydrogen, which are adsorbed on the platinum surface ($H^+ + e^- \rightarrow H_{ad}$) and absorbed into the platinum lattice ($H^+ + e^- \rightarrow H_{ab}$) while peak (I) is attributed to oxidation of hydrogen atoms adsorbed on the surface of platinum ($H_{ad} \rightarrow H^+ + e^-$) and peak (II) to the oxidation of hydrogen absorbed into the platinum metal lattice ($H_{ab} \rightarrow H^+ + e^-$) as shown in (**Scheme 4.1**) below this findings can be related to the following literature [17, 26, 40, 50].

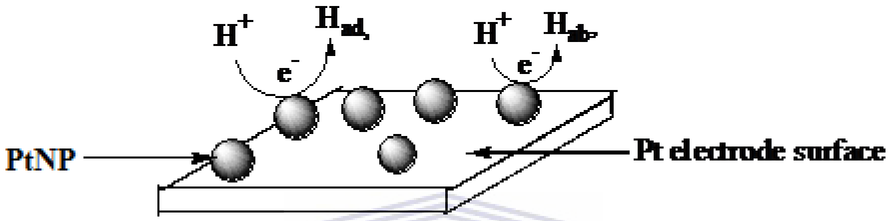

Scheme 4. 1: Schematic representation of the surface of Pt electrode with Pt nanoparticles.

The proton reduction takes place on the surface of the Pt nanoparticles. Similar oxidation peak were also observed in (**Figure 4.12**), the square wave voltammetry was also recorded over a potential window of -1000 mV to +400 mV.

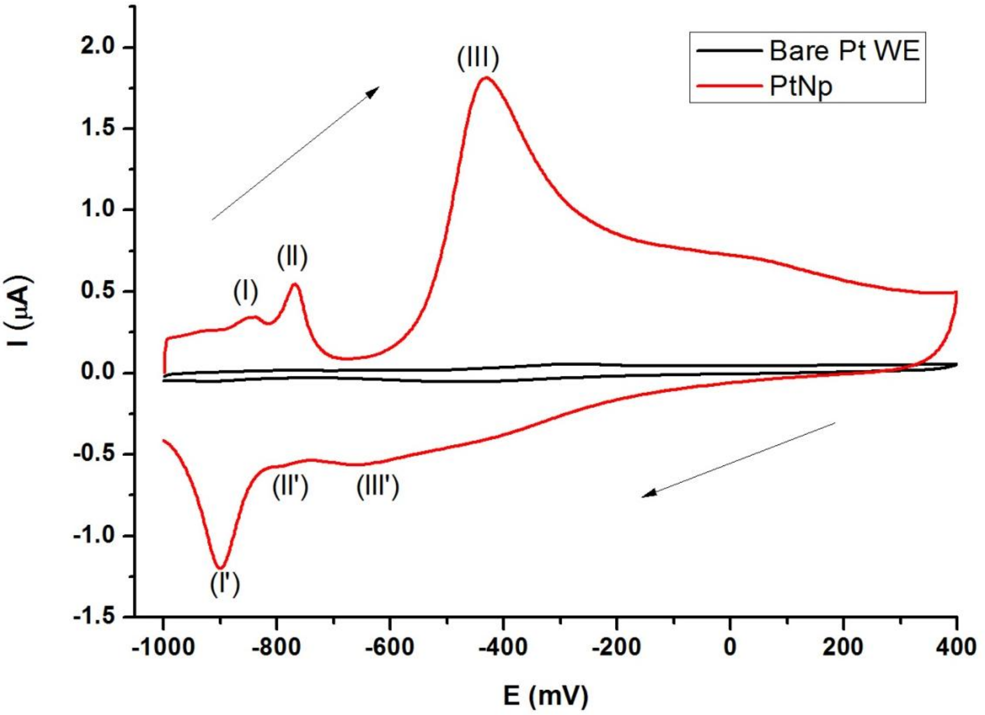

Figure 4. 11: Cyclic voltammogram of Pt/PtNP electrode in 0.5 M ammonia and 1 M KOH aqueous solution: Scan rate, 50 mV.s^{-1}.

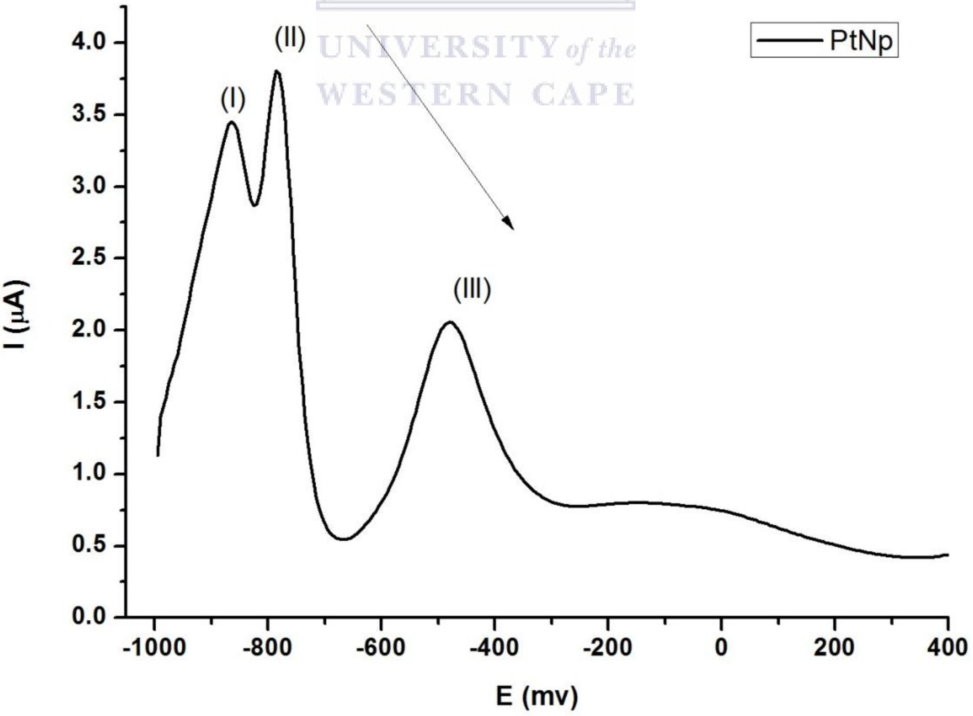

Figure 4. 12: Square wave voltammetry of Pt nanoparticles drop coated on Pt electrode in 0.5 M ammonia and 1 M KOH aqueous solution: Scan rate, 50 mV.s^{-1}.

It can be seen from (**Figure 4.13**) that the peak currents (I_p) of Pt nanoparticles film on Pt electrode increased linearly with scan rates (v) rates up to 100 $mV.s^{-1}$. The results show that the Pt nanoclusters film was stable and electrochemically active in 0.5 M ammonia and 1 M KOH solution. (**Figure 4.14**) shows a plot of anodic and cathodic peak currents versus scan rate for redox peaks (III)/ (III') that showed a close linear dependence with the scan rate a characteristic feature of surface confined species. Additionally, the voltammetric data were subjected to analysis by plotting log (I_p) versus log scan rate (v). The value of the slope of the linear plot of log I_p versus log v can be used to elucidate the nature of the processes influencing the electrochemistry of the surface confined species. Slopes with values of 1.0 and 0.5 refer to adsorption-controlled and diffusion-controlled electrochemical processes, respectively. Intermediate values for the slope indicate mixed diffusion/adsorption-controlled electrochemical processes. In this work, the plots of log I_p versus log v (not shown) gave slopes of 0.4 for both the anodic and cathodic peaks which showed the occurrence of diffusion controlled electrochemistry of the Pt system and that the Pt nanoparticles film was a monolayer. A lot of literature reported on electrocatalysis of Pt nanoparticles for ammonia oxidation and the results are more or less the same with the need to improve the efficiency of the catalyst as reported by Endo et al [62].

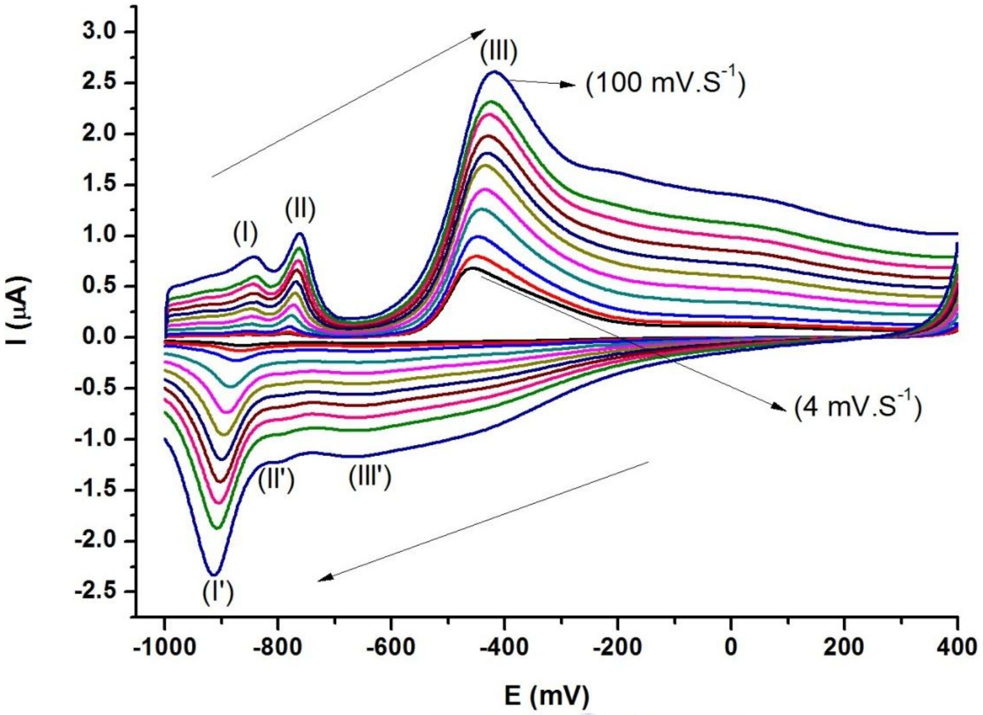

Figure 4. 13: Cyclic voltammogram in test solution 0.5 M ammonia and 1 M KOH of Pt nanoparticles modified on Pt electrode at different scan rates; 4, 6, 10, 20, 30, 40, 50, 60, 70, 80, and 100 mV.s^{-1} respectively.

The electrochemical kinetics was exacted from the different scan rates by using Randles-Sevčik equation below (4.7) explained extensively in chapter 3.

$$I_p = (2.99 \times 10^5) n (\alpha n_\alpha)^{1/2} A C_0 D^{1/2} \upsilon^{1/2} \qquad (4.7)$$

The Brown Anson model was used using the equation below (4.8).

$$I_p = \frac{n^2 F^2 \Gamma A \upsilon}{4RT} \qquad (4.8)$$

The kinetics of ammonia in KOH is shown in (**Table 4.3**) below;

Electrode	**n**	**α**	**Γ (mol.cm^{-2})**	**Kinetic process**	**Redox process**	**Diffusion coefficient (cm^{-2}.s^{-1})**
PtNP	1	0.5	1.09 x 10^{-11}	Diffusion	Irreversible	1.97 x 10^{-7}

Table 4. 3: Electrochemical parameters of nanoalloy systems.

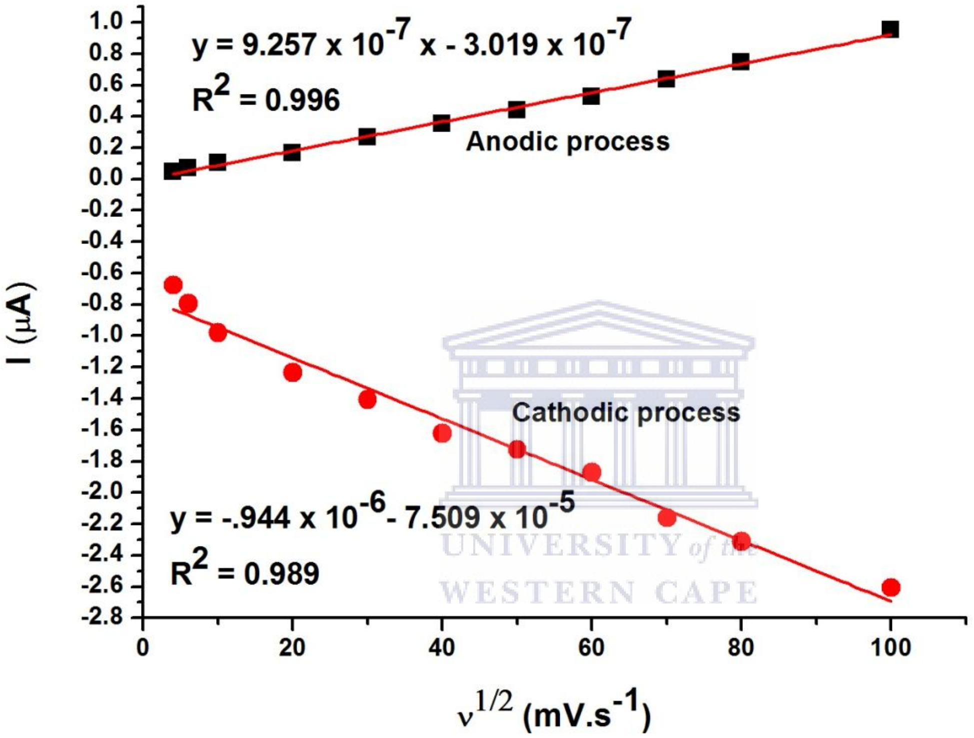

Figure 4. 14: Randles-Sevčik plot of PtNP/Pt. Conditions are as in Figure 4.13.

4.1.4.3 Electrochemistry impedance spectroscopy of the Pt nanoparticles for oxidation of ammonia in 1 M KOH

Electrochemical impedance is a powerful technique for investigating the kinetics of nanoparticles for electrooxidation in fuel cells. However, impedance spectroscopy also allows the detection of change in capacitance due to electrode modification. The Nyquist plot of impedance spectra in (**Figure 4.15**) for both PtNP and bare Pt working electrode includes a semicircle portion and a linear portion, with the former at higher frequencies corresponding to the electron transfer process and the latter at lower frequencies corresponding to the diffusion process. The charge transfer resistance (R_{ct}) at the electrode surface is equal to the semicircle diameter, which can be used to describe the interface properties of the electrode [4, 28, 158, 188].

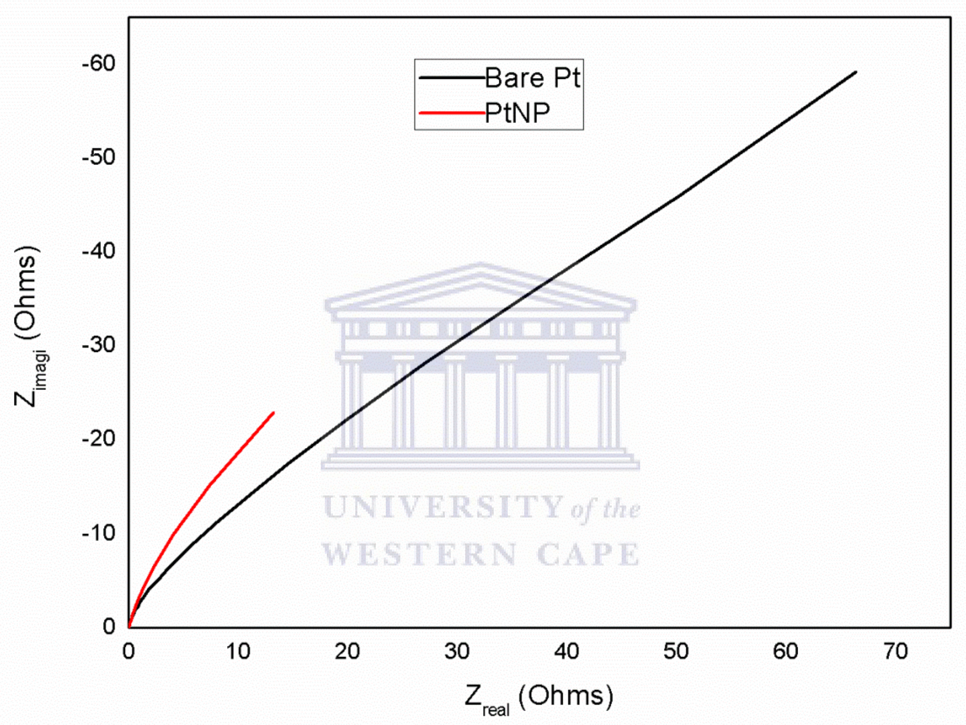

Figure 4. 15: Nyquist plot of the electrooxidation of 0.5 M ammonia on bare Pt electrode and Pt nanoparticles in 1 M KOH.

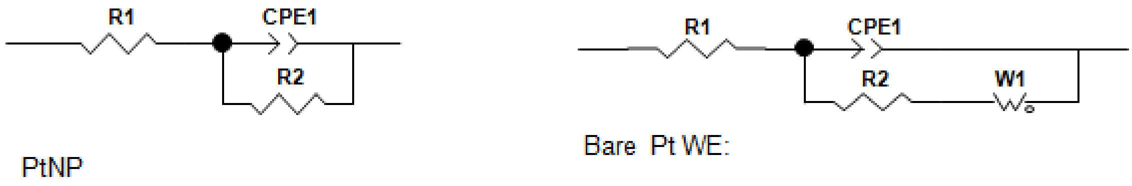

Figure 4. 16: Equivalent circuit for bare Pt electrode and Pt nanoparticles.

In (**Figure 4.15**) the charge transfer resistance (R_{ct}) of PtNP was the lowest (R_{ct} = 1.943 x 10^6 Ω) compared to that of bare Pt working electrode| (2.0604 x 10^6 Ω), indicating that the Pt nanoparticles have good conductivity and played an important role in accelerating the transfer of electrons. This can be attributed to the increased catalytic and improved conductivity properties portrayed by nanoalloys. The impedance parameters (**Table 4.4**) were obtained by fitting using an equivalent circuit (**Figure 4.16**) and the fitting errors were less than 4 %. Rs is the solution resistance, Rct is the charge transfer resistance, and CPE (constant phase element) is a distributive element that models the double layer capacitance owing to surface in homogeneity and Z_w (w) Warburg measures mass transport.

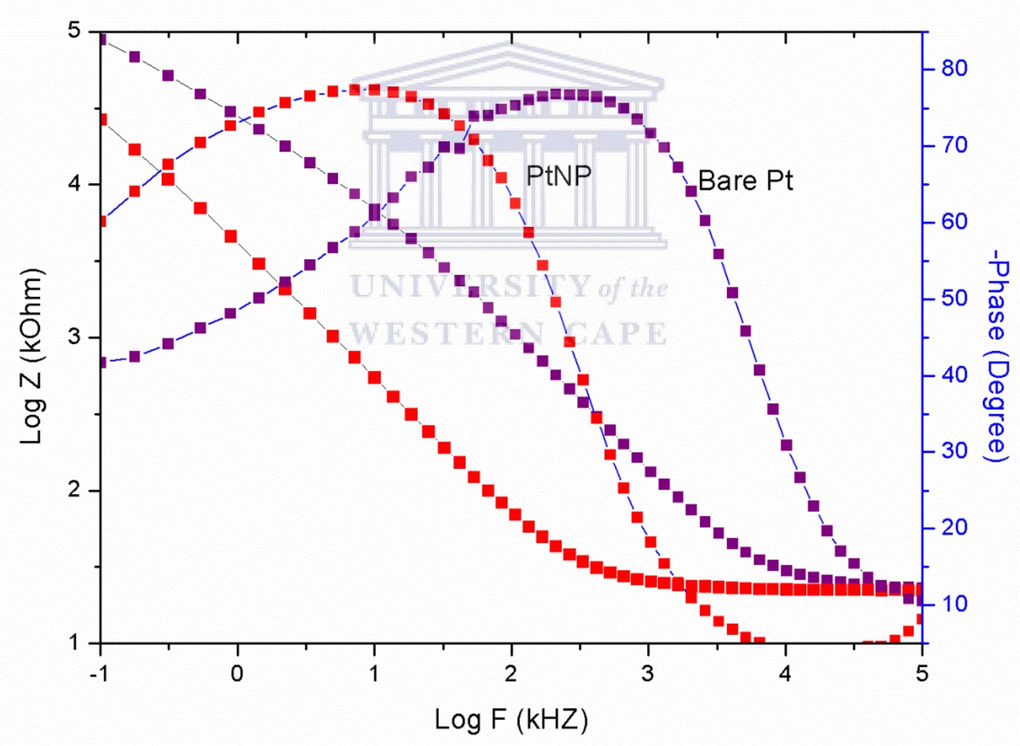

Figure 4. 17: Bode plot of 0.5 M ammonia on bare Pt electrode and Pt nanoparticles in 1 M KOH.

In (**Figure 4.17**) shows plots of phase angle changes with frequency for the bare Pt and Pt nanoparticles. Bode plots showed remarkable differences in the electronics of bare Pt and Pt nanoparticles interfaces. The frequency of maximum phase angle increased from bare Pt to Pt nanoparticles with the phase angle decreasing from semi-metallic value for bare Pt (77˚) to semiconductor value for Pt nanoparticles (76˚).

Electrode	ω_{max} (HZ)	R_{ct} (Ω)	C_{dl} (μF)	Γ (s.rad^{-1})	I_0 (A)
PtNP	2635.73	1.943 x 10^{6}	1.9527 x 10^{-10}	3.7941 x10^{-4}	1.3 x 10^{-8}
Bare Pt	2635.73	2.0605 x 10^{6}	1.8413 x 10^{-10}	3.7939 x 10^{-4}	1.2 x 10^{-8}

Table 4. 4: EIS parameters of bare Pt working electrode and Pt nanoparticles in 1 M KOH (data obtained from the circuit fitting of Figure 4.16).

4.1.5 Sub conclusion

Platinum nanoparticles where characterized by XRD, it was found that the crystalline planes of the face centre cubic Pt are composed of pure crystalline Pt nanoparticles. The mean particle size of the electrocatalyst was calculated which was 0.018 nm with a lattice parameter of 2.085 nm. Structural characterization was further confirmed with FTIR and UV-vis, where characteristic peaks of PVP capped Pt nanoparticles were between 1182 and 1645 cm^{-1}, between 1428 and 2876 cm^{-1} for C-H bands for presence of nitrogen atom of PVP chemisorbing on Pt^{2+} ion. The UV-vis spectroscopy for Pt nanoparticles showed no peak which was an indication that the nanoparticles where completely reduced. HRTEM and HRSEM where used for morphological analysis, both techniques were able to prove that the nanoparticles where poly-orientated as confirmed by XRD. The average particle size was between 2.1 nm and 5 nm, meaning the nanoparticles were agglomerated to some extent. The voltammogram shows voltammetric profiles very similar to those obtained for the corresponding metals in bulk state. No evidence was found in relation to the presence of preferential surface orientation and therefore, the surface of the nanoparticles can be considered as polyoriented or polycrystalline. This relates very clearly with the information obtained in XRD, HRTEM and HRSEM. The oxidation peak for ammonia oxidation was at a -431 mV, the reaction was diffusion controlled with diffusion coefficient of 1.97 x 10^{-7} $cm^{-2}.s^{-1}$. Electrochemical impedance spectroscopy was done and obtained the charge transfer resistance for platinum nanoparticles was lower than the charge transfer resistance of bare platinum electrode. The EIS revealed that platinum had good conductivity with increased catalytic properties.

CHAPTER 5

Summary

This is the second part of three chapters outlining and discussing the results obtained from this study. This chapter deals specifically with the characterisation of binary nanoparticles such as PtIr, PtRu and PtTe for its subsequent applications in the oxidation of ammonia. The chapter clearly illustrates how the nanoparticles were successfully characterized by spectroscopic methods such as FTIR, UV-vis, HRTEM, and HRSEM for morphological analysis and XRD for structural analysis. The electrochemical properties of these nanoparticles were interrogated using techniques such as CV, SWV and EIS. The potential application of the nanoparticles as electrocatalysts for ammonia electro-oxidation for fuel cell application was further investigated.

5.0 Results and Discussion (Part 2)

5.1 Bi-Metallic Catalyst

Pt-based bimetallic materials PtMe (Me = Ir, Ru, Ni, Pd, Rh, Cu, Ag and Au) are the most commonly used catalysts in ammonia oxidation reaction [62]. The increased activity over these multicomponent catalysts compared to their monometallic Pt counterpart has predominantly been attributed to bifunctional effect and ligand or electronic effect [46, 193]. The reason why Ir and Ru enhance the activity might be explained by their activity at the dehydrogenisation steps of NH_3 at a lower potential, at which ammonia oxidation can never start on the surface of pure Pt [62]. These studies are all supportive of a mechanism for the dinitrogen formation originally suggested by Gerischer and Mauerer [72]:

$\mathrm{NH_3\ (aq)} \rightarrow \mathrm{NH_{3,ads}}$ ……………………………………..(1)

$\mathrm{NH_{3,ads}} \leftrightarrow \mathrm{NH_{2,ads}} + \mathrm{H^+} + \mathrm{e^-}$ …………………………….(2)

$\mathrm{NH_{2,ads}} \rightarrow \mathrm{NH_{ads}} + \mathrm{H^+} + \mathrm{e^-}\ \mathrm{(rds)}$ ………………(3)

$\mathrm{NH_{x,ads}} + \mathrm{NH_{y,ads}} \rightarrow (\mathrm{x}+\mathrm{y})\,\mathrm{H^+} + (\mathrm{x}+\mathrm{y})\,\mathrm{e^-}$ ….(4)

$\mathrm{NH_{ads}} \rightarrow \mathrm{N_{ads}} + \mathrm{H^+} + \mathrm{e^-}$ ………………………………(5)

5.1.1 Structural Characterization by XRD, IR spectroscopy and UV-vis.

XRD measurements were used to identify the prepared pure Pt and bimetallic nanoparticles. It can be seen from (**Figure 5.1**) that all the peaks in the XRD pattern of pure Pt were well indexed to Pt (discussed in Chapter 4) with high crystallization. As the bimetallic nanoparticles are formed, all the peaks in the XRD patterns of PtIr, PtRu and PtTe are shifted slightly to larger 2θ values (right shift) with respect to the pure Pt, indicating the decreased d spacing and contraction of the lattice constant, due to the incorporation of increasing amounts of the smaller metal atoms into the Pt fcc lattice. No Pt or other metal peaks appear, indicating that bimetallic nanostructures or alloys were formed. The absence of Ru peaks can be attributed to the coincidence that the signal peaks of both Pt and Ru elements appear at almost the same positions. The Pt element being a much larger size atom it therefore exhibits a more pronounced signal pattern than that of the small size Ru atom counterpart. It can also be as a result of the incorporation of the relative small size of the Ru atom into the fcc structure of Pt indicating an alloy formation between Pt and Ru. Diffraction peaks corresponding to RuO_2 (101), (200) and (211) were observed as shown by the arrows in (**Figure 5.1**). This is due to the formation of different crystalline structure which also promotes the formation of ruthenium oxides and improves alloying. However, it should be emphasized that the intensity of RuO_2 is considerably very weak, in itself an indication that RuO_2 is present only in small quantities. The peak at 2θ 39.7°, 46.2°, 67.4°, 81.2° and 85.7° can be assigned to the (111), (200), (220),(311) and (222) crystalline planes of face centred cubic (fcc) PtIr, PtRu and PtTe respectively, which indicates that the nanoparticles are composed of pure crystalline Pt. The XRD was commonly employed to calculate the mean particle size of the electrocatalyst nanoparticles material using Scherrer’s equation explained in chapter 3, and using the platinum diffraction peak (111). The strongest and sharpest diffraction peak for PtIr, PtRu and PtTe at around $2\theta = 39.8°$, 40° and 39.6° respectively is indexed as (111).

$$D = \frac{0.9\,\lambda}{\beta(2\theta)\cos\theta} \qquad (5.1)$$

The catalyst showed relatively small particle size which is known to enhance the electrochemical surface area of the catalyst. Lattice parameter was calculated using the following equation:

$$a_{fcc} = \frac{\sqrt{2}\lambda}{\sin\theta} \qquad (5.2)$$

The calculated values of the average particle size and lattice parameter are presented in (**Table 5.1**) below. The is a slight decrease of lattice parameter between PtTe, PtIr and PtRu nanoparticles which proves that essentially intermixing was complete to form binary nanoparticles [58, 108, 127, 182].

Catalyst	**Particle size (nm)**	**Lattice parameter (a_{fcc}) (nm)**
PtNP	0.018	2.085
PtIrNP	1.297	5.157
PtRuNP	2.084	5.132
PtTeNP	2.198	5.182

Table 5. 1: Summary of average particle size and lattice parameter of PtIrNP, PtRuNP and PtTeNP electrocatalysts obtained from XRD measurements.

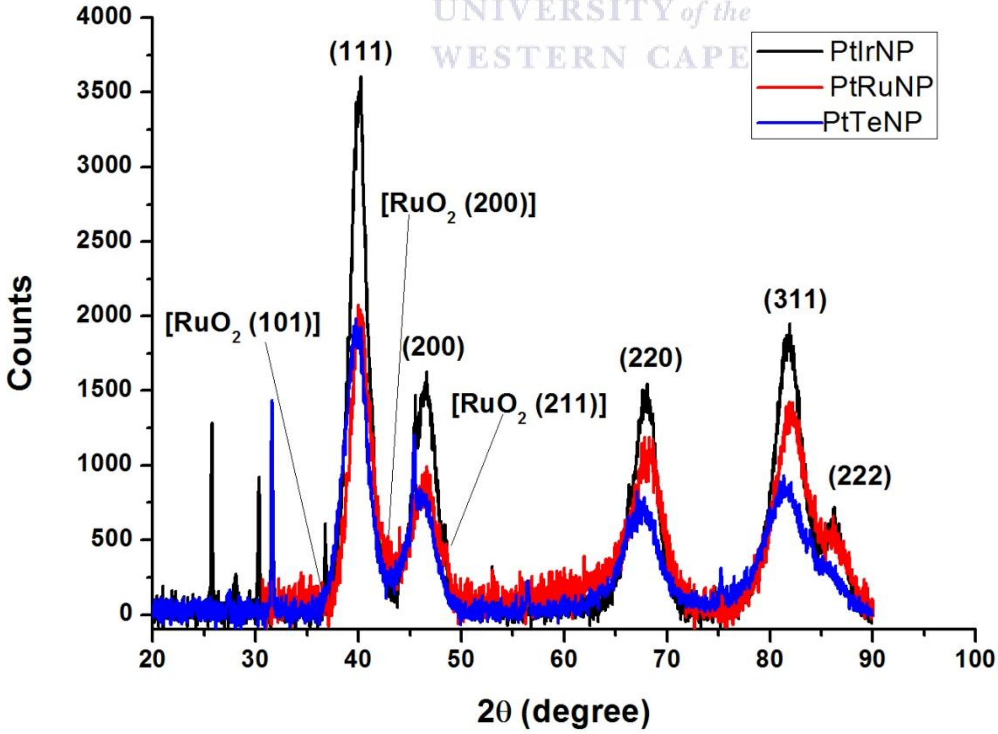

Figure 5. 1: XRD pattern of PtIr, PtRu and PtTe nanoparticles electrocatalysts.

FTIR spectrum in (**Figure 5.2**) shows the IR spectra in the 400–4500 cm^{-1} range of PVP capped PtIr, PtRu and PtTe nanoparticles; the broad absorption band centered at 3218 cm^{-1} and 3409 cm^{-1} (PtIrNP), 3215 cm^{-1} and 3381 cm^{-1} (PtRuNP) and 3437 cm^{-1} (PtTe) is attributed to O-H stretching mode of H_2O absorbed on the surface of the product. The most striking evidence from FTIR spectrum of the PVP stabilized Pt is the broad peak between 1201 cm^{-1} and 1651 cm^{-1} which corresponds to C-N stretching motion and C=O stretching motion of monomer for PVP, respectively [42, 68, 99]. The narrow absorption peak centered at 1421 cm^{-1} and 2890 cm^{-1} occurred in (**Figure 5.2)** is ascribed to the C–H bonding due to the presence of PVP. This may be due to the formation of coordinate bond between the nitrogen atom of the PVP and the Pt^{2+}, Ir^{3+}, Ru^{3+} and Te^{2+} [18].

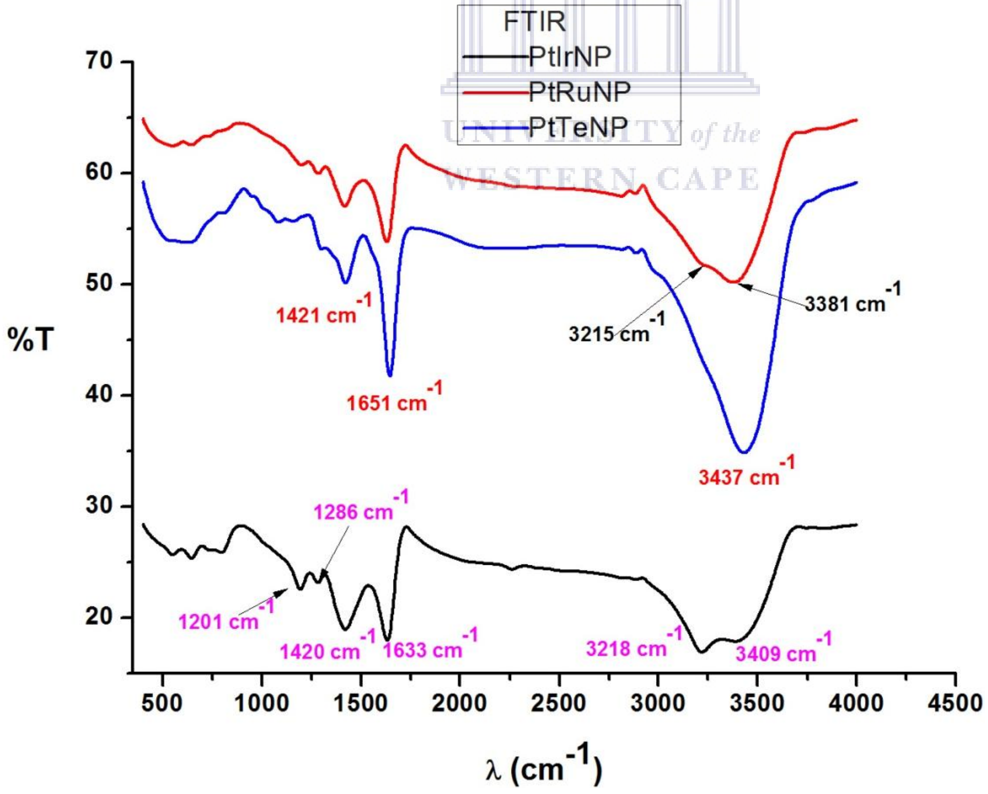

Figure 5. 2: FTIR of PtIrNP, PtRuNP and PtTeNP capped with PVP.

The formation of the nanoparticles by reduction of Pt^{2+}, Ir^{3+}, Ru^{3+} and Te^{+} ions was confirmed by the use of UV-visible spectroscopy. (**Figure 5.3)** shows the UV-visible spectra of IrCl$_2$, RuCl$_3$ and NaHTe solutions while (**Figure 5.4)** shows the UV-visible spectra of PtIr, PtRu, and PtTe nanoparticles. The absorption peaks observed at 307 nm for Ru^{3+}, 316 nm for Te^{+} ions and Ir^{3+} ions there was no peak observed. The peaks disappeared after reduction of the salts indicating that the metal ions were completely reduced. The synthesised nanoparticles showed no absorption peaks indicating a complete reduction of the metal ions to zero-valent nanoparticles, exhibiting an exponential graph shape. The colour of the solution turned from pale yellow to black also indicating complete reduction of metal ions[166].

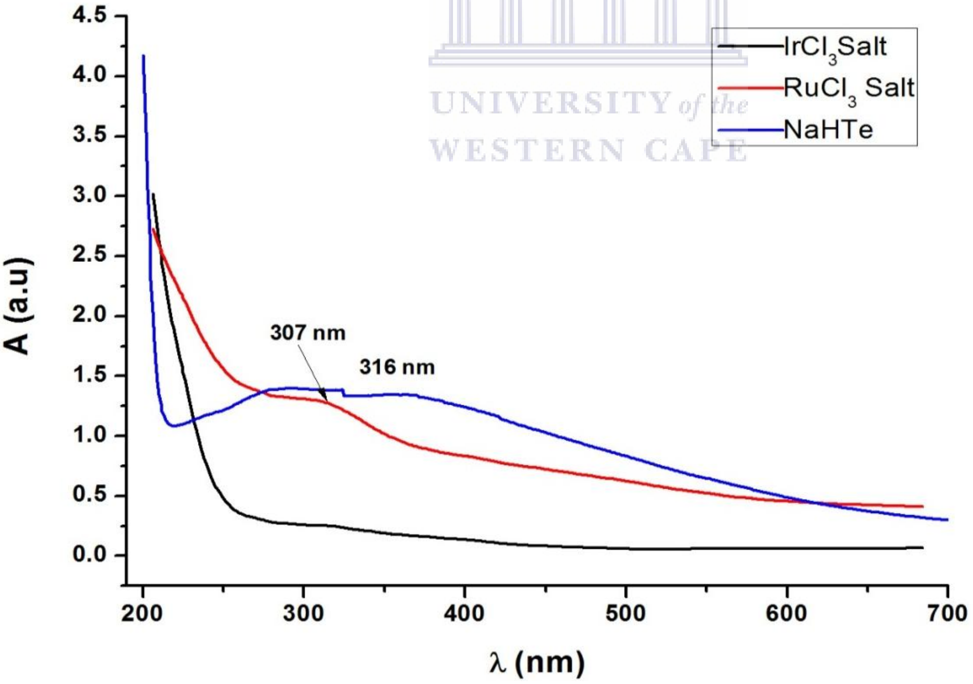

Figure 5. 3: UV-vis spectra of iridium (lll) chloride, ruthenium (lll) chloride and sodium hydrogen telluride solutions.

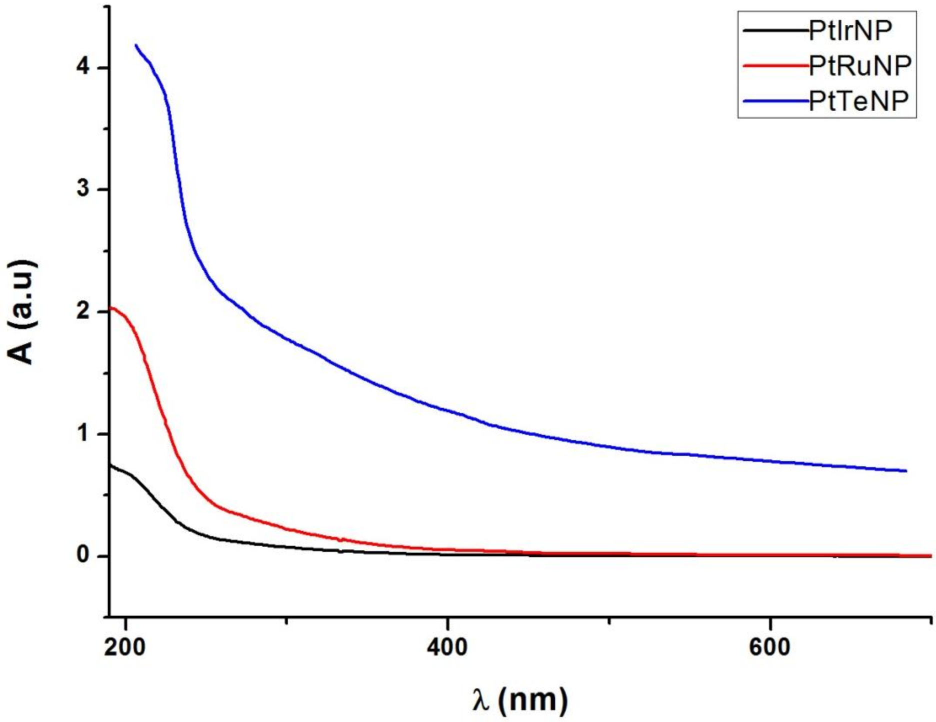

Figure 5. 4: UV-vis spectra of PtIrNP, PtRuNP and PtTe nanoparticles.

5.1.2 Morphological Characterization by HRTEM and HRSEM

5.1.2.1 HRTEM and EDX for morphological characterization of PtIrNP, PtRuNP and PtTeNP.

The size, shape and crystallinity of the nanoparticles were investigated by high resolution transmission electron microscope (HRTEM). (**Figure 5.5 [(a) and (b)]**) shows typical HRTEM images of the prepared PtIr nanoparticles, PtIr It was observed that the spherical, cubic poly-orientated metal nanoparticles are uniformly dispersed on the Cu grid with few agglomerates on some parts of the sample which is very different from what was reported by Boggs et al [26]. (**Figure 5.5 [(c) and (d)**]) shows typical HRTEM images of the prepared PtRu nanoparticles and it was observed that the spherical nanoparticles were uniformly dispersed on Ni grid without any agglomeration of the sample, Baranova et al [18] reported similar results. Finally PtTe nanoparticles (**Figure 5.5 [(e) and (f)]**) show images of PtTe nanoparticles that were agglomerated on the Ni grid with some poly-orientated nanoparticles dispersed on the grid [18]. The uniformity of the catalyst particle distribution is known to be important factor for electro-catalytic activity. The nanoparticles produced were found to be well dispersed; HRTEM images of a single particle (not shown) revealed atomic lattice fringes demonstrating the crystalline nature of the nanoparticles. Since the particle size and particle morphology greatly influences the electro-chemical activity of the catalyst owing to the relationship between catalytic activity and surface structure, HRTEM analysis of PtIr, PtRu and PtTe nanoparticles electro-catalyst was therefore carried out before the comparison of its catalytic activity. It can be clearly observed that nanoparticles are poly-orientated which is in agreement with the results obtained in the XRD that PtIr, PtRu and PtTe nanoparticles showed different diffraction patterns. The crystallite size L_v was determined using the simple Scherrer equation:

$$L_v = \varphi \frac{\lambda}{\mathrm{FWHM}\ \cos\emptyset} \quad (5.3)$$

Where L_v is the Scherrer length, φ is the shape factor (0.89 for spherical crystallite), λ the radiation wavelength (1.5406 Å), FWHM the full width at half-maximum, and θ the angle at the maximum intensity. Apparently Lv is extracted from the diffraction peak located close to $2\theta = 40°$, which corresponds to the (111) crystallographic plane of platinum. The average particle size for PtIr nanoparticles is 3.2 nm – 5 nm shows that the platinum nanoparticles clusters agglomerate to some extent, PtRu nanoparticles is 0.5 nm – 2 nm which shows that the PtRu nanoparticles are not agglomerated and PtTe nanoparticles is 2.3 nm – 5 nm which shows that the nanoparticles are agglomerated to some extent[150, 175, 180].

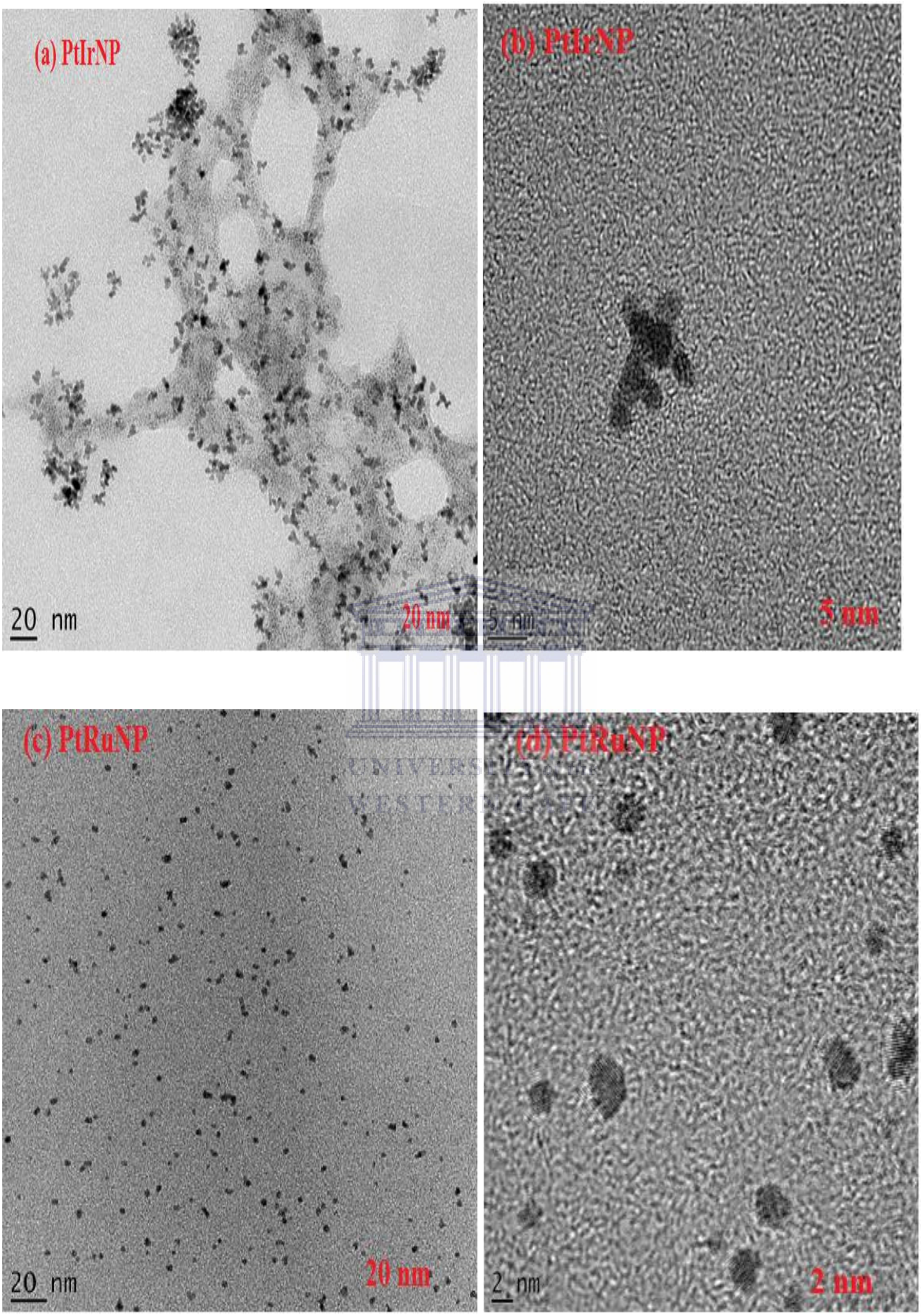
(a) PtIrNP
20 nm
20 nm
(b) PtIrNP
5 nm
5 nm
(c) PtRuNP
20 nm
20 nm
(d) PtRuNP
2 nm
2 nm

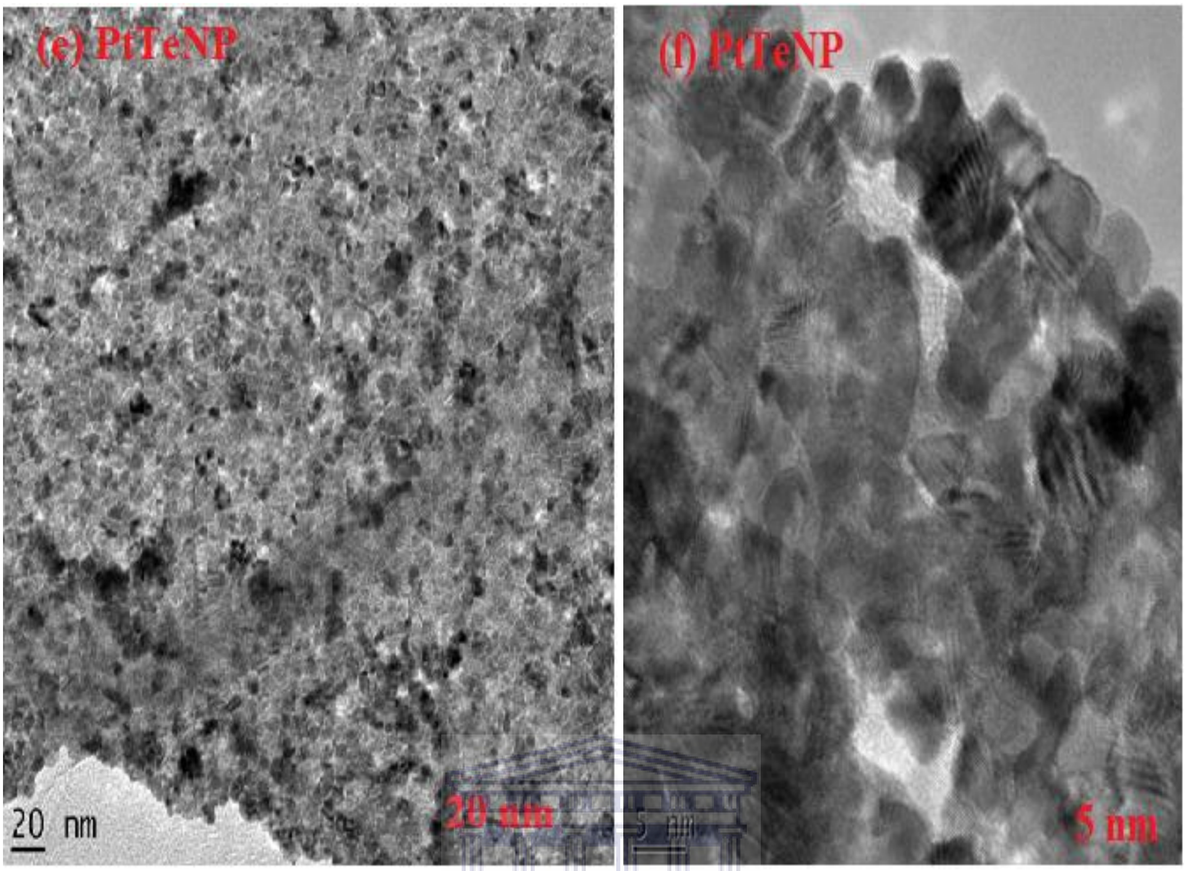

Figure 5. 5: HRTEM images of Pt nanoparticles (a) and (b) PtIrNP, (c) and (d) PtRuNP and (e) and (f) PtTeNP.

Selected area electron diffraction pattern (SAED) shown in **Figure 5.6** for PtIr, PtRu and PtTe nanoparticles shows characteristic electron diffraction rings of PtIr, PtRu and PtTe, further indicating that the catalyst structure is made of nanoparticles. They exhibit a high crystallinity as can be deduced from the SAED pattern [**Figure 5.6** (a), (b) and (c)] which shows diffraction rings that are consistent with the presence PtIrNP, PtRuNP and PtTeNP. The high crystallinity of the synthesised PtRu nanostructures is also evidenced which reveals well-defined (0 0 2) lattice fringes.

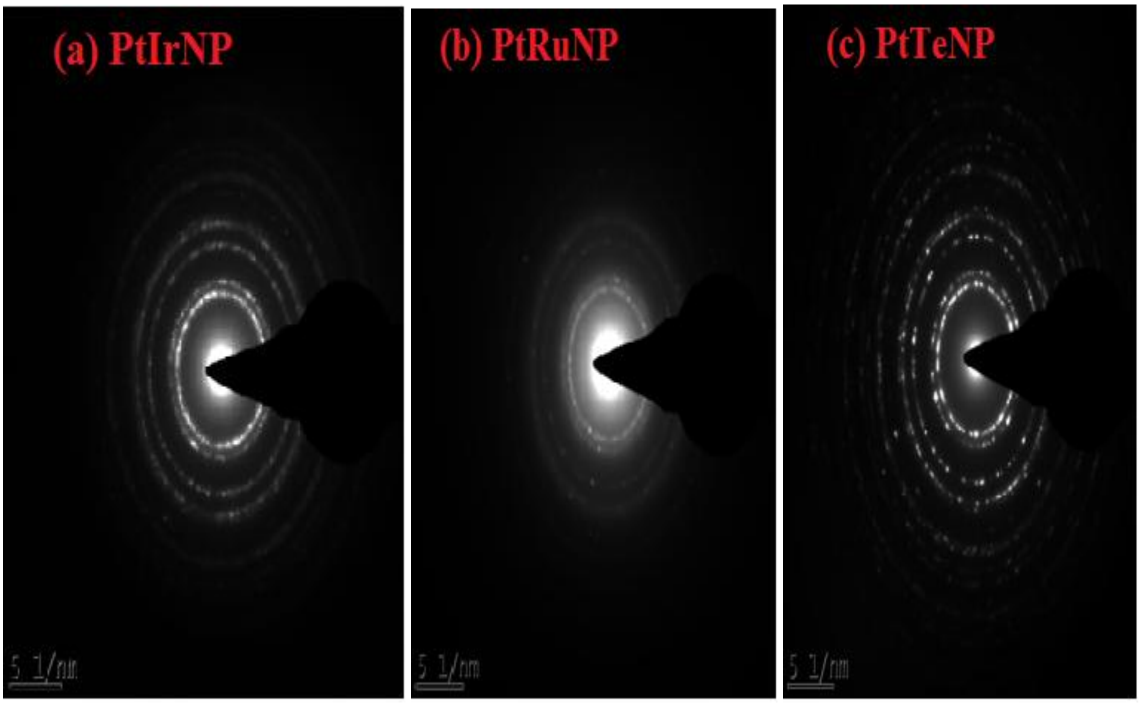

Figure 5. 6: Selected area electron diffraction pattern (SAED) of PtIrNP, PtRuNP and PtTeNP.

To investigate the elemental composition of the prepared nanoparticles PtIr, PtRu and PtTe nanoparticles were characterised using EDX. The EDX analysis (**Figure 5.7** (a), (b), and (c)) of the synthesised PtIr, PtRu and PtTe nanoparticles revealed the elemental composition of the nanoparticles and showed that all the three elements; Pt, Ir, Ru and Te were present in the nanoalloy systems. However, other elemental signals were also recorded namely; carbon, oxygen, copper and nickel. The presence of carbon may have originated from contamination during sample preparation, the oxygen was due to the presence of PVP in the nanoparticles while copper and nickel is as a result of the copper grid and nickel grid onto which the nanoparticles were immobilised for the HRTEM analysis [175].

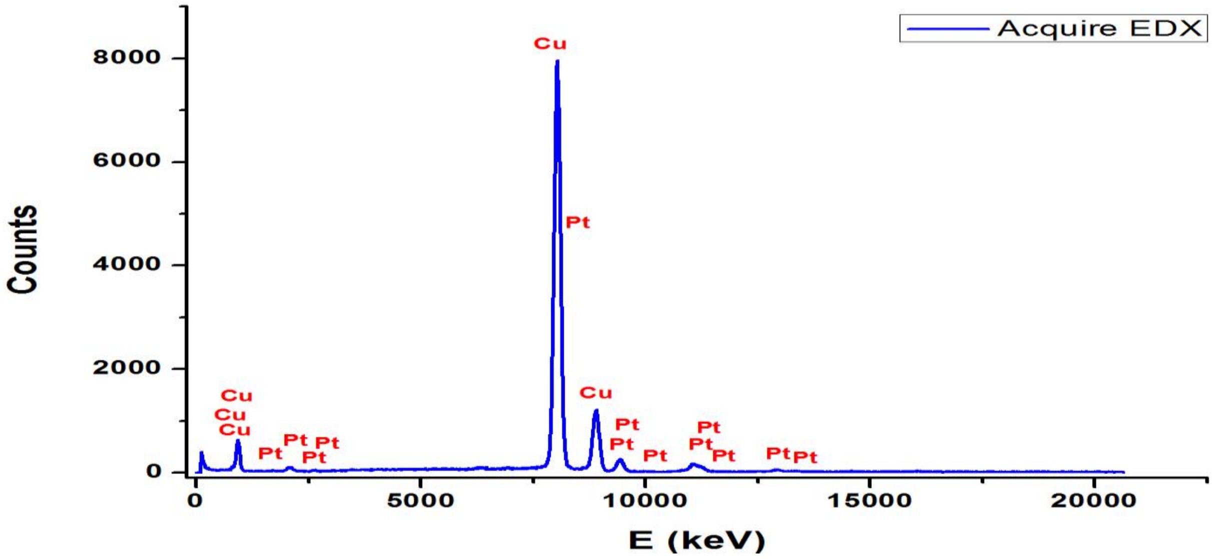

Figure 5. 7 (a): Energy dispersive X-ray spectrum of PtIr nanoparticles.

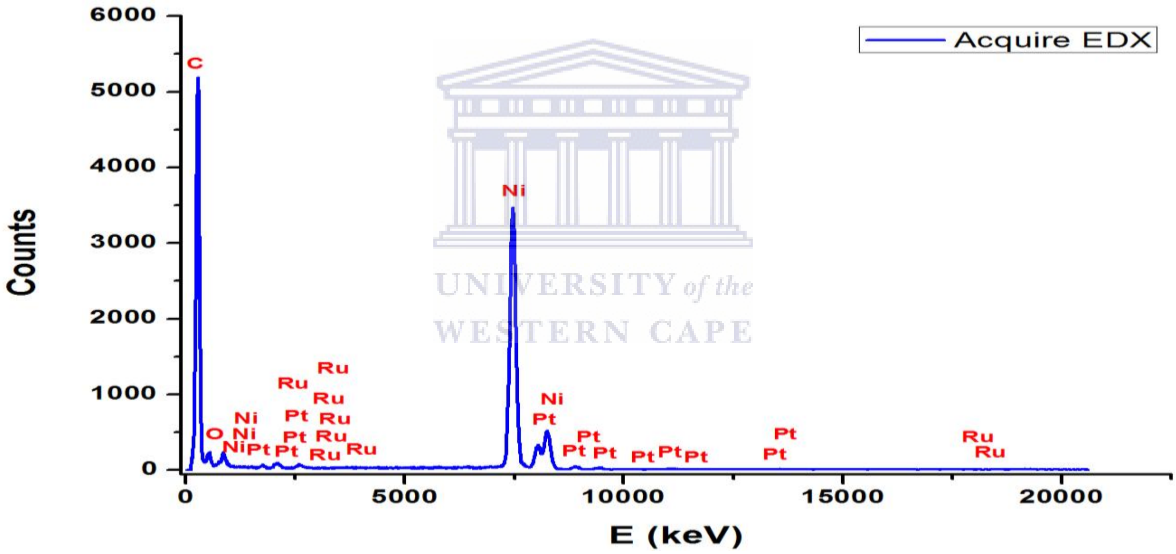

Figure 5.7 (b): Energy dispersive X-ray spectrum of PtRu nanoparticles.

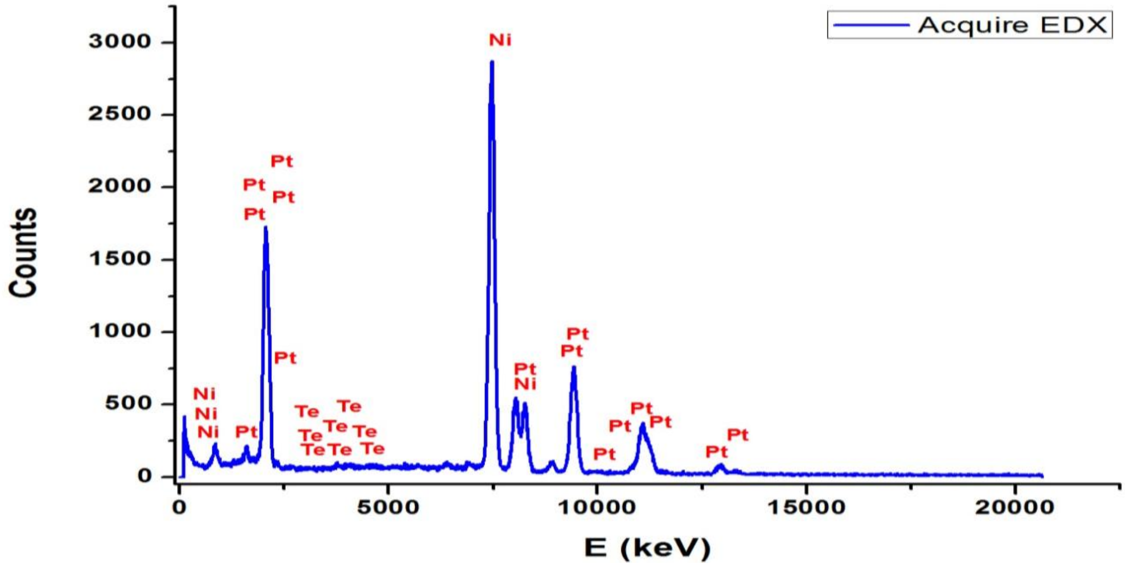

Figure 5.7 (c): Energy dispersive X-ray spectrum of PtIr nanoparticles.

5.1.2.2 HRSEM and EDS for morphological characterization of PtIrNP, PtRuNP and PtTeNP.

The HRSEM image of the PtIrNP, PtRuNP and PtTeNP shown in (**Figure 5.8 [(a) to (f)]**) reveals that the nanoparticles were homogeneously dispersed as small, spherical and uniform bright spots on the carbon support. In order to verify the particle size of the deposited nanoparticles, HRSEM analyses was carried out for all the nanoparticles, which were prepared by PtIr, PtRu and PtTe nanoparticles deposited on to carbon supports, as shown in Figure 5.8 [(a) and (b) PtIr], [(c) and (d) PtRu] and [(e) and (f) PtTe] nanoparticles. In general, the particles exhibit uniform size and cubic, spherical shape in general poly-orientated as observed using XRD and HRTEM. The PtIr, PtRu and PtTe nanoparticles showed that the Pt was incorporated with Ir, Ru and Te because the shape of the nanoparticles changed in support of the information obtained for HRTEM that the nanoparticles were poly-orientated. They appear to be homogeneously distributed over the entire support surface. In the case shown the particles are approximately 46 nm in diameter for all different types of carbon electrode. The binary platinum particle size, as seen in HRSEM images, is rather bigger than that which was calculated via XRD and HRTEM. This may be due to either the impossibility of observing small particles by HRSEM or because the observed particles are, in fact, aggregations of smaller particles. In order to overcome these short comings, HRTEM observations were made with the PtIr nanoparticles on Cu grid and PtRu and PtTe on Ni grid as a means of characterisation. In an fcc unit cell the atoms touch along the face diagonals and the lattice parameter may be calculated from the following equation;

$$4\mathrm{r} = \mathrm{a}(2)^{1/2} \qquad (5.4)$$

Where r is the radius of PtIrNP = 0.03186 nm, PtRuNP = 0.031506 nm and PtTeNP = 0.021771 nm

For the hcp close packing arrangement, the lattice parameters a (=*b*) and c may be calculated from the radius as follows using equations 5.5 and 5.6:

$$\mathrm{a} = 2\mathrm{r} \qquad (5.5)$$

and

$$2a = \left[\left({}^{a}/_{\sqrt{3}}\right)^2 + \left({}^{c}/_{2}\right)^2\right]^{1/2} \qquad (5.6)$$

The lattice parameter a = 9 x 10^{-2} nm for PtIr favour FCC closed packing nanoparticles, a = 6 x 10^{-2} nm for PtRu nanoparticles favour hexagonal closed packing and a = 4 x 10^{-2} nm for PtTe favour trigonal planar packing nanoparticles with small particle size and irregular shape and size distribution. The c = 1.7 x 10^{-1} nm for PtRu and c = 1.1 x 10^{-1} nm for PtTe nanoparticles.

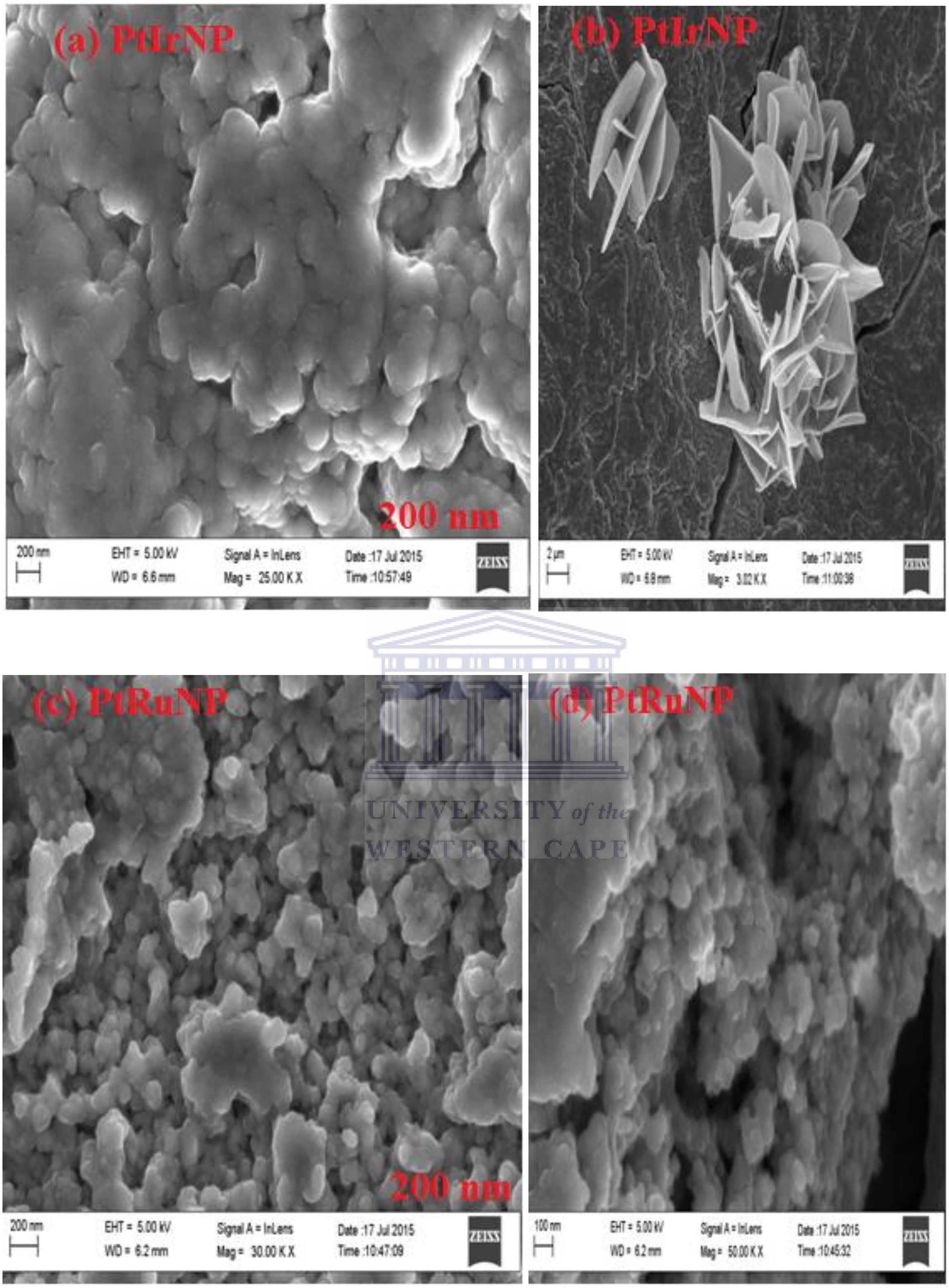
(a) PtIrNP
200 nm
200 nm
EHT = 5.00 kV
WD = 6.6 mm
Signal A = InLens
Mag = 25.00 K X
Date :17 Jul 2015
Time :10:57:49
ZEISS
(b) PtIrNP
2 µm
EHT = 5.00 kV
WD = 6.8 mm
Signal A = InLens
Mag = 3.02 K X
Date :17 Jul 2015
Time :11:00:38
ZEISS
(c) PtRuNP
200 nm
200 nm
EHT = 5.00 kV
WD = 6.2 mm
Signal A = InLens
Mag = 30.00 K X
Date :17 Jul 2015
Time :10:47:09
ZEISS
(d) PtRuNP
100 nm
EHT = 5.00 kV
WD = 6.2 mm
Signal A = InLens
Mag = 50.00 K X
Date :17 Jul 2015
Time :10:45:32
ZEISS

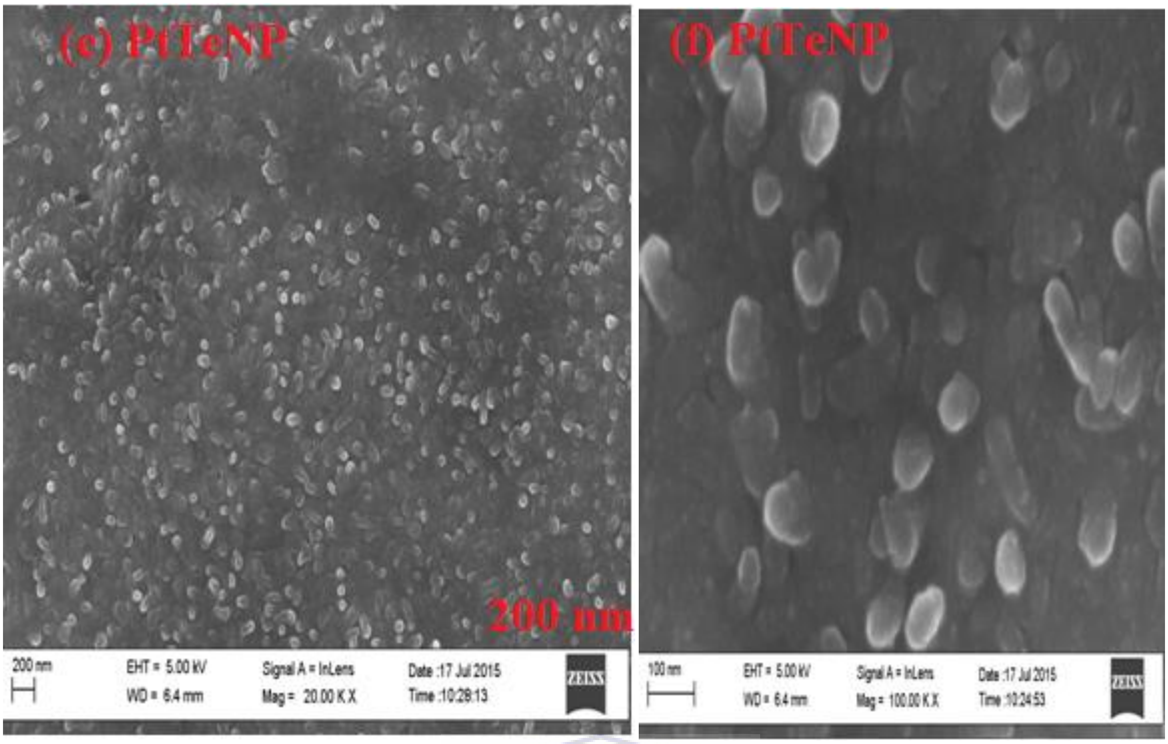

Figure 5. 8: HRSEM images of Pt nanoparticles (a) and (b) PtIrNP, (c) and (d) PtRuNP and (e) and (f) PtTeNP.

Energy dispersive spectroscopy (EDS) detector which is connected to the HRSEM was used in this study to investigate the elemental composition of the electrocatalyst synthesized shown in **Figure 5.9** (a), (b) and (c) below. It can be observed there is sodium, chloride which could be contaminates obtained during sample preparation and carbon is from the carbon paste used to prepare the sample and oxygen is from PVP. After taking HRSEM images, the samples was then scanned on six different areas to obtain the average wt. % of the metals which can be observed in Table 5.2 giving the elemental analysis of PtIr, PtRu and PtTe nanoparticles.

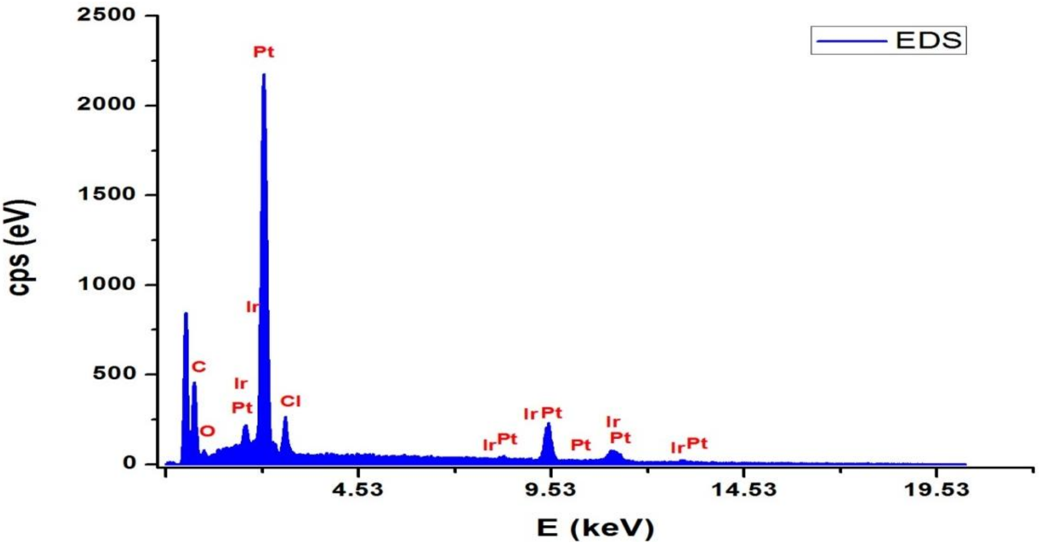

Figure 5. 9 (a): Energy dispersive spectroscopy (EDS) of PtIr nanoparticles.

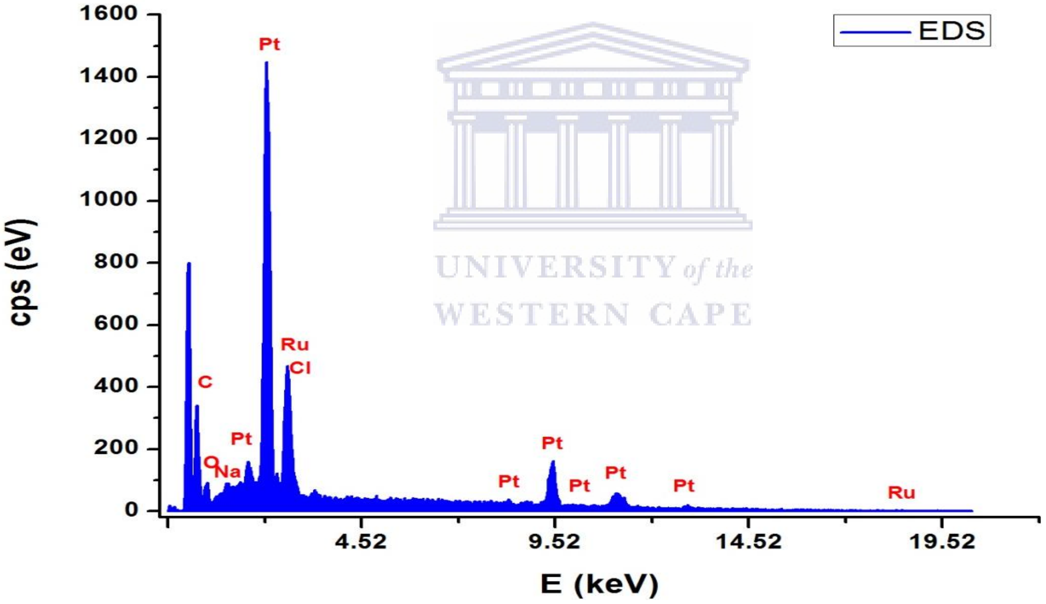

Figure 5.9 (b): Energy dispersive spectroscopy (EDS) of PtRu nanoparticles.

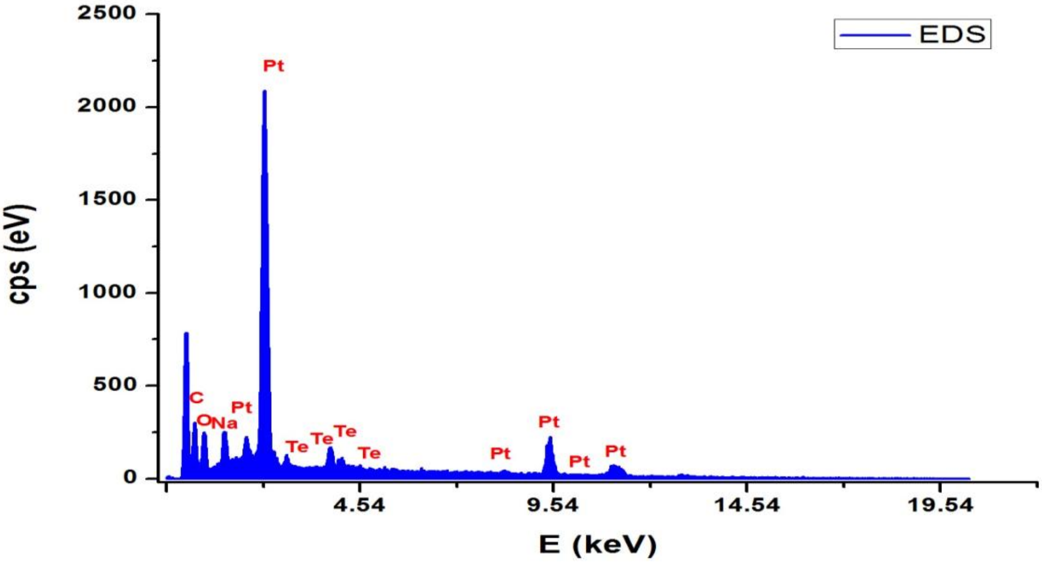

Figure 5.9 (c): Energy dispersive spectroscopy (EDS) of PtTe nanoparticles.

Catalysts	**Atomic %**							
	Pt	**Ir**	**Ru**	**Te**	**C**	**O**	**Cl**	**Na**
PtIr	8.62	2.43			81.01	4.87	2.03	1.05
PtRu	7.83		4.09		77.96	8.15	1.04	0.93
PtTe	10.37			7.18	58.4	22.37	0.6	1.08

Table 5. 2: Energy dispersive spectroscopy (EDS) elemental analysis results for PtIr, PtRu and PtTe nanoparticles.

5.1.3 Electrochemical characterization of PtIr, PtRu and PtTe nanoparticles by CV, SWV and EIS

5.1.3.1 Electrochemical characterization of PtIrNP, PtRuNP and PtTeNP in 0.5 M H_2SO_4

No evidences are found in relation to the presence of preferential surface orientation and therefore, the surface of the nanoparticles can be considered as polyoriented or polycrystalline. In addition, these base voltammograms clearly evidence the cleanliness of the surface of the nanoparticles. In (**Figure 5.10**) characteristic voltammograms for platinum electrodes are reported with different orientations in contact with the solution and that for the electrode with a polyoriented surface. Electrochemistry provides some surface sensitive reactions that can be used as a tool to characterise the surface structure. In the case of platinum based metal, it is known that the so-called hydrogen adsorption/desorption process is very sensitive to the Pt surface structure and this fact is put in evidence as shown in the voltammetric profiles in (**Figure 5.10**). The potential window for all the nanoparticles was -200 mV to +1500 mV with a scan rate of 50 mV.s^{-1}, Figure 5.10 (a) PtIrNP showed two redox peaks there was oxidation of Ir (0) and Pt to PtO and Ir (III) at peak (I) with the following peak potential 1313 mV and reduction of PtO and Ir (III) to Pt and Ir in peak (II) with peak potential of 300 mV. This proved that the nanoparticles are pure and suitable for electrocatalysis of ammonia. Further more in Figure 5.10 (b) PtRuNP showed a reduction peak at peak potential 980 mV with no evidence of clear oxidation peak. Finally in (**Figure 5.10 (c)**) PtTe showed two oxidation peaks at peak potential 752 mV and 1313 mV which relate to the initial dissolution of Tellurium which led to accumulate of $HTeO_2^+$ cations (I) in solution at the electrolyte surface and subsequent solid TeO_2 (II) formation.

$Te \rightarrow HTeO_2^+ + 2\bar{e}$ (I) and

$HTeO_2^+ \rightarrow TeO_2 + 2\bar{e}$ (II).

(I') reduction of TeO_2 to Te; $TeO_2 + 2\bar{e} \rightarrow Te$, all of the nanoparticles are clean and can be used in the electrocatalysis of ammonia for application in fuel cells. Endo et al [62] found that at high oxidation potential the current density j was higher for PtIr $x \leq 0.8$ and PtRu $x \leq 0.4$ than Pt which suggested a positive cooperation of Ir and Ru with Pt electrocatalysis. On the other hand the addition of Ni to Pt did not yield positive results in the aim of finding alternative electrocatalyst [62].

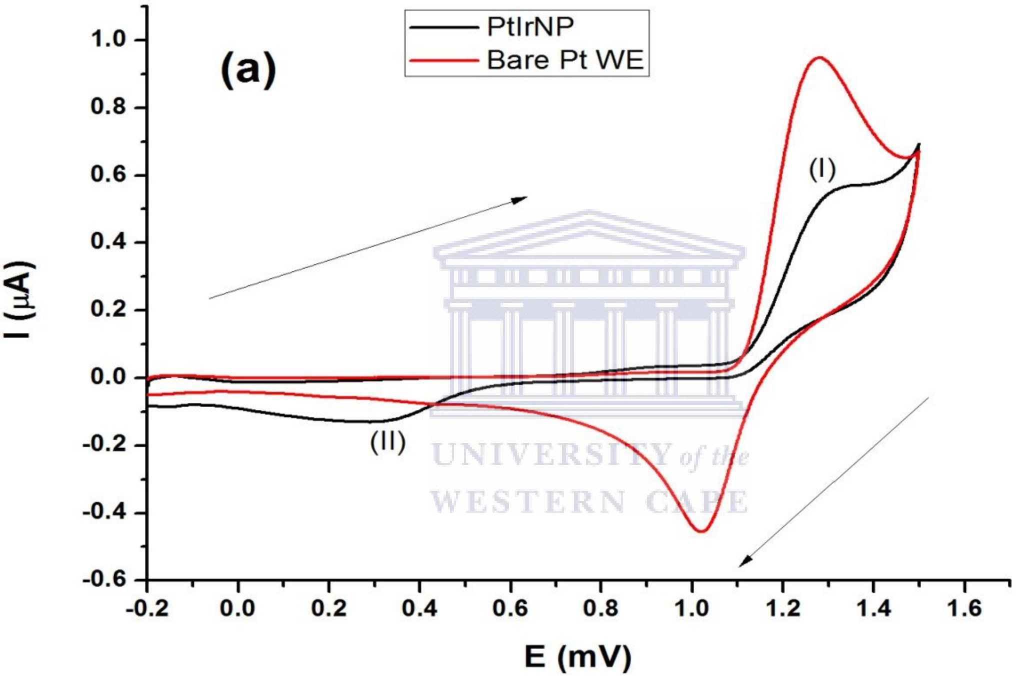

Figure 5. 10 (a): Cyclic voltammogram of (a) PtIr nanoparticles modified Pt electrode; Test solution, 0.5 M H_2SO_4: Scan rate, 50 $mV.s^{-1}$.

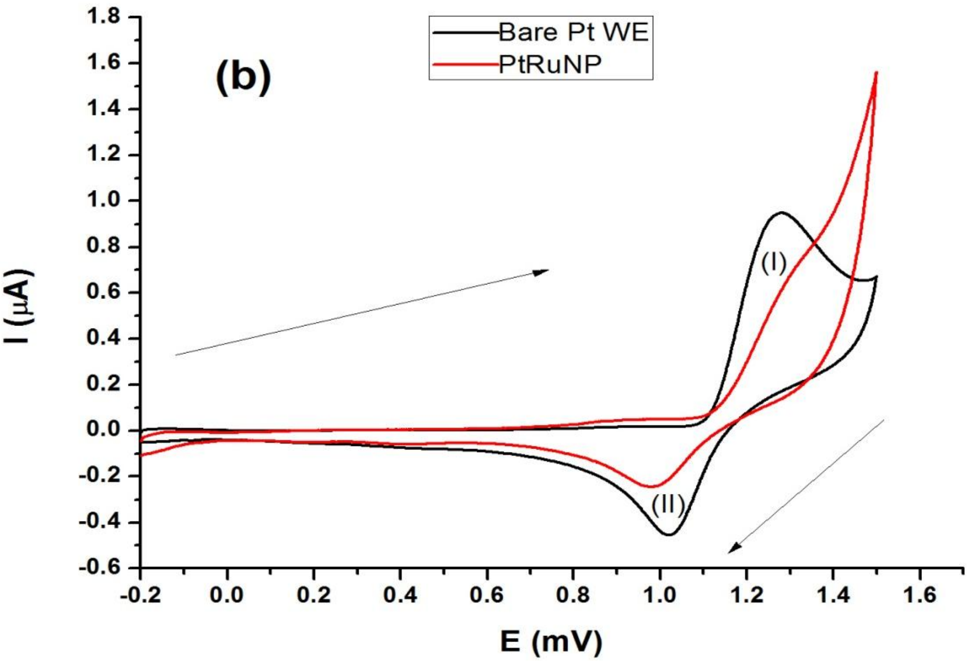

Figure 5.10 (b): Cyclic voltammogram of (b) PtRu nanoparticles modified Pt electrode; Test solution, 0.5 M H_2SO_4: Scan rate, 50 mV.s^{-1}.

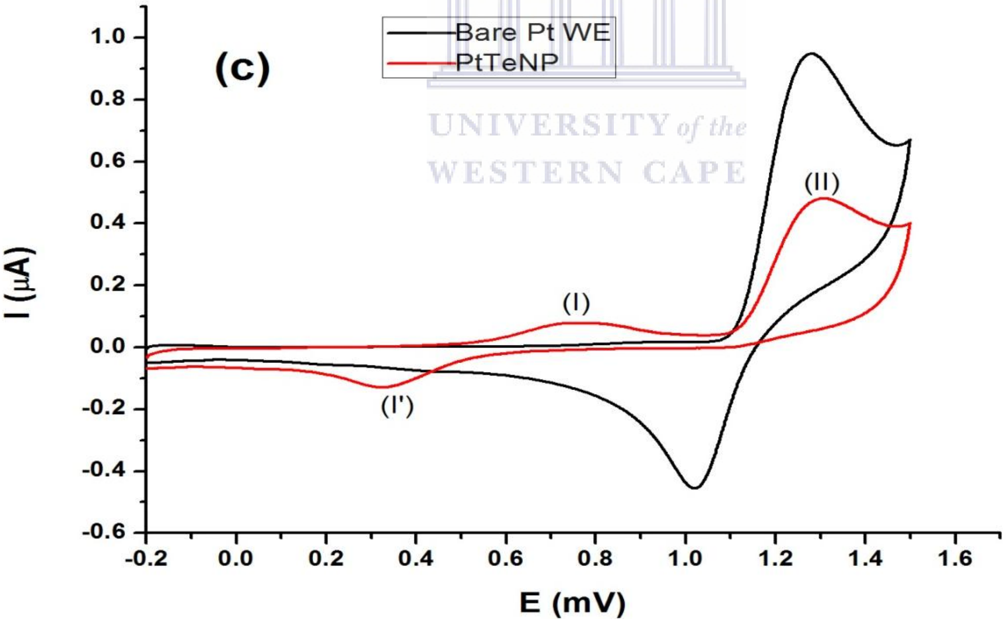

Figure 5.10 (c): Cyclic voltammogram of (c) PtTe nanoparticles modified Pt electrode; Test solution, 0.5 M H_2SO_4: Scan rate, 50 mV.s^{-1}.

In the second part of the study, the experiments were conducted using CV curves at different scan rates from 4 to 100 mV.s^{-1} in a 0.5 M H_2SO_4 medium. The PtIr, PtRu and PtTe nanoparticles electrocatalyst in 0.5 M H_2SO_4 displayed good reactivity in the potential window -200 mV to +1500 mV from the scan rate was 4 till 100 mV.s^{-1}, respectively in (**Figure 5.11 [(a), (b) and (c)]**). The increase in the current density with the increase in the potential scan rate is attributed to the excitation signal caused during the charging of the interface capacitance by the charge transfer process. The presence of a platinum base metal catalyst, the absorption can be assumed to promote the formation of the electro-catalytically active phase of PtO. Hence, this indicates that the electrochemical catalytic behaviour of the catalyst, but also related to the catalyst surface composition. Choose to show PtIr nanoparticles as representative nanoparticles for calculation of kinetics of the electrode, PtRu and PtTe nanoparticles gave similar kinetics as PtIr. The anodic peak (I_{pa}) and cathodic peak current (I_{pc}) of PtIr nanoparticles electrode is linearly dependent on the scan rate (υ) gave a regression equation I_{pa} (I) = -0.289 x + (-37.413) (R^2 = 0.965) and I_{pc} (II) = 0.109 x + 9.636 (R^2 = 0.971). This revealed that the electrode contained a thin electroactive surface bound catalyst film; the kinetic process that controls the peak is diffusion controlled reaction. This was confirmed by plotting log of cathodic current against the log of scan rate which gave a slope of 0.523, 0.452 and 0.509 for PtIr, PtRu and PtTe nanoparticles respectively. Based on plotting peak potential against log scan rate the reduction of PtIr, PtRu and PtTe nanoparticles behaved in an irreversible manner ($I_{pa}/I_{pc} \neq 1$ and $\Delta E_p > 59$ mV). The number of electrons transferred was estimated by integrating CV of the reduction peak to obtain the amount of charge (C) involved in the reaction and substituting appropriately in the Laviron's equation. It showed that the nanoparticles electrochemistry is a two, one and one- electron process for PtIr, PtRu and PtTe nanoparticles respectively.

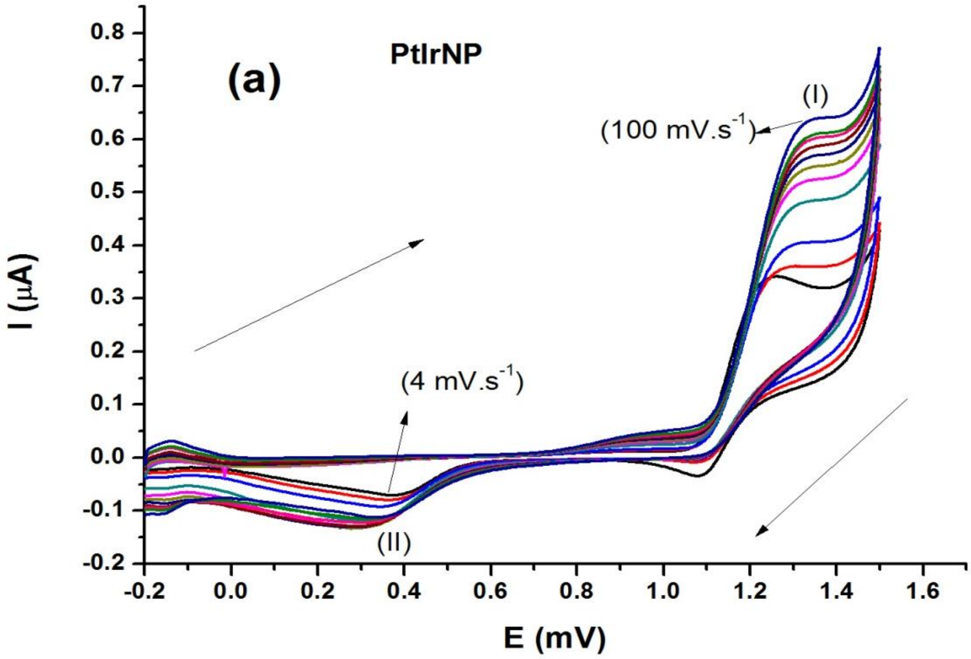

Figure 5. 11 (a): Cyclic voltammogram in test solution 0.5 M H_2SO_4 of (a) PtIr nanoparticles modified on Pt electrode at different scan rates; 4, 6, 10, 20, 30, 40, 50, 60, 70, 80, and 100 mV.s^{-1} respectively.

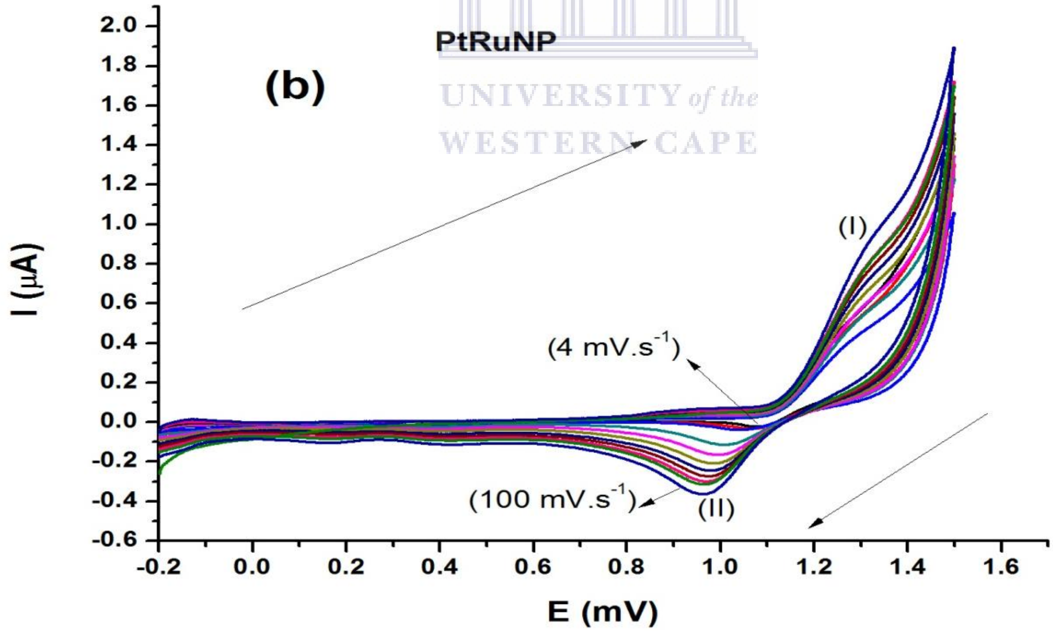

Figure 5.11(b): Cyclic voltammogram in test solution 0.5 M H_2SO_4 of (b) PtRu nanoparticles modified on Pt electrode at different scan rates; 4, 6, 10, 20, 30, 40, 50, 60, 70, 80, and 100 mV.s^{-1} respectively.

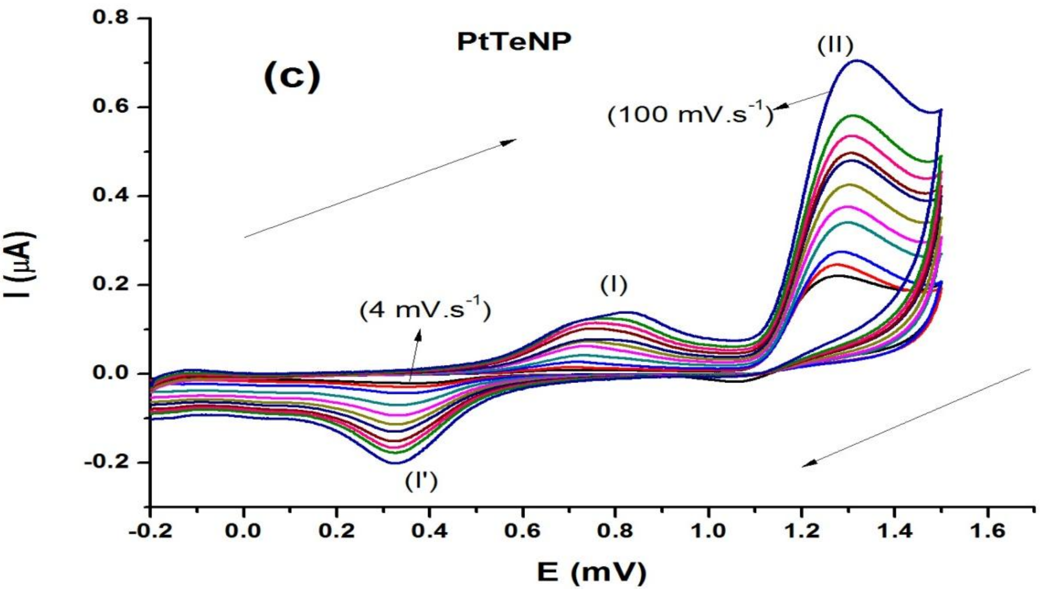

Figure 5.11 (c): Cyclic voltammogram in test solution 0.5 M H_2SO_4 of (c) PtTe nanoparticles modified on Pt electrode at different scan rates; 4, 6, 10, 20, 30, 40, 50, 60, 70, 80, and 100 mV.s^{-1} respectively.

Randles-Sevčik equation was used to study the kinetics of the electrode, in (**Figure 5.12**) indicated that the electrochemical reaction rate is fast and oxidation of Pt to PtO and Ir (0) to Ir (III) and the reduction of PtO on Pt and Ir (0) to Ir electrode is a typical diffusion-controlled process. A linear relationship between $E_{pa,\ c}$ and log *v* was obtained, indicated the oxidation reduction of PtIr was an irreversible electrode process.

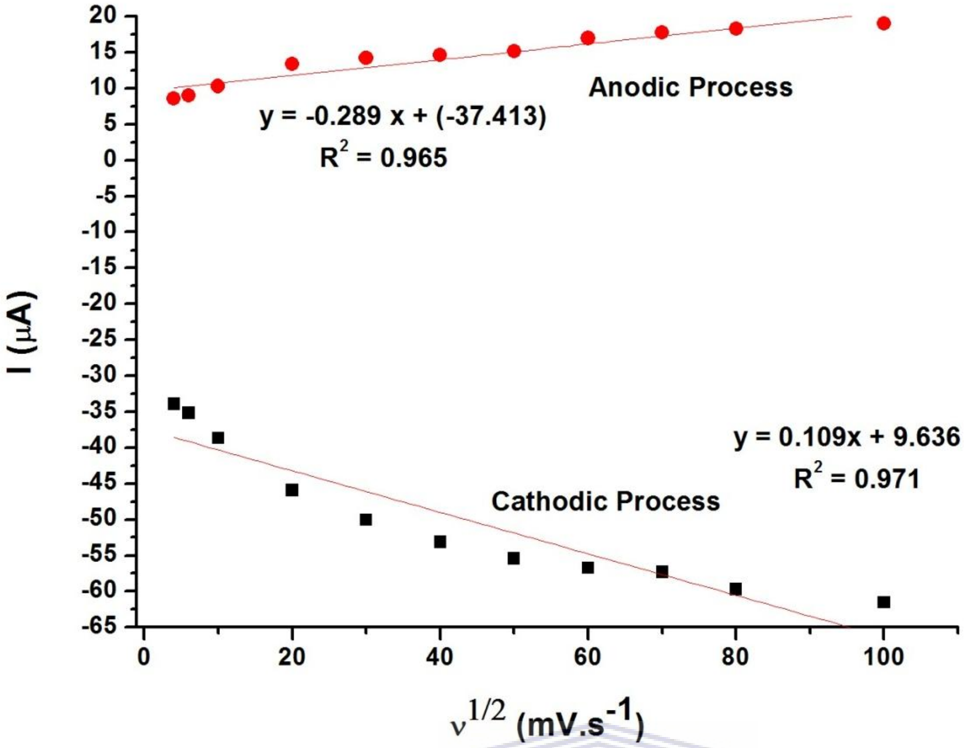

Figure 5. 12: Randles-Sevčik plot of PtIr. Conditions are as in Figure 5.11 (a).

5.1.3.2 Electrochemistry of the PtIr, PtRu and PtTe nanoparticles for oxidation of ammonia in 1 M KOH

Ammonia oxidation was carried out on bimetallic Pt-based nanoparticles in 0.5 M NH_4OH +1 M KOH and (**Figure 5.13**) compares CVs obtained at 50 mV.s^{-1}. Ammonia oxidation takes place effectively in alkaline medium. It is thus of interest to interrogate the behaviour of the nanoparticles in alkaline medium. The CVs were recorded over a potential range of -1000 mV and +400 mV at a scan rate of 50 mV .s^{-1}. Three oxidation peaks were observed at **Figure 5.13** (a), (b) and (c) for PtIr, PtRu and four oxidation peaks for PtTe nanoparticles; for peak (I), E_{pa} = -801 mV, -860 mV and -795 mV followed at more positive potentials by peaks (II), E_{pa} = -737 mV, -770 mV and -721 mV, peak (III), E_{pa} = -383 mV, -402 mV and -346 mV for PtIrNP, PtRuNP and PtTeNP respectively, peak (IV), E_{pa} = -427 mV for PtTeNP. On the cathodic scan, Three reduction peaks were also observed (III'), E_{pc} = -404 mV,-162 mV and -363 mV followed by (II') E_{pc} = -761 mV, -889 mV and -749 mV and peak (I'), E_{pc} = -870 mV, for PtRu there is no peak and for PtTeNP is -846 mV. The CV measurements using Pt drop coated Pt nanoparticles clearly show that various platinum redox processes can occur. These observed peaks are related to platinum oxidation states such as Pt (0) that undergo several redox reactions such as Pt (0) nanoparticles deposit or Pt (0) oxidation to Pt (II) and Pt (IV) and platinum oxidation. The shape of the peaks (I)/ (I') and (II)/ (II') in the voltammograms are explained taking into consideration one of the most important properties of Pt which is the ability to adsorb, on its surface, and absorb, within its lattice, hydrogen. Peaks (II') and (I') are due to the reduction of hydrogen, which are adsorbed on the platinum surface ($H^+ + e^- \rightarrow H_{ad}$) and absorbed into the platinum lattice ($H^+ + e^- \rightarrow H_{ab}$) while peak (I) is attributed to oxidation of hydrogen atoms adsorbed on the surface of platinum ($H_{ad} \rightarrow H^+ + e^-$) and peak (II) to the oxidation of hydrogen absorbed into the platinum metal lattice ($H_{ab} \rightarrow H^+ + e^-$). Oxidation of Ru (0) to Ru (III), Ir (0) to Ir (III) and the initial dissolution of Tellurium led to accumulate of $HTeO_2^+$ cations (III) in solution at the electrolyte surface and subsequent solid TeO_2 (IV) formation.

$Te \rightarrow HTeO_2^+ + 2\bar{e}$ (III) and

$HTeO_2^+ \rightarrow TeO_2 + 2\bar{e}$ (IV).

Peak (III') is the reduction of PtO to Pt, Ir (III) to Ir (0), Ru (III) to Ru (0) and reduction of peak IV' TeO_2 to Te; $TeO_2 + 2\bar{e} \rightarrow Te$. The proton reduction takes place on the surface of the Pt nanoparticles. Similar oxidation peaks were also observed in (**Figure 5.14 [(a), (b) and (c)]**), the square wave voltammetry was also recorded over a potential window of -1000 mV to +400 mV, square wave was used due to it good sensitivity. Vitse et al [174] reported that the efficiency improved by bimetallic PtIr and PtRu current density of 100 mA and this results certified ammonia as a potential alternative low cost, low temperature and high purity fuel source [174]. In this results Te showed positive co-operation with Pt electrocatalysis more than (Ir and Ru), alternative catalyst with better performance than other bimetallic found in literature

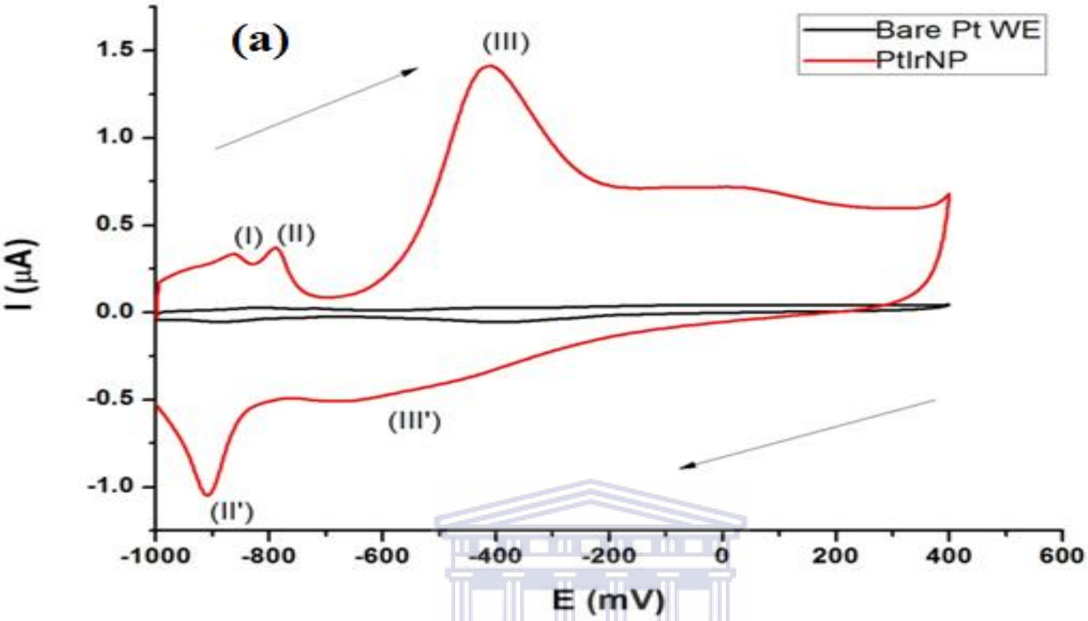

Figure 5. 13 (a): Cyclic voltammogram of Pt/PtIrNP electrode in 0.5 M ammonia and 1 M KOH aqueous solution: Scan rate, 50 mV.s^{-1}.

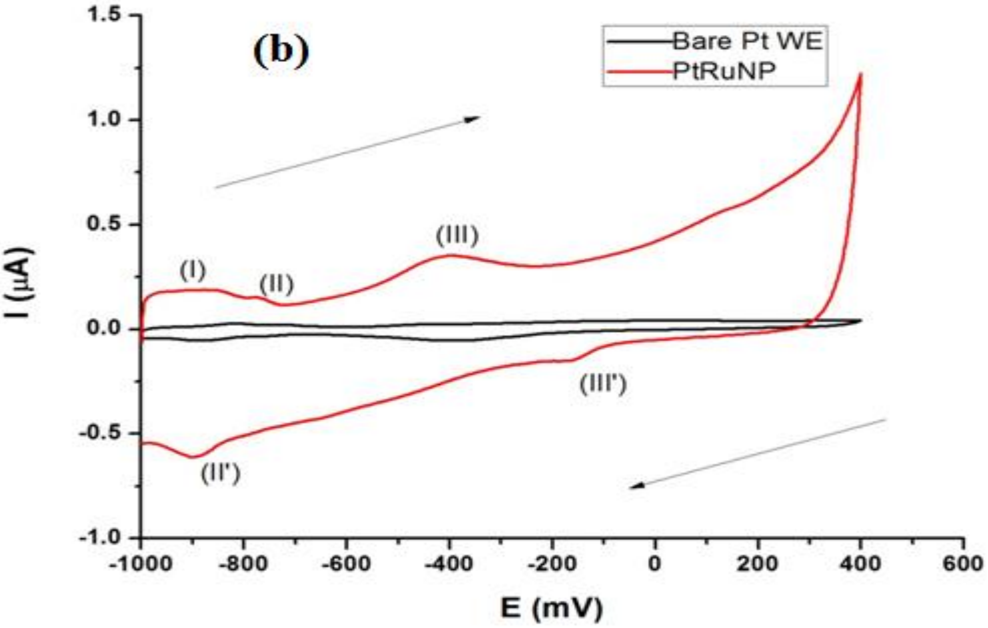

Figure 5.13 (b): Cyclic voltammogram of Pt/PtRuNP electrode in 0.5 M ammonia and 1 M KOH aqueous solution: Scan rate, 50 mV.s^{-1}.

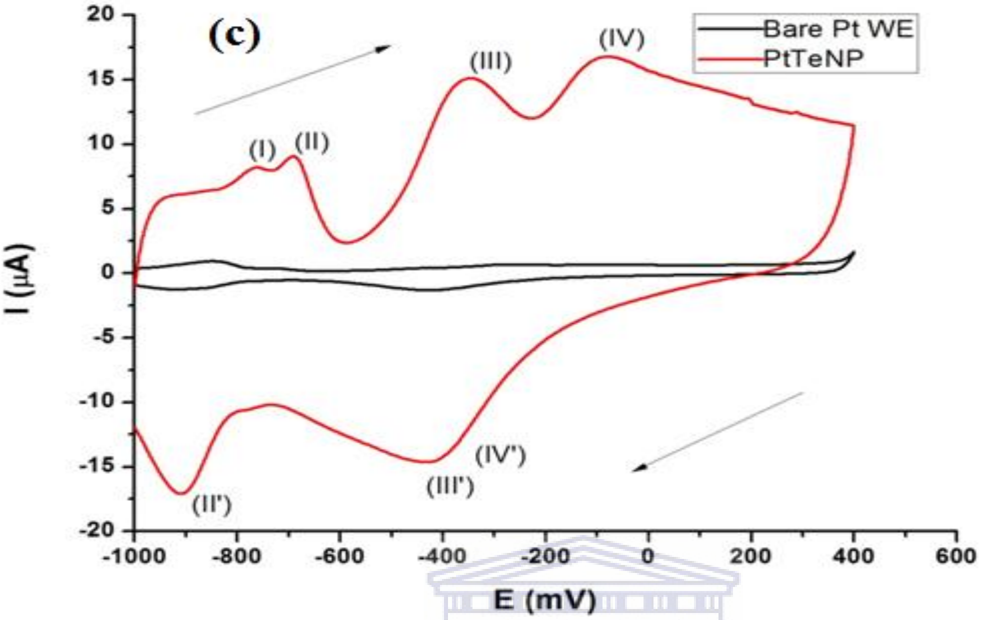

Figure 5.13 (c): Cyclic voltammogram of Pt/PtTeNP electrode in 0.5 M ammonia and 1 M KOH aqueous solution: Scan rate, 50 mV.s^{-1}.

The surface active sites of the Pt electrode are expected to become less available when coated with nanoparticles. In (**Table 5.3**) PtIr nanoclusters was found to give higher peak current than PtRu but PtRu has lower overpotential than PtIr. PtTe nanoparticles are found to give higher peak current than PtIr and PtRu nanoparticles. PtTe nanoparticles have lower over potential than PtIr and PtRu nanoparticles. PtIr nanoparticles were initially considered as a promising candidate for ammonia oxidation, now PtTe nanoparticles synthesised in this study gives much better results than PtIr and PtRu nanoparticles. Lomocso et al [109] found that PtIr had good catalytic activity for ammonia oxidation as compared PtPd and PtSnO$_2$ nanoparticles [109]. Telluride has been studied for synthesis of quantum dots for photoluminescence and never been studied for fuel cell application. Mtungwana et al [124] reported ZnTe nanoparticles for photoluminescence and Tubtimtae et al [164] studied CuTe quantum dots for solar cell [164]. This is very interesting finding of telluride co-operation with Pt based on its previous application.

Electrode	**E_{pa} (mV)**	**i_{pa} (A)**
PtNP	-431	1.726×10^{-4}
PtIrNP	-383	1.982×10^{-5}
PtRuNP	-402	2.342×10^{-5}
PtTeNP	-346	1.276×10^{-3}

Table 5. 3: Data points of oxidation of ammonia extracted from binary nanoparticles cyclic voltammetry in Figure 5.13 (a), (b) and (c).

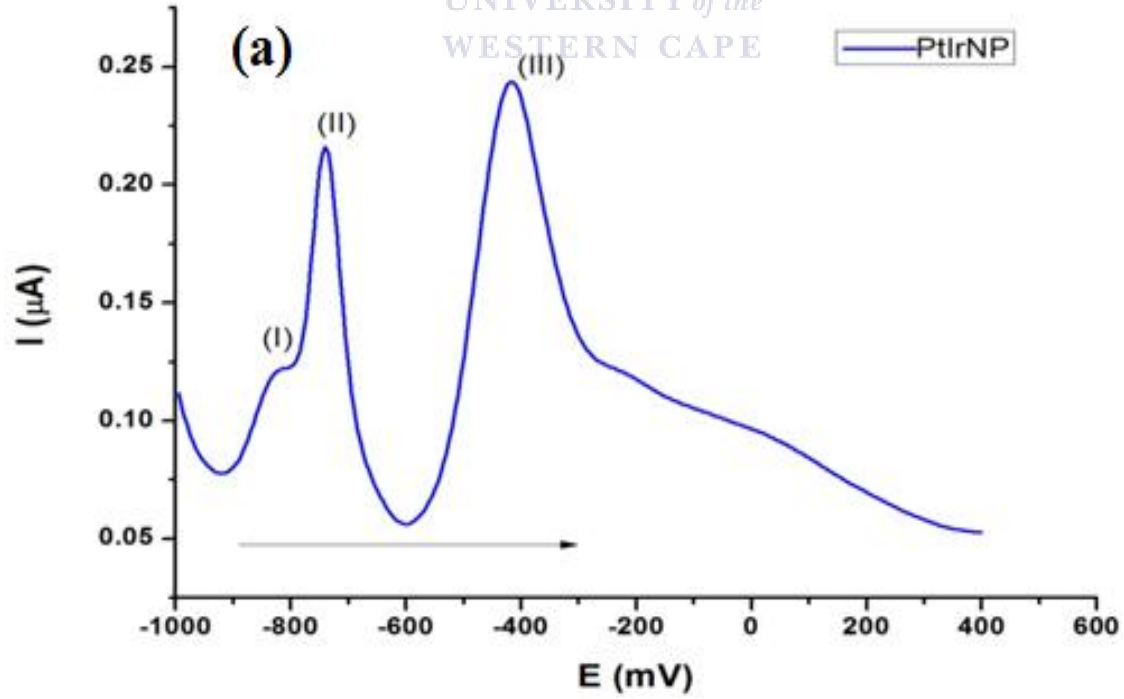

Figure 5. 14 (a): Square wave voltammetry of (a) PtIr nanoparticles drop coated on Pt electrode in 0.5 M ammonia and 1 M KOH aqueous solution: Scan rate, 50 mV.s^{-1}.

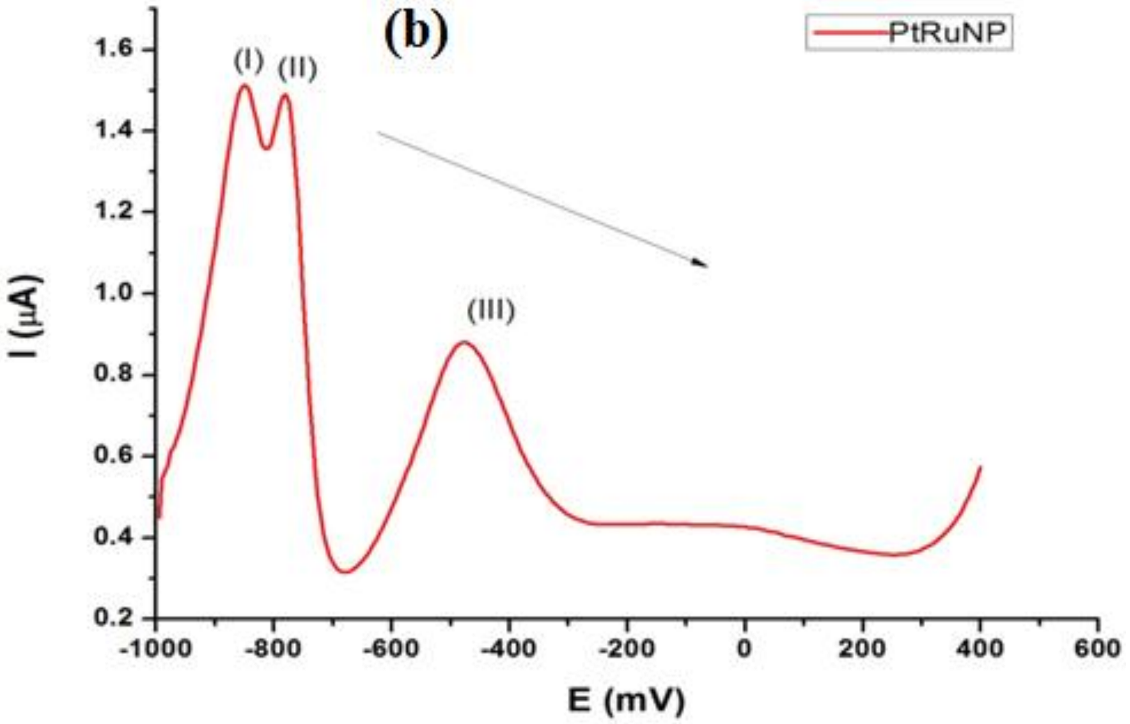

Figure 5.14 (b): Square wave voltammetry of (b) PtRu nanoparticles drop coated on Pt electrode in 0.5 M ammonia and 1 M KOH aqueous solution: Scan rate, 50 mV.s^{-1}.

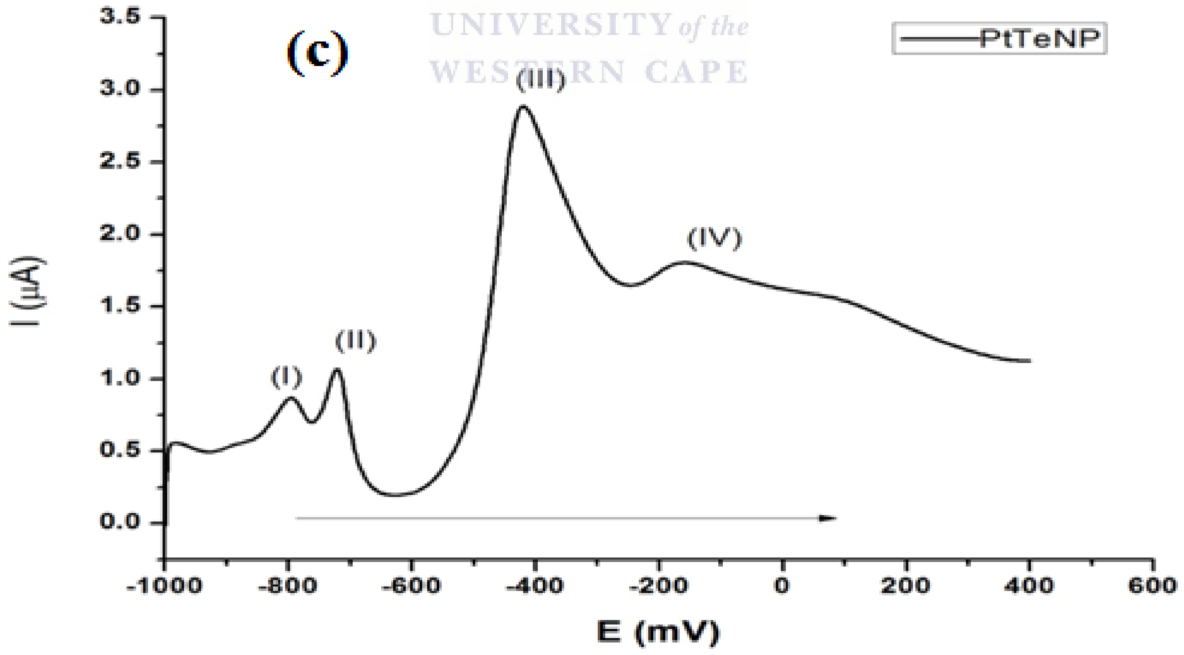

Figure 5.14 (c): Square wave voltammetry of (c) PtTe nanoparticles drop coated on Pt electrode in 0.5 M ammonia and 1 M KOH aqueous solution: Scan rate, 50 mV.s^{-1}.

In order to study the nature of the oxidation of ammonia, we performed the CVs at different scan rates (**Figure 5.15 [(a), (b) and (c)]**) measured on PtIrNP, PtRuNP and PtTeNP electrode in 0.5 M ammonia and 1 M KOH solution. The anodic peak currents increased significantly with the increasing potential scan rate. It can be seen that the peak currents (I_p) of PtIr, PtRu and PtTe nanoparticles film on Pt electrode increased linearly with scan rates (v) rates up to 100 $mV.s^{-1}$. The results show that the Pt based metal nanoclusters films were stable and electrochemically active in 0.5 M ammonia and 1 M KOH solution.

In (**Figure 5.16)** shows a plot of anodic and cathodic peak currents versus scan rate for redox peaks (III)/(III') that showed a close linear dependence with the scan rate a characteristic feature of PtTeNP as a representative nanoparticles surface confined species. Additionally, the voltammetric data were subjected to analysis by plotting log (I_p) versus log scan rate (v). The value of the slope of the linear plot of log I_p versus log v can be used to elucidate the nature of the processes influencing the electrochemistry of the surface confined species. Slopes with values of 1.0 and 0.5 refer to adsorption-controlled and diffusion-controlled electrochemical processes, respectively. Intermediate values for the slope indicate mixed diffusion/adsorption-controlled electrochemical processes. In this work, the plots of log I_p versus log υ (not shown) gave slopes of 0.38, 0.35 and 0.46 for PtIrNP, PtRu and PtTeNP respectively for both the anodic and cathodic peaks which showed the occurrence of diffusion controlled electrochemistry of the Pt based binary system and that the PtIr, PtRu and PtTe nanoparticles films were a monolayer film.

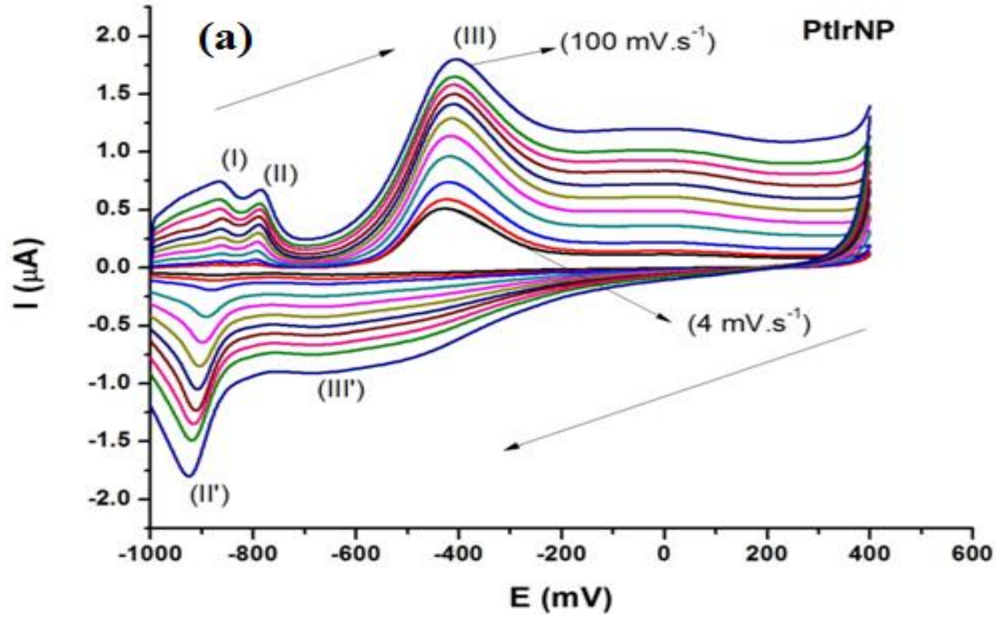

Figure 5. 15 (a): Cyclic voltammogram in test solution 0.5 M ammonia and 1 M KOH of PtIr nanoparticles modified on Pt electrode at different scan rates; 4, 6, 10, 20, 30, 40, 50, 60, 70, 80, and 100 mV.s^{-1} respectively.

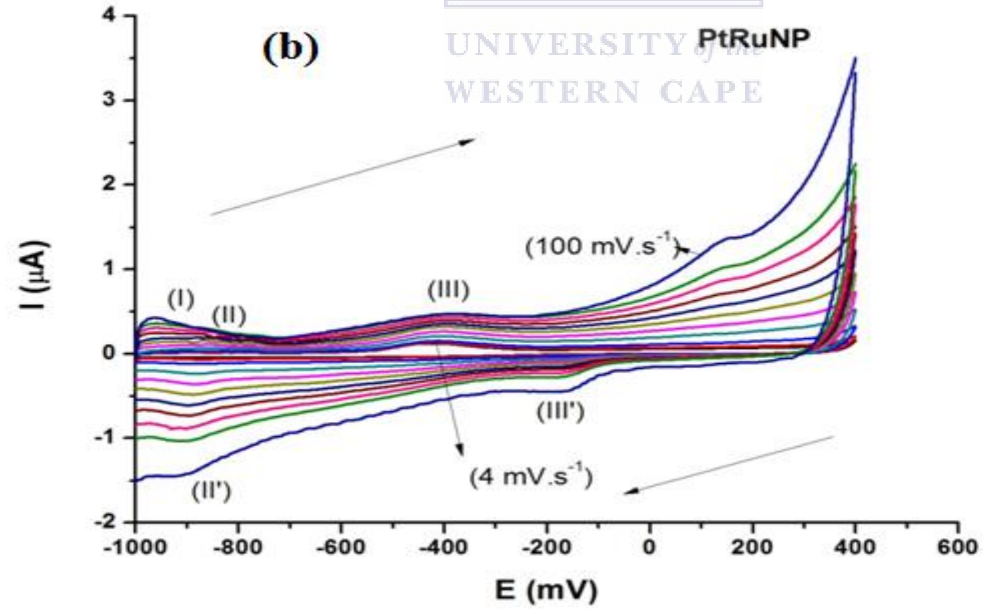

Figure 5.15 (b): Cyclic voltammogram in test solution 0.5 M ammonia and 1 M KOH of PtRu nanoparticles modified on Pt electrode at different scan rates; 4, 6, 10, 20, 30, 40, 50, 60, 70, 80, and 100 mV.s^{-1} respectively.

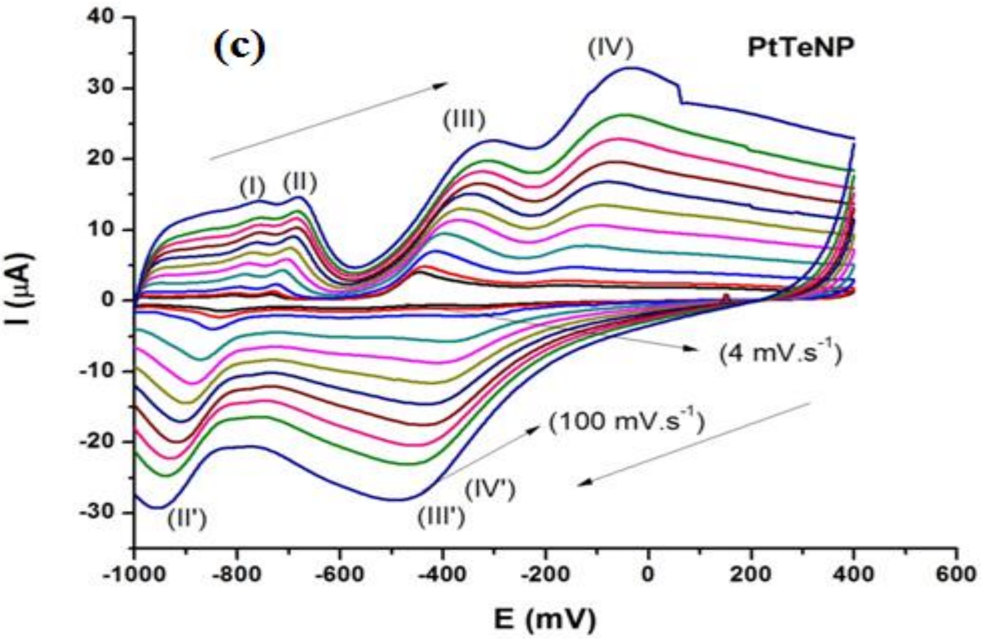

Figure 5.15 (c): Cyclic voltammogram in test solution 0.5 M ammonia and 1 M KOH of PtTe nanoparticles modified on Pt electrode at different scan rates; 4, 6, 10, 20, 30, 40, 50, 60, 70, 80, and 100 mV.s^{-1} respectively.

The electrochemical kinetics was exacted from the different scan rates by using Randles-Sevčik equation below (4.7) explained extensively in chapter 3.

$$I_p = (2.99 \times 10^5) n (\alpha n_\alpha)^{1/2} A C_0 D^{1/2} \upsilon^{1/2} \qquad (5.7)$$

The Brown Anson model was used using the equation below (5.8).

$$I_p = \frac{n^2 F^2 \Gamma A \upsilon}{4RT} \qquad (5.8)$$

The kinetics of ammonia in KOH is shown in (**Table 5.4**) below;

Electrode	n	α	Γ (mol.cm^{-2})	Kinetic process	Redox process	Diffusion coefficient (cm^{-2}.s^{-1})
PtNP	1	0.5	1.09 x 10^{-11}	Diffusion	Irreversible	1.97 x 10^{-7}
PtIrNP	2	0.5	3.49 x 10^{-13}	Diffusion	Irreversible	1.08 x 10^{-5}
PtRuNP	1	0.5	1.35 x 10^{-12}	Diffusion	Irreversible	1.75 x 10^{-5}
PtTeNP	1	0.5	6.38 x 10^{-11}	Diffusion	Irreversible	1.58 x 10^{-4}

Table 5. 4: Electrochemical parameters of nanoalloy systems.

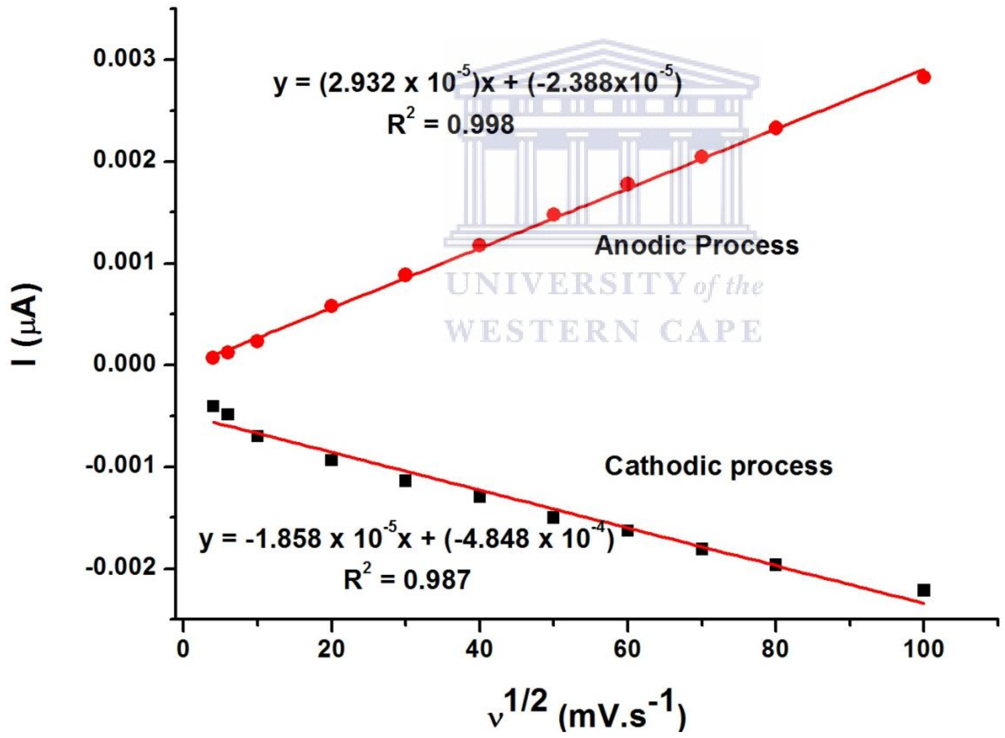

Figure 5. 16: Randles-Sevčik plot of PtTe for peak III and III'. Conditions are as in Figure 5.15 (c).

5.1.3.3 Electrochemistry impedance spectroscopy of the Pt nanoparticles for oxidation of ammonia in 1 M KOH

Electrochemical impedance is a powerful technique for investigating the kinetics of nanoparticles for electrooxidation in fuel cells. However, impedance spectroscopy also allows the detection of change in capacitance due to electrode modification. The Nyquist plot of impedance spectra in (**Figure 5.17**) for PtIrNP, PtRuNP and PtTeNP immobilized on Pt working electrode includes a semicircle portion and a linear portion, with the former at higher frequencies corresponding to the electron transfer process and the latter at lower frequencies corresponding to the diffusion process. The charge transfer resistance (R_{ct}) at the electrode surface is equal to the semicircle diameter, which can be used to describe the interface properties of the electrode. it can be seen from the results presented that by loading binary nanoparticles can effectively enhance the activity of ammonia electrooxidation.

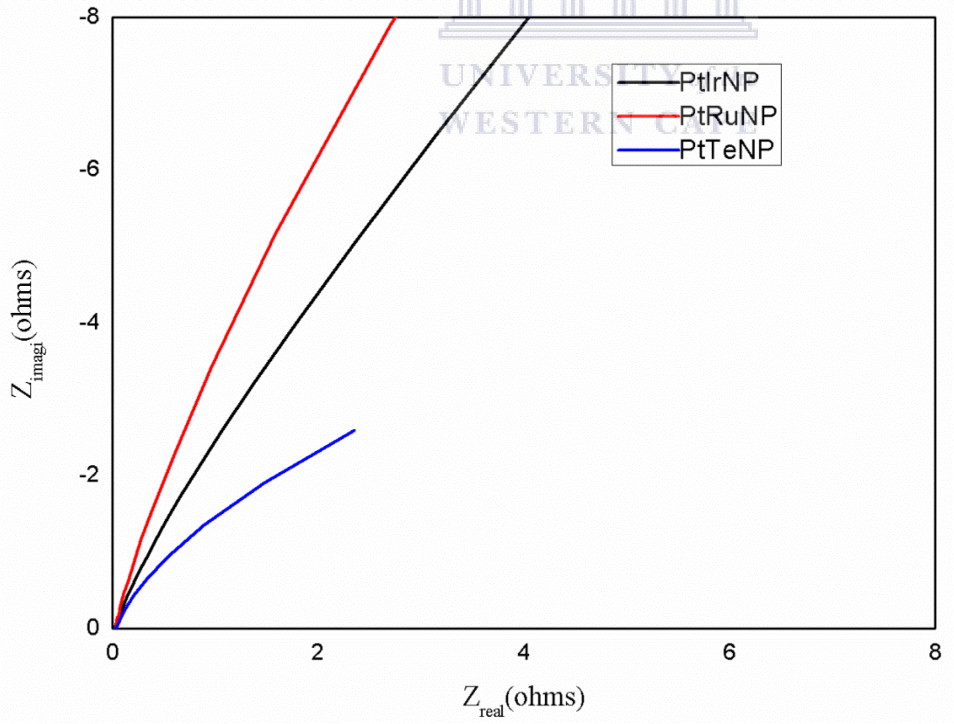

Figure 5. 17: Nyquist plot of the electrooxidation of 0.5 M ammonia on PtIrNP, PtRuNP and PtTeNP immobilized on Pt electrode in 1 M KOH.

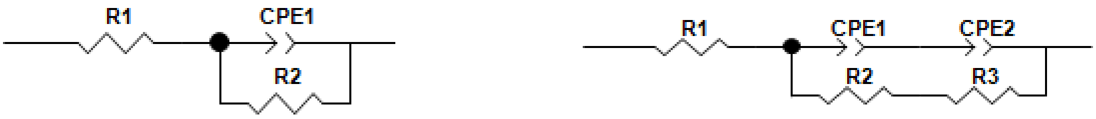

PtIrNP and PtRuNP

PtTeNP

Figure 5. 18: Equivalent circuit for PtIr, PtRu and PtTe nanoparticles.

In (**Figure 5.17**) the charge transfer resistance (R_{ct}) of PtRuNP was the lowest (R_{ct} = 91004 Ω) compared to that of bare PtIrNP and PtTeNP working electrode (1.7707 x 10^5 Ω and 4.8323 x 10^{14} Ω, 3.0507 x 10^{12} Ω), indicating that the PtRu and PtIr nanoparticles have good conductivity as compared to PtTeNP and played an important role in accelerating the transfer of electrons. This can be attributed to the increased catalytic and improved conductivity properties portrayed by nanoparticles. The impedance parameters (**Table 5.4**) were obtained by fitting using an equivalent circuit (**Figure 5.18**) and the fitting errors were less than 2 %. R_s is the solution resistance, R_{ct} is the charge transfer resistance, and CPE (constant phase element) is a distributive element that models the double layer capacitance owing to surface in homogeneity and Z_w (w) Warburg measures mass transport.

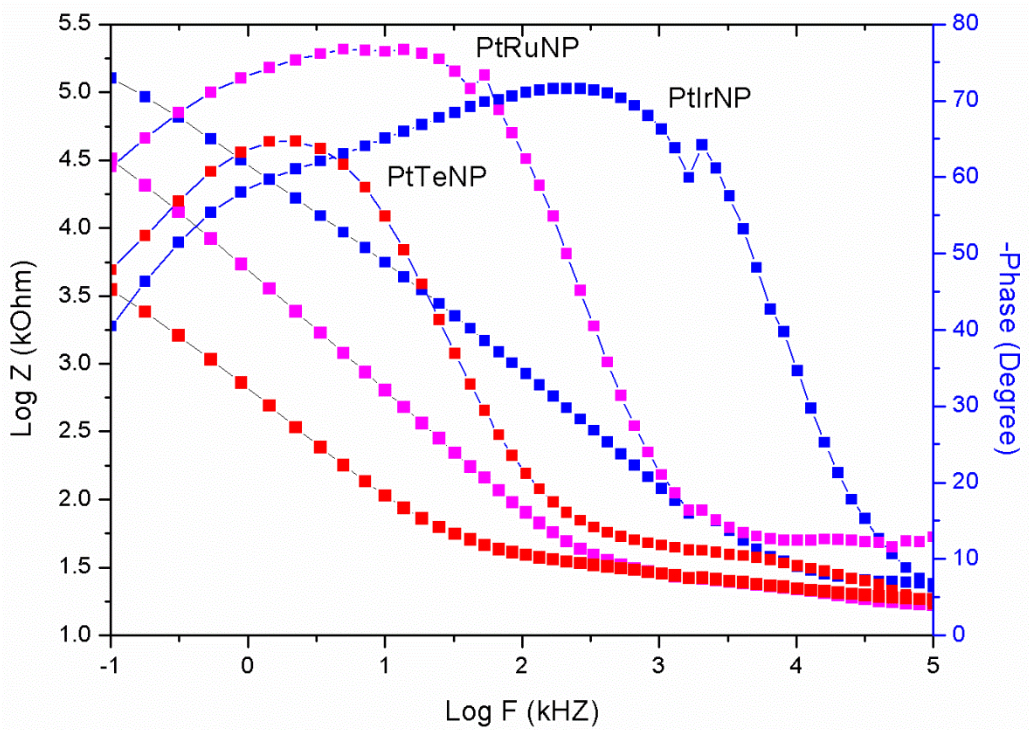

Figure 5. 19: Bode plots of 0.5 M ammonia on PtIr, PtRu and PtTe nanoparticles in 1 M KOH.

Figure 5.19 shows plots of phase angle changes with frequency for PtIr, PtRu and PtTe nanoparticles. Bode plots showed remarkable differences in the electronics of bare PtIr, PtRu and PtTe nanoparticles interfaces. The frequency of maximum phase angle increased from bare PtTe, PtIr to PtRu nanoparticles with the phase angle decreasing from semi-metallic value for PtRu (78°) to semiconductor value for PtIr (73°) and PtTe (65°) nanoparticles. The Bode plot gives direct information on the frequency and phase angle. The frequency at maximum phase is a useful parameter in determining the double layer capacitance using equation 5.9:

$$\omega_{\varnothing\max} = \frac{\left(1 + \frac{R_{ct}}{R_{sol}}\right)}{R_{ct}C_{dl}} \tag{5.9}$$

In most applications however, analysis of both Bode and Nyquist plots is highly advised in order to conclusively study electrochemical processes at interfaces shown in (**Table 5.5**).

Electrode	ω_{max} (HZ)	R_{ct} (Ω)	C_{dl} (µF)	Γ (s.rad^{-1})	I_0 (A)
Bare Pt	2635.73	2.0605×10^{6}	1.8413×10^{-10}	3.7939×10^{-4}	1.2×10^{-8}
PtNP	2635.73	1.943×10^{6}	1.9527×10^{-10}	3.7941×10^{-4}	1.3×10^{-8}
PtIrNP	2635.73	1.7707×10^{5}	2×10^{-9}	3.5414×10^{-4}	7.2×10^{-8}
PtRuNP	1329.65	91004	8×10^{-9}	7.2803×10^{-4}	2.82×10^{-9}
PtTeNP	2098.21	4.8323×10^{14}	9.8627×10^{-19}	4.7659×10^{-4}	6.19×10^{11}
		3.0507×10^{12}	1.5623×10^{-16}	4.766×10^{-4}	8.42×10^{-15}

Table 5. 5: EIS parameters of bare PtIr, PtRu and PtTe nanoparticles in 1 M KOH (data obtained from the circuit fitting of Figure 5.18).

5.1.4 Sub-conclusion

All the peaks in the XRD patterns of PtIr, PtRu and PtTe are shifted slightly to larger 2θ values (right shift) with respect to the pure Pt, indicating the decreased d spacing and contraction of the lattice constant, due to the incorporation of increasing amounts of the smaller metal atoms into the Pt fcc lattice. No Pt or other metal peaks appear, indicating that bimetallic nanostructures or alloys were formed. PtIr, PtRu and PtTe particle size 1.297, 2.084 and 2.198 nm and lattice parameter 5.157, 5.132 and 5.182 nm. The FTIR spectrum of the PVP stabilized binary Pt based nanoparticles showed broad peaks between 1201 cm^{-1} and 1651 cm^{-1} which corresponds to C-N stretching motion and C=O stretching motion of monomer for PVP, respectively. The narrow absorption peaks centered at 1421 cm^{-1} and 2890 cm^{-1} occurred in is ascribed to the C–H bonding due to the presence of PVP. This was due to the formation of coordinate bond between the nitrogen atom of the PVP and the Pt^{2+}, Ir^{3+}, Ru^{3+} and Te^{2+}. The UV-vis showed that the peaks disappeared after reduction of the salts indicated that the metal ions were completely reduced. The synthesised nanoparticles showed no absorption peaks indicated a complete reduction of the metal ions to zero-valent nanoparticles, exhibiting an exponential graph shape. Morphological analysis was done with HRTEM with the average particle size for PtIr nanoparticles was 3.2 nm – 5 nm showed that the PtIr nanoparticles clusters agglomerated to some extent, PtRu nanoparticles was 0.5 nm – 2 nm which showed that the PtRu nanoparticles are not agglomerated and PtTe nanoparticles was 2.3 nm – 5 nm which shows that the nanoparticles were agglomerated to some extent. The Selected area electron diffraction pattern (SAED) for PtIr, PtRu and PtTe nanoparticles showed characteristic electron diffraction rings for PtIr, PtRu and PtTe, further indicating that the catalyst structure were made of nanoparticles. They exhibited a high crystallinity which was deduced from the SAED pattern. Further morphological characterization was carried out by HRSEM which revealed that the nanoparticles were homogeneously dispersed as small, spherical and uniform bright spots on the carbon support. In that case the particles were approximately 46 nm in diameter for all different types of carbon electrode. The binary platinum particle size for HRSEM was rather bigger than that which was calculated via XRD and HRTEM. This was due to either the impossibility of observing small particles by HRSEM or because the observed particles were, in fact, aggregations of smaller particles. Energy dispersive spectroscopy/ X-ray (EDS/EDX) were used to investigate the elemental composition of the electrocatalyst synthesized. Electrochemical characterization of nanoparticles in acidic medium showed characteristic peaks of all nanoparticles and showed that the nanoparticles formed composites with the increase in peak current density. The increase in the current density with the increase in the potential scan rate was attributed to the excitation signal caused during the charging of the interface capacitance by the charge transfer process. Ammonia oxidations the electrocatalyst were interrogated electrochemical and it was found that PtIr nanoclusters to give higher peak current than PtRu even though PtRu had lower overpotential than PtIr. PtTe nanoparticles were found to give higher peak current than PtIr and PtRu nanoparticles. PtTe nanoparticles had lower over potential than PtIr and PtRu nanoparticles. PtIr nanoparticles were initially considered as a promising candidate for ammonia oxidation in literature but now PtTe nanoparticles synthesised in this study gives much better results than PtIr and PtRu nanoparticles. The kinetics of the nanoparticles were determined and it was found that all the nanoparticles were diffusion controlled with PtIr being a two electron process while PtRu and PtTe were a one electron process. The study of EIS found that the charge transfer resistance (Rct) at the electrode surface was equal to the semicircle diameter, which was used to describe the interface properties of the electrode. it was observed from the results presented that by loading binary nanoparticles can effectively enhance the activity of ammonia electrooxidation charge transfer resistance (Rct) of PtRuNP was the lowest (Rct = 91004 Ω) compared to that of bare PtIrNP and PtTeNP working electrode (1.7707×10^{5} Ω and 4.8323×10^{14} Ω, 3.0507×10^{12} Ω), indicating that the PtRu, PtIr and PtTe nanoparticles have good conductivity as and played an important role in accelerating the transfer of electrons. This can be attributed to the increased catalytic and improved conductivity. The bode plot showed the frequency of maximum phase angle increased from bare electrode, PtTe, PtIr to PtRu nanoparticles with the phase angle decreasing from semi-metallic value for PtRu (78°) to semiconductor value for PtIr (73°) and PtTe (65°) nanoparticles. The Bode plot gave direct information on the frequency and phase angle. The frequency at maximum phase was a useful parameter in determining the double layer capacitance.

CHAPTER 6

Summary

This is the third and final part of three chapters outlining and discussing the results obtained from this study. This chapter deals specifically with the characterisation of ternary nanoparticles such as PtIrTe and PtRuTe for its subsequent applications in the oxidation of ammonia. The chapter clearly illustrates how the nanoparticles were successfully characterized by spectroscopic methods such as FTIR, UV-vis, HRTEM, and HRSEM for morphological analysis and XRD for structural analysis. The electrochemical properties of these nanoparticles were interrogated using techniques such as CV, SWV and EIS. The potential application of the nanoparticles as electrocatalysts for ammonia electro-oxidation for fuel cell application was further investigated and concluded.

6.0 Results and Discussion (Part 3)

6.1 Ternary Catalyst

The application of ternary metal nanoparticles can significantly enhance the catalytic activity toward ammonia oxidation. The role of the third component is to help in reduce NH adsorption on Pt [10]. The enhanced catalytic activity has been attributed by a number of factors including the change in Pt–Pt inter atomic distance, number of Pt nearest neighbours, Pt 5d band vacancy, and Pt metal content on particle surface. To further improve the catalytic activity for oxygen reduction of platinum, ternary catalysts formed by various transition metals are currently investigated [9].

6.1.1 Structural Characterization by XRD, IR spectroscopy and UV-vis.

XRD is a bulk method, and reveals information on the bulk structure of the catalyst and its support. Measurements were used to identify the prepared pure Pt, bimetallic and ternary nanoparticles. It can be seen from (**Figure 6.1**) that all the peaks in the XRD pattern of pure Pt were well indexed to Pt (discussed in Chapter 4 and Chapter 5) with high crystallization. As the ternary nanoparticles are formed, all the peaks in the XRD patterns of PtRuTe nanoparticles are shifted slightly to larger 2θ values (right shift) with respect to the pure Pt, indicating the decreased d spacing and contraction of the lattice constant, due to the incorporation of increasing amounts of the smaller metal atoms into the Pt fcc lattice. No Pt or other metal peaks appear, indicating that ternary nanostructures or alloys were formed. It was also observed that the diffraction peaks for PtIrTe nanoparticles did not shift to higher values, in itself an indication that not all of Ir and Te formed alloy with Pt. PtRuTe nanoparticles showed no apparent peaks corresponding to the hexagonal-close-pack (hcp) phase of the Ru element. The Pt element being a much larger size atom it therefore exhibits a more pronounced signal pattern than that of the small size Ir, Ru and Te atom counterpart. It can also be as a result of the incorporation of the relative small size of the Ir, Ru and Te atom into the fcc structure of Pt indicating an alloy formation between Pt and Ir, Ru, Te. Diffraction peaks corresponding to RuO_2 (101), (200) and (211) were observed as shown by the arrows in (**Figure 6.1**). This is due to the formation of different crystalline structure which also promotes the formation of ruthenium oxides and improves alloying. However, it should be emphasized that the intensity of RuO_2 is considerably very weak, in itself an indication that RuO_2 is present only in small quantities. Diffraction peaks corresponding to Te were also observed and shown by an arrow. The peak at 2θ 39.6°and 40.3°, 46.6°, 67° and 69.02°, 84.18° and 85.7° can be assigned to the (111), (200), (220),(311) and (222) crystalline planes of face centred cubic (fcc) PtIrTe and PtRuTe nanoparticles respectively, which indicates that the nanoparticles are composed of pure crystalline Pt. The XRD was commonly employed to calculate the mean particle size of the electrocatalyst nanoparticles material using Scherrer's equation explained in chapter 3, and using the platinum diffraction peak (111). The strongest and sharpest diffraction peak for PtIrTe and PtRuTe at around 2θ = 39.6°, 40° and 40.3° respectively is indexed as (111).

$$D = \frac{0.9\,\lambda}{\beta(2\theta)\cos\theta} \qquad (6.1)$$

The catalyst showed relatively small particle size which is known to enhance the electrochemical surface area of the catalyst. Lattice parameter was calculated using the following equation:

$$a_{fcc} = \frac{\sqrt{2}\lambda}{\sin\theta} \qquad (6.2)$$

The calculated values of the average particle size and lattice parameter are presented in (**Table 6.1**) below. The is a slight decrease of lattice parameter between PtIrTe and PtRuTe nanoparticles which proves that essentially intermixing was complete to form ternary nanoparticles [58, 147].

Catalyst	**Particle size (nm)**	**Lattice parameter (a_{fcc}) (nm)**
PtNP	0.018	2.085
PtIrNP	1.297	5.157
PtRuNP	2.084	5.132
PtTeNP	2.198	5.182
PtIrTeNP	1.378	6.432
PtRuTeNP	1.457	6.325

Table 6. 1: Summary of average particle size and lattice parameter of PtIrTeNP and PtRuTeNP electrocatalysts obtained from XRD measurements.

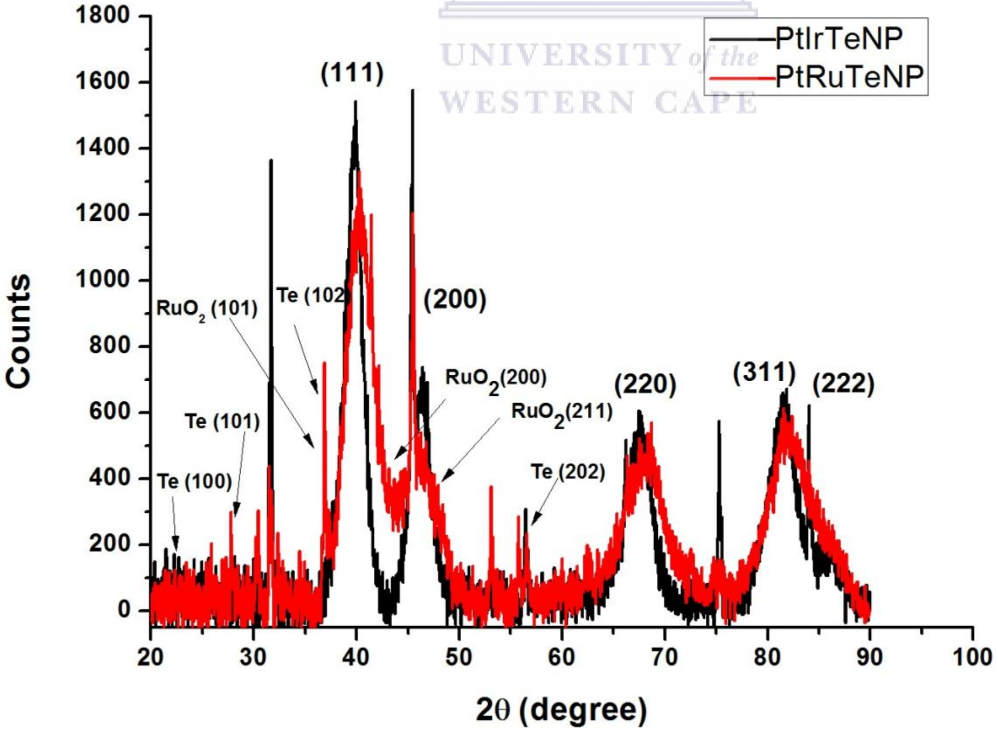

Figure 6. 1: XRD pattern of PtIrTe and PtRuTe nanoparticles for electrocatalysis.

In fine nanocrystals capped with large number of PVP molecules, each PVP molecule chemisorbs with its oxygen atom in the ring. In large nanocrystals are capped by small number of PVP molecules, each PVP molecule chemisorbs with both oxygen and nitrogen atom in the ring, which obviously affect the structure of PVP molecule and even result in breaking of involved C-N bonds of some chemisorbed PVP molecule. FTIR spectrum in (**Figure 6.2)** shows the IR spectra in the 400–4500 cm^{-1} range of PVP capped PtIrTe and PtRuTe nanoparticles; the broad absorption band centered at 3377 cm^{-1} (PtRuTeNP) and 3394 cm^{-1} (PtIrNP) is attributed to O-H stretching mode of H_2O absorbed on the surface of the product. The most striking evidence from FTIR spectrum of the PVP stabilized Pt is the broad peak between 1288 cm^{-1} and 1638 cm^{-1} which corresponds to C-N stretching motion and C=O stretching motion of monomer for PVP, respectively. The narrow absorption peak centered at 1420 cm^{-1} and 2880 cm^{-1} occurred in (**Figure 6.2)** is ascribed to the C–H bonding due to the presence of PVP. This may be due to the formation of coordinate bond between the nitrogen atom of the PVP and the Pt^{2+}, Ir^{3+}, Ru^{3+} and Te^{2+} ions [42, 68, 99]. These results showed that PVP chemisorbs with its oxygen atom in the ring, the charge transfer during electrochemical studies will occur from the chemisorbed PVP ligand to the nanoparticles.

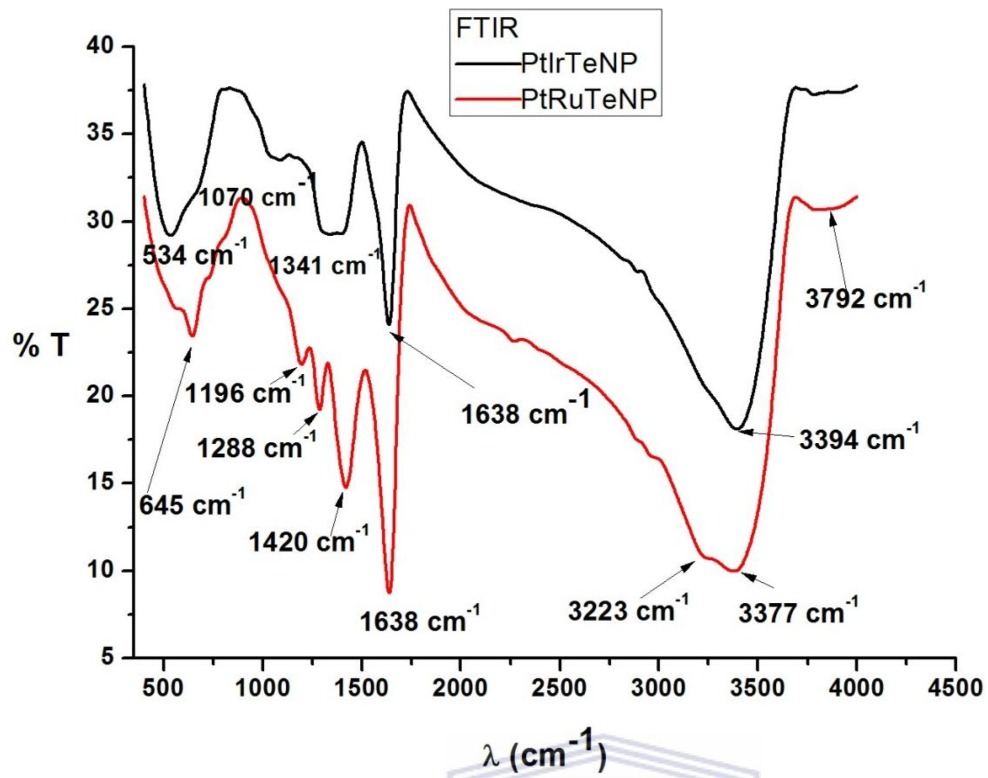

Figure 6. 2: FTIR spectrum for PtIrTe and PtRuTe nanoparticles.

In **(Figure 6.3)** shows the UV-visible spectra of PtIrTe and PtRuTe nanoparticles, there is no absorption peaks observed for Ir^{3+}, Ru^{3+}, Te^{+} ions. The peaks disappeared after reduction of the salts indicating that the metal ions were completely reduced. The synthesised nanoparticles showed no absorption peaks indicating a complete reduction of the metal ions to zero-valent nanoparticles, exhibiting an exponential graph shape [67]. The colour of the solution turned from pale yellow to black also indicating complete reduction of metal ions.

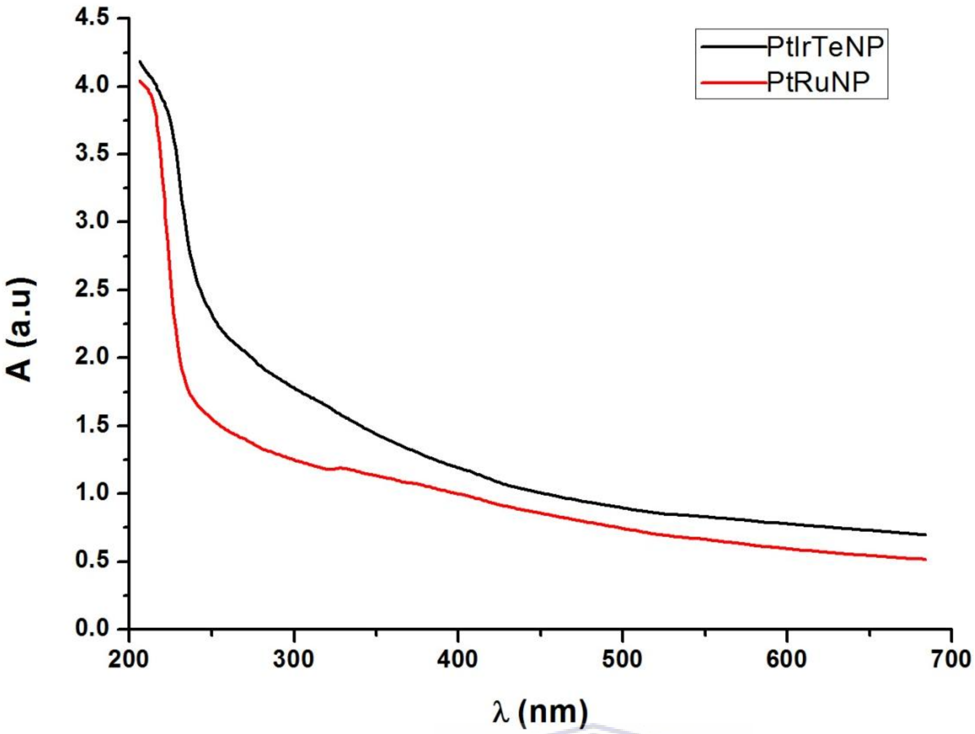

Figure 6. 3: UV-visible spectra of PtIrTe and PtRuTe nanoparticles.

6.1.2 Morphological Characterization by HRTEM and HRSEM

6.1.2.1 HRTEM and EDX for morphological characterization of PtIrNP, PtRuNP and PtTeNP.

HRTEM is one of the most important required methods for the characterization of nano material. It has the unique ability to prove the size, shape and crystallinity of the nanoparticles. (**Figure 6.4 [(a) and (c)]**) shows a HRTEM image of PtIrTe and PtRuTe nanoalloys drop coated onto copper grid, respectively. PtIrTe nanoalloys formed nanoclusters with no evidence of preferential surface orientation and therefore, the surface of the nanoalloys can be considered as polyoriented. Furthermore the PtRuTe nanoalloys were not aggregated, were dispersed uniformly with morphology of sphere shape and narrow size distribution. The uniformity of the catalyst particle distribution is known to be important factor for electro-catalytic activity.

The nanoparticles produced were found to be well dispersed; HRTEM images of a single particle (not shown) revealed atomic lattice fringes demonstrating the crystalline nature of the nanoparticles. Since the particle size and particle morphology greatly influences the electro-chemical activity of the catalyst owing to the relationship between catalytic activity and surface structure, HRTEM analysis of PtIrTe and PtRuTe nanoparticles electro-catalyst was therefore carried out before the comparison of its catalytic activity. It can be clearly observed that nanoparticles are poly-orientated which is in agreement with the results obtained in the XRD that PtIrTe and PtRuTe nanoparticles showed different diffraction patterns. The crystallite size L_v was determined using the simple Scherrer equation:

$$L_v = \varphi \frac{\lambda}{\text{FWHM} \cos \emptyset} \qquad (6.3)$$

Where L_v is the Scherrer length, φ is the shape factor (0.89 for spherical crystallite), λ the radiation wavelength (1.5406 Å), FWHM the full width at half-maximum, and θ the angle at the maximum intensity. Apparently Lv is extracted from the diffraction peak located close to $2\theta = 40°$, which corresponds to the (111) crystallographic plane of platinum. Antolini E et al (2007) reported is similar findings for ternary nanoalloys [9]. The average particle size for PtRuTe nanoparticles is 1.5 nm – 5 nm shows that the platinum nanoparticles clusters agglomerate to some extent, PtIrTe nanoparticles is 0.6 nm – 2 nm which shows that nanoparticles are agglomerated at some areas [87, 150, 175, 180].

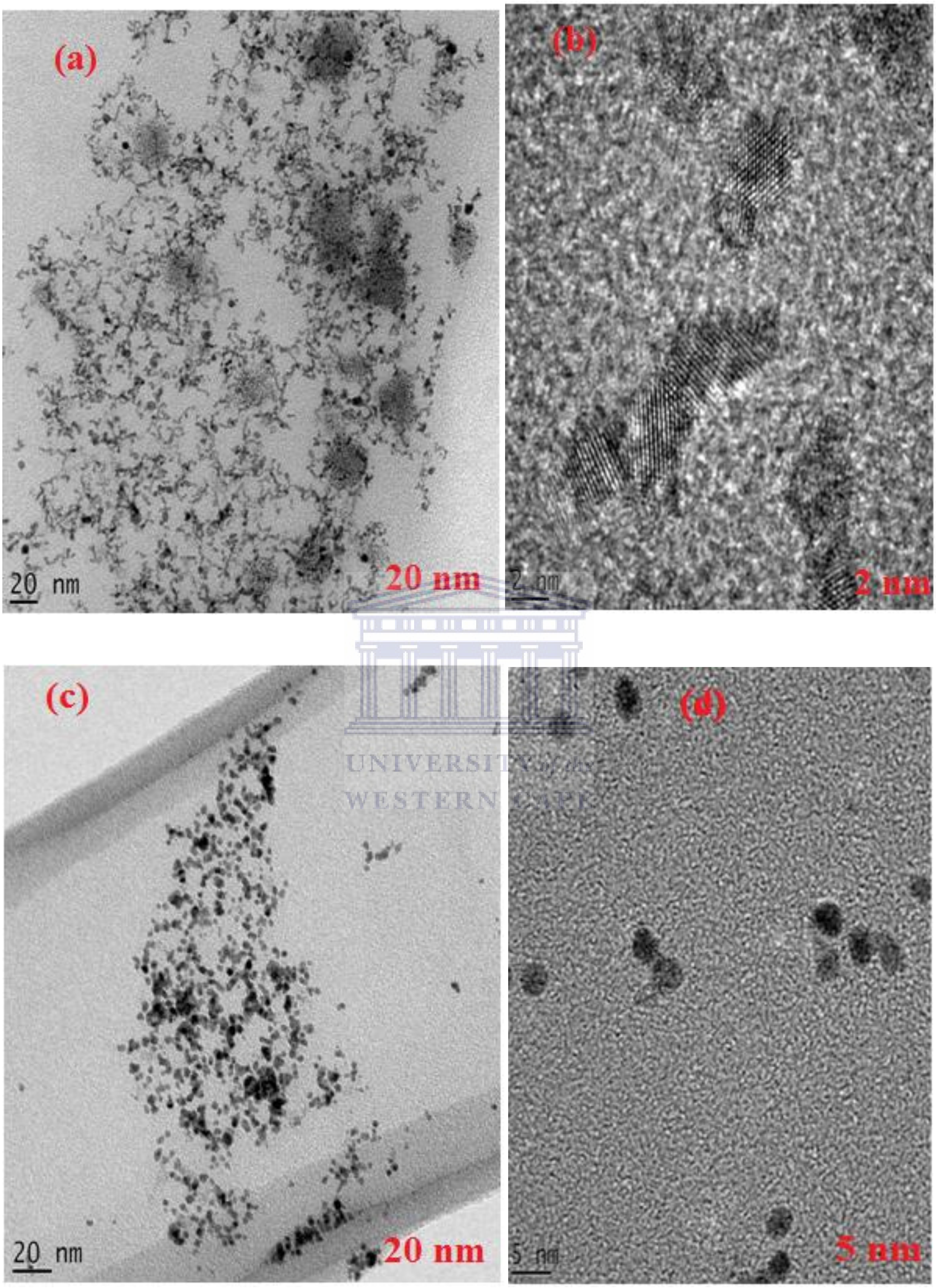

Figure 6. 4: HRTEM images of [(a) and (b)] PtIrTe nanoparticles and [(c) and(d)] PtRuTe nanoparticles.

Selected area electron diffraction pattern (SAED) shown in (**Figure 6.5**) for PtIrTe and PtRuTe nanoparticles shows characteristic electron diffraction rings of PtIrTe and PtRuTe, further indicating that the catalyst structure is made of nanoparticles. They exhibit a high crystallinity as can be deduced from the SAED pattern [**Figure 6.5 (a) and (b)**] which shows diffraction rings that are consistent with the presence PtIrTeNP and PtRuTeNP. The high crystallinity of the synthesised PtRuTe nanostructures is also evidenced which reveals well-defined (0 0 2) lattice fringes.

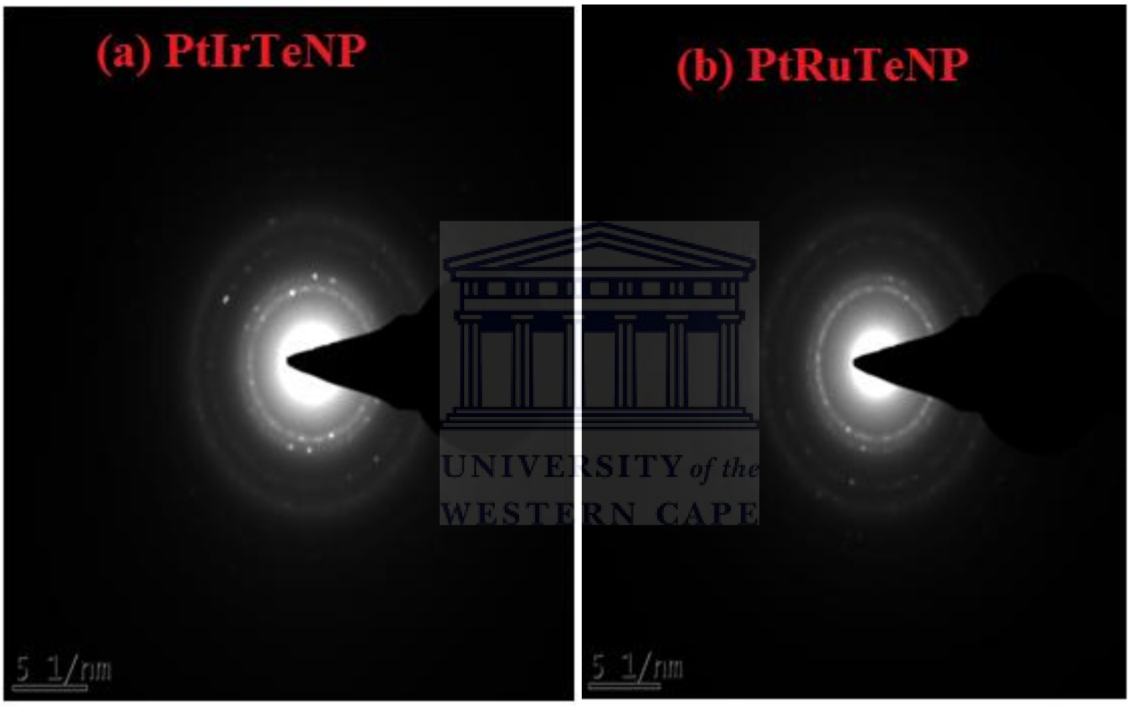

Figure 6. 5: Selected area electron diffraction pattern (SAED) of PtIrTe and PtRuTe nanoparticles.

EDX to investigate elemental composition of prepared nanoalloys, measurements of (**Figure 6.6 [(a) and (b)])** revealed that all three elements are present PtMeTe (Me = Ir, Ru) in the nanoparticles system respectively. However other elemental signals were recorded namely oxygen and copper, the presence of oxygen is due to the presence of PVP in the nanoalloys while copper is a result of copper grid onto which the nanoalloys are immobilized for HRTEM analysis. **Figure 6.6 (a)** In the case of PtIrTe EDX was employed to determine the atomic composition of the sample due to the overlapping of the Pt and Ir signals. The Ir signal could not be observed. **Figure 6.6 (b)** the bulk atomic compositions are very close to the nominal composition as expected from the synthesis of ternary nanoparticles.

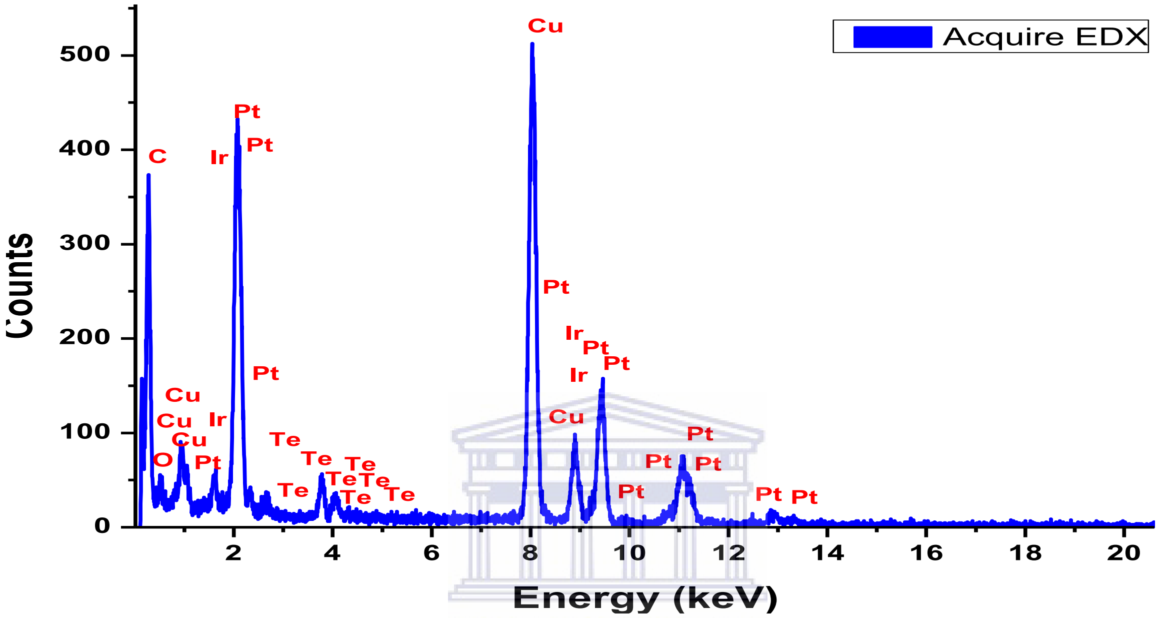

Figure 6. 6 (a): Energy dispersive x-ray spectrum of PtIrTe nanoparticles.

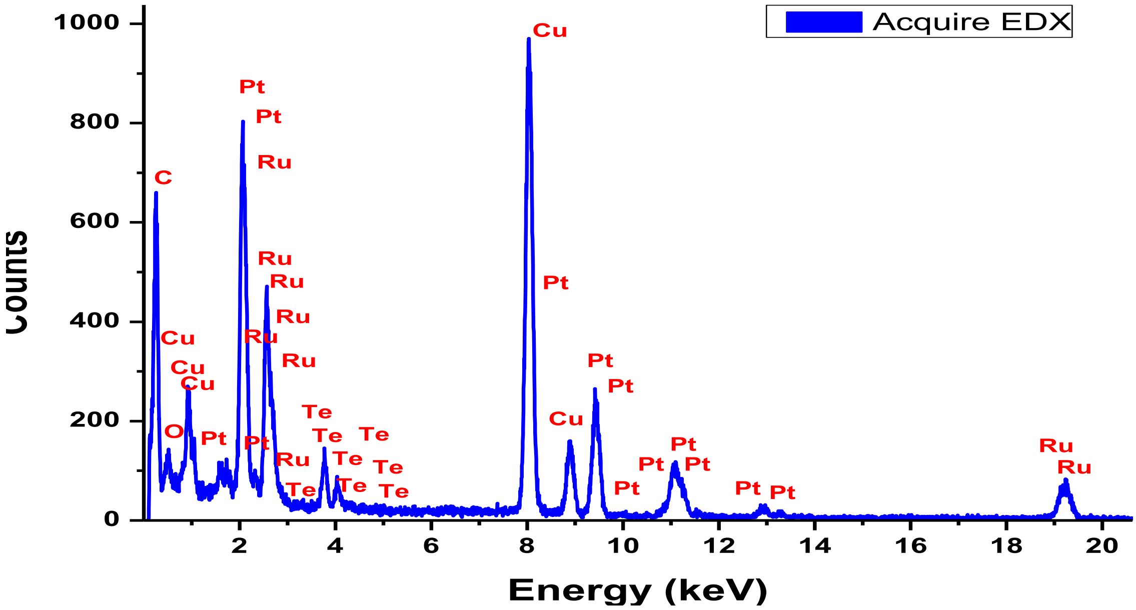

Figure 6.6 (b): Energy dispersive x-ray spectrum of PtRuTe nanoparticles.

6.1.2.2 HRSEM and EDS for morphological characterization of PtIrTeNP and PtRuTeNP.

The HRSEM image of the PtIrTeNP and PtRuTeNP shown in (**Figure 6.7 [(a) to (d)]**) reveals that the nanoparticles were well dispersed as small, spherical and uniform bright spots on the carbon support. In order to verify the particle size of the deposited nanoparticles, HRSEM analyses was carried out for all the nanoparticles, which were prepared by depositing PtIrTe and PtRuTe nanoparticles onto a carbon support. In general, the particles exhibit uniform size and shape in general poly-orientated as observed using XRD and HRTEM. The PtIrTe and PtRuTe nanoparticles showed that the Pt was incorporated with Ir, Ru and Te because the shape of the nanoparticles changed in support of the information obtained for HRTEM that the nanoparticles were poly-orientated. They appear to be homogeneously distributed over the entire support surface. In the case shown the particles are approximately 23 nm in diameter for all different types of carbon electrode. The ternary platinum nanoparticles particle size, as seen in HRSEM images, is rather bigger than that which was calculated via XRD and HRTEM. This may be due to either the impossibility of observing small particles by HRSEM or because the observed particles are, in fact, aggregations of smaller particles. In order to overcome these short comings, HRTEM observations were made with the PtIrTe and PtRuTe nanoparticles on Cu grid as a means of characterisation. In an FCC unit cell the atoms touch along the face diagonals and the lattice parameter may be calculated from the following equation;

$$4\mathrm{r} = \mathrm{a}(2)^{1/2} \quad (6.4)$$

Where r is the radius of PtIrTeNP = 3.919 x 10^{-3} nm and PtRuTeNP = 3.875 x 10^{-3} nm

For the hcp close packing arrangement, the lattice parameters a (=b) and c may be calculated from the radius as follows using equations 6.5 and 6.6:

$$a = 2r \qquad (6.5)$$

and

$$2a = \left[\left({}^{a}/_{\sqrt{3}}\right)^2 + \left({}^{c}/_{2}\right)^2\right]^{1/2} \qquad (6.6)$$

The lattice parameter a = 1.108 x 10^{-2} nm for PtIrTe and a = 1.096 x 10^{-2} nm which they both favour FCC closed packing nanoparticles [139].

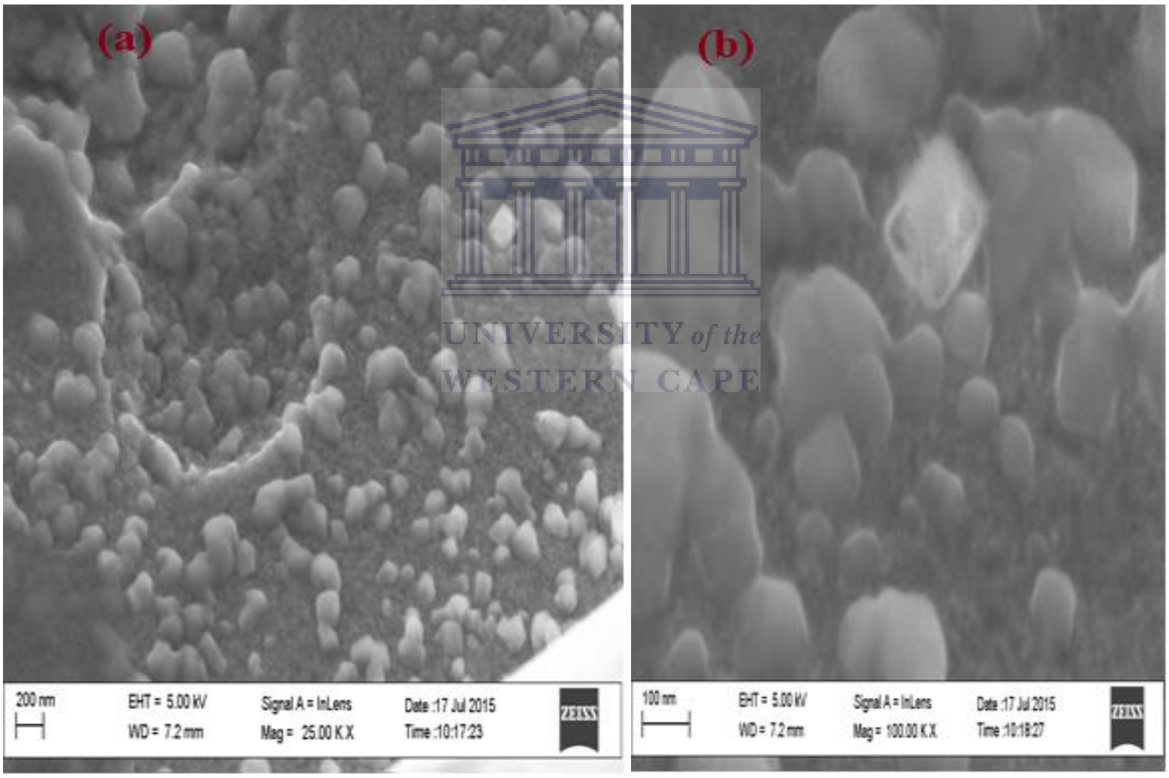

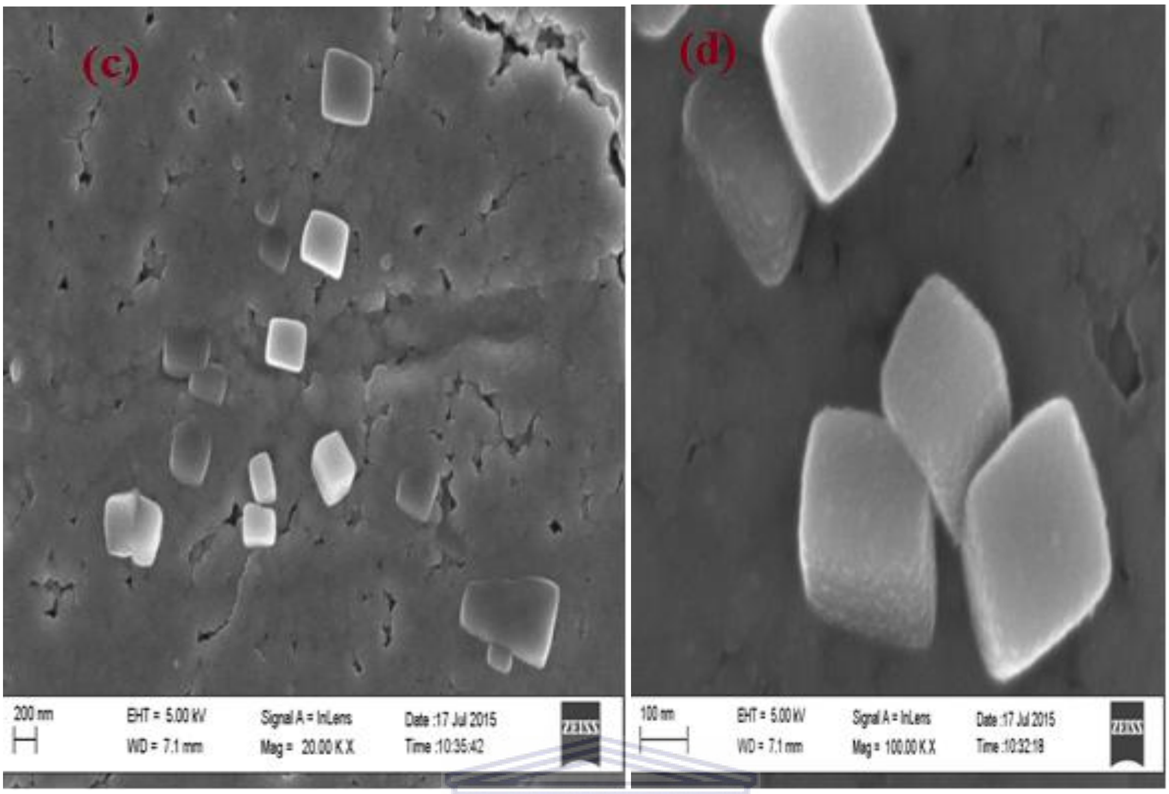

Figure 6. 7: HRSEM images of PtIrTe nanoparticles [(a) and (b)] and PtRuTe nanoparticles [(c) and (d)].

6.1.3 Electrochemical characterization of PtIr, PtRu and PtTe nanoparticles by CV, SWV and EIS

6.1.3.1 Electrochemical characterization of PtIrNP, PtRuNP and PtTeNP in 0.5 M H_2SO_4

In (**Figure 6.8 [(a) and (b)]**) the base voltammograms clearly evidence the cleanliness of the surface of the nanoparticles. The characteristic voltammograms for platinum electrodes are reported with different orientations in contact with the solution and that for the electrode with a polyoriented surface. Electrochemistry provides some surface sensitive reactions that can be used as a tool to characterise the surface structure. In the case of platinum based metal, it is known that the so-called hydrogen adsorption/desorption process is very sensitive to the Pt surface structure and this fact is put in evidence as shown in the voltammetric profiles in (**Figure 6.8)**. The potential window for all the nanoparticles was -200 mV to +1500 mV with a scan rate of 50 mV.s^{-1}, (a) PtIrTeNP showed three redox peaks there was oxidation of Ir(0) to Ir (III), Pt to PtO and Te to $HTeO_2$. Further oxidation to TeO_2. At peak (I) with peak potential of 1280 mV the oxidation peak of Ir (III), PtO, $HTeO_2$ followed by further oxidation to TeO_2 and reduction peak of Ir (III) , PtO and TeO_2 to Ir, Pt and Te is peak (I') and (II') with peak potential of 1055 mV and 350 mV. This proved that the nanoparticles are pure and suitable for electrocatalysis of ammonia. Further more in (**Figure 6.8 (b)**) PtRuTeNP showed three redox peaks with oxidation peak (I) at peak potential 1291 mV for PtO, Ru (III) and TeO_2 with reduction peaks (I') and (II') at peak potential 1055 mV and 377 mV to Pt (0), Ru(0) and Te (0). Both of the nanoparticles are clean and can be used in the electrocatalysis of ammonia in alkaline medium for application in fuel cells [15, 40, 47, 54, 58-59, 62]. Antolini E et al [9, 10] reported on PtRu were tested for methanol or ethanol to improve CO tolerance. Literature findings regarding ternary nanoparticles containing PtRu can be summarized as follows; PtRuMo and PtRuW, Mo and W in a catalyst are in an oxide form and do not form ternary alloy [9, 10]. Herbani Y et al [78] reported that AuPtAg capped with PVP for electrooxidation of ammonia. A small number of articles report on ternary nanoparticles applied for ammonia oxidation, HRTEM nanoparticles crystalline were not phase segregated [78].

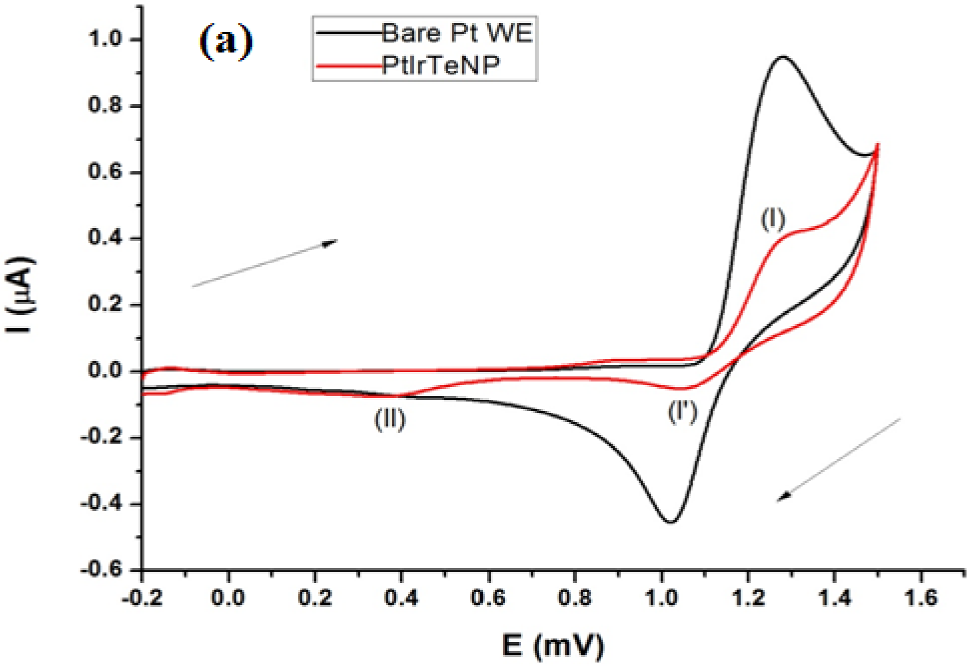

Figure 6. 8 (a): Cyclic voltammograms of (a) PtIrTe nanoparticles modified on Pt electrode; Test solution, 0.5 M H_2SO_4: Scan rate, 50 mV.s^{-1}.

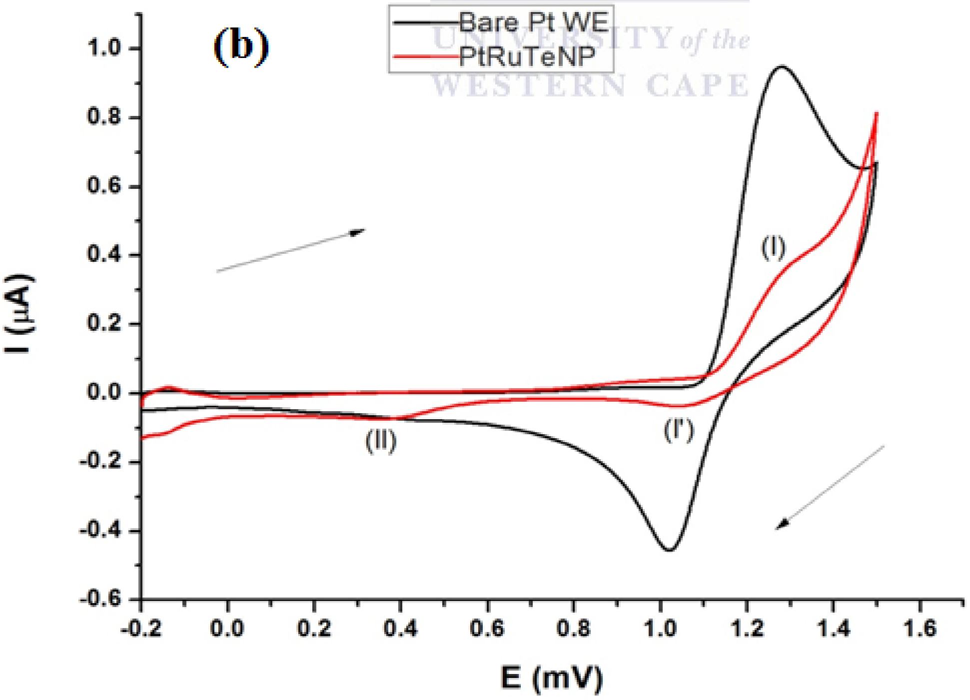

Figure 6.8 (b): Cyclic voltammograms of (b) PtRuTe nanoparticles modified on Pt electrode; Test solution, 0.5 M H_2SO_4: Scan rate, 50 mV.s^{-1}.

To study the kinetics of the electrode system the experiments were conducted using CV curves at different scan rates from 4 to 100 mV.s^{-1} in a 0.5 M H_2SO_4 medium. The PtIrTe and PtRuTe nanoparticles electrocatalyst in 0.5 M H_2SO_4 displayed good reactivity in the potential window -200 mV to +1500 mV from the scan rate was 4 till 100 mV.s^{-1}, respectively in (**Figure 6.9 [(a) and (b)]**). The increase in the current density with the increase in the potential scan rate is attributed to the excitation signal caused during the charging of the interface capacitance by the charge transfer process. The presence of a platinum base metal catalyst, the absorption can be assumed to promote the formation of the electro-catalytically active phase of PtO. Hence, this indicates that the electrochemical catalytic behaviour of the catalyst, but also related to the catalyst surface composition. Choose to show PtIrTe nanoparticles as representative nanoparticles for calculation of kinetics of the electrode; PtRuTe nanoparticles gave similar kinetics as PtIrTeNP. The anodic peak (I_{pa}) and cathodic peak current (I_{pc}) for PtIrTe nanoparticles electrode is linearly dependent on the scan rate (υ) gave a regression equation I_{pa} (I) = -0.199 x + (-29.762) (R^2 = 0.986) and I_{pc} (II) = 0.103 x + 0.670 (R^2 = 0.998). This revealed that the electrode contained a thin electroactive surface bound catalyst film; the kinetic process that controls the peak is diffusion controlled reaction. This was confirmed by plotting log of cathodic current against the log of scan rate which gave a slope of 0.532 and 0.498 for PtIrTe and PtRuTe nanoparticles respectively. Based on plotting peak potential against log scan rate the reduction of PtIrTe and PtRuTe nanoparticles behaved in an irreversible manner ($I_{pa}/I_{pc} \neq 1$ and $\Delta E_p > 59$ mV). The number of electrons transferred was estimated by integrating CV of the reduction peak to obtain the amount of charge (C) involved in the reaction and substituting appropriately in the Laviron's equation. It showed that the nanoparticles electrochemistry is a one- electron process for PtIrTe and PtRuTe nanoparticles respectively [15, 40, 47, 54, 58-59, 62].

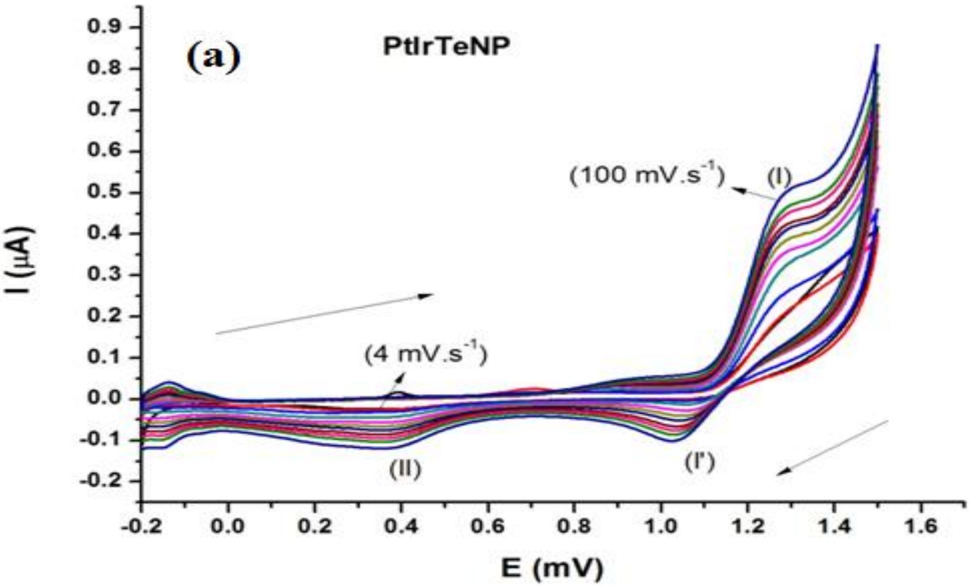

Figure 6. 9 (a): Cyclic voltammogram in test solution 0.5 M H_2SO_4 of (a) PtIrTe nanoparticles modified on Pt electrode at different scan rates; 4, 6, 10, 20, 30, 40, 50, 60, 70, 80, and 100 mV.s^{-1} respectively.

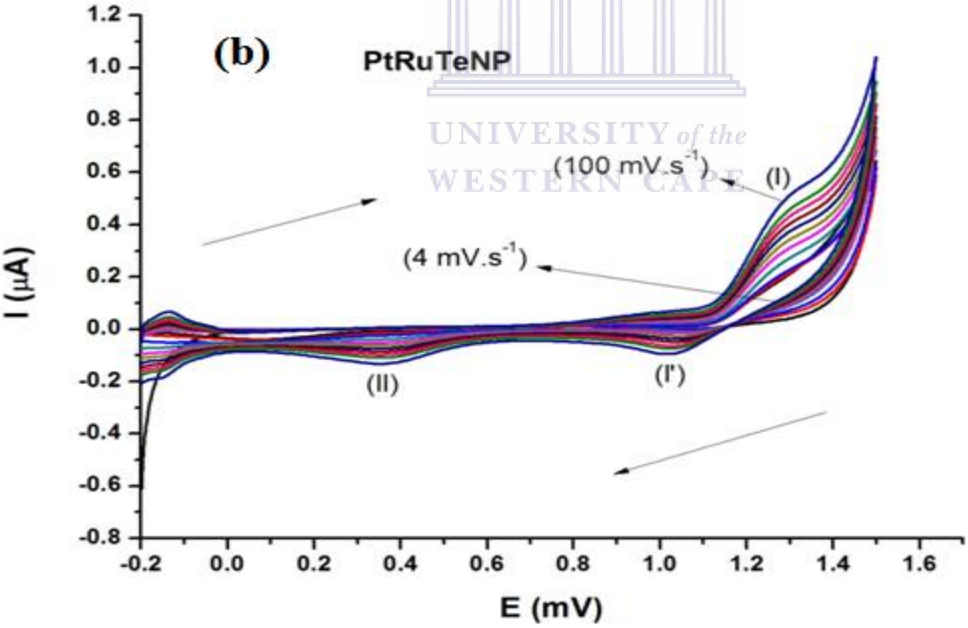

Figure 6.9 (b): Cyclic voltammogram in test solution 0.5 M H_2SO_4 of (b) PtRuTe nanoparticles modified on Pt electrode at different scan rates; 4, 6, 10, 20, 30, 40, 50, 60, 70, 80, and 100 mV.s^{-1} respectively.

Randles-Sevčik equation was used to study the kinetics of the electrode, in Figure 6.10 indicated that the electrochemical reaction rate is fast and oxidation of Pt to PtO, Ir (0) to Ir (III), Ru (0) to Ru (III) and Te (0) to TeO_2 and the reduction of PtO on Pt, Ir (0) to Ir, Ru (III) to Ru (0), TeO_2 to Te (0) electrode is a typical diffusion-controlled process. A linear relationship between $E_{pa,\,c}$ and log v was obtained, indicated the oxidation reduction of PtIrTe and PtRuTe was an irreversible electrode process.

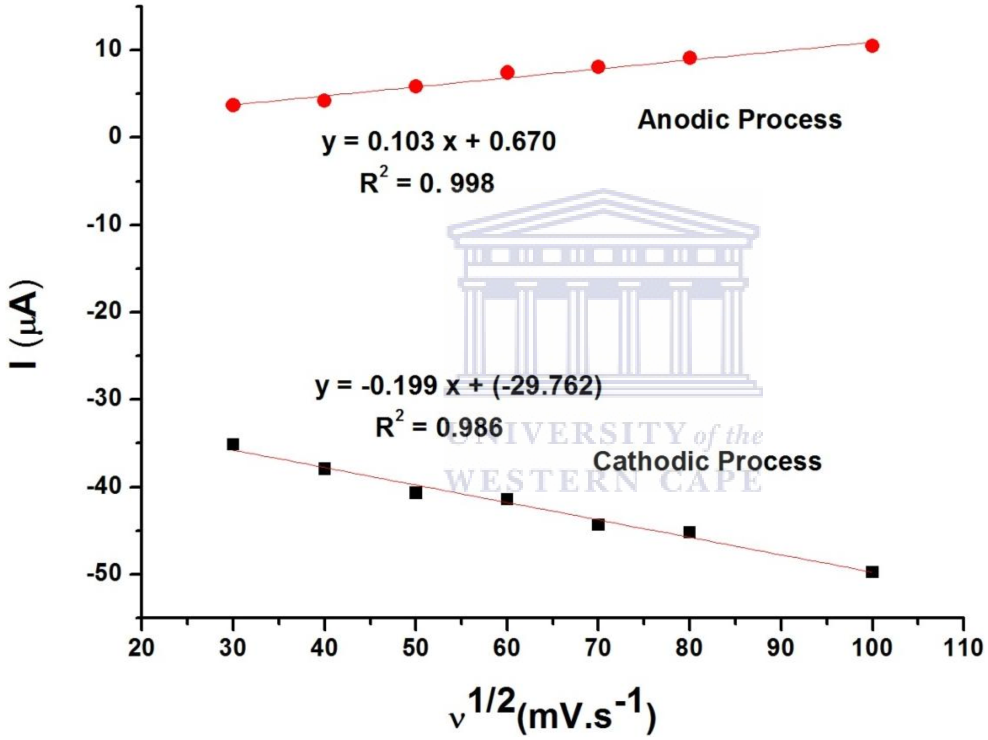

Figure 6. 10: Randles-Sevčik plot of PtIrTe nanoparticles for peaks I and I'. Conditions are as in Figure 6.9 (a).

6.1.3.2 Electrochemistry of the PtIrTe and PtRuTe nanoparticles for oxidation of ammonia in 1 M KOH

Typical cyclic voltammetry of PtIrTe electrocatalyst is shown in (**Figure 6.11 (a))** were ammonia oxidation was carried out in 0.5 M NH_4OH + 1 M KOH at room temperature, with a scan rate of 50 mV.s^{-1}. The CVs are recorded over a potential range of -1000 mV and +400 mV; the solid black curves are in the absence of NH_3 as a reference. The following peaks observed in (**Figure 6.11 (a)**) at peak (I/I´) and (II/II´) are due to the one of the properties of Pt which is the ability to adsorb on its surface, and absorb, within its lattice, hydrogen. Ammonia oxidation starts at lower potential -402 mV on PtIrTe catalyst if compared to Pt nanoalloys and most bimetallic reported in literature. Peak (III) can be related to the different possible Pt, Ir and Te oxidation states, where Pt^0 is oxidized to Pt^{2+} and form platinum oxide layer, Ir^0 to Ir^{3+} and the initial dissolution of tellurium led to accumulation of $HTeO_2^+$ cation in solution at the electrode surface. Subsequent solid TeO_2 formation can be observed in Peak (IV) with a potential of -119 mV [77]. It is important to observe that reduction peak (IV' and III') of the ternary nanoalloys. (**Figure 6.12 (a))** the oxidation peaks that were observed in the CV of the PtIrTe in the presence of ammonia were confirmed with SWV due to its high sensitivity. (**Figure 6.11 (b))** show clear oxidation peaks at (III) of PtRuTe with an over potential of -375 mV that is lower than that of PtIrTe nanoalloys. The peak current of PtIrTe nanoalloys is 2.401 x 10^{-4} A which is higher than that of the PtRuTe nanoalloys of 1.258x10^{-5} A. The overpotential of ammonia oxidation increased with the addition of Te to PtIr nanoalloys than that of PtRu, which indicated the oxidation was facilitated by that reason. This is interesting observation since PtIr had better catalytic activity due to lower over potential as compared to PtRu. These results indicate that addition of Te to the binary nanoalloys to form ternary nanoalloys has advantages for ammonia electro-oxidation. Recent studies have shown that bimetallic electrodes have promising catalytic activity for ammonia oxidation. Te lowered poisoning of the surface by N_{ads} and improved the catalytic activity of PtRu due to the synergetic interaction between the three metals. (**Figure 6.12 (b))** is the SWV of PtRuTe to confirm the oxidation peaks of ammonia due to its high sensitivity [7, 9-10, 81-82, 162].

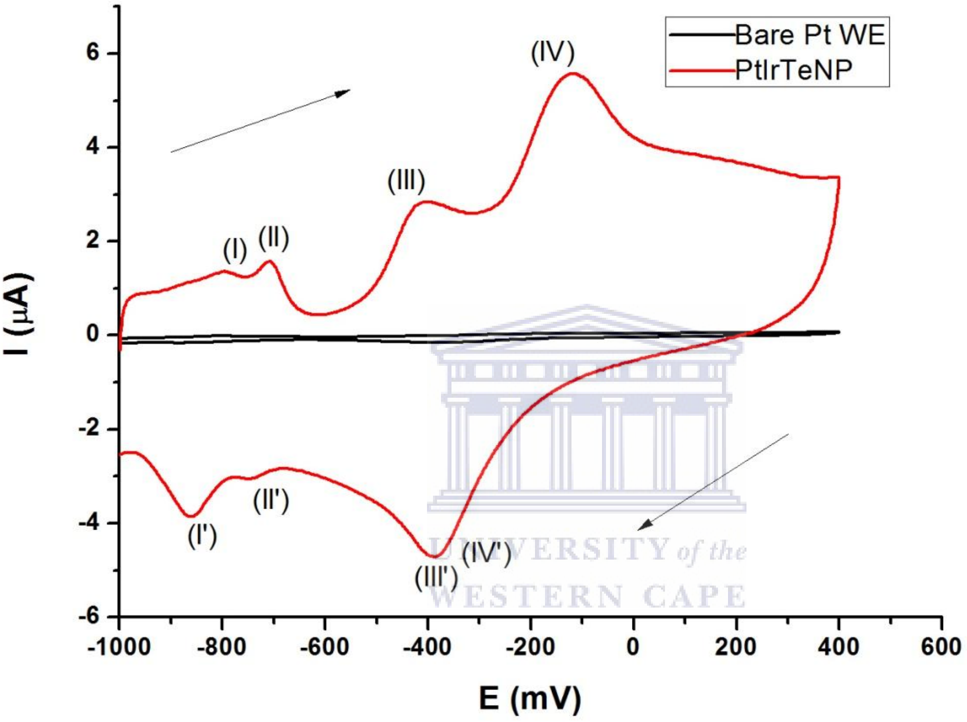

Figure 6. 11 (a): Cyclic voltammogram of PtIrTeNP electrode drop coated on Pt electrode in 0.5 M ammonia and 1 M KOH aqueous solution: Scan rate, 50 mV.s^{-1}.

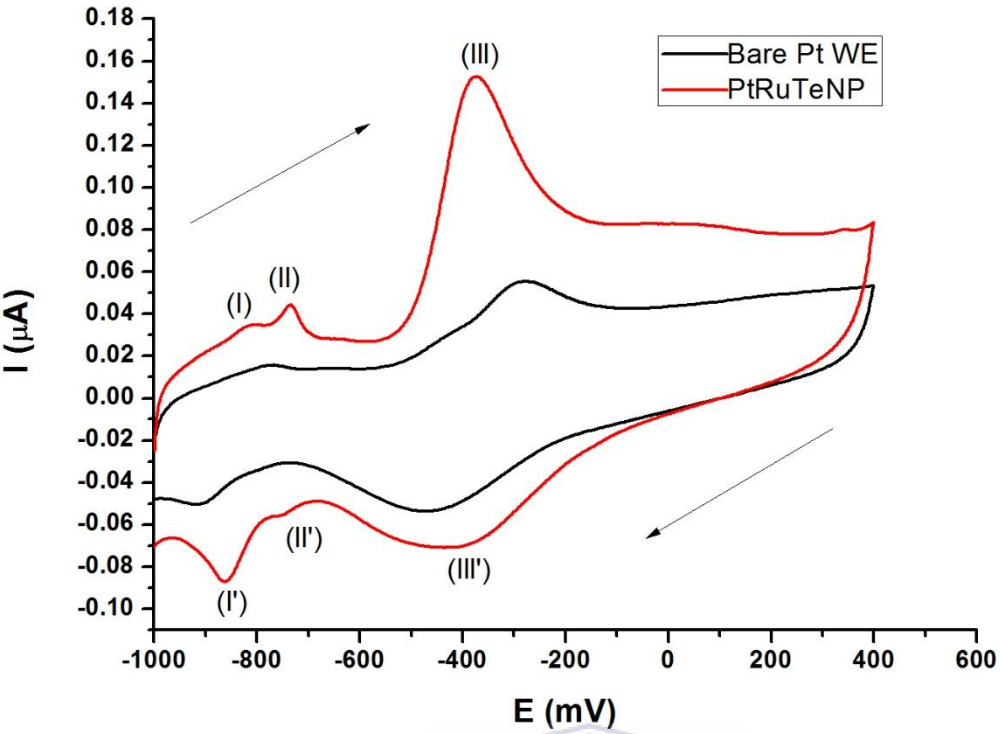

Figure 6.11 (b): Cyclic voltammogram of PtRuTeNP electrode drop coated on Pt electrode in 0.5 M ammonia and 1 M KOH aqueous solution: Scan rate, 50 mV.s^{-1}.

In (**Table 6.2**) PtIrTe nanoclusters were found to give slightly higher peak current and higher overpotential than PtRuTe. This can be explained by co-operative effects between Pt and the noble metals Ir and Te. These results showed that PtIrTe and PtRuTe nanoclusters are suitable electrocatalyst for ammonia oxidation based on their reduced overpotential and increased current properties. PtTe nanoparticles are found to give higher peak current than PtIr and PtRu nanoparticles. PtTe nanoparticles have lower over potential than PtIr and PtRu nanoparticles. PtIr nanoparticles were initially considered as a promising candidate for ammonia oxidation, now PtTe nanoparticles synthesised in this study gives much better results than PtIr and PtRu nanoparticles. The surface active sites of the Pt electrode were expected to become less available when coated with nanoparticles, the exact expectations were realised when nanoparticles were introduced to the electrode surface [7, 9-10, 81-82, 162].

Electrode	**E_{pa} (mV)**	**i_{pa} (A)**
PtNP	-431	1.726×10^{-4}
PtIrNP	-383	1.982×10^{-5}
PtRuNP	-402	2.342×10^{-5}
PtTeNP	-346	1.276×10^{-3}
PtIrTeNP	-405	2.401×10^{-4}
PtRuTeNP	-375	1.258×10^{-5}

Table 6. 2: Data points of oxidation of ammonia extracted from ternary nanoparticles (PtIrTe and PtRuTe) cyclic voltammetry in Figure 6.11 (a) and (b).

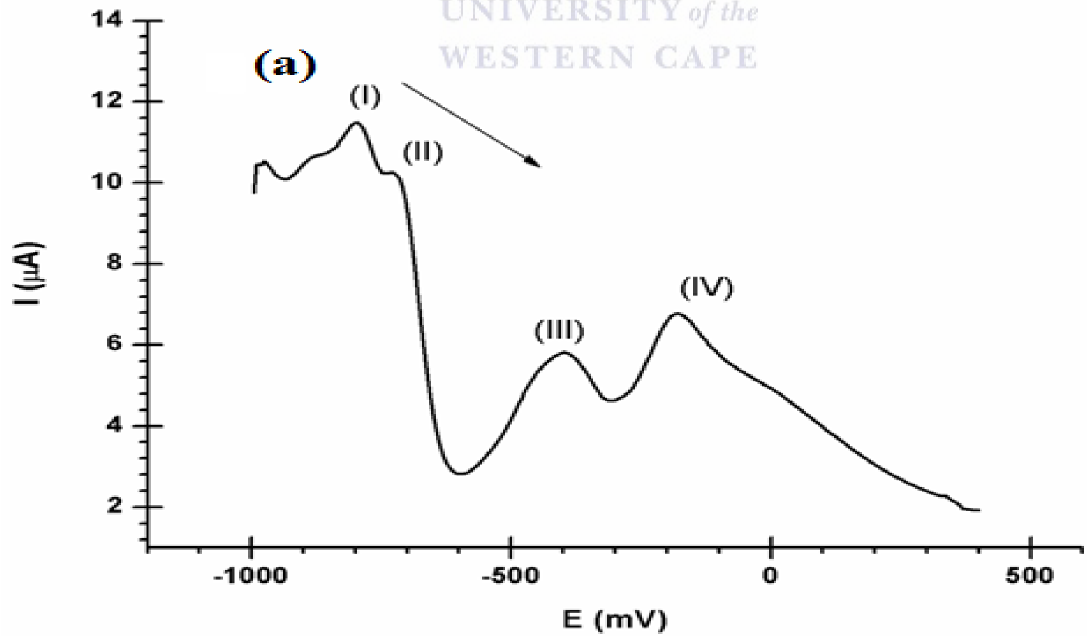

Figure 6. 12 (a): Square wave voltammetry of (a) PtIrTe nanoparticles drop coated on Pt electrode in 0.5 M ammonia and 1 M KOH aqueous solution: Scan rate, 50 mV.s^{-1}.

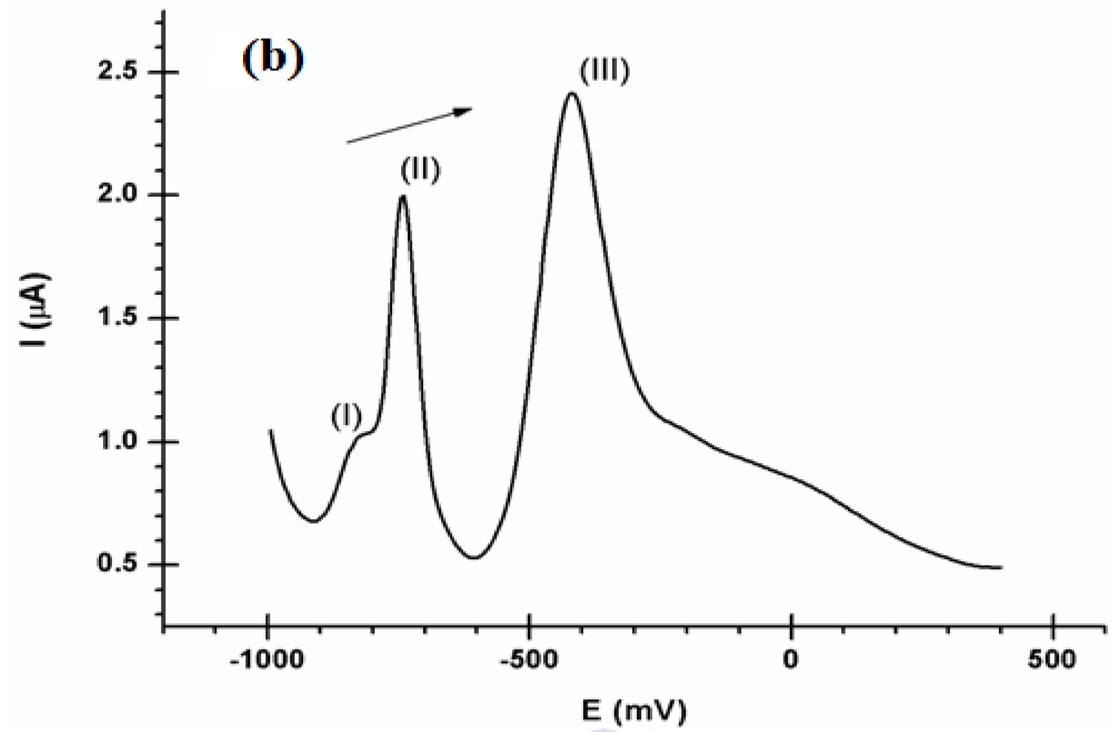

Figure 6.12 (b): Square wave voltammetry of (b) PtRuTe nanoparticles drop coated on Pt electrode in 0.5 M ammonia and 1 M KOH aqueous solution: Scan rate, 50 mV.s^{-1}.

The results of CV of ternary nanoalloys on Pt electrode in the potential window -1000 mV to +400 mV at different scan rates in 0.5 M NH_4OH + 1 M KOH are shown in (**Figure 6.13 [(a) and 6.13 (b)]**) for PtMeTe (Me = Ir, Ru), respectively. The anodic peak current (I_{pa}) of PtIrTe nanoalloy electrode is linearly dependent on the scan rate (υ) gave a regression equation $I_{pa\,(III)} = 2.332 \times 10^{-6} x + 96967 \times 10^{-5}$ ($R^2 = 0.998$); $I_{pa\,(IV)} = 6.088 \times 10^{-6} x + (-2.577 \times 10^{-5})$ ($R^2 = 0.989$). The anodic peak current of PtRuTe electrode versus scan rate gave the following regression equation $I_{pa} = 4.274 \times 10^{-8} x + 8.403 \times 10^{-6}$ ($r^2 = 0.999$). This revealed that the electrode contained a thin electroactive surface bound catalyst film, the kinetic process that controls the peak is diffusion and adsorption controlled reaction for PtIrTe nanoalloys and diffusion controlled reaction for PtRuTe nanoalloys. This was confirmed by plotting log of anodic current against the log of scan rate which gave a slope of 0.4683, 1.3377 for PtIrTe and 0.4729 for PtRuTe thus confirming the solid TeO_2 formed at potential -119 mV for PtIrTe is adsorption controlled. Based on plotting peak potential against log scan rate the reduction of PtIrTe and PtRuTe nanoalloys behaved in an irreversible manner ($I_{pa}/I_{pc} \neq 1$ and $\Delta E_p > 59$ mV). In order to estimate the number of electron transferred is due to the integration of the CV of the oxidation peak to obtain the amount of charge (c) involved in the reaction and substituting appropriately in the Laviron's equation. It showed that the nanoalloys electrochemistry is a one- electron process. The surface concentration (Γ) of PtIrTe was estimated to be 1.29 x 10^{-11} mol cm^{-2} which was found to be higher than the surface coverage of PtRuTe nanoalloys which was 2.82 x 10^{-13} mol cm^{-2} on Pt electrode, this Γ values in impedance analysis represents over 95% coverage. The electrochemical kinetics are shown in detail in (**Table 6.3)** below, the kinetics were calculated using Randles-Sevčik equation and Brown Anson model explained in (chapter 3) and the obtained results are summarised [7, 9-10, 81-82, 162]. Bagot et al [15] showed that PtRuOs, PtRuIr, PtRuPd and PtRuRh formed a nano alloys which showed excellent catalytic activity for methanol fuel cell application [15]. Hung et al [81-82] reported on PtPdRh which yielded good catalytic for fuel cell application [81-82]. The order of stability was reported as Pt > PtRuW, PtRuPd > PtRu. The steady state performance were found in the order PtRuW, PtRuPd > PtRu > Pt reported by Luo et al [114] and Zhang et al [191]. The results reported in this thesis for ternary nanoparticles yielded better catalytic activity than those reported in literature. Su et al [157] reported on TeBiPb applied for thermoelectric materials, it has never been reported in literature were Te was used to form ternary nanoparticles and applied for fuel cell. This ternary materials synthesised and applied for ammonia catalysis have not been reported in literature to date, this findings give an interesting point of view regarding ammonia fuel cells.

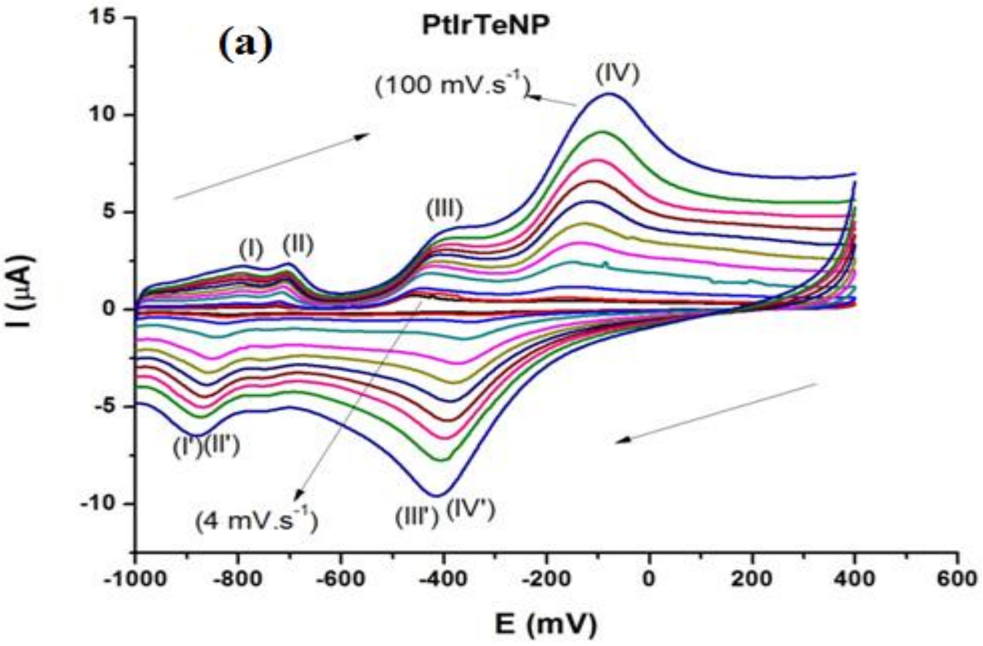

Figure 6. 13 (a): Cyclic voltammogram in solution 0.5 M ammonia and 1 M KOH of PtIrTe nanoparticles modified on Pt electrode at different scan rates; 4, 6, 10, 20, 30, 40, 50, 60, 70, 80, and 100 mV.s^{-1} respectively.

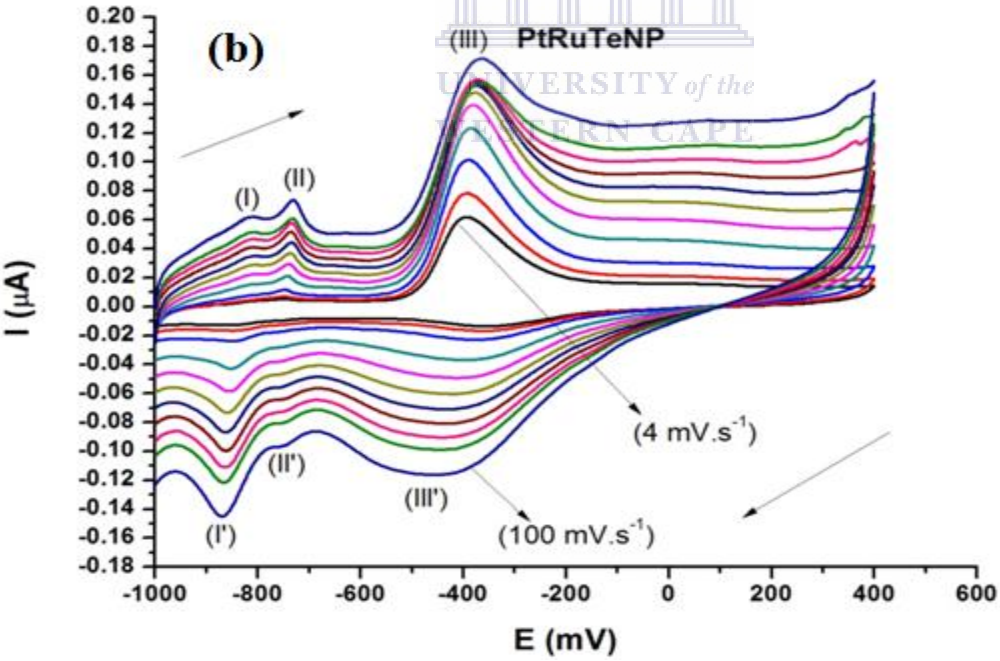

Figure 6.13 (b): Cyclic voltammogram in solution 0.5 M ammonia and 1 M KOH of PtRuTe nanoparticles modified on Pt electrode at different scan rates; 4, 6, 10, 20, 30, 40, 50, 60, 70, 80, and 100 mV.s^{-1} respectively.

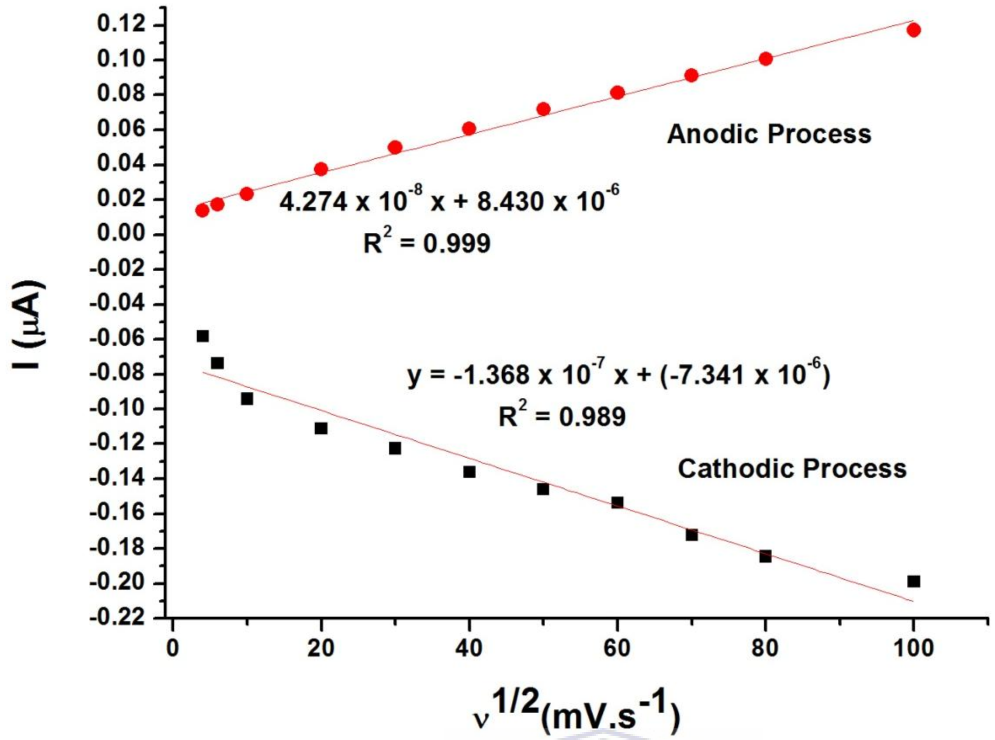

Figure 6. 14: Randles-Sevčik plot of PtRuTe for peaks III and III'. Conditions are as in Figure 6.13 (b).

Electrode	**n**	**α**	**Γ (mol.cm^{-2})**	**Kinetic process**	**Redox process**	**Diffusion coefficient (cm^{-2}.s^{-1})**
PtNP	1	0.5	1.09 x 10^{-11}	Diffusion	Irreversible	1.97 x 10^{-7}
PtIrNP	2	0.5	3.49 x 10^{-13}	Diffusion	Irreversible	1.08 x 10^{-5}
PtRuNP	1	0.5	1.35 x 10^{-12}	Diffusion	Irreversible	1.75 x 10^{-5}
PtTeNP	1	0.5	6.38 x 10^{-11}	Diffusion	Irreversible	1.58 x 10^{-4}
PtIrTeNP	1	0.5	1.29 x 10^{-11}	Diffusion	Irreversible	1.38 x 10^{-6}
PtRuTeNP	1	0.5	2.82 x 10^{-13}	Diffusion	Irreversible	2.05 x 10^{-6}

Table 6. 3: Electrochemical parameters of nanoalloy systems.

6.1.3.3 Electrochemistry impedance spectroscopy of the Pt nanoparticles for oxidation of ammonia in 1 M KOH

Electrochemical impedance is a powerful technique for investigating the kinetics of nano structured catalysts for electro-oxidation of ammonia for fuel cell application. The purpose of employing impedance spectra is to obtain the electrocatalytic activity in terms of charge-transfer resistance. Electrochemical impedance measurements of PtIrTe and PtRuTe nanoalloys catalysts at various formal potentials from -453 mV and -375 mV were performed in 0.5 M NH_4OH+ 1 M KOH solution. The charge transfer resistance (R_{ct}) of Nyquist semicircle as shown in (**Figure 6.15**) for PtIrTe (67645 Ω) which is higher than the R_{ct} for two semicircles for PtRuTe (35.3 Ω, 62030 Ω). This meant that the conductivity of the catalysts facilitated the flow of charge through the nanoalloys onto the surface of the electrode. This difference in charge transfer resistance revealed that PtRuTe nanoalloys had an obvious advantage in reaction activity. Kinetic parameters shown in (**Table 6.4**) of the electrode system were estimated to ascertain the catalytic and conductivity of the nanoalloys. The impedance parameters such as R_{ct} were obtained by fitting the equivalent circuit shown in (**Figure 6.16)** with fitting error less than 4 %. Charge transfer (I_0) and time constant (τ) for PtRuTeNP is higher than PtIrTeNP, these meant the flow of charge through the PtRuTeNP onto the surface of the electrode is faster than PtIrTeNP electrode [21, 73, 89, 188].

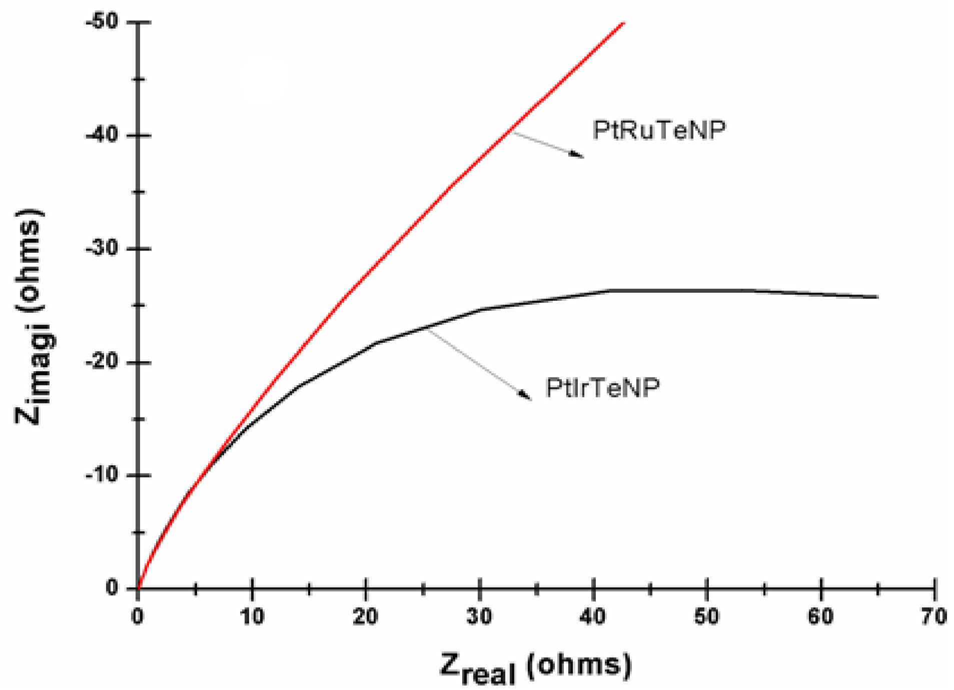

Figure 6. 15: Nyquist plot of the electrooxidation of 0.5 M ammonia on PtIrTe and PtRuTe nanoparticles in 1 M KOH.

The impedance data were fitted using the randles equivalent circuits shown in (**Figure 6.16)** depicts the equivalent circuit for the impedance depicts the equivalent circuit for the impedance spectra without pseudo-inductive behaviour, where R_1 is the solution resistance, R_{ct} is the charge-transfer resistance, and the constant phase element CPE2 is the electric double-layer capacitance used instead of a capacitor to account for the porous catalysts. A parallel constant-phase element (CPE1) and resistor R_2 and R_3 were added in series to fit the high frequency impedance data, which were attributed to a charge-transfer process at the outermost surface of the electrode [4].

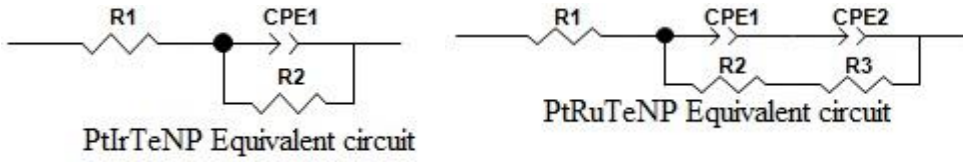

Figure 6. 16: Equivalent circuit PtIrTe and PtRuTe nanoparticles.

In (**Figure 6.17)** from the bode plot it is observed at low frequency PtRuTe nanoalloys have a higher total impedance as compared to PtIrTe, at higher frequencies the total impedance is more or less the same but with PtRuTeNP slightly high. Phase angle values for PtIrTeNP and PtRuTeNP is 72.09° and 71.29° respectively, showed semiconductor behaviour due to the presence of Te in the catalysts [115, 158].

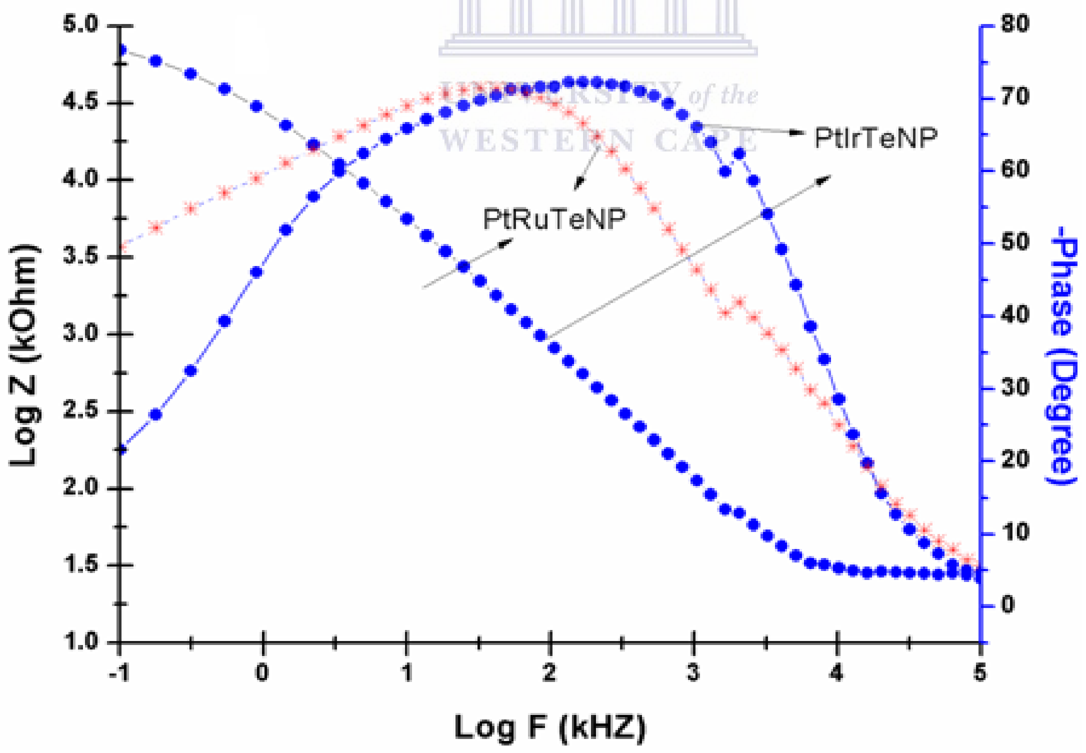

Figure 6. 17: Bode plot of 0.5 M ammonia on PtIrTe and PtRuTe nanoparticles in 1 M KOH.

Electrode	ω_{max} (HZ)	R_{ct} (Ω)	C_{dl} (μF)	Γ (s.rad^{-1})	I_0 (A)
Bare Pt	2635.73	2.0605×10^{6}	1.8413×10^{-10}	3.7939×10^{-4}	1.2×10^{-8}
PtNP	2635.73	1.943×10^{6}	1.9527×10^{-10}	3.7941×10^{-4}	1.3×10^{-8}
PtIrNP	2635.73	1.7707×10^{5}	2×10^{-9}	3.5414×10^{-4}	7.2×10^{-8}
PtRuNP	1329.65	91004	8×10^{-9}	7.2803×10^{-4}	2.82×10^{-9}
PtTeNP	2098.21	4.8323×10^{14}	9.8627×10^{-19}	4.7659×10^{-4}	6.19×10^{11}
		3.0507×10^{12}	1.5623×10^{-16}	4.766×10^{-4}	8.42×10^{-15}
PtIrTeNP	64214.15	67645	2.3021×10^{-10}	1.5572×10^{-5}	3.79×10^{-7}
PtRuTeNP	3310.92	35.3	8.556×10^{-6}	3.0203×10^{-4}	7.2743×10^{-4}
		62030	6×10^{-9}	3.7218×10^{-4}	4.13×10^{-7}

Table 6. 4: Kinetic parameters of modified Pt electrode with ternary nanoalloys.

6.1.4 Sub-conclusion

This chapter reports ternary nanoparticles were successfully formed and confirmed with XRD which yielded peaks patterns of PtRuTe nanoparticles which were shifted slightly to larger 2θ values (right shift) with respect to the pure Pt, indicating the decreased d spacing and contraction of the lattice constant, due to the incorporation of increasing amounts of the smaller metal atoms into the Pt fcc lattice. It was also observed that the diffraction peaks for PtIrTe nanoparticles did not shift to higher values, in itself an indication that not all of Ir and Te formed alloy with Pt. PtRuTe nanoparticles showed no apparent peaks corresponding to the hexagonal-close-pack (hcp) phase of the Ru element. The Pt element being a much larger size atom it therefore exhibits a more pronounced signal pattern than that of the small size Ir, Ru and Te atom counterpart. The particle size 1.378 nm and 1.457 nm for PtIrTe and PtRuTe nanoparticles and lattice parameters 6.432 nm and 6.325 nm respectively. FTIR and UV-vis were also used to further confirm the structure and the oxidation state of the nanoparticles. Morphological characterization further proved the nanoparticles were formed and poly-orientated. The particles sizes were determined by HRSEM were approximately 32 nm in diameter for all different types of carbon electrode. The ternary platinum nanoparticles particle size was rather bigger than that which was calculated via XRD. This was maybe due to either the impossibility of observing small particles by HRSEM or because the observed particles are, in fact, aggregations of smaller particles. To overcome the shortcoming presented by HRSEM it was necessary to introduce another technique which was HRTEM. The average particle size in HRTEM for PtRuTe nanoparticles was 1.5 nm – 5 nm showed that the platinum nanoparticles clusters agglomerate to some extent, PtIrTe nanoparticles was 0.6 nm – 2 nm which showed that the nanoparticles are agglomerated at some areas, which was in good agreement with XRD analysis. The voltammetric studies stated that PtRuTe nanoalloys showed a lower overpotential towards the electro-oxidation of ammonia as opposed to PtIrTe nanoalloys with a good current density which translated to better catalytic activity. Te lowered poisoning of the surface by N_{ads} and improved catalytic activity of PtRu due to the synergetic interactions. The kinetics from voltammetry was determined and it was found that both the catalytic nanoalloys were a one electron process reaction which showed irreversible properties. The surface concentration (Γ) of PtIrTe was estimated to be 1.29 x 10^{-11} mol cm^{-2} which was found to be higher than the surface coverage of PtRuTe nanoalloys which was 2.82 x 10^{-13} mol cm^{-2} on Pt electrode, this Γ values in impedance analysis represents over 95 % coverage. The stability test was performed to assess the reproducibility of the catalyst in order to further study the material using impedance studies; it was found both of the catalysts were stable. The Nyquist plot showed charge transfer resistance that revealed PtRuTeNP had an obvious advantage in reaction activity than PtIrTeNP. Bode plot phase angle analysis data confirmed that the catalysts are highly conductive semiconductors. The kinetic studies performed indicated the catalysts were found to exhibit high conductivity which facilitated the flow of charge through the nanoalloys to the electrode surface thus confirming their abilities as excellent ammonia electrocatalysts for hydrogen production.

CHAPTER 7

Summary

This chapter revisits the specific objectives of the study to report whether the aims of this dissertation were achieved and to give an overview of the success and shortcomings of the study. Also reported here is an indication of which areas of this study warrant further investigations in the future.

7.1 Conclusion

Clean energy supply and environmental protection are two major driving forces for the development of electrocatalysts for ammonia electro-oxidation. While ammonia-containing wastewater has a detrimental effect on the environment, ammonia provides a promising alternative for clean energy supply due to several interesting features, such as high hydrogen content, high energy density and well established ammonia distribution infrastructure. Electro-oxidation of ammonia has attracted much attention since it eliminates ammonia pollutants in wastewater and, furthermore, offers a significant advantage in cost and convenience as an alternative fuel for clean energy supply.

However, the widespread application of ammonia electrooxidation technologies has been largely hindered by the insufficient performance of the electrocatalysts and the requirement of the usage of high Pt loadings. Current efforts are underway to overcome these challenges by developing electrocatalysts with improved performance and lower Pt loading. The design of a high performance electrocatalyst for ammonia oxidation is closely related to the development of either new Pt-based electrocatalysts to improve activity and reduce Pt loading or Pt-free electrocatalysts. The objective of this study was to investigate and develop novel electrocatalysts that were highly specific and selective for production of hydrogen using ammonia as a fuel source, the main objective being enhancing the durability of the electro-catalyst. Telluride was, thus, chosen for this study as it possesses special properties such as good electronic, physical and mechanical properties which have made it to be proposed as replacement for the traditional transitional metals and metal oxides as alternate support for fuel cell catalysts. In addition, literature has revealed that electro-catalyst supported on these materials show improved activity and stability. However, it is well-known that all transitional metals and metal oxide materials suffer from nitrogen absorption under the operating conditions of the fuel cell, which in due time, leads to performance decrease due to accelerated loss of active surface area of the catalyst. In order to account for the instability of transitional metals and metal oxides, this study chose to investigate the possibility of conductive telluride on platinum group metals. The electrocatalysts were prepared binary and ternary nanoparticles from platinum group metals and telluride for ultra sensitivity for high performance fuel cell. It is confirmed from literature that the most researched binary nanoparticles for oxidation of ammonia for hydrogen production was binary PtIr and PtRu nanoparticles. They have short coming that is why in this study ultrasensitive Te was introduced to observe how that catalytic ability will be affected in the aim of searching for novel and better materials for application in ammonia oxidation for fuel cells application.

The nanoalloys were successfully synthesized and capped with poly vinyl pyrrolidone (PVP) the role or effect of stabilizers on particle size was due to the steric effect and chemical bonding. The stabilization of colloidal metal particles with polymer in water was often discussed by the adsorption of the polymer on the colloidal particles. These large adsorbates provided a steric barrier which prevented close contact of metal nanoclusters to each other as discussed in chapter 4 to 6. The interaction between the surface of the metal particles and the polymer was considered to be hydrophobic. However coordination of the polymer to metal particles has been proposed by the shift of the C=O stretching in the IR spectra of the PVP surrounding nanoparticles. It is reported that carbonyl group of PVP partly coordinate to the surface Pt, Ir, Ru and Te atoms. The study showed that particles which were stabilized by PVP were small and remains stabilized even after six months.

In (**Table 7.1**) x-ray diffraction (XRD) revealed that all prepared electro-catalysts possessed the face-centred-cubic structure of the poly-crystalline Pt. Peak shifts to higher values and increase in the lattice parameter were observed, confirming alloying of Ir, Ru and Te into the Pt structure to form binary and ternary alloy with Pt.

Catalyst	Particle size (nm)	Lattice parameter (a_{fcc}) (nm)
PtNP	0.018	2.085
PtIrNP	1.297	5.157
PtRuNP	2.084	5.132
PtTeNP	2.198	5.182
PtIrTeNP	1.378	6.432
PtRuTeNP	1.457	6.325

Table 7. 1: Summary of average particle size and lattice parameter of PtNP, PtIrNP, PtRuNP, PtTeNP, PtIrTeNP and PtRuTeNP electrocatalysts obtained from XRD measurements.

The structural characterization was further confirmed with FTIR and UV-vis and it was confirmed with FTIR the formation of binary and ternary nanoparticles capped with PVP. UV-vis was able to show the oxidation state of the nanoparticles by obtained an exponential graph shape which indicated complete reduction because there was no peak observed. Morphological characterization in the form of high resolution scanning electron microscope (HRSEM) revealed the formation of poly-orientated nanoparticles with average particle size of 23- 46 nm with slightly aggregated crystalline materials. The elemental composition of the alloy nanoparticles measured using energy dispersive spectroscopy (EDS) showed the presence of the four elements; Pt, Ir, Ru and Te. High resolution transmission electron microscopy (HRTEM) revealed the formation of crystalline non-aggregated 0.6-5 nm sized nanoparticles. The good agreement of the reported results with those previously published confirms that the electrocatalytic behaviour of 0.6-5 nm nanoparticles fits perfectly with that obtained with the corresponding bulk alloys. In this way, either surface properties such as hydrogen/anion adsorption–desorption or electrocatalytic activities toward ammonia oxidation are perfectly comparable for bulk and dispersed materials. This situation points out that no special size effects appear at this stage. The elemental composition of the alloy nanoparticles measured using energy dispersive X-ray (EDX) showed the presence of the four elements; Pt, Ir, Ru and Te. Selected area electron diffraction pattern (SAED) nanoparticles showed characteristic electron diffraction rings of Pt, PtIr, PtRu, PtTe, PtIrTe and PtRuTe, further indicating that the catalysts structures were made of nanoparticles.

Furthermore, the performance of direct ammonia fuel cells severely degraded by the accumulation of N_{ad} on the anode. This deterioration induced by N_{ad} accumulation could be recovered by the current loading treatment in hydrogen fuel. Throughout this study, it was clarified that the enhancement of electrocatalytic activity of the anodes was the important development strategy for the realization of direct ammonia fuel cells. Novel PVP capped PtTe, PtIrTe and PtRuTe were successfully synthesised and applied for electrocatalysis of ammonia for hydrogen production. The electrocatalytic behaviour of the PtIrTe and PtRuTe nanoparticles for ammonia oxidation in KOH solution showed reduced overpotential properties and an increased current density compared to the bare Pt nanoparticles electrode thus providing a promising alternative for development of low-cost and high-performance electrocatalyst for electro-oxidation of ammonia.

The results reported in this work demonstrate the importance of controlling the intrinsic structural properties of Pt nanoparticles; in terms of nature of the active sites and the effect of adding adatoms in order to understand their catalytic properties. Of all the electrocatalysts that were synthesised, PtTe nanoalloys were found to be the most active electrocatalyst in terms of maximising the oxidation of ammonia. In terms of minimising the ammonia oxidation overpotential, catalyst selection was ranked as follows PtTe > PtRuTe> PtIr > PtRu > PtIrTe> Pt. With regards to maximising the exchange current density, the ranking is PtTe > PtIrTe > Pt > PtRu > PtIr > PtRuTe as shown in (**Table 7.2)**. The results indicate that having novel tri-metallic and PtTe catalysts have advantages for ammonia electro-oxidation.

Electrode	**E_{pa} (mV)**	**i_{pa} (A)**
PtNP	-431	1.726×10^{-4}
PtIrNP	-383	1.982×10^{-5}
PtRuNP	-402	2.342×10^{-5}
PtTeNP	-346	1.276×10^{-3}
PtIrTeNP	-405	2.401×10^{-4}
PtRuTeNP	-375	1.258×10^{-5}

Table 7. 2: CV oxidation peak parameters Pt, PtIr, PtRu, PtTe, PtIrTe and PtRuTe nanoparticles in 0.5 M ammonia and 1 M KOH.

The above results provide convincing evidence, we believe, for the applicability of the Gerischer et al [72] mechanism for the ammonia oxidation on transition metal electrodes, and for the identification of N_{ads} as an inactive surface poison under electrochemical conditions.

A large body of work supports the mechanism first proposed by Gerischer and Mauerer in which the key intermediates are partly dehydrogenated ammonia molecules $NH_{x(ads)}$. However, a complete model of the reaction mechanism should also establish the identification of the active intermediates, i.e. the exact nature of the N_2 formation step [72]. It is clear that it must involve a hydrogenated nitrogen species, but its exact valence remains elusive. It seems that we may not even exclude a reaction of the type

$NH_{ads} + N_{ads} \rightarrow N_2 + H^+ + e^-$, i.e.

A step involving a hydrogenated surface species and atomic nitrogen, also the exact role of the co-adsorbing OH^- ions should be established. We believe that such a more detailed model would enable a better understanding and design of bimetallic and tri-metallic catalysts, such as platinum– iridium, platinum- ruthenium, platinum- telluride, platinum- iridium- telluride and platinum- ruthenium- telluride the activity of which is higher than of the individual metals. This kind of insight would also allow a pre-selection of test catalysts.

The kinetics and electrochemical conductivity for all the nanoparticles was determined as shown in (**Table 7.3**). In terms of minimising charge transfer resistance (R_{ct}) the nano catalysts selection were ranked as follows PtRuTe > PtIrTe > PtRu > PtIr > Pt > Bare Pt electrode > PtTe. That meant that the conductivity of the catalysts facilitated the flow of charge through the nanoalloys onto the surface of the electrode. This difference in charge transfer resistance revealed that PtRuTe and PtIrTe nanoalloys had an obvious advantage in reaction activity. The application of ternary metal nanoparticles has significantly enhanced the catalytic activity toward ammonia oxidation. The role of the third component (Te) was to help in reduction N_{ads} adsorption on Pt. The enhanced catalytic activity has been attributed by a number of factors including the change in Pt–Pt inter atomic distance, number of Pt nearest neighbours, Pt 5d band vacancy, and Pt metal content on particle surface.

Electrode	**ω_{max} (HZ)**	**R_{ct} (Ω)**	**C_{dl} (μF)**	**Γ (s.rad^{-1})**	**I_0 (A)**
Bare Pt	2635.73	2.0605×10^{6}	1.8413×10^{-10}	3.7939×10^{-4}	1.2×10^{-8}
PtNP	2635.73	1.943×10^{6}	1.9527×10^{-10}	3.7941×10^{-4}	1.3×10^{-8}
PtIrNP	2635.73	1.7707×10^{5}	2×10^{-9}	3.5414×10^{-4}	7.2×10^{-8}
PtRuNP	1329.65	91004	8×10^{-9}	7.2803×10^{-4}	2.82×10^{-9}
PtTeNP	2098.21	4.8323×10^{14}	9.8627×10^{-19}	4.7659×10^{-4}	6.19×10^{11}
		3.0507×10^{12}	1.5623×10^{-16}	4.766×10^{-4}	8.42×10^{-15}
PtIrTeNP	64214.15	67645	2.3021×10^{-10}	1.5572×10^{-5}	3.79×10^{-7}
PtRuTeNP	3310.92	35.3	8.556×10^{-6}	3.0203×10^{-4}	7.2743×10^{-4}
		62030	6×10^{-9}	3.7218×10^{-4}	4.13×10^{-7}

Table 7. 3: Kinetic parameters obtained from fitted equivalent circuit for monometallic, binary and ternary nanoparticles in 0.5 M ammonia and 1 KOH.

This study has addressed the issue of beneficiation of platinum group metals fully in terms of fuel cell application and has also devised means on how to save for cheaper and much more efficient catalysts. These are very much promising results for the future for successful advancement of fuel cell technology in South Africa and the scientific world at large.

7.1.1 Mono-metallic catalysts

- Sodium borohydride proved to be the best reducing agents by producing the most electrochemically active catalyst for ammonia oxidation capped with poly vinyl pyrrolidone (PVP).
- The synthesised platinum nanoparticles showed no absorption peaks during ultra violet visible spectroscopy, it showed an exponentially shaped graph indicating a complete reduction of the metal salts. The colour of the solution turned from pale yellow to dark brown then finally to black.
- X-ray diffraction confirmed that the platinum electro-catalysts possessed the face-centred-cubic structure of the poly-crystalline Pt with a particle size and lattice parameter as shown in (Table 7.1).
- Platinum nanoalloy catalyst are able to produce nano- sized particles in the range 2,1 to 5 nm therefore does possess a larger electrochemically active surface area with respect to its formation of nano-sized particles and polyoriented particle size distribution.
- In terms of minimising the ammonia oxidation overpotential platinum nanoalloys were ranked the least performing nanoalloys at -431 mV, with regards to maximising the exchange current density; platinum nanoalloys were ranked the third from the top most performing nanoalloys at 1.726 x 10^4 A shown in (Table 7.2).
- Performance of direct ammonia fuel cells severely degraded by the accumulation of N_{ad} on the anode, enhancement of electrocatalytic activity of the anodes was the important development strategy for the realization of direct ammonia fuel cells
- The electrochemical conductivity for platinum nanoalloys was determined in terms of minimising charge transfer resistance (R_{ct}) the nano catalysts selection were ranked at firth form the top performing nanoalloys. This difference in charge transfer resistance

revealed that platinum nanoalloys had an obvious disadvantage in reaction activity as shown in (Table 7.3)

- It was evident from the obtained results that monometallic nanoalloys are unable to address the issue of beneficiation of platinum as fuel cell electrocatalyst because of numerous short coming as discussed above.

7.1.2 Bimetallic catalysts

- The bimetallic nanoalloys catalyst synthesized can be used for ammonia oxidation as it proved effective in the removal of N_{ads}.
- PtIr, PtRu and PtTe catalyst synthesized via the variable-temperature programmed method does possess a larger electrochemically active surface area with respect to its formation of nano-sized particles and poly-orientated particle size distribution of 3.2-5 nm PtIr, 0.5-2 nm PtRu and 2.3-5 nm PtTe nanoalloys.
- X-ray diffraction (XRD) revealed that all prepared electro-catalysts the peak shifted to higher values and increase in the lattice parameter were observed, confirming alloying of Ir, Ru and Te into the Pt structure to form binary nanoalloy with Pt shown in (Table 7.1).
- The importance of controlling the intrinsic structural properties of Pt nanoparticles; in terms of nature of the active sites and the effect of adding adatoms in order to understand their catalytic properties.
- All of binary electrocatalysts that were synthesised, novel PtTe nanoalloys were found to be the most active electrocatalyst in terms of maximising the oxidation of ammonia. In terms of minimising the ammonia oxidation overpotential, catalyst selection was ranked as follows PtTe > PtIr > PtRu. With regards to maximising the exchange current density, the ranking is PtTe > PtRu > PtIr as shown in (Table 7.2).

- Electrochemical conductivity for all the nanoalloys was determined in terms of minimising charge transfer resistance (R_{ct}) the binary nano catalysts selection were ranked as follows PtRu > PtI r> PtTe. That meant that the conductivity of the catalysts facilitated the flow of charge through the nanoalloys onto the surface of the electrode as shown in (Table 7.3).
- The role of the introduction (Te) component to platinum has improved significantly in reduction N_{ads} adsorption on Pt. The enhanced catalytic activity has been attributed by a number of factors.
- The results indicate that having novel PtTe binary catalyst had advantages for ammonia electro-oxidation with short coming related to charge transfer resistance which indicated that the PtRu and PtIr nanoparticles had good conductivity as compared to PtTeNP. This necessitated the synthesis of ternary nanoalloys to observe how telluride will influence conductivity and electrocatalysis of nanoalloys.

7.1.3 Ternary catalysts

- The novel ternary nanoalloy catalyst PtIrTe and PtRuTe proved to be the most effective ternary catalyst for ammonia oxidation.
- Peak shifts to higher values and increase in the lattice parameter were observed during XRD analysis, confirming alloying of Ir, Ru and Te into the Pt structure to form ternary alloy with Pt.
- Nanocatalysts possess a large electrochemically active surface area with respect to its narrow particle size distribution and increased mass activity with PtIrTe nanoalloys with particle size of 0.6-2 nm and PtRuTe nanoalloys with particle size of 1.5-5 nm.
- Maximising the oxidation of ammonia by minimising the ammonia oxidation overpotential, catalysts selection was ranked as follows PtRuTe > PtIrTe, with regards

to maximising the exchange current density, the ranking is PtIrTe > PtRuTe. The results indicate that having novel tri-metallic and PtTe catalysts have advantages for ammonia electro-oxidation as shown in (Table 7.2).

- The kinetics and electrochemical conductivity for ternary nanoalloys was determined by means of minimising charge transfer resistance (R_{ct}) the nano catalysts selection were ranked as follows PtRuTe > PtIrTe . That meant that the conductivity of the catalysts facilitated the flow of charge through the nanoalloys onto the surface of the electrode.
- Charge transfer resistance revealed that PtRuTe and PtIrTe nanoalloys had an obvious advantage in reaction activity. The application of ternary metal nanoparticles had significantly enhanced the catalytic activity toward ammonia oxidation. The role of the third component (Te) has helped in reduction of N_{ads} adsorption on Pt. The enhanced catalytic activity had been attributed by a number of factors including the change in Pt–Pt inter atomic distance, number of Pt nearest neighbours, Pt 5d band vacancy, and Pt metal content on particle surface.
- Novel ternary nanoalloys (PtIrTe and PtRuTe) and PtTe have improved ammonia oxidation significantly and has performed much better than nanoalloys reported in literature to date.

7.2 Recommendations

The following further investigations are recommended as a follow up to the research activities and results obtained in this PhD study:

- The metal concentrations used previously in this research were in support of mass activity with an increased number of active sites where as in future the concentrations of the metal combinations could be varied and the optimum ratio could be determined.
- Investigate electrocatalytic behaviour preferentially oriented Pt group metals nanoalloy systems supported on multi-walled carbon nanotubes towards the oxidation of ammonia.
- Te showed good catalytic behaviour towards ammonia oxidation, it will be worth investigating the catalytic behaviour if a ternary metal is formed by Ag, Te and Pt as a base metal for oxidation of ammonia for fuel cell applications.

CHAPTER 8

8.1 References

1. Alagharu, V., S. Palanki, K.N. West, Analysis of ammonia decomposition reactor to generate hydrogen for fuel cell applications, Journal Power Sources. 195 (2010) 829-833.
2. Alvarez, J., J. Liu, E. Roman, A.E. Kaifer, Water-soluble platinum and palladium nanoparticles modified with thiolated [small beta]-cyclodextrin, Chemical Communications. 13 (2000) 1151-1152.
3. Amemiya, S., Scanning electrochemical microscopy in characterization of materials. 2002, John Wiley & Sons, Inc.
4. Amirudin, A., D. Thieny, Application of electrochemical impedance spectroscopy to study the degradation of polymer-coated metals, Progress in Organic Coatings. 26 (1995) 1-28.
5. Amphlett, J.L., G. Denuault, Scanning electrochemical microscopy (secm): An investigation of the effects of tip geometry on amperometric tip response, Journal of Physical Chemistry .B. 102 (1998) 9946-9951.
6. Ando, Y., K. Sasaki, R. Adzic, Electrocatalysts for methanol oxidation with ultra low content of Pt and Ru, Electrochemistry Communications. 11 (2009) 1135-1138.
7. Antoine, O., Y. Bultel, R. Durand, Oxygen reduction reaction kinetics and mechanism on platinum nanoparticles inside nafion, Journal of Electroanalytical Chemistry. 499 (2001) 85-94.
8. Antolini, E., Carbon supports for low-temperature fuel cell catalysts, Applied Catalysis B: Environmental. 88 (2009) 1-24.

9. Antolini, E., Platinum-based ternary catalysts for low temperature fuel cells: Part i. Preparation methods and structural characteristics, Applied Catalysis B: Environmental. 74 (2007) 324-336.

10. Antolini, E., Platinum-based ternary catalysts for low temperature fuel cells: Part ii. Electrochemical properties, Applied Catalysis B: Environmental. 74 (2007) 337-350.

11. Antolini, E., The stability of molten carbonate fuel cell electrodes: A review of recent improvements, Applied Energy. 88 (2011) 4274-4293.

12. Appleby, A.J., Chemistry, electrochemistry, and electrochemical applications | platinum group elements, in Encyclopedia of electrochemical power sources, J. Garche, Editor. 2009. Elsevier: Amsterdam. p. 853-875.

13. Appleby, A.J., Fuel cells – overview | introduction, in Encyclopedia of electrochemical power sources, J. Garche, Editor. 2009. Elsevier: Amsterdam. p. 277-296.

14. Atilgan, B., A. Azapagic, Life cycle environmental impacts of electricity from fossil fuels in turkey, Journal of Cleaner Production. 106 (2015) 555-564.

15. Bagot, P.A.J., A. Cerezo, G.D.W. Smith, 3d atom probe study of gaseous adsorption on alloy catalyst surfaces iii: Ternary alloys – no on Pt–Rh–Ru and Pt–Rh–Ir, Surface Science. 602 (2008) 1381-1391.

16. Baker, L., The evolving role of finance in south africa's renewable energy sector, Geoforum. 64 (2015) 146-156.

17. Bandarenka, A.S., M.T.M. Koper, Structural and electronic effects in heterogeneous electrocatalysis: Toward a rational design of electrocatalysts, Journal of Catalysis. 308 (2013) 11-24.

18. Baranova, E.A., C. Bock, D. Ilin, D. Wang, B. MacDougall, Infrared spectroscopy on size-controlled synthesized pt-based nano-catalysts, Surface Science. 600 (2006) 3502-3511.

19. Behling, N.H., Chapter 3 - history of alkaline fuel cells, in Fuel cells, N.H. Behling, Editor. 2013, Elsevier. p. 37-51.

20. Benito, P., V. Dal Santo, V. De Grandi, M. Marelli, G. Fornasari, R. Psaro, A. Vaccari, Coprecipitation versus chemical vapour deposition to prepare rh/ni bimetallic catalysts, Applied Catalysis B: Environmental. 179 (2015) 150-159.

21. Berce, P., S. Skale, M. Slemnik, Electrochemical impedance spectroscopy study of waterborne coatings film formation, Progress in Organic Coatings. 82 (2015) 1-6.

22. Bergbreiter, D.E., G.L. Parsons, Polymer-bound titanium olefin isomerization catalysts, Journal of Organometallic Chemistry. 208 (1981) 47-53.

23. Bernardis, F.L., R.A. Grant, D.C. Sherrington, A review of methods of separation of the platinum-group metals through their chloro-complexes, Reactive and Functional Polymers. 65 (2005) 205-217.

24. Bharadwaj, S.R., S. Varma, B.N. Wani, 16 - electroceramics for fuel cells, batteries and sensors, in Functional materials, S.B.K. Tyagi, Editor. 2012, Elsevier: London. p. 639-674.

25. Biswas, R., P. Deb, S. Das, Novel optoelectronic properties in barbed wire nanophotonic structures of indium telluride, Optical Materials. 47 (2015) 586-588.

26. Boggs, B.K., G.G. Botte, Optimization of Pt–Ir on carbon fiber paper for the electro-oxidation of ammonia in alkaline media, Electrochim. Acta. 55 (2010) 5287-5293.

27. Bond, G.C., Supported metal catalysts: Some unsolved problems, Chemical Society Reviews. 20 (1991) 441-475.

28. Bonitz, V.S., B.R. Hinderliter, G.P. Bierwagen, Random and systematic error as a function of sample area in electrochemical impedance spectroscopy data, Progress in Organic Coatings. 77 (2014) 2100-2106.

29. Bozbag, S.E., C. Erkey, Supercritical fluids in fuel cell research and development, J. Supercrit. Fluids. 62 (2012) 1-31.

30. Bradley, J.M., A. Hopkinson, D.A. King, Control of a biphasic surface reaction by oxygen coverage: The catalytic oxidation of ammonia over Pt{100}, The Journal of Physical Chemistry. 99 (1995) 17032-17042.

31. Brown, A.P., F.C. Anson, Cyclic and differential pulse voltammetric behavior of reactants confined to the electrode surface, Analytical Chemistry. 49 (1977) 1589-1595.

32. Bunce, N.J., D. Bejan, Mechanism of electrochemical oxidation of ammonia, Electrochimica Acta. 56 (2011) 8085-8093.

33. Buonomano, A., F. Calise, G. Ferruzzi, A. Palombo, Molten carbonate fuel cell: An experimental analysis of a 1 kw system fed by landfill gas, Applied Energy. 140 (2015) 146-160.

34. Candido, L., J.A.C.P. Gomes, Evaluation of anode materials for the electro-oxidation of ammonia and ammonium ions, Materials Chemistry and Physics. 129 (2011) 1146-1151.

35. Cao, T.F., Y.T. Mu, J. Ding, H. Lin, Y.L. He, W.Q. Tao, Modeling the temperature distribution and performance of a pem fuel cell with thermal contact resistance, International Journal of Heat and Mass Transfer. 87 (2015) 544-556.

36. Carden, A., M.D. Morris, Application of vibrational spectroscopy to the study of mineralized tissues (review), Journal of Biomedical Optics. 5 (2000) 259-268.

37. Carrette, L., K.A. Friedrich, U. Stimming, Fuel cells: Principles, types, fuels, and applications, ChemPhysChem. 1 (2000) 162-193.

38. Cassir, M., A. Ringuedé, V. Lair, 17 - molten carbonates from fuel cells to new energy devices, in Molten salts chemistry, F.L. Groult, Editor. 2013, Elsevier: Oxford. p. 355-371.

39. Chang, B.Y., S.M. Park, Electrochemical impedance spectroscopy, Annual Review of Analytical Chemistry. 3 (2010) 207-229.

40. Chang, S.H., M.H. Yeh, J. Rick, W.N. Su, D.G. Liu, J.F. Lee, C.C. Liu, B.J. Hwang, Bimetallic catalyst of ptir nanoparticles with high electrocatalytic ability for hydrogen peroxide oxidation, Sensors and Actuators B: Chemical. 190 (2014) 55-60.

41. Chellappa, A.S., C.M. Fischer, W.J. Thomson, Ammonia decomposition kinetics over Ni-Pt/Al_2O_3 for pem fuel cell applications, Applied Catalysis A: General. 227 (2002) 231-240.

42. Chen, L., W. Zhao, Y. Jiao, X. He, J. Wang, Y. Zhang, Characterization of ag/pt core-shell nanoparticles by uv–vis absorption, resonance light-scattering techniques, Spectrochimica Acta Part A: Molecular and Biomolecular Spectroscopy. 68 (2007) 484-490.

43. Chen, S., S. Lee, Top as ligand and solvent to synthesize silver telluride nanosheets, Materials Research Bulletin. 71 (2015) 30-36.

44. Chen, X., Y. Wang, L. Cai, Y. Zhou, Maximum power output and load matching of a phosphoric acid fuel cell-thermoelectric generator hybrid system, Journal of Power Sources. 294 (2015) 430-436.

45. Cheng, F., H. Ma, Y. Li, J. Chen, $Ni_{1-x}Pt_x$ (x = 0−0.12) hollow spheres as catalysts for hydrogen generation from ammonia borane, Inorganic Chemistry. 46 (2007) 788-794.

46. Chepuri , R.K., D.C. Rao, Trivedi., Chemical and electrochemical depositions of platinum group metals and their applications, Coordination Chemistry Review. 246 (2005) 613-631.

47. Choi, W.C., J.D. Kim, S.I. Woo, Quaternary pt-based electrocatalyst for methanol oxidation by combinatorial electrochemistry, Catalysis Today. 74 (2002) 235-240.

48. Climent, V., J.M. Feliu, Cyclic voltammetry, in Reference module in chemistry, molecular sciences and chemical engineering. 2015, Elsevier.

49. Coggon, J.A., G.M. Nowell, D.G. Pearson, T. Oberthür, J.P. Lorand, F. Melcher, S.W. Parman, The 190Pt–186Os decay system applied to dating platinum-group element mineralization of the bushveld complex, south africa, Chemical Geology. 302–303 (2012) 48-60.

50. Colindres, S.C., J.R.V. García, J.A.T. Antonio, C.A. Chavez, Preparation of platinum-iridium nanoparticles on titania nanotubes by mocvd and their catalytic evaluation, Journal of Alloys Compound. 483 (2009) 406-409.

51. Comotti, M., S. Frigo, Hydrogen generation system for ammonia–hydrogen fuelled internal combustion engines, International Journal of Hydrogen Energy. 40 (2015) 10673-10686.

52. Cox, B., K. Treyer, Environmental and economic assessment of a cracked ammonia fuelled alkaline fuel cell for off-grid power applications, Journal of Power Sources. 275 (2015) 322-335.

53. Crundwell, F.K., M.S. Moats, V. Ramachandran, T.G. Robinson, W.G. Davenport, Chapter 33 - production of flotation concentrates containing platinum-group metals, in Extractive metallurgy of nickel, cobalt and platinum group metals, F.K.C.S.M.R.G.R.G. Davenport, Editor. 2011, Elsevier: Oxford. p. 415-427.

54. de Vooys, A.C.A., M.T.M. Koper, R.A. van Santen, J.A.R. van Veen, The role of adsorbates in the electrochemical oxidation of ammonia on noble and transition metal electrodes, Journal of Electroanalytical Chemistry. 506 (2001) 127-137.

55. Deng, Q., M. Smetanin, J. Weissmüller, Mechanical modulation of reaction rates in electrocatalysis, Journal of Catalysis. 309 (2014) 351-361.

56. Denver, C., Ammonia as a hydrogen source for fuel cells: A review. 2012.

57. Dicks, A.L., Fuel cells – molten carbonate fuel cells | overview, in Encyclopedia of electrochemical power sources, J. Garche, Editor. 2009, Elsevier: Amsterdam. p. 446-453.

58. Ding, J., K.Y. Chan, J. Ren, F.S. Xiao, Platinum and platinum–ruthenium nanoparticles supported on ordered mesoporous carbon and their electrocatalytic performance for fuel cell reactions, Electrochimica Acta. 50 (2005) 3131-3141.

59. Domínguez-Domínguez, S., J. Arias-Pardilla, Á. Berenguer-Murcia, E. Morallón, D. Cazorla-Amorós, Electrochemical deposition of platinum nanoparticles on different carbon supports and conducting polymers, Journal of Applied Electrochemistry. 38 (2008) 259-268.

60. Doña Rodríguez, J.M., J.A. Herrera Melián, J. Pérez Peña, Determination of the real surface area of pt electrodes by hydrogen adsorption using cyclic voltammetry, Journal of Chemical Education. 77 (2000) 1195.

61. El-Nagar, G.A., M.S. El-Deab, A.M. Mohammad, B.E. El-Anadouli, Promoting effect of hydrocarbon impurities on the electro-oxidation of formic acid at pt nanoparticles modified gc electrodes, Electrochimica Acta. 180 (2015) 268-279.

62. Endo, K., K. Nakamura, Y. Katayama, T. Miura, Pt–Me (Me = Ir, Ru, Ni) binary alloys as an ammonia oxidation anode, Electrochimica Acta. 49 (2004) 2503-2509.

63. Engstrom, R.C., C.M. Pharr, Scanning electrochemical microscopy, Analytical Chemistry. 61 (1989) 1099-1104.

64. Falcão, D.S., V.B. Oliveira, C.M. Rangel, A.M.F.R. Pinto, Review on micro-direct methanol fuel cells, Renewable and Sustainable Energy Reviews. 34 (2014) 58-70.

65. Farooque, M.,H. Maru, Fuel cells – molten carbonate fuel cells | full-scale prototypes, in Encyclopedia of electrochemical power sources, J. Garche, Editor. 2009, Elsevier: Amsterdam. p. 508-518.

66. Feng, L., W. Cai, C. Li, J. Zhang, C. Liu, W. Xing, Fabrication and performance evaluation for a novel small planar passive direct methanol fuel cell stack, Fuel. 94 (2012) 401-408.

67. Forina, M., P. Oliveri, L. Bagnasco, R. Simonetti, M.C. Casolino, F. Nizzi Grifi, M. Casale, Artificial nose, nir and uv–visible spectroscopy for the characterisation of the pdo chianti classico olive oil, Talanta. 144 (2015) 1070-1078.

68. Formo, E., E. Lee, D. Campbell, Y. Xia, Functionalization of electrospun tio2 nanofibers with Pt nanoparticles and nanowires for catalytic applications, Nano Letters. 8 (2008) 668-672.

69. Franco-Junior, E., A.C.G. Lopes, H.B. Suffredini, P. Homem-de-Mello, Simple model to study heterogeneous electrocatalysts, Journal of Power Sources. 273 (2015) 360-367.

70. Ganesh, V., D. Latha Maheswari, S. Berchmans, Electrochemical behaviour of metal hexacyanoferrate converted to metal hydroxide films immobilized on indium tin oxide electrodes catalytic ability towards alcohol oxidation in alkaline medium, Electrochimica Acta. 56 (2011) 1197-1207.

71. Gemo, N., S. Sterchele, P. Biasi, P. Centomo, P. Canu, M. Zecca, A. Shchukarev, K. Kordas, T.O. Salmi, J.P. Mikkola, The influence of catalyst amount and pd loading on

the H_2O_2 synthesis from hydrogen and oxygen, Catalysis Science & Technology. 5 (2015) 3545-3555.

72. Gerischer, H., A. Mauerer, Untersuchungen zur anodischen oxidation von ammoniak an platin-elektroden, Journal of Electroanalytical Chemistry Interfacial Electrochemistry. 25 (1970) 421-433.

73. Gomadam, P.M., J.W. Weidner, Analysis of electrochemical impedance spectroscopy in proton exchange membrane fuel cells, International Journal of Energy Research. 29 (2005) 1133-1151.

74. Green Jr, L., An ammonia energy vector for the hydrogen economy, International Journal of Hydrogen Energy. 7 (1982) 355-359.

75. Habrioux, A., W. Vogel, M. Guinel, L. Guetaz, K. Servat, B. Kokoh, N. Alonso-Vante, Structural and electrochemical studies of Au–Pt nanoalloys, Physical Chemistry Chemical Physics. 11 (2009) 3573-3579.

76. He, L.L., P. Song, J.J. Feng, W.H. Huang, Q.L. Wang, A.J. Wang, Simple wet-chemical synthesis of alloyed PdAu nanochain networks with improved electrocatalytic properties, Electrochimica Acta. 176 (2015) 86-95.

77. He, Z., J. Chen, D. Liu, H. Zhou, Y. Kuang, Electrodeposition of Pt–Ru nanoparticles on carbon nanotubes and their electrocatalytic properties for methanol electrooxidation, Diamond& Related Materials. 13 (2004) 1764-1770.

78. Herbani, Y., T. Nakamura, S. Sato, Synthesis of platinum-based binary and ternary alloy nanoparticles in an intense laser field, Journal of Colloid and Interface Science. 375 (2012) 78-87.

79. Heying, B., S. Haverkamp, U.C. Rodewald, H. Eckert, S.C. Peter, R. Pöttgen, The germanides sctge (t = Co, Ni, Cu, Ru, Rh, Pd, Ag, Ir, Pt, Au) – structure and 45sc solid state nmr spectroscopy, Solid State Sciences. 39 (2015) 15-22.

80. Huang, Z.Z., S. Ye, W. Xia, Y.H. Yu, Y. Tang, Wittig-type olefination catalyzed by peg-telluride, The Journal of Organic Chemistry. 67 (2002) 3096-3103.

81. Hung, C.M., Complex ptpdrh nanoparticles: Synthesis, characterization, and performance in the electrocatalytic oxidation of ammonia, Powder Technology. 232 (2012) 18-23.

82. Hung, C.M., Electrochemical properties of ptpdrh alloy catalysts for ammonia electrocatalytic oxidation, International Journal of Hydrogen Energy. 37 (2012) 13815-13821.

83. Idowu, M., E. Lamprecht, T. Nyokong, Interaction of water soluble thiol capped cdte quantum dots and bovine serum albumin, Journal of Photochemistry and Photobiology A: Chemistry. 198 (2008) 7-12.

84. Jana, N.R., L. Gearheart, C.J. Murphy, Wet chemical synthesis of silver nanorods and nanowires of controllable aspect ratio, Chemical Communications, (2001) 617-618.

85. Janarthanan, R., A. Serov, S.K. Pilli, D.A. Gamarra, P. Atanassov, M.R. Hibbs, A.M. Herring, Direct methanol anion exchange membrane fuel cell with a non-platinum group metal cathode based on iron-aminoantipyrine catalyst, Electrochimica Acta. 175 (2015) 202-208.

86. Jensen, J.O., A.P. Vestbø, Q. Li, N.J. Bjerrum, The energy efficiency of onboard hydrogen storage, Journal of Alloys and Compounds. 446–447 (2007) 723-728.

87. Jinschek, J.R.,S. Helveg, Image resolution and sensitivity in an environmental transmission electron microscope, Micron. 43 (2012) 1156-1168.

88. Jishi, Z., W. Li, H. Xiangming, W. Chunrong, J. Changyin, Kinetic investigation of licoo2 by electrochemical impedance spectroscopy (eis), International Journal of Electrochemical Science. 5 (2010) 478-488.

89. Kashyap, D., P.K. Dwivedi, J.K. Pandey, Y.H. Kim, G.M. Kim, A. Sharma, S. Goel, Application of electrochemical impedance spectroscopy in bio-fuel cell characterization: A review, International Journal of Hydrogen Energy. 39 (2014) 20159-20170.

90. Kissinger, P.T., W.R. Heineman, Cyclic voltammetry, Journal of Chemical Education. 60 (1983) 702.

91. Koper, M.T.M., Structure sensitivity and nanoscale effects in electrocatalysis, Nanoscale. 3 (2011) 2054-2073.

92. Koponen, S.E., P.G. Gordon, S.T. Barry, Principles of precursor design for vapour deposition methods, Polyhedron.

93. Krogscheepers, C., S.J. Gossel, Input cost and international demand effects on the production of platinum group metals in south africa, Resources Policy. 45 (2015) 193-201.

94. Kundu, P.P., K. Dutta, 6 - hydrogen fuel cells for portable applications, in Compendium of hydrogen energy, M.B.B.N. Veziroğlu, Editor. 2016, Woodhead Publishing: Oxford. p. 111-131.

95. Kurzweil, P., History | fuel cells, in Encyclopedia of electrochemical power sources, J. Garche, Editor. 2009, Elsevier: Amsterdam. p. 579-595.

96. Kwak, J., A.J. Bard, Scanning electrochemical microscopy. Theory of the feedback mode Analytical Chemistry 61 (1989) 1221-1227.

97. Lan, R., J.T.S. Irvine, S. Tao, Ammonia and related chemicals as potential indirect hydrogen storage materials, International Journal of Hydrogen Energy. 37 (2012) 1482-1494.

98. Lan, R., S. Tao, Ammonia as a suitable fuel for fuel cells, Frontiers in Energy Research. 2 (2014).

99. Lee, H., S.E. Habas, S. Kweskin, D. Butcher, G.A. Somorjai, P. Yang, Morphological control of catalytically active platinum nanocrystals, Angewandte Chemie. 118 (2006) 7988-7992.

100. Lee, S.I., J. Kim, J.W. Son, J.H. Lee, B.K. Kim, H.J. Je, H.W. Lee, H. Song, K.J. Yoon, High performance air electrode for solid oxide regenerative fuel cells fabricated by infiltration of nano-catalysts, Journal of Power Sources. 250 (2014) 15-20.

101. Li, X., I.M. Hsing, The effect of the pt deposition method and the support on pt dispersion on carbon nanotubes, Electrochimica Acta. 51 (2006) 5250-5258.

102. Liang, H., H. Su, B.G. Pollet, S. Pasupathi, Development of membrane electrode assembly for high temperature proton exchange membrane fuel cell by catalyst coating membrane method, Journal of Power Sources. 288 (2015) 121-127.

103. Liang, K.C., F.M. Yeh, C.G. Wu, H.M. Lee, Gasoline production by dehydration of dimethyl ether with nh4-zsm-5 catalyst, Energy Procedia. 75 (2015) 554-559.

104. Liang, Y., M.L. Harrell, D.E. Bergbreiter, Using soluble polymers to enforce catalyst-phase-selective solubility and as antileaching agents to facilitate homogeneous catalysis, Angewandte Chemie International Edition. 53 (2014) 8084-8087.

105. Liu, J., C. Zhong, Y. Yang, Y.T. Wu, A.K. Jiang, Y.D. Deng, Z. Zhang, W.B. Hu, Electrochemical preparation and characterization of pt particles on ito substrate: Morphological effect on ammonia oxidation, International Journal of Hydrogen Energy. 37 (2012) 8981-8987.

106. Liu, W., L. Wan, J. Liu, M. Zhao, Z. Zou, Performance improvement of the open-cathode proton exchange membrane fuel cell by optimizing membrane electrode assemblies, International Journal of Hydrogen Energy. 40 (2015) 7159-7167.

107. Liu, Y., X.J. Jin, D.D. Dionysiou, H. Liu, Y.M. Huang, Homogeneous deposition-assisted synthesis of iron–nitrogen composites on graphene as highly efficient non-precious metal electrocatalysts for microbial fuel cell power generation, Journal of Power Sources. 278 (2015) 773-781.

108. Liu, Z., X.Y. Ling, X. Su, J.Y. Lee, Carbon-supported pt and ptru nanoparticles as catalysts for a direct methanol fuel cell, The Journal of Physical Chemistry B. 108 (2004) 8234-8240.

109. Lomocso, T.L., E.A. Baranova, Electrochemical oxidation of ammonia on carbon-supported bi-metallic PtM (M; Ir, Pd, SnO_x) nanoparticles, Electrochimica Acta. 56 (2011) 8551-8558.

110. Lordi, V., N. Yao, J. Wei, , Method for supporting platinum on single-walled carbon nanotubes for a selective hydrogenation catalyst, Chemistry of Materials. 13 (2001) 733-737.

111. Lototskyy, M.V., M.W. Davids, I. Tolj, Y.V. Klochko, B.S. Sekhar, S. Chidziva, F. Smith, D. Swanepoel, B.G. Pollet, Metal hydride systems for hydrogen storage and supply for stationary and automotive low temperature pem fuel cell power modules, International Journal of Hydrogen Energy. 40 (2015) 11491-11497.

112. Lovrić, M., Square-wave voltammetry, in Electroanalytical methods, F. Scholz, et al., Editors. 2010, Springer Berlin Heidelberg. p. 121-145.

113. Lowndes, D.H., C.M. Rouleau, T. Thundat, G. Duscher, E.A. Kenik, S.J. Pennycook, Silicon and zinc telluride nanoparticles synthesized by pulsed laser ablation: Size distributions and nanoscale structure, Applied Surface Science. 127–129 (1998) 355-361.

114. Luo, J., J. Yin, R. Loukrakpam, B.N. Wanjala, B. Fang, S. Shan, L. Yang, M. Nie, M.S. Ng, J. Kinzler, Y.S. Kim, K.K. Luo, C.J. Zhong, Design and electrochemical

characterization of ternary alloy electrocatalysts for oxygen reduction reaction, Journal of Electroanalytical Chemistry. 688 (2013) 196-206.

115. Ma, Z., R. Venkataraman, M. Farooque, Fuel cells – molten carbonate fuel cells | modeling, in Encyclopedia of electrochemical power sources, J. Garche, Editor. 2009, Elsevier: Amsterdam. p. 519-532.

116. Mallick, R.K., S.B. Thombre, N.K. Shrivastava, A critical review of the current collector for passive direct methanol fuel cells, Journal of Power Sources. 285 (2015) 510-529.

117. Mamlouk, M., K. Scott, An investigation of Pt alloy oxygen reduction catalysts in phosphoric acid doped pbi fuel cells, Journal of Power Sources. 196 (2011) 1084-1089.

118. Mayer, T., D. Kreyenberg, J. Wind, F. Braun, Feasibility study of 2020 target costs for pem fuel cells and lithium-ion batteries: A two-factor experience curve approach, International Journal of Hydrogen Energy. 37 (2012) 14463-14474.

119. McLean, G.F., T. Niet, S. Prince-Richard, N. Djilali, An assessment of alkaline fuel cell technology, International Journal of Hydrogen Energy. 27 (2002) 507-526.

120. Mehmood, A., M.A. Scibioh, J. Prabhuram, M.-G. An, H.Y. Ha, A review on durability issues and restoration techniques in long-term operations of direct methanol fuel cells, Journal of Power Sources. 297 (2015) 224-241.

121. Meisel, T., J. Moser, Reference materials for geochemical pge analysis: New analytical data for Ru, Rh, Pd, Os, Ir, Pt and Re by isotope dilution icp-ms in 11 geological reference materials, Chemical Geology. 208 (2004) 319-338.

122. Meyer, E., Atomic force microscopy, Progress in Surface Science. 41 (1992) 3-49.

123. Miley, G.H., N. Luo, J. Mather, R. Burton, G. Hawkins, L. Gu, E. Byrd, R. Gimlin, P.J. Shrestha, G. Benavides, J. Laystrom, D. Carroll, Direct $NaBH_4/H_2O_2$ fuel cells, Journal of Power Sources. 165 (2007) 509-516.

124. Mntungwa, N., V.S. Rajasekhar Pullabhotla, N. Revaprasadu, A facile hybrid route to luminescent znte nanoparticles, Materials Letters. 81 (2012) 108-111.

125. Mnwana, S., Mining and ‘community’ struggles on the platinum belt: A case of sefikile village in the north west province, south africa, The Extractive Industries and Society. 2 (2015) 500-508.

126. Mpinga, C.N., J.J. Eksteen, C. Aldrich, L. Dyer, Direct leach approaches to platinum group metal (pgm) ores and concentrates: A review, Minerals Engineering. 78 (2015) 93-113.

127. Mu, Y., H. Liang, J. Hu, L. Jiang, L. Wan, Controllable pt nanoparticle deposition on carbon nanotubes as an anode catalyst for direct methanol fuel cells, The Journal of Physical Chemistry B. 109 (2005) 22212-22216.

128. Mudiraj, S.P., M.A.R. Biswas, W.E. Lear, O.D. Crisalle, Comprehensive mass transport modeling technique for the cathode side of an open-cathode direct methanol fuel cell, International Journal of Hydrogen Energy. 40 (2015) 8137-8159.

129. Muradov, N., 17 - low-carbon production of hydrogen from fossil fuels, in Compendium of hydrogen energy, V. Subramani, A. Basile, T.N. Veziroğlu, Editors. 2015, Woodhead Publishing: Oxford. p. 489-522.

130. Nebatti, A., C. Pflitsch, B. Curdts, B. Atakan, Using the acetylacetonates of zinc and aluminium for the metalorganic chemical vapour deposition of aluminium doped zinc oxide films, Materials Science in Semiconductor Processing. 39 (2015) 467-475.

131. Neudeck, A., L. Dunsch, Cyclic voltammetry at microstructured electrodes, Journal of Electroanalytical Chemistry. 370 (1994) 17-32.

132. Ni, Z., J. Liu, Y. Wu, B. Liu, C. Zhao, Y. Deng, W. Hu, C. Zhong, Fabrication of platinum submonolayer electrodes and their high electrocatalytic activities for ammonia oxidation, Electrochimica Acta. 177 (2015) 30-35.

133. Nicollet, C., A. Flura, V. Vibhu, A. Rougier, J.M. Bassat, J.C. Grenier, $La_2NiO_{4+\delta}$ infiltrated into gadolinium doped ceria as novel solid oxide fuel cell cathodes: Electrochemical performance and impedance modelling, Journal of Power Sources. 294 (2015) 473-482.

134. Ochoa Muñoz, Y.H., M. Ponce, J.E. Rodríguez Páez, Comparative study of two wet chemical methods of basno3 synthesis: Mechanism of formation of mixed oxide, Powder Technology. 279 (2015) 86-95.

135. Olu, P.Y., F. Deschamps, G. Caldarella, M. Chatenet, N. Job, Investigation of platinum and palladium as potential anodic catalysts for direct borohydride and ammonia borane fuel cells, Journal of Power Sources. 297 (2015) 492-503.

136. Oswin, H.G., M. Salomon, The anodic oxidation of ammonia at platinum black electrodes in aqueous KOH electrolyte, Canadian Journal of Chemistry. 41 (1963) 1686-1694.

137. Papapolymerou, G., V. Bontozoglou, Decomposition of NH_3 on Pd and Ir comparison with Pt and Rh, Journal of Molecular Catalysis A: Chemical. 120 (1997) 165-171.

138. Penner, S.S., Steps toward the hydrogen economy, Energy. 31 (2006) 33-43.

139. Phelane, L., F.N. Muya, H.L. Richards, P.G.L. Baker, E.I. Iwuoha, Polysulfone nanocomposite membranes with improved hydrophilicity, Electrochimica Acta. 128 (2014) 326-335.

140. Pollet, B.G., S. Pasupathi, G. Swart, K. Mouton, M. Lototskyy, M. Williams, P. Bujlo, S. Ji, B.J. Bladergroen, V. Linkov, Hydrogen south africa (hysa) systems

competence centre: Mission, objectives, technological achievements and breakthroughs, International Journal of Hydrogen Energy. 39 (2014) 3577-3596.

141. Qianli, M., P. RanRan, T. Longzhang, M. Guangyao, Direct utilization of ammonia in intermediate-temperature solid oxide fuel cells, Electrochemistry Communications. 8 (2006) 1791-1795.

142. Ramesh, S., A.N. Natasha, C.Y. Tan, L.T. Bang, A. Niakan, J. Purbolaksono, H. Chandran, C.Y. Ching, W.D. Teng, Characteristics and properties of hydoxyapatite derived by sol–gel and wet chemical precipitation methods, Ceramics International. 41 (2015) 10434-10441.

143. Rezaei Niya, S.M., M. Hoorfar, Study of proton exchange membrane fuel cells using electrochemical impedance spectroscopy technique – a review, Journal of Power Sources. 240 (2013) 281-293.

144. Riwotzki, K., M. Haase, Wet-chemical synthesis of doped colloidal nanoparticles: Yvo4:Ln (ln = eu, sm, dy), The Journal of Physical Chemistry B. 102 (1998) 10129-10135.

145. Rosca, V., M.T.M. Koper, Electrocatalytic oxidation of hydrazine on platinum electrodes in alkaline solutions, Electrochimica Acta. 53 (2008) 5199-5205.

146. Roullier, L., E. Laviron, Voltammetric behaviour of electrodes modified by a thick coating of a monomer: Electron transfer controlby an intermediate electrochemically induced dissolution, Journal of Electroanalytical Chemistry. 134 (1982) 181-186.

147. Ryland, A.L., X-ray diffraction, Journal of Chemical Education. 35 (1958) 80.

148. Sakamoto, T., D. Matsumura, K. Asazawa, U. Martinez, A. Serov, K. Artyushkova, P. Atanassov, K. Tamura, Y. Nishihata, H. Tanaka, Operando xafs study of carbon supported ni, nizn, and co catalysts for hydrazine electrooxidation for use in anion exchange membrane fuel cells, Electrochimica Acta. 163 (2015) 116-122.

149. Schlapbach, L., A. Zuttel, Hydrogen-storage materials for mobile applications, Nature. 414 (2001) 353-358.

150. Schneider, S., A. Surrey, D. Pohl, L. Schultz, B. Rellinghaus, Atomic surface diffusion on pt nanoparticles quantified by high-resolution transmission electron microscopy, Micron. 63 (2014) 52-56.

151. Shaikh, S.P.S., A. Muchtar, M.R. Somalu, A review on the selection of anode materials for solid-oxide fuel cells, Renewable and Sustainable Energy Reviews. 51 (2015) 1-8.

152. Shakerian, F., K.H. Kim, J.E. Szulejko, J.W. Park, A comparative review between amines and ammonia as sorptive media for post-combustion co2 capture, Applied Energy. 148 (2015) 10-22.

153. Shrestha, S., M.P. Harold, K. Kamasamudram, Experimental and modeling study of selective ammonia oxidation on multi-functional washcoated monolith catalysts, Chemical Engineering Journal. 278 (2015) 24-35.

154. Silva, J.C.M., S.G. da Silva, R.F.B. De Souza, G.S. Buzzo, E.V. Spinacé, A.O. Neto, M.H.M.T. Assumpção, Ptau/c electrocatalysts as anodes for direct ammonia fuel cell, Applied Catalysis A: General. 490 (2015) 133-138.

155. Steele, B.C.H., Fuel-cell technology: Running on natural gas, Nature. 400 (1999) 619-621.

156. Strmcnik, D., K. Kodama, D. Van der Vliet, J. Greeley, V.R. Stamenkovic, N.M. Marković, The role of non-covalent interactions in electrocatalytic fuel-cell reactions on platinum, Nature chemistry. 1 (2009) 466-472.

157. Su, L., Y.X. Gan, Formation and thermoelectric property of TiO_2 nanotubes covered by Te–Bi–Pb nanoparticles, Electrochimica Acta. 56 (2011) 5794-5803.

158. Sun, C., Z. Xie, C. Xia, H. Li, L. Chen, Investigations of mesoporous CeO_2–Ru as a reforming catalyst layer for solid oxide fuel cells, Electrochemistry Communications. 8 (2006) 833-838.

159. Sun, Q., S. Kim, Synthesis of nitrogen-doped graphene supported Pt nanoparticles catalysts and their catalytic activity for fuel cells, Electrochimica Acta. 153 (2015) 566-573.

160. Suzuki, S., H. Muroyama, T. Matsui, K. Eguchi, Fundamental studies on direct ammonia fuel cell employing anion exchange membrane, Journal of Power Sources. 208 (2012) 257-262.

161. Tang, T.H., P.H. Su, Y.C. Liu, T.L. Yu, Polybenzimidazole and benzyl-methyl-phosphoric acid grafted polybenzimidazole blend crosslinked membrane for proton exchange membrane fuel cells, International Journal of Hydrogen Energy. 39 (2014) 11145-11156.

162. Tayal, J., B. Rawat, S. Basu, Bi-metallic and tri-metallic Pt–Sn/C, Pt–Ir/C, Pt–Ir–Sn/C catalysts for electro-oxidation of ethanol in direct ethanol fuel cell, International Journal of Hydrogen Energy. 36 (2011) 14884-14897.

163. Tian, N., Z.Y. Zhou, S.G. Sun, Platinum metal catalysts of high-index surfaces: From single-crystal planes to electrochemically shape-controlled nanoparticles, The Journal of Physical Chemistry C. 112 (2008) 19801-19817.

164. Tubtimtae, A., S. Phadungdhitidhada, D. Wongratanaphisan, A. Gardchareon, S. Choopun, Tailoring $Cu_{2-x}Te$ quantum-dot-decorated ZnO nanoparticles for potential solar cell applications, Current Applied Physics. 14 (2014) 772-777.

165. Ukropec, R., B.F.M. Kuster, J.C. Schouten, R.A. van Santen, Low temperature oxidation of ammonia to nitrogen in liquid phase, Applied Catalysis B: Environmental. 23 (1999) 45-57.

166. Uríčková, V., J. Sádecká, Determination of geographical origin of alcoholic beverages using ultraviolet, visible and infrared spectroscopy: A review, Spectrochimica Acta Part A: Molecular and Biomolecular Spectroscopy. 148 (2015) 131-137.

167. Van Ravenswaay, J.P., T.H. Roos, A.K.J. Surridge-Talbot, S. Xosa, C. Sattler, Development of a solar fuels roadmap for south africa, Energy Procedia. 69 (2015) 1838-1848.

168. Varcoe, J.R., R.C.T. Slade, E. Lam How Yee, An alkaline polymer electrochemical interface: A breakthrough in application of alkaline anion-exchange membranes in fuel cells, Chemical Communications, (2006) 1428-1429.

169. Vargas-Uscategui, A., E. Mosquera, B. Chornik, L. Cifuentes, Electrocatalysis of the hydrogen evolution reaction by rhenium oxides electrodeposited by pulsed-current, Electrochimica Acta. 178 (2015) 739-747.

170. Verda, V., A. Sciacovelli, Design improvement of circular molten carbonate fuel cell stack through cfd analysis, Applied Thermal Engineering. 31 (2011) 2740-2748.

171. Vesztergom, S., M. Ujvári, G.G. Láng, Dual cyclic voltammetry with rotating ring–disk electrodes, Electrochimica Acta. 110 (2013) 49-55.

172. Vidal-Iglesias, F.J., J. Solla-Gullón, V. Montiel, J.M. Feliu, A. Aldaz, Screening of electrocatalysts for direct ammonia fuel cell: Ammonia oxidation on PtMe (Me: Ir, Rh, Pd, Ru) and preferentially oriented Pt(100) nanoparticles, Journal of Power Sources. 171 (2007) 448-456.

173. Vishnyakov, V.M., Proton exchange membrane fuel cells, Vacuum. 80 (2006) 1053-1065.

174. Vitse, F., M. Cooper, G.G. Botte, On the use of ammonia electrolysis for hydrogen production, Journal of Power Sources. 142 (2005) 18-26.

175. Walther, T., I.M. Ross, Aberration corrected high-resolution transmission and scanning transmission electron microscopy of thin perovskite layers, Physics Procedia. 40 (2013) 49-55.

176. Wang, C., S. Bai, Y. Xiong, Recent advances in surface and interface engineering for electrocatalysis, Chinese Journal of Catalysis. 36 (2015) 1476-1493.

177. Wang, C., H. Gao, X. Chen, W.Z. Yuan, Y. Zhang, Enabling carbon nanofibers with significantly improved graphitization and homogeneous catalyst deposition for high performance electrocatalysts, Electrochimica Acta. 152 (2015) 383-390.

178. Wang, T., Y. Fan, X. Wang, L. Chou, H. Lin, Selectivity enhancement of comos catalysts supported on tri-modal porous Al_2O_3 for the hydrodesulfurization of fluid catalytic cracking gasoline, Fuel. 157 (2015) 171-176.

179. Wang, Z.W., R.E. Palmer, Chapter 6 - atomic-scale structure analysis by advanced transmission electron microscopy, in Frontiers of nanoscience, T. Tatsuya,H. Hannu, Editors. 2015, Elsevier. p. 127-159.

180. Williams, D., C.B. Carter, The transmission electron microscope, in Transmission electron microscopy. 1996, Springer US. p. 3-17.

181. Wu, B., X. Gao, M.-W. Chen, Y.-G. Zhou, Direct amination of 2-(1-tosylalkyl)phenols with aqueous ammonia: A metal-free synthesis of primary amines, Tetrahedron Letters. 56 (2015) 1135-1137.

182. Xing, Y., Synthesis and electrochemical characterization of uniformly-dispersed high loading pt nanoparticles on sonochemically-treated carbon nanotubes, The Journal of Physical Chemistry B. 108 (2004) 19255-19259.

183. Yang, D.S., M.S. Kim, M.Y. Song, J.S. Yu, Highly efficient supported ptfe cathode electrocatalysts prepared by homogeneous deposition for proton exchange membrane fuel cell, International Journal of Hydrogen Energy. 37 (2012) 13681-13688.

184. Yao, K., Y.F. Cheng, Electrodeposited Ni–Pt binary alloys as electrocatalysts for oxidation of ammonia, Journal of Power Sources. 173 (2007) 96-101.

185. Yao, K., Y.F. Cheng, Fabrication by electrolytic deposition of Pt–Ni electrocatalyst for oxidation of ammonia in alkaline solution, International Journal of Hydrogen Energy. 33 (2008) 6681-6686.

186. Yezer, B.A., A.S. Khair, P.J. Sides, D.C. Prieve, Use of electrochemical impedance spectroscopy to determine double-layer capacitance in doped nonpolar liquids, Journal of Colloid and Interface Science. 449 (2015) 2-12.

187. Yin, S.F., B.Q. Xu, X.P. Zhou, C.T. Au, A mini-review on ammonia decomposition catalysts for on-site generation of hydrogen for fuel cell applications, Applied Catalysis A: General. 277 (2004) 1-9.

188. Yuan, H., D. Guo, X. Qiu, W. Zhu, L. Chen, Influence of metal oxides on pt catalysts for methanol electrooxidation using electrochemical impedance spectroscopy, Journal of Power Sources. 188 (2009) 8-13.

189. Zamfirescu, C., I. Dincer, Ammonia as a green fuel and hydrogen source for vehicular applications, Fuel Processes of Technology. 90 (2009) 729-737.

190. Zhang, B., D.D. Ye, J. Li, X. Zhu, Q. Liao, Air-breathing microfluidic fuel cells with a cylinder anode operating in acidic and alkaline media, Electrochimica Acta. 177 (2015) 264-269.

191. Zhang, H., N. Toshima, Preparation of novel au/pt/ag trimetallic nanoparticles and their high catalytic activity for aerobic glucose oxidation, Applied Catalysis A: General. 400 (2011) 9-13.

192. Zhang, L., J. Zhang, D.P. Wilkinson, H. Wang, Progress in preparation of non-noble electrocatalysts for pem fuel cell reactions, Journal of Power Sources. 156 (2006) 171-182.

193. Zhang, X., K.Y. Chan, Water-in-oil microemulsion synthesis of platinum−ruthenium nanoparticles, their characterization and electrocatalytic properties, Chemistry of Materials. 15 (2003) 451-459.

194. Zhang, X., L. Guo, H. Liu, Recovery mechanisms in proton exchange membrane fuel cells after accelerated stress tests, Journal of Power Sources. 296 (2015) 327-334.

195. Zhang, Y., A. Smirnova, A. Verma, R. Pitchumani, Design of a proton exchange membrane (pem) fuel cell with variable catalyst loading, Journal of Power Sources. 291 (2015) 46-57.

196. Zhang, Z., P. Bi, P. Jiang, M. Fan, S. Deng, Q. Zhai, Q. Li, Production of gasoline fraction from bio-oil under atmospheric conditions by an integrated catalytic transformation process, Energy. (2014) DOI 10.1016/j.energy.2015.07.009.